



ÉCOLE
CENTRALE LYON

N° d'ordre NNT : 2021LYSEC49

THÈSE DE DOCTORAT DE L'UNIVERSITÉ DE LYON
opérée au sein de
l'Ecole Centrale de Lyon

École Doctorale N° ED165
Mécanique, Énergétique, Génie Civil et Acoustique (MEGA)

Spécialité/discipline de doctorat :
Biomécanique

Soutenue publiquement le 16/12/2021, par :
Anaïs Moravia

***In vitro* circulatory mock loop study of
non-Newtonian hemodynamics in aorta
phantoms: application to aortic dissection**

Devant le jury composé de :

Bettina FROHNAPFEL	Professeure	Karlsruher Institut für Technologie	Rapporteuse
Nadjia KACHENOURA	Directrice de Recherche	Université Sorbonne	Rapporteuse
Philippe VÉZIN	Directeur de Recherche	Université Gustave Eiffel	Examineur
Jacques OHAYON	Professeur des Universités	Université de Savoie	Président du jury
Phillipe TRESSON	Praticien Hospitalier	Hospices Civils de Lyon	Examineur
Serge SIMOENS	Directeur de Recherche	Ecole Centrale Lyon	Directeur de thèse
Benyebka BOU-SAÏD	Professeur des Universités	INSA Lyon	Co-directeur de thèse
Mahmoud EL HAJEM	Maitre de Conférences	INSA Lyon	Co-directeur de thèse
Pascale KULISA	Chargée de Recherche	Ecole Centrale Lyon	Invitée
Patrick LERMUSIAUX	Professeur des Universités	Hospices Civils de Lyon	Invité

Remerciements

Mes premiers remerciements vont à mes directeurs et encadrants de thèse Serge Simoëns, Benyebka Bou-Saïd et Mahmoud El Hajem pour m’avoir guidée tout au long de ce projet. Je souhaite remercier Serge Simoëns de m’avoir donnée la possibilité de travailler sur ce sujet de thèse passionnant. Au-delà de ses qualités scientifiques, je retiendrai de lui sa joie de vivre, son enthousiasme face à la recherche et sa curiosité communicative. Je remercie également Benyebka Bou-Saïd pour sa disponibilité, son pragmatisme, la confiance qu’il m’a témoignée et son implication dans le projet de sa préparation jusqu’à son aboutissement. Enfin je remercie Mahmoud El Hajem pour son soutien à la fois scientifique, technique et humain ainsi que pour ses indispensables conseils sur le plan expérimental qui m’ont permis de progresser dans ce travail de recherche.

Je tiens à exprimer ma vive gratitude envers Nadja Kachenoura et Bettina Frohnepfel qui ont accepté la charge de rapporteuse pour mon travail de thèse. Je remercie également tous les membres du jury pour l’intérêt porté à mon travail et le temps qu’ils y ont consacré.

Mes remerciements vont également à mes collègues du LMFA, du LaMCoS ainsi que nos collaborateurs des HCL qui ont contribué à l’avancée et au bon déroulement de ce projet de thèse. Je pense en particulier à Arthur Buridon dont l’enthousiasme face au projet et le soutien technique ont fortement enrichi le banc expérimental. Je pense également Benjamin Bognic qui a pris la relève et que je remercie pour sa disponibilité et ses aides multiples durant le développement du banc. Je souhaite également remercier Pascale Kulisa pour sa collaboration attentive, le partage de ses connaissances, les nombreuses discussions que nous avons eues et bien sûr, les tea time du mercredi.

Je remercie très chaleureusement l’équipe TMI — la tMitics — et sa horde de doctorants avec qui j’ai passé trois superbes années. Une équipe de choc aussi performante en science qu’en humour, jeux de mots habiles, accents en tout genre, lancer de carapaces de tortue, shoot laser, (triple) burger, dégustation de pâtisseries chinoises et j’en passe. Une grande famille Lyonnaise avec ses anciens et ses nouveaux à qui je souhaite le meilleur pour la suite.

Enfin je souhaite vivement remercier mes parents et mon fiancé Antoine (assistant thésard n°1) pour leur soutien sans faille, leurs encouragements et leur profond intérêt pour mon projet de thèse. En plus d’un soutien moral, ils ont enrichi des discussions scientifiques, linguistiques, pédagogiques et esthétiques tout au long de mon projet de thèse ainsi que lors de la préparation de ce manuscrit. Merci de m’avoir accompagnée dans cette belle aventure scientifique.

Abstract

Cardiovascular diseases (CVDs) including diseases of the heart and circulatory system are the leading causes of death in the European Union and accounted for about 37% of all deaths in 2017 (OECD (2020)). Among CVDs, we can mention atherosclerosis, aneurysm and aortic dissection (AD). AD is a life-threatening pathology that develops when a tear occurs in the inner layer of the aorta. Blood surges into the tear and a secondary channel develops in between aorta layers. AD results in higher risks of rupture and malperfusion which makes of aortic dissection a pathology with a high mortality rate, difficult to detect in time and to treat in a lasting way. The mechanisms of its development are still poorly understood. Beyond purely biological concepts, fluid dynamics and biomechanics have contributed to AD understanding and pointed out some culprits such as alteration in stress patterns, flow distribution, and vortical flows. However, one of the main limitations in analyzing and understanding these mechanisms is flow visualization. *In vivo*, routine traditional imaging that gives access to fluid velocities such as 4D-MRI or US-doppler suffers from low time and space resolutions. This is one reason why alternative techniques are developed with artificial circulation emulations to overcome human body observation limitations.

The present work proposes an *in vitro* blood flow investigation. An aortic flow simulator was designed to emulate blood flow in aorta models (healthy and pathological) with biofidelic properties. The goal is to explore aorta hemodynamics and address the limitations encountered with *in vivo* traditional imaging as a complementary tool. Particle Image Velocimetry was implemented to accurately measure fluid velocities and compute quantities of interests in the context of disease mechanism understanding (shear rate, shear stress, vorticity, etc). The bench is a circulatory mock loop that accurately recreates the cardiovascular system flowrate and pressure conditions. It accommodates healthy and pathological patient-specific aorta models – also called phantoms – and a panel of inflow conditions as a versatile tool. Phantoms with specific optical and mechanical features were manufactured with silicone injection and 3D printing to approach human aorta behavior. Different blood mimicking fluid were designed to investigate the impact of the more complex non-Newtonian representation of blood compared with the Newtonian simplification. Indeed, the shear-thinning behavior of blood is often neglected in the literature claiming that the Newtonian representation is equivalent. The present work shows that the Newtonian fluid flow in a healthy aorta phantom tends to underestimate shear stress and vortex displacement which could lead to misinterpretation of risky areas and pathological mechanisms. The non-Newtonian representation is, therefore, more adapted to investigate aorta hemodynamics. Finally, the experimental bench was developed in close connection with numerical simulations that focused on aided surgery for aortic dissection. Non-Newtonian flow visualizations were achieved with the *in vitro* simulator and PIV on patient-specific aortic dissection phantoms and compared with numerical results on the same models. It allowed confrontation of both model approaches and opened perspectives for numerico-experimental methods. The developed aortic simulator is a powerful tool to better analyze and understand aortic hemodynamics to complement *in vivo* and *in silico* investigations.

Résumé

Les maladies cardiovasculaires (MCV), y compris les maladies cardiaques et circulatoires, sont la principale cause de décès dans l'Union Européenne et représentaient environ 37% des décès en 2017 (OCDE). Parmi les MCV on peut citer les pathologies artérielles telles que l'athérosclérose, les anévrysmes et la dissection aortique. Cette dernière se développe à la suite d'une déchirure dans la paroi interne de l'aorte. Le sang y pénètre et crée un chenal secondaire entre les couches de la paroi. Des risques de rupture et de malperfusion en découlent et font de la dissection aortique une pathologie à fort taux de mortalité, difficile à détecter et à traiter de façon durable. Les mécanismes de son développement sont encore mal connus. Au-delà des concepts purement biologiques, la dynamique des fluides et la biomécanique ont contribué à leur compréhension et ont mis en évidence certains liens avec l'altération des contraintes aux parois, la distribution des flux et les écoulements tourbillonnaires. Cependant, l'une des principales limites est la visualisation des écoulements. *In vivo*, l'imagerie médicale traditionnelle donnant accès à des écoulements telle que l'IRM-4D ou l'US-doppler souffre de faibles résolutions spatio-temporelles. Des techniques alternatives sont alors développées grâce à des émulateurs de circulation sanguine – *in vitro* ou *in silico* - pour surmonter les limites de l'observation directe *in vivo*.

Ce travail propose une étude des flux sanguins *in vitro*. Un simulateur a été conçu pour reproduire les écoulements sanguins sur modèles d'aorte biofidèles (saines et pathologiques). L'objectif est d'explorer l'hémodynamique de l'aorte et de surmonter les limites rencontrées avec l'imagerie médicale traditionnelle comme outil complémentaire. La vélocimétrie par image de particules a été mise en œuvre pour mesurer avec précision les vitesses des fluides et calculer les quantités d'intérêt liées à la compréhension des mécanismes de la maladie (taux de cisaillement, contrainte de cisaillement, tourbillon, etc.). Le banc est un circuit hydraulique qui recrée avec précision les conditions de débit et de pression du système cardiovasculaire. Il s'adapte à des modèles d'aorte patient-spécifique - également appelés fantômes - sains et pathologiques et à un large panel de conditions d'écoulement. Des fantômes dotés de caractéristiques optiques et mécaniques spécifiques ont été fabriqués par injection de silicone et impression 3D pour se rapprocher du comportement de l'aorte humaine. Différents fluides imitant le sang ont été conçus pour étudier l'impact de la représentation non-newtonienne plus complexe du sang par rapport à la simplification newtonienne. En effet, le comportement rhéofluidifiant du sang est souvent négligé dans la littérature en affirmant que la représentation newtonienne est équivalente. Cette étude montre que les écoulements newtoniens dans un fantôme d'aorte sain ont tendance à sous-estimer la contrainte de cisaillement et le déplacement des vortex. Cela peut conduire à une mauvaise interprétation des zones à risque et des mécanismes pathologiques. La représentation non-newtonienne est donc plus adaptée à l'étude de l'hémodynamique aortique. Enfin, le banc expérimental a été développé en lien étroit avec des simulations numériques centrées sur la chirurgie assistée pour la dissection aortique. Des visualisations d'écoulements non-newtoniens ont été réalisées avec le simulateur *in vitro* et la PIV sur des fantômes de dissection aortique patient-spécifique et comparées aux résultats numériques sur les mêmes modèles. Cela a permis la confrontation des deux approches et l'ouverture de perspectives sur des méthodes numériques-expérimentales. Le simulateur aortique développé est un outil puissant pour mieux analyser et comprendre l'hémodynamique aortique afin de compléter les investigations *in vivo* et *in silico*.

Résumé long (FR)

Les maladies cardiovasculaires (MCV), y compris les maladies cardiaques et circulatoires, sont la principale cause de mortalité dans l'Union Européenne et représentaient environ 37% des décès en 2017. Parmi les MCV on peut citer les pathologies artérielles telles que l'athérosclérose, les anévrismes et la dissection aortique. Cette dernière se développe à la suite d'une déchirure dans la paroi interne de l'aorte. Le sang y pénètre et crée un chenal secondaire entre les couches de la paroi. En découlent des risques accrus de rupture et de malperfusion des organes qui font de la dissection aortique une pathologie à fort taux de mortalité, difficile à détecter et à traiter de façon durable. Les mécanismes de son développement sont encore mal connus et les facteurs fréquemment impliqués dans l'expansion de cette maladie ne sont pas seulement biologiques. La dynamique des fluides et la biomécanique ont contribué à sa compréhension et ont mis en évidence certaines corrélations avec l'altération des schémas de contraintes aux parois, la distribution des écoulements, les flux tourbillonnaires et hélicoïdaux. Cependant, l'une des principales limites est la visualisation des écoulements. *In vivo*, l'imagerie médicale traditionnelle donnant accès à des écoulements telles que l'IRM-4D ou l'US-doppler souffre de faibles résolutions spatio-temporelles. Des techniques alternatives sont alors développées grâce à des émulateurs de circulation sanguine — *in vitro* ou *in silico* — pour surmonter les limites de l'observation du corps humain.

Du côté de l'*in vitro*, des bancs expérimentaux sont développés mettant en scène des représentations physiques de l'aorte, du sang et de la circulation. Des éléments artificiels ou *ex vivo* peuvent être introduits en fonction du degré de biofidélité, des simplifications de représentations hémodynamiques et des possibilités expérimentales. Communément, des répliques d'aortes — appelées fantômes — sont réalisées à partir de scanner ou IRM de patient afin d'obtenir une géométrie patient-spécifique. Cet aspect est non négligeable lorsque l'on sait que les pathologies aortiques sont fortement liées à des facteurs géométriques. Néanmoins, la majorité des études utilisent des modèles simplifiés à parois rigides s'éloignant ainsi de la souplesse de l'aorte humaine et des réponses mécaniques qui en découlent. D'autre part, divers fluides analogues au sang sont proposés dans la littérature en faisant le choix d'imiter le caractère rhéofluidifiant du sang ou de le simplifier par une représentation newtonienne. La constante amélioration de ces répliques d'aorte et de sang permettent de se rapprocher des propriétés *in vivo* et de proposer des simulateurs d'écoulement plus réalistes. Néanmoins, à notre connaissance, aucune étude ne propose à la fois des fantômes d'aorte de géométrie réelle dont les parois ont des propriétés mécaniques biofidèles avec une représentation non-Newtonienne de sang. Enfin l'approche *in vitro* permet de bénéficier des techniques de visualisation des écoulements issues de la mécanique des fluides. Celles-ci permettent d'atteindre des résolutions spatio-temporelles bien plus élevées que l'imagerie médicale classique. L'objectif de la thèse est de développer un simulateur d'écoulement aortique représentant les propriétés non-newtonienne du sang et les propriétés mécaniques de l'aorte pour mener des analyses d'écoulement grâce à une technique de visualisation haute définition : la vélocimétrie par image de particules (PIV). Des études *in vitro* de cas patient-spécifiques sont menées sur des patients atteints de dissections aortiques. Ce projet est développé en lien étroit avec

des simulations numériques (thèse parallèle) et des données cliniques afin de proposer un outil complémentaire à l'*in vivo* et à l'*in silico* dans le cadre de la compréhension des mécanismes à l'origine de cette pathologie.

Le manuscrit se compose de quatre chapitres. Le premier chapitre introduit les concepts fondamentaux étudiés dans la thèse. Les propriétés du système cardiovasculaire, de l'aorte et du sang sont décrites afin de définir l'environnement du système et ses propriétés physiques. Une section est dédiée aux concepts de l'hémodynamique mettant en avant la complexité de ce type d'écoulement selon trois propriétés majeures : le comportement non-Newtonien du sang, les écoulements pulsés et les parois souples des vaisseaux. Enfin les pathologies aortiques (en particulier la dissection aortique) et les traitements correspondants sont abordés dans la dernière partie. Cela est illustré par une revue de littérature sur la surveillance, l'analyse et le traitement des pathologies aortique via différentes approches : *in vitro*, *ex vivo*, *in vitro* et *in silico*. La thèse se positionne sur la branche *in vitro*, non pas comme substitut aux autres méthodes mais comme complément bénéficiant des outils de mesure de la mécanique des fluides classique.

Le deuxième chapitre porte sur la conception du banc expérimental. Le simulateur d'écoulement aortique est composé de trois éléments principaux : un circuit imitant la circulation cardiaque, un fluide analogue au sang et un fantôme d'aorte. Une technique de visualisation — la PIV — est mise en place afin de visualiser en 2D les écoulements dans le fantôme d'aorte avec une haute résolution spatiale et temporelle (en dessous de $1 \times 1 \text{ mm}^2$). La fonction du circuit est de reproduire les débits et pressions pulsés dans le fantôme d'aorte associé à un système de contrôle et d'enregistrement des données en temps réel. Le circuit peut accueillir le fantôme d'aorte, conduire et préserver le fluide de travail et permettre des accès optiques pour l'équipement PIV. Dans un second temps, un fluide analogue au sang est fabriqué pour imiter certaines propriétés rhéologiques du sang, en particulier son aspect rhéofluidifiant. Le fluide est composé d'eau, de glycérine, de gomme xanthane pour le caractère non-newtonien et de sel pour ajuster son indice de réfraction et ainsi limiter les corrections optiques post-PIV. Enfin, un fantôme d'aorte transparent (pour les accès optiques) avec des parois souples et une élasticité réaliste est fabriqué par injection de silicone afin de se rapprocher des interactions *in vivo* entre la paroi des vaisseaux et le fluide. Chaque élément est conçu pour améliorer la biofidélité du banc expérimental et satisfaire aux exigences des moyens de mesures optiques.

Dans le troisième chapitre, le simulateur d'écoulement aortique est testé sur un fantôme d'aorte abdominale dont la géométrie est réaliste et les parois souples. Les fluides analogues au sang Newtonien et non-Newtonien sont souvent considérés comme équivalents dans les expériences de simulateur *in vitro* sur les artères larges mais sur des modèles souvent simplifiés. Dans cette étude, une comparaison entre fluide Newtonien et non-Newtonien est menée sur le banc expérimental sous condition d'écoulements pulsés dans notre modèle d'aorte souple plus réaliste. Dans ce type de géométrie, l'hypothèse Newtonienne semble inadaptée car elle sous-estime la complexité de la distribution des écoulements, l'amplitude des contraintes aux parois et le déplacement des vortex. Dans le contexte de la compréhension des mécanismes conduisant aux maladies cardiovasculaires, cette simplification peut notamment conduire à une mauvaise interprétation des zones à risques. L'hypothèse non-Newtonienne est donc adoptée pour le banc expérimental. Enfin, ces

expériences sont utilisées pour évaluer les performances du banc concernant la reproductibilité cycle-à-cycle, la réponse mécanique du fantôme aux écoulements pulsés, la vitesse de l'onde de pouls et l'élasticité du matériau. Ces aspects sont quantifiés et semblent en accord avec les données *in vivo*, ce qui fait du banc un outil *in vitro* intéressant pour reproduire et analyser les écoulements aortiques dans l'optique d'étudier des cas pathologiques.

Le quatrième et dernier chapitre est dédié à l'étude de cas de dissection aortique grâce au simulateur d'écoulement conçu, développé et testé dans les chapitres précédents. A défaut de pouvoir utiliser l'injection de silicone sur des géométries aussi complexes, deux nouveaux fantômes d'aorte présentant une dissection sont fabriqués par impression 3D pour obtenir un matériau transparent et ainsi satisfaire aux exigences de la PIV. L'impression 3D n'a pas permis d'obtenir des matériaux souples, les parois sont donc rigides. Des visualisations d'écoulement avec fluide non-Newtonien sont conduites dans des zones critiques des fantômes : forte réduction dans le faux chenal, site d'entrée de la dissection et entrée de l'aorte. Enfin, une confrontation préliminaire est menée entre le modèle *in vitro* présenté dans cette thèse et des simulations numériques de type CFD (Computational Fluid Dynamics). Les vitesses et distributions des écoulements sont analysés et comparés à des simulations sur les mêmes modèles. Ces simulations sont issues d'une thèse parallèle axée sur l'aide virtuelle à la chirurgie (Pan (2021)) et ont montré des écoulements similaires à ceux calculés par PIV malgré des différences dans le paramétrage des conditions limites (modèles Windkessel non optimisés). Ces résultats sont particulièrement encourageants pour la suite du projet vers une approche combinée numérique-expérimentale de l'analyse et du traitement de la dissection aortique.

En conclusion, la thèse se positionne sur une approche *in vitro* de l'étude des écoulements hémodynamiques sur fantôme d'aorte. Dans un premier temps, un modèle d'aorte saine aux propriétés mécaniques biofidèles est implémenté dans le banc expérimental. Dans un second temps, la pathologie de la dissection aortique est investiguée sur deux cas patient-spécifiques. Un nouvel outil de reproduction et de visualisation d'écoulement est proposé pour améliorer la compréhension des mécaniques pathologiques artériels. La composante la plus avancée du banc par rapport à la littérature est la combinaison de fantômes à géométries patient-spécifiques et la composante non-newtonienne du fluide analogue au sang. Cette dernière est apparue non négligeable lors d'expériences comparatives entre fluide newtonien et non-newtonien au risque de mal interpréter la structure des écoulements. L'une des difficultés est la préservation des propriétés rhéofluidifiantes le long de l'expérience qui est assurée ici par le circuit hydraulique avec une pompe à cavité progressive qui minimise les cisaillements. Enfin l'une des plus grandes difficultés est la fabrication de fantôme d'aorte à la fois souple et transparent. Un tel fantôme a été réalisé avec succès sur une modèle d'aorte saine avec une réponse mécanique réaliste grâce au matériau silicone. Dans le cas des dissections aortiques, des modèles transparents à parois rigides ont été fabriqués par impression 3D. Cette technique permet une fabrication rapide sur géométrie complexe (deux chenaux parallèles et tortueux) mais pas encore l'alliance transparence/souplesse. La visualisation des écoulements est réalisée par PIV dans des zones critiques avec des champs de vitesse de qualité plus ou moins bonne en fonction du fantôme. Celui-ci étant le point le plus critique dans la qualité des images

produites. Néanmoins une comparaison avec des simulations numériques a permis une inter-validation des deux approches grâce à des résultats en accord en terme de distribution d'écoulements, de contraintes de cisaillement et de vorticité. Le modèle *in vitro* permet ainsi de raccrocher le modèle virtuel à une composante physique et une référence comparative. Inversement, le modèle *in silico* permet une analyse plus complète des composantes hémodynamiques (visualisation 3D, champs de pression, etc.). Enfin le banc est construit en échelle 1 afin de permettre une comparaison directe avec des données *in vivo*. Une future application du banc sera l'entraînement à la chirurgie qui pourra se mettre en place par la fabrication rapide de fantôme d'aorte correspondant à un patient et en implémentant ses conditions de débits et pressions grâce à l'adaptabilité du contrôle des cycles. Le banc a été conçu de façon à accueillir à différents modèles d'aorte et conditions de cycles ce qui en fait un outil puissant pour l'étude des écoulements artériels *in vitro* et un complément pertinent à l'*in vivo* et l'*in silico*.

Contents

Nomenclature	xiii
1 Background	5
1.1 Cardiovascular system anatomy and physiology	8
1.1.1 Cardiovascular system	8
1.1.2 Aorta geometry and morphology	10
1.1.3 Aorta histology and mechanical properties	10
1.1.4 Blood rheology	15
1.1.4.1 Blood function and composition	15
1.1.4.2 Rheology and rheometry	15
1.1.4.3 Blood viscosity	18
1.1.4.4 Other rheological properties	22
1.2 Hemodynamical flows	25
1.2.1 Basic concepts : pressure and flow distribution	25
1.2.2 Pressure wave propagation	26
1.2.3 Fluid mechanics governing equations	28
1.2.4 Flow characterisation using dimensional analysis	29
1.2.5 Blood flow simplified models	31
1.2.6 Channel geometry and singularities	37
1.2.7 Compliant walls and Windkessel models	39
1.3 Effects of pathologies on hemodynamics (and vice versa)	40
1.3.1 Aorta pathologies	40
1.3.2 Hemodynamics : the key to understand diseases and develop treatments	44
1.3.3 From <i>in vivo</i> to <i>in silico</i> approach	46
1.3.4 Our trends in the <i>in vitro</i> approach	53
1.4 Conclusion	53
2 <i>In vitro</i> setup : how to mimic and assess aortic flows ?	55
2.1 Background	58
2.2 Circulatory mock loop	58
2.2.1 Mock loop setup	58
2.2.2 Pulsatile flow control : waveform and reproducibility	61
2.3 Particle Image Velocimetry	63
2.3.1 Principle	63

2.3.2	Implementation on the experimental setup	67
2.4	Aorta phantoms	71
2.4.1	Phantom properties	71
2.4.2	Geometry reconstitution	73
2.4.3	Manufacturing technique	74
2.4.4	Compliant phantom: Young's modulus	75
2.4.5	Refractive indexes	76
2.5	Blood mimicking fluid	76
2.5.1	Composition and target properties	77
2.5.2	Non-Newtonian BMF in the literature	79
2.5.3	Fabrication and viscometry	80
2.5.4	Results	81
2.5.5	Discussion and limitations	88
2.6	Conclusion	89
3	Abdonimal aortic flow with Newtonian and non-Newtonian blood mim-	
	icking fluid	91
3.1	Background	94
3.2	Materials and methods	96
3.2.1	Experimental setup	96
3.2.2	PIV measurements	98
3.2.3	Image post-processing	99
3.3	Newtonian vs non-Newtonian BMF: flow analysis	101
3.3.1	Wall displacement	101
3.3.2	Inflow conditions	101
3.3.3	Flow distribution	104
3.3.4	Vortex tracking	107
3.3.5	Shear rates and shear stresses	110
3.4	Discussion	113
3.4.1	Related geometry flow distribution	113
3.4.2	Limitations	114
3.4.3	Newtonian versus non-Newtonian representation	115
3.5	Phantom performances : pressure wave velocity and elasticity	116
3.5.1	The lnD-V method	116
3.5.2	PWV and elasticity evaluation with PIV	117
3.5.3	Limitations	121
3.6	Conclusion	122
4	Aortic dissection case studies	125
4.1	Background	128
4.2	Aorta phantoms	129
4.2.1	Phantom properties and geometry	130
4.2.2	3d printing testing approach	131
4.2.3	Refractive indexes	133
4.3	Materials and methods	136

4.3.1	Experimental setup	136
4.3.2	PIV measurements	138
4.3.3	Image post-processing	140
4.4	Flow analysis: AD1 case	141
4.4.1	Flow distribution	141
4.4.2	Vortices	145
4.4.3	Discussion and limitations	146
4.5	Flow analysis: AD2 case	147
4.5.1	Flow distribution	147
4.5.2	Shear quantities and vortices	148
4.5.3	Discussion	153
4.6	Comparison with numerical simulation: preliminary study	155
4.6.1	Simulation setup	155
4.6.2	Results and discussion	157
4.6.3	Limitations and perspectives	163
4.7	Conclusion	164
A	Experimental setup	185
B	Sensors installation and characteristics	189
C	BMF fabrication and rheometry	193
C.1	Fabrication	193
C.2	Rheometry	194
D	Newtonien vs non-Newtonian velocity fields	195
E	Vortex identification	197
E.0.1	Vorticity	197
E.0.2	Swirling strength	198
E.0.3	Practical case on AA phantom	199
E.0.4	Practical case on AD phantoms	200
F	Gradient underestimation	203
G	3D printing techniques : resins and material jetting	205
H	Aortic dissection phantoms	209

Nomenclature

Abbreviations

AA	Abdominal Aorta
AD	Aortic Dissection
BMF	Blood Mimicking Fluid
CFD	Computational Fluid Dynamics
CVD	Cardiovascular Disease
DIC	Digital Image Correlation
DLP	Digital Light Processing
EVAR	Endovascular aortic repair
FL	False lumen
FSI	Fluid-Solid Interaction
HB	Human Blood
Ht%	Hematocrit percentage
LCD	Liquid Crystal Display
MRI	Magnetic Resonance Imaging
NRMSE	Normalized Root Mean Square Error
PIV	Particle Image Velocimetry
PTV	Particle ImTracking Velocimetry
PWV	Pressure Wave Velocity
RANS	Reynolds Average Navier Stokes Equations
RBCs	Red Blood Cells

RI	Refractive index
ROI	Region-of-interest
SLA	Stereolithography
TL	True lumen
US	Ustrasound
Wat	Water
WBCs	White Blood Cell
WSS	Wall Shear Stress

Chemistry

CO ₂	Carbone dioxide
O ₂	Dioxygen
EDTA	Ethylenediaminetetraacetic acid
Gly	Glycerin
KSCN	Potassium thiocyanate
NaCl	Sodium chloride
NaI	Sodium iodide
NaSCN	Sodium thiocyanate

PAA	Polyacrylamide
PMMA	Polymethyl methacrylate
XG	Xanthan Gum

Dimensionless numbers

α	Womersley number
Re	Reynolds number

St	Stokes number	μ	viscosity
Redundant symbols		ω	vorticity
Δt	PIV time lapse between a pair of images	ρ	Fluid density
Λ_{XYic}	Oriented swirling strength in XY plane	τ	Shear stress
		P	Pressure
μ_0	Zero shear rate viscosity	Q	Flowrate
μ_∞	Infinite shear rate viscosity	T	Cycle period

Introduction

Cardiovascular diseases (CVDs) including diseases of the heart and circulatory system are the leading cause of death in the European Union and accounted for about 37% of all deaths in 2017 (OECD (2020)). The risk of death or disability increases with age and mostly concerns people over 65 years old. In Europe about 20% of the population is over 65. According to Eurostat (2021), in 2050, this age group will represent 30% of the population. The European and world population are continuously aging and the incidence of cardiovascular diseases will inevitably increase. In addition, CVDs involve serious comorbidity risks when contracting other diseases. In the past two years, CVDs and related risks factor (hypertension and diabetes) were among the leading comorbidity of severe COVID-19 cases (Naeini et al. (2021); Bae et al. (2021)). This is one more reason for global health research to focus on the causes, diagnosis, treatment, and prevention of CVDs.

Factors that have frequently been implicated in the development and expansion of cardiovascular diseases are not only purely biological. Fluid dynamics and biomechanics have contributed to their understanding and pointed out some culprits such as alteration in stress patterns, flow distribution and vortical flows (Bürk et al. (2012); Kolipaka et al. (2017)). However, one of the main limitation in analyzing and understanding disease mechanisms is flow visualization. Indeed, one may not understand a phenomenon if it cannot accurately be observed and described. *In vivo*, traditional imaging that gives access to fluid velocities such as 4D flow MRI or US-doppler has revolutionized medical imaging but still suffers from low time and space resolutions (Lotz et al. (2002); Medero et al. (2018)). This is one reason why alternative techniques are developed with artificial circulation emulations to overcome human body observation limitations.

In silico models mimic *in vivo* conditions with numerical simulations thanks to the improvement of computational power. It has increased the amount and enlarged the panel of physical quantities that could be assessed simultaneously. However, one of the main difficulty is to accurately represent human circulation conditions in a virtual environment. Extrapolating conclusions and insights from a simulation to real life can be hazardous and still requires a first validation with physical models before using the computed information (Bonfanti et al. (2020); Soudah et al. (2015)). Therefore, *in vitro* benchtop experiments are also developed with physical representations of aorta, blood and circulation (Deplano et al. (2007); Büsen et al. (2017); Thirugnanasambandam et al. (2021)). This approach benefits from fluid mechanics traditional flow visualization techniques such as particle tracking and particle image velocimetry with much higher resolutions than 4D-MRI and US-doppler. In the literature, a large amount of *in vitro* studies proposed new ways to investigate aortic flow focusing on diseases such as atherosclerosis (Walker et al. (2014)),

aneurysm (Deplano et al. (2014)), and aortic dissection (Bonfanti et al. (2020)) with those enriched flow and velocity fields visualization techniques. These *in vitro* approaches are not intended to replace but to complement medical imaging with alternative tools. The present study mainly focuses on this last pathology hemodynamics: aortic dissection.

Among CVDs, aortic dissection (AD) is a life threatening condition in which a tear occurs in the inner layer of the aortic wall. Blood surges into the tear, causing the separation (dissection) of aorta layers and the formation of a blood channel in between the layers. This secondary channel is called the "false lumen" as opposed to the "true lumen" which is the aorta original path for blood. AD is a low incidence condition among cardiovascular diseases (about 5 to 30 cases per 1 million people per year in western countries) but has a high morbidity and mortality rate. As an example, a study from Melvinsdottir et al. (2016) on acute thoracic aortic dissection showed that 21.4% of patients who arrived at the hospital died within 24h and 30-day mortality still reaches 45.2% of patients. AD is a complex pathology, difficult to treat and strongly related to hemodynamics and vessel geometrical features. Indeed, true and false lumen flow interactions, pressure distributions, low wall shear stress regions can effect the dissection expansion and perfusion of surrounding organs (Nienaber et al. (2016); Clough et al. (2012)).

The present thesis is part of a broader project named @NEDA for the analysis and treatment of aortic dissection with numerico-experimental tools involving three research entities: LMFA (Ecole Centrale Lyon), LaMCoS (INSA de Lyon) and the Hopital Louis Pradel (Hospices Civils de Lyon). The goal is to combine *in vitro* and *in silico* models of AD to investigate hemodynamical flows in this pathology. The present work focuses on the experimental part of the project consisting in designing an aortic flow simulator that is used to emulate blood flow in aorta models (healthy and pathological) with biofidelic properties. The objective is to implement a high resolution flow visualization device to explore aorta hemodynamics and address the limitations encountered with *in vivo* traditional imaging as a complementary tool. We will implement Particle Image Velocimetry to accurately measure fluid velocities and compute quantities of interests in the context of disease mechanism understanding (shear rate, shear stress, vorticity, etc). The bench should accommodate healthy and pathological aorta models and a panel of inflow conditions as a versatile tool (figure 1). Furthermore, the experimental bench is developed in close connection with numerical simulation from a parallel PhD thesis which focuses on aided surgery for AD (Pan et al. (2020)). It will allow confrontation and inter-validation of both model approaches.

The thesis is organized in four chapters. The first one focuses on the general concepts of hemodynamics used in this work. It also provides a short literature review about aortic flow studies from the *in vivo* to the *in silico* point of view in order to set the current work positioning and objectives. The second chapter describes the process of designing the aortic flow simulator in terms of circulatory mock loop, aorta model, blood mimicking fluid, and visualization technique. The third chapter is an experimental study of aortic flows in a healthy model to investigate the impact of blood mimicking fluid choice on flows (Newtonian vs non-Newtonian). The simulator accuracy and limitations are also addressed to evaluate the designed system. Finally, the last chapter explores hemodynamics in aor-

tic dissection models thanks to the simulator. Preliminary comparisons with numerical simulations are provided to confront and complement *in vitro* results.

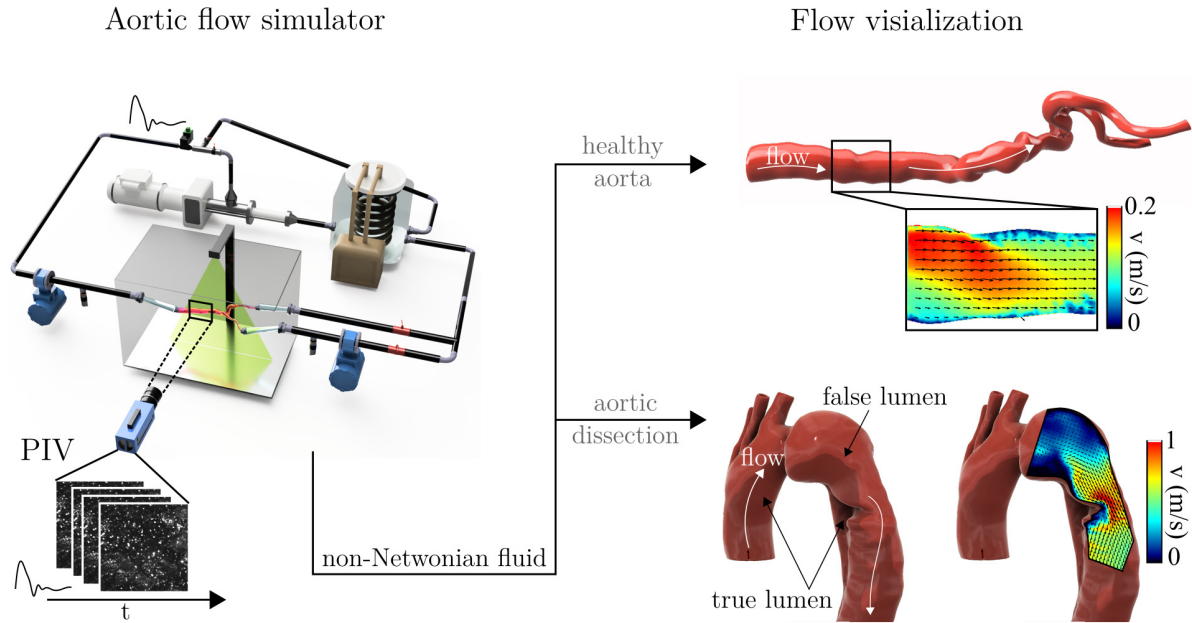


Figure 1: Aortic flow simulator and flow visualization with on healthy aorta and AD.

CHAPTER 1

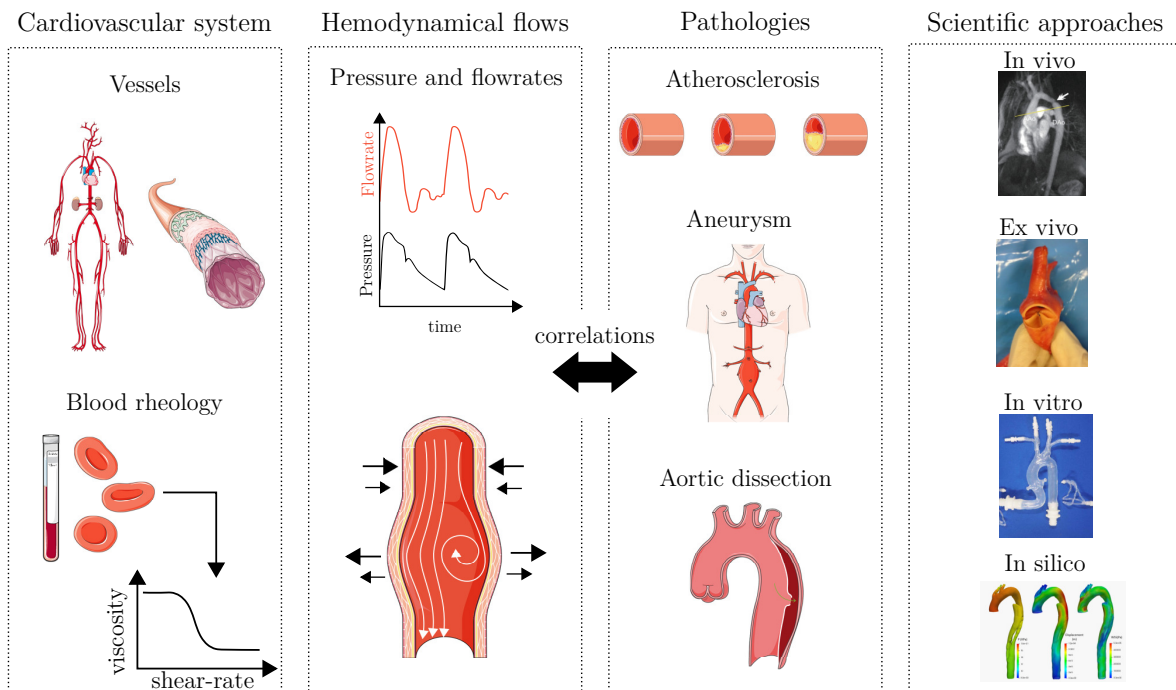
Background

Contents

1.1	Cardiovascular system anatomy and physiology	8
1.1.1	Cardiovascular system	8
1.1.2	Aorta geometry and morphology	10
1.1.3	Aorta histology and mechanical properties	10
1.1.4	Blood rheology	15
1.2	Hemodynamical flows	25
1.2.1	Basic concepts : pressure and flow distribution	25
1.2.2	Pressure wave propagation	26
1.2.3	Fluid mechanics governing equations	28
1.2.4	Flow characterisation using dimensional analysis	29
1.2.5	Blood flow simplified models	31
1.2.6	Channel geometry and singularities	37
1.2.7	Compliant walls and Windkessel models	39
1.3	Effects of pathologies on hemodynamics (and vice versa)	40
1.3.1	Aorta pathologies	40
1.3.2	Hemodynamics : the key to understand diseases and develop treatments	44
1.3.3	From <i>in vivo</i> to <i>in silico</i> approach	46
1.3.4	Our trends in the <i>in vitro</i> approach	53
1.4	Conclusion	53

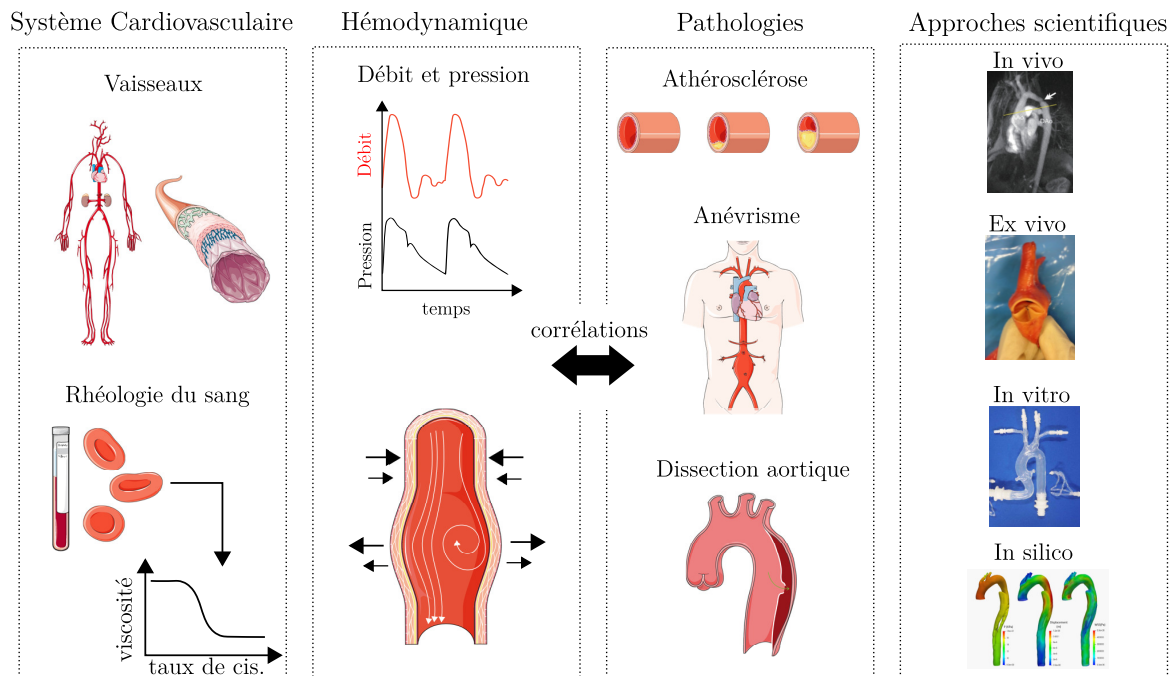
Abstract

This chapter provides an introduction to the main concepts studied in this thesis. The cardiovascular system, aorta and blood properties are described in the first section to define the system environment and physical properties. It includes an anatomical and physiological overview of the circulatory system and the aorta, followed by a depiction of blood rheological properties which focuses on its non-Newtonian behavior. The second section deals with mathematical hemodynamics concepts and models to describe the complexity of blood flows. More specifically, three main properties are discussed : fluid non-Newtonian behavior, oscillatory flow and compliant walls. Finally, aortic diseases and treatments are addressed in the last part to emphasize their close connection with hemodynamical flows. It is illustrated by a literature review on hemodynamics studies about monitoring, analyzing and treating aortic diseases with different scientific approaches: *in vivo*, *in vitro* and *in silico*. This chapter conclusion defines the present study positioning among these approaches and its main scientific goals.



Résumé

Ce chapitre introduit les concepts fondamentaux étudiés dans cette thèse. Les propriétés du système cardiovasculaire, de l'aorte et du sang sont décrites dans la première section afin de définir l'environnement du système et ses propriétés physiques. Sont inclus, un aperçu de l'anatomie et de la physiologie du système cardiovasculaire suivi d'une description de la rhéologie du sang en se focalisant sur ses propriétés non-Newtoniennes. La deuxième section porte sur les concepts mathématiques de l'hémodynamique et les modèles décrivant la complexité des écoulements sanguins. Plus précisément les trois principales propriétés abordées sont : le comportement non-Newtonien du fluide, les écoulements pulsés et les parois souples des vaisseaux. Enfin, les pathologies aortiques et les traitements sont abordés dans la dernière partie afin d'expliquer leurs liens étroits avec les flux hémodynamiques. Ceci est illustré par une revue bibliographique sur la surveillance, l'analyse et le traitement des pathologies aortiques via différentes approches : *in vivo*, *in vitro* et *in silico*. Le chapitre se conclut par une définition des objectifs et du positionnement de cette thèse parmi ces différentes approches.



1.1 Cardiovascular system anatomy and physiology

The study of hemodynamics requires some knowledge of the cardiovascular anatomy and physiology. This section provides a brief overview of the cardiovascular system, aorta and blood rheology to set the foundations of later discussed blood flow analysis, development of pathologies and experimental designs to mimic and analyze hemodynamical flows.

1.1.1 Cardiovascular system

The cardiovascular system is a network of vessels through which the blood is pumped around the body in order to transport respiratory gases, nutrients and metabolic products. The system organs consist of arteries, veins, the heart and a conveyed fluid: blood. The **heart** is located in the thorax between the two lungs. This muscle organ pumps blood into the circulatory system through blood vessels. There are three main kinds of blood vessels: arteries, veins and capillaries [Marieb and Hoehn \(2014\)](#). **Arteries** transport oxygenated blood from the heart to other organs while **veins** carry back blood from organs to the heart. In distributed organs, connection between veins and arteries is ensured by micro-vessels called **capillaries** (figure 1.1).

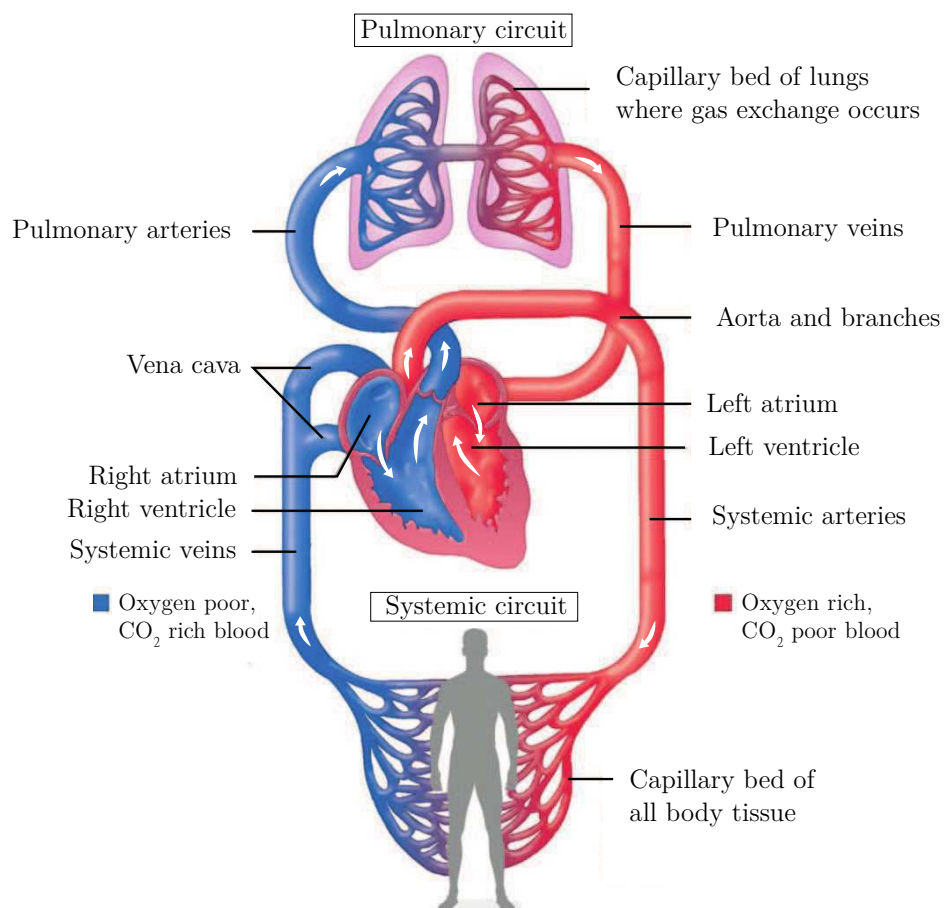


Figure 1.1: Human aorta anatomy.

The system can be divided into two sub-systems, each of them ensuring different functions.

- **Pulmonary circulation:** transports deoxygenated blood from the heart to lungs alveoli where the fluid receives O_2 and releases CO_2 . Oxygenated blood is then moved back to the heart where it will be pumped to the rest of the body through the other sub-system. The pulmonary circulation is a low-pressure circulation (25-30 mmHg) to optimize gas exchanges in the lungs without damaging alveoli and capillaries.
- **Systemic circulation:** carries oxygenated blood from the heart to the rest of the body and then brings it back to the heart. Blood is pumped under high pressure (140-90 mmHg) in the aorta and branching to ensure oxygen distribution and waste collection in tissues all around the body. Then, veins bring back the fluid to the heart to re-inject it in the pulmonary sub-system.

To ensure cross flow between pulmonary and systemic circulation, the heart pumps blood from one system to the other. Thus, the heart acts as a double pump made up of four cavities: right and left atrium — where blood enters the heart — and right and left ventricles — where blood is pumped out of the heart (figure 1.1). This double pump function imposes a pulsatile cardiac cycle with two phases: **diastole** and **systole**. **Diastole** corresponds to the ventricle relaxation phase when blood flows from right and left atrium to their respective ventricle. **Systole** consists in the contraction of both ventricles to eject blood into the two sub-systems. In addition, to ensure unidirectional and two phases flow, valves between atrium and ventricle prevent back flow in the atrium during ventricle contraction. While valves between ventricles and arteries prevent blood from leaving the heart during diastole. Figure 1.2 depicts the different phases of the cardiac cycle with pressure depending on the location (from ventricle to aorta).

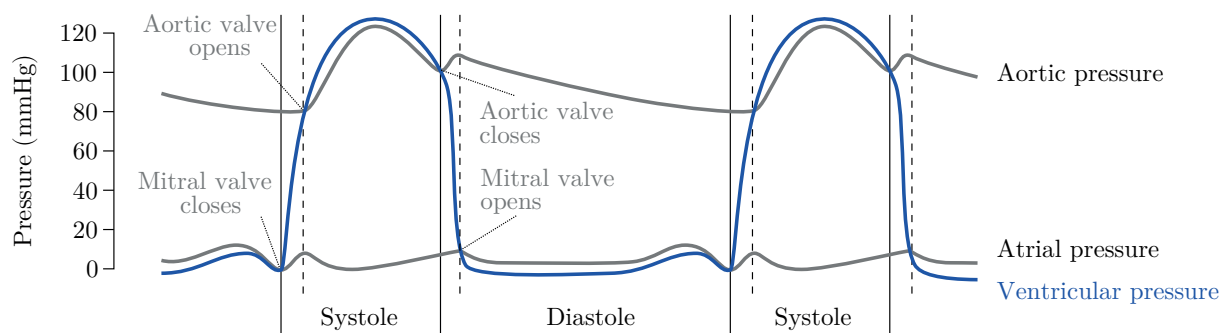


Figure 1.2: Pressure diagram representing two successive cardiac cycles. Atrial, ventricular, and aortic pressures are shown with their systolic-diastolic patterns. Note that curves exhibit different characteristic profiles regarding shapes and magnitude with slight time delay due to successive valve openings.

This study mainly focuses on the aorta – which is part of the systemic circulation – and the cardiac cycle two-phases mode (systole/diastole). For more details on the cardiovascular system, the reader is referred to the textbook [Marieb and Hoehn \(2014\)](#).

1.1.2 Aorta geometry and morphology

Arteries are blood vessels that transport high pressure blood expelled from the heart to the rest of the body. These muscular and elastic pipes can expand and contract their walls when heart forces blood to flow into the arterial lumen. The aorta is the largest artery and arises from the heart left ventricle before descending close to the anterior face of the backbone. It is anatomically divided in two sections: thoracic and abdominal aorta. The **thoracic aorta** is emerging from the heart and terminates at the diaphragm. The most superior division of the aorta consists of the ascending aorta, the aortic arch with pronounced curvature and the straight descending aorta. The **abdominal aorta** begins at the diaphragm and terminates in two bifurcating branches called **common iliac** arteries which supply lower limbs (Marieb and Hoehn (2014)). On its downward path, the aorta gives rise to other major arteries to supply specialised organs (figure 1.3). An overview of morphological characteristics are given in table 1.1. These data correspond to healthy vessels but can evolve with pathologies development as discussed later in this chapter.

Table 1.1: Diameter and length of normal aorta and largest branches at proximal segments. Sources from [a] Craiem et al. (2016)[b] Dotter et al. (1950) [c] Joh et al. (2013), [d] Bărdaş and Bordei (2018) and [e] Kahraman et al. (2006).

		Diameter (mm)	Length (mm)
Thoracic aorta	Ascending aorta	32.3 ± 3.4	33.2 ± 15.07 [b]
	Aortic arch	27.8 ± 2.4	
	Descending aorta	24.7 ± 2.2 [a]	
Abdominal aorta	Suprarenal segment	21.4 ± 3.1	$165.3\text{--}183.0$ [d]
	Infrarenal segment	18.3 ± 3.2 [c]	
Aorta branches	Brachiocephalic	12.07 ± 1.58	
	Left subcalvian	9.04 ± 1.74	
	Left common carotid	7.15 ± 0.92	
	Left iliac	9.54 ± 1.32	
	Right iliac	9.10 ± 1.38 [e]	

1.1.3 Aorta histology and mechanical properties

Histology

Histology refers to the micro-anatomy of tissues and organs. An overview of the blood vessel histology allows to understand its behavior and identify its weaknesses that can explain some diseases.

At the cellular and molecular level, blood vessels are made up of two main proteins — elastin and collagen — which almost entirely govern aorta's passive mechanical properties, while smooth muscle cells mainly define active mechanical properties (Marieb and Hoehn (2014)). First, elastin is a distensible fiber with elastic modulus of about 0.5 MPa

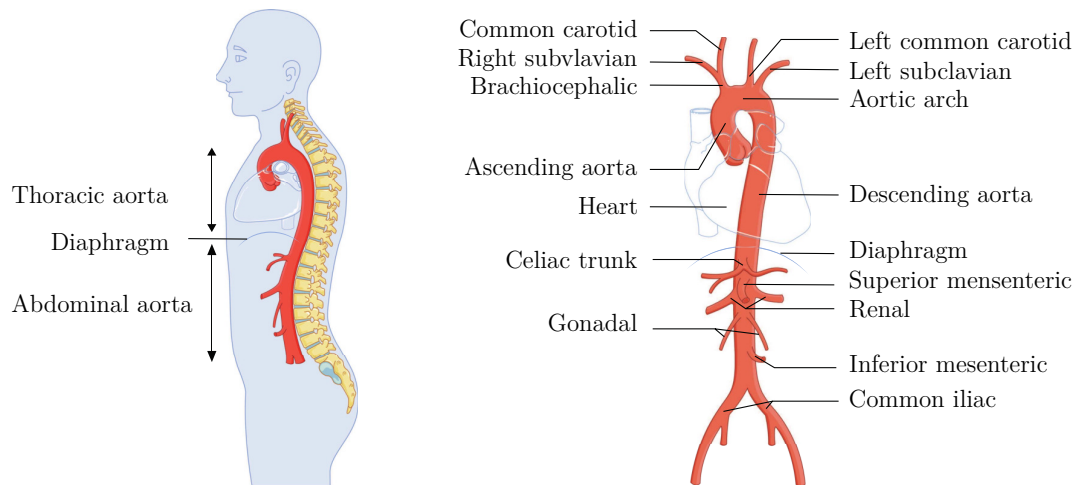


Figure 1.3: Human aorta anatomy. Illustration adapted from Servier Medical ART (smart.servier.com)

(Fung (1993)) which is mainly involved in the elastic property of aorta at low strain. Elastin stores energy during cardiac cycle when pressure increases and helps the tissue resume to its initial shape when pressure drops (Payan and Ohayon (2017)). Collagen are wavy form fibers associated with vessel walls stiffness and strength. Their elastic modulus is about 0.5 GPa (Fung (1993)) and the material stiffness depends on the amount and orientation of fibers. Indeed, fibers exhibit increasing level of organization and circumferential alignment with increasing pressure. The vessel becomes stiffer and limits aortic distension (Payan and Ohayon (2017)). Finally, smooth muscle cells have low impact on mechanical properties. They respond to cyclic stretch and can modulate their elasticity to meet physiological needs and regulate blood flow by contracting or relaxing. These components, are organized with different distributions and orientations along the vessels to adapt various type of loads.

At the tissue scale, the arterial wall is organized in three layers: intima, media and adventitia as shown on figure 1.4.

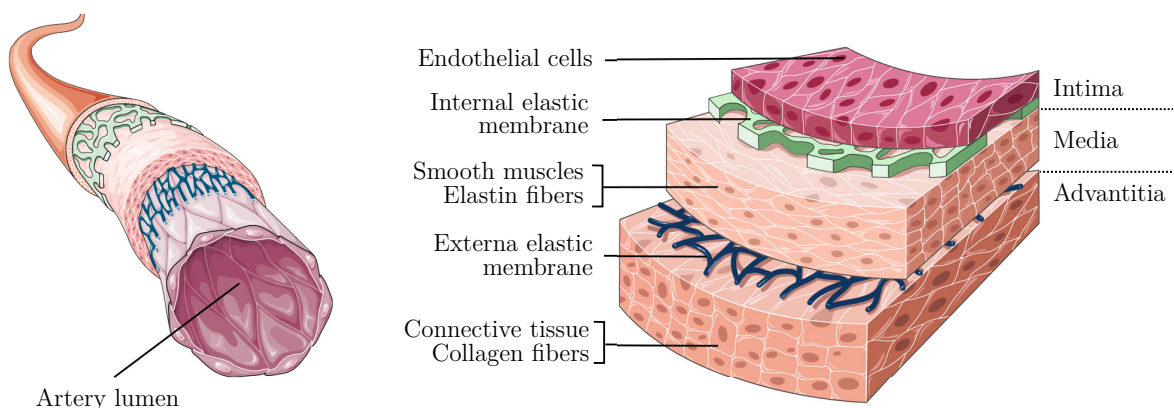


Figure 1.4: Aortic wall layers and internal structure (smart.servier.com).

- The **intima** is the innermost layer of the artery and consists of a fine network of endothelial cells. This smooth surface composed of a basal membrane and a subendothelial layer minimizes friction between the circulating blood and the vessel's internal walls. Healthy intima does not have a significant contribution to the mechanical behavior of the artery. However, aging and pathologies lead to the subendothelial layer thickening which provides stiffness to the material resulting in alteration of mechanical properties.
- The **media** is the thicker layer of the artery wall. It is separated from the intima and the adventitia by internal and external elastic laminae. The media consists of muscle cells intertwined with elastin fibers that circle the vessels and give viscoelastic properties. This muscle layer provides support for the vessel and allows lumen diameter change to regulate blood flow and pressure.
- The **adventitia** is the outermost layer of the arterial wall. It is mostly composed of stiff and strong collagen fibers that act as a reinforced support. This layer is also supplied by blood vessels to fuel the tissue and nerves which allows muscle stimulation.

This description applies to a normal healthy aorta, however, throughout life, arteries are modified by physiological load, aging and pathologies. Layers properties can be altered because of modification of composition, thickness, organization, etc. As an example, aging causes elastin fibers fragmentation and stiff collagen fibers become prevalent over smooth muscle tissues. This weakening of the arterial walls due to tissue elasticity degradation can lead to permanent enlargement of the lumen. Weakened arteries are likely to develop pathologies such as aortic aneurysm and aortic dissection which will be discussed later in this chapter.

Tissue general properties

The aorta is a mechanical system that responds to pressure applied by the conveyed fluid: blood. Relations between applied constraints and aorta deformation are interesting features to understand the interaction between the flow and the piping system. This section is mainly focused on mechanical properties that can be associated with those fluid/walls interactions.

The previously described structure, composition and organization give general mechanical properties of aortic wall tissues. First, histology description shows that arterial wall is an **heterogeneous** material. Nonetheless, depending on the study scale, one may assume that each layer (intima, media and adventitia) has homogeneous mechanical properties ([Humphrey \(2002\)](#)). This hypothesis is particularly accepted for large vessel hemodynamics studies such as the aorta at a macroscopic level.

In addition, aorta is considered as an **incompressible** solid. To prove that, [Carew et al. \(1968\)](#) conducted experiments on dogs to measure the change in aortic wall volume under stretch. Maximum volume variation was only of 0.165% with inflation test imposing pressures from 161 to 202 mmHg (higher than normal human blood pressure). He

concluded that for most cases under physiological conditions, artery wall can be regarded as incompressible.

During cardiac cycle, the aorta diameter varies in a range from 2.7% to 8 % (Amabili et al. (2020)). Considering large strain domain, arterial vessels exhibit **nonlinear** stress-strain response (Fung (1993); Humphrey (2002)). As mentioned earlier, stiffening of the arterial wall due to fibrils organisation depends on the loading pressure. Elastin plays a more important role at low pressure while collagen takes the lead at high pressure which participates to the non-linear response. In addition to non-linearity, aorta is considered as **anisotropic** which can also be explained by the formally described fibril organization. A large majority of studies use a simplified isotropic model of the aortic wall. However, findings on the influence of anisotropy on the development of aortic aneurysms questions the use of isotropic models (Rodríguez et al. (2008); Wilson et al. (2012)). For instance, Vande Geest et al. (2006) has shown stronger anisotropic behavior in aneurysm regions of the aorta which may help understanding some injury mechanisms.

Non-linear and anisotropic behavior are illustrated on Holzapfel (2006) experiment and modeling. Loading were applied on each vessel layers under circumferential and axial directions. Layers clearly exhibit large discrepancies in mechanical responses in both directions.

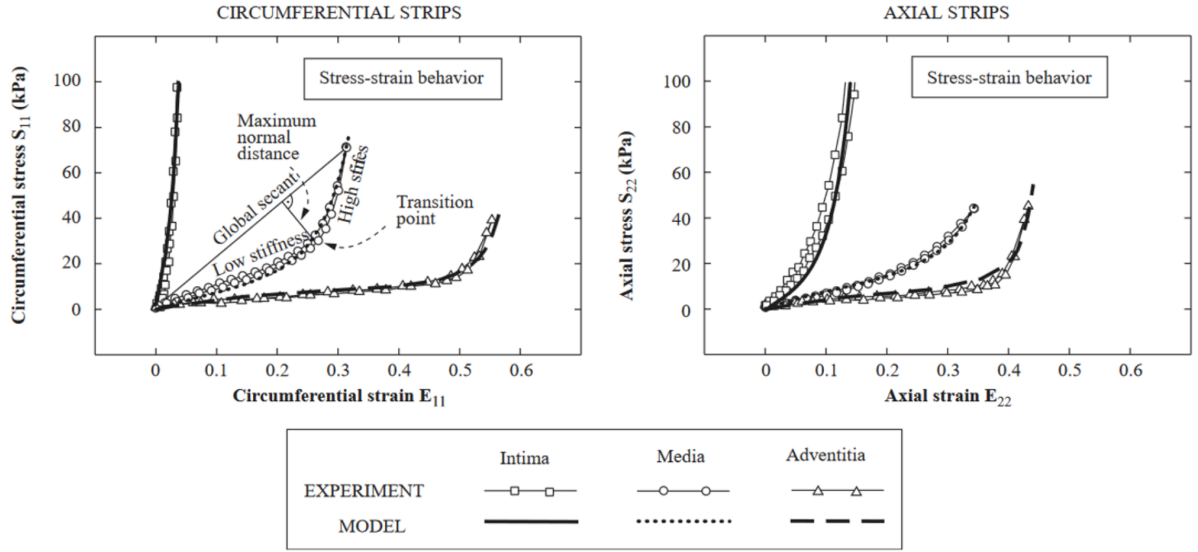


Figure 1.5: Stress-strain (second Piola-Kirchhoff stresses S_{11} , S_{22} - Green Lagrange strains E_{11} , E_{22}) response on isolated samples of the three main arterial wall layers under circumferential and axial direction. A comparison is achieved between experimental data and a predictive model (extracted from Holzapfel (2006)).

Another major property of arterial walls is **viscoelasticity** which was investigated in many experimental studies on *in vivo* or *ex vivo* aortas (Imura et al. (1990); Valdez-Jasso et al. (2011); Amabili et al. (2020)). In most cases, the relation between vessel inner pressure and diameter was measured simultaneously to show the viscoelastic response. The associated stress-strain curves exhibited cyclic behavior which is characteristic of a viscoelastic response (figure 1.6). As mentioned earlier, the aortic wall stores energy when pressure increases and restores this energy when unloaded. For viscoelastic materials,

there is a delay between the application of the stress and the deformation of walls which can be characterized by cyclic shape of the strain-stress graph. Valdez-Jasso et al. (2011) conducted *in vivo* experiments to highlight this viscoelastic behavior which is characterized by a cyclic applied pressure - aorta area graph on figure 1.6. This phenomenon has a strong impact on blood flows and will be discussed in parallel with hemodynamical concerns in section 1.2.

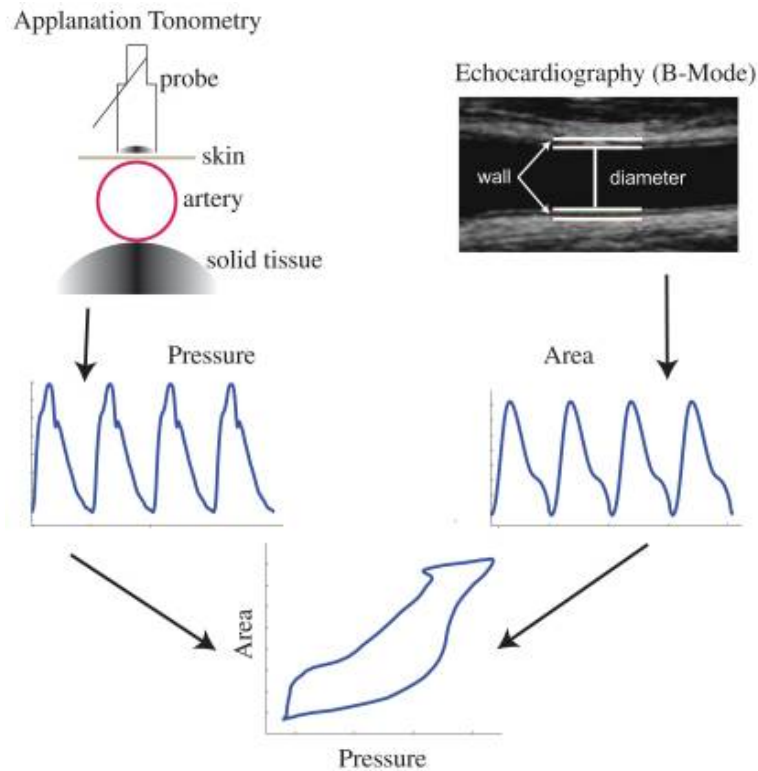


Figure 1.6: *In vivo* experiment on human carotid artery. Applanation tonometry and B-mode echographic images were used to assess pressure and vessel area change and draw pressure-diameter relationship Valdez-Jasso et al. (2011).

These general mechanical properties provide a non-exhaustive list of major characteristics considered in building aortic mechanical models. Many experimental studies enabled quantification of those physical quantities (deformation, elongation, stress, rupture, etc.), identified relationship between them and constitutive laws. Specifically, they focus on the relation between aorta deformation applied stress. As a non-exhaustive list, we may cite the model proposed by Ogden and Hill (1972), Vito and Hickey (1980) and Humphrey (1995). Please refer to the thesis of Menut (2017) for a more detailed explanation of each mechanical model. Constant technological progress in measuring instrument provides increasingly accurate data, large scale studies and more reliable *in vivo* assessments thanks to minimally and non invasive techniques that help refining those mechanical models .

1.1.4 Blood rheology

To properly describe aortic hemodynamical flow, mechanical properties of the piping system has to be associated with a solid knowledge of the conveyed fluid rheology. Rheology is the science of deformation and flow of materials. When applied to blood, it involves investigating blood components interactions, flow properties, and physiological factors such as temperature, pressure or pathologies. This section provides an overview of some blood rheological properties with particular attention to Red Blood Cells which almost entirely dictate blood's mechanical behavior. Note that the system is highly complex with cross-mechanisms between biology, physiology and fluid mechanics. The presented models are representation of global blood rheological behavior.

1.1.4.1 Blood function and composition

Human blood is a complex suspension of cells — red blood cells, white blood cells and platelets — in a fluid called plasma which contains organic mineral salts and proteins.

- **Plasma** is an extracellular fluid made up of proteins, nutrients, enzymes, wastes, hormones and dissolved gases. Plasma acts as a transport medium for the following constitutive cells (figure 1.7).
- **Platelets** are fragments of larger cells in the bone marrow. They help forming blood clot to stop bleeding and favor wound healing.
- **White blood cells (WBCs)**, also known as **leukocytes**, accounts for only 1% of blood volume. They are part of the immune system and are involved in protecting the organism against infectious diseases by attacking bacteria, viruses and germs.
- **Red blood cells (RBCs)**, also known as **erythrocytes**, are disc-shaped cells with thick rim and thin center. Their diameter is approximately 6-8 μm and their thickness is about 2-3 μm . These elastic biconcave discs can stretch, fold and squeeze through narrow vessels and get back to their initial shape in larger lumen. 33% of RBCs cytoplasm is made of a solution of hemoglobin that can carry oxygen and carbon dioxide. The biconcave shape provides large ratio surface to volume which favors O_2 and CO_2 diffusion between hemoglobin and their environment.

Hematocrit is a measure of formed elements in blood. It is the percentage of blood cells volume (RBCs, WBCs and platelets) divided by the total volume of blood. As 97-99% of blood cells are RBCs, hematocrit is often related to the ratio of RBCs in blood. Hematocrit varies among individuals because of various factors such as sex, infections, low-oxygen environment or dehydration. For this study, we will confine ourselves to the hematocrit percentage of a healthy individual around 45 Ht%.

1.1.4.2 Rheology and rheometry

"Rheology" refers to the science while "rheometry" refers to the experimental techniques used to determine rheological properties. Among those properties, we mainly focus on **viscosity** as a fluid global property and we do not detail blood components interactions.

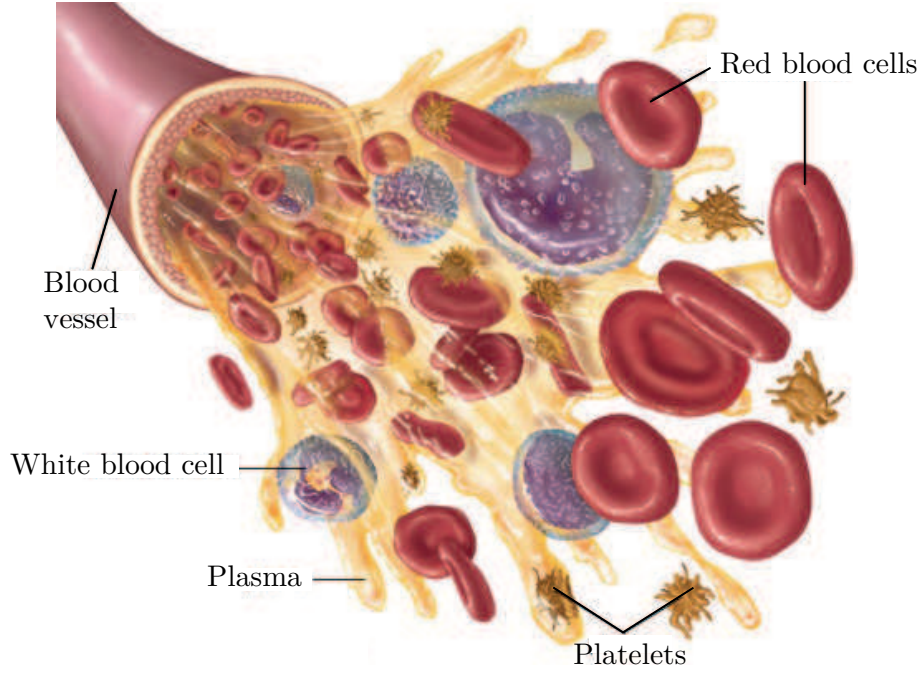


Figure 1.7: Blood composition, @ 2006 Encyclopedia Britannica

The notion of viscosity reflects the resistance of a material to flow. Let us consider a 2D two plates model to mathematically define this notion. A Newtonian fluid is entrapped in between two horizontal plates. The lower one is fixed while the upper plate goes on translation movement horizontally an parallel to the other. The upper plate drags the fluid by applying a shear stress on it. If the flow is assumed to be laminar, the fluid can be decomposed into infinitesimally thin layers (parallel to the plate) which velocity linearly varies with their distance to the moving plate as shown on figure 1.8. Each layer applies a stress on others to allow the upper plate to move. When considering all the layers frictions, the whole system's shear stress is defined as follow

$$\tau = \frac{F}{A}, \quad (1.1.1)$$

with A the plates area and F the force required to move the upper plate.

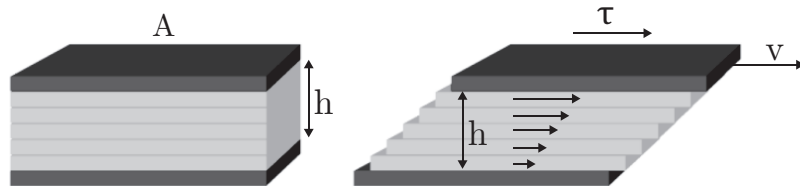


Figure 1.8: The two-plates system to explain shear stress when the upper one is horizontally moving compared to the lower one.

The shear rate is defined as the velocity gradient

$$\dot{\gamma} = \frac{v}{h}, \quad (1.1.2)$$

where v is the velocity of the upper plate and h is the distance between the fixed and the moving plate.

Finally, the viscosity of the fluid is defined as a ratio between shear stress and shear-rate

$$\mu = \frac{\tau}{\dot{\gamma}}. \quad (1.1.3)$$

According to the two previous equations, the more viscous is the fluid, the more stress needs to be applied to move the plate at a certain speed v . This relation refers to the notion of viscosity as a resistance to the flow outlined at the beginning of this section.

For complex fluids, the relation between shear stress and shear rate is not that straightforward. Time and shear rate may influence the shear stress which leads to a more general formulation of the viscosity such that

$$\mu(\dot{\gamma}, t) = \frac{\tau(\dot{\gamma}, t)}{\dot{\gamma}}. \quad (1.1.4)$$

Then, viscosity can no longer be defined for a fluid under any conditions, but for a fluid subjected to specific conditions such as applied shear-rate, or time after applied stress, etc.

Fluids can be classified as **Newtonian** or **non-Newtonian** according to the dependence of their viscosity to applied shear-rate. A Newtonian fluid shows a linear relationship between shear-stress and shear-rate. In other words, its viscosity stays constant when subjected to various shear-rates. Conversely, a non-Newtonian fluid viscosity broadly depends on the applied shear-rate. Two types of non-Newtonian behaviors are shown on figure 1.9. A **shear-thinning** behavior exhibits a decreasing viscosity when shear rate increases while a **shear-thickening** behavior corresponds to an increase in viscosity when shear rate increases.

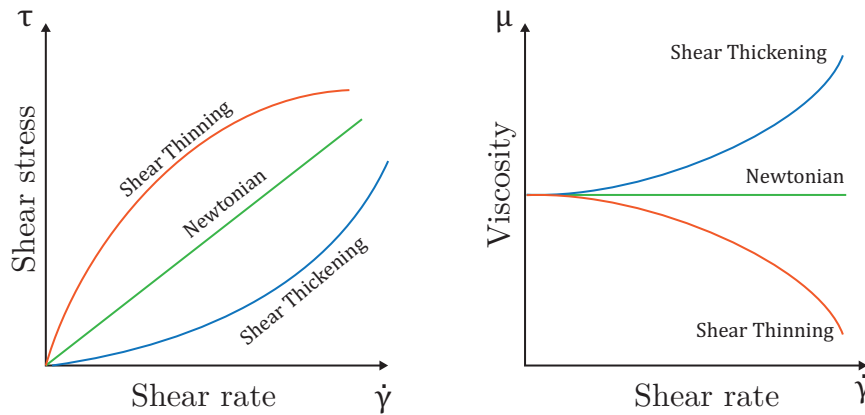


Figure 1.9: Shear stress - shear rate and viscosity - shear rate profiles for Newtonian, shear-thinning and shear thickening fluids.

Rheometry is the method to assess rheological properties of a fluid and is technically more challenging for non-Newtonian fluids as shear-rate conditions become a parameter which locally varies as a function of instantaneous flow stress. When only focusing on viscosity, it consists in measuring the stress when applying controlled shear on the fluid. In accordance with equation 1.1.4, this method allows to determine the fluid viscosity for a chosen range of shear-rates. The three main used rheometers for blood viscometry are couette, cone-plate and capillary rheometers. The systems are depicted on figure 1.10.

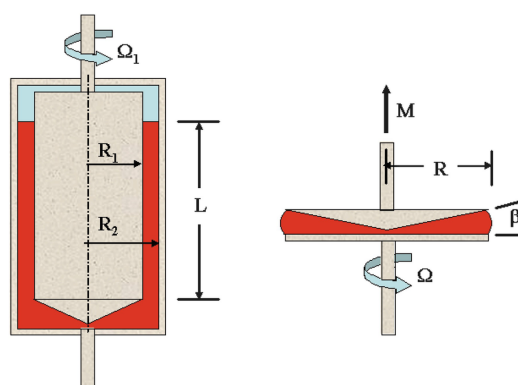


Figure 1.10: Two commonly used rheometers: Couette (left) and cone-plate (right) where the fluid is represented in red, Ω is the rotational speed, M the measured torque and β the cone angle (Galdi et al. (2008)).

Couette viscometer is a concentric-cylinder viscometer. The fluid is placed in the gap between two cylinders (left on figure 1.10). One cylinder is stationary while the other one rotates with indicated motor rotation speed to impose shear-rate in the fluid. Measurement of the torque allows to determine fluid viscosity knowing radius and rotation speed. Depending on models, the torque can be measured on the rotating cylinder that drags the fluid or on the stationary one that keeps it still. The major drawback of Couette viscometer is that shear-rate is non-homogeneous into the gap. Applied shear-rate depends on the radius to the central axis. In the case of non-Newtonian fluid, viscosity directly depends on shear-rate. As a consequence, shear rate is not uniform in the sample and neither is viscosity which may lead to direct unsatisfactory results and needs for post-measurement corrections.

Cone-plate rheometers are made up of a fixed lower plate and rotating cone like upper plate. The cone is pointing on the lower plate and the fluid is placed between the fixed plates and the rotating cone (right on figure 1.10). Rotational speed is imposed to the cone and the torque is measured to determine fluid viscosity knowing plate gap, cone angle and diameter. The cone shape provides increasing gap from the center to the edge of the device. Thus, homogenized shear-rates into the fluid volume are obtained regardless of their distance to the rotating axe.

1.1.4.3 Blood viscosity

Blood is known to be a shear-thinning fluid and was investigated in numerous studies based on experimental methods taking into account the non-Newtonian specificity. In most blood rheometric measurements, human blood samples are collected from donors. EDTA (Ethylenediaminetetraacetic acid) or heparin is added to the samples to prevent clotting. Then, viscosity is assessed with a rheometer while maintaining the fluid at a physiological temperature of 37°C. Figure 1.11 shows different results of blood samples with different rheometry techniques. This geometry is more adapted in the context of shear-thinning fluid measurements.

Differences between viscosity curves were observed and may not only depend on the measurement method but also on blood samples. Indeed, a collection of blood samples exhibit large discrepancies regarding composition, hematocrit, component behavior etc.

Their role is described in the next paragraph and offers clues in understanding the shear-thinning profile of viscosity and potential differences between donors.

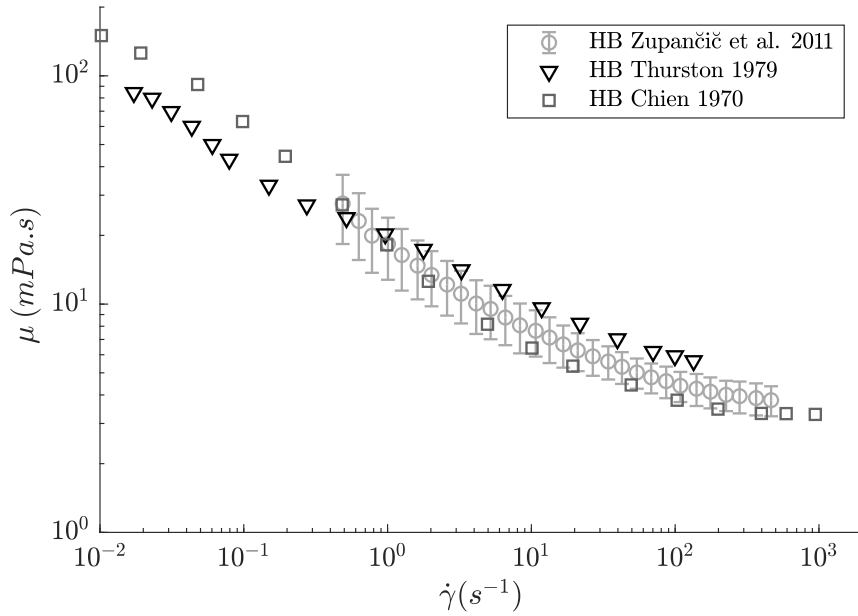


Figure 1.11: Viscosity under shear rate sweeps in three studies. [Thurston \(1979\)](#) conducted experiments on samples from one donor with 43%Ht and oscillatory tube viscometer. [Chien \(1970\)](#) measures blood viscosity of 45%Ht blood samples with a couette rheometer. [Zupančič Valant et al. \(2011\)](#) provided a mean viscosity curve from 6 patients with standard deviation bars, viscometry was achieved with a cone-plate rheometer.

Red blood cells: aggregation, dispersion and deformability

Plasma is a Newtonian fluid which viscosity varies between 1.10 and 1.35 cP (mPa.s) at 37°C ([Baskurt \(2003\)](#)). It has been shown that RBCs in the cellular phase participate to the increase of overall viscosity and provide non-Newtonian properties ([Thurston \(1979\)](#)). [Chien et al. \(1966\)](#) proved that viscosity decreases when the fluid is subjected to increasing shear rate but also varies depending on hematocrit, and thus, on RBCs concentration. Indeed, increasing hematocrit in blood results in increasing overall viscosity and steepening of the shear-thinning slope ([Chien et al. \(1966\)](#); [Thurston and Henderson \(2006\)](#)).

To explain this phenomenon, studies have highlighted two main RBCs behaviors that reflect the shear-thinning property of whole blood:

- **Deformability:**

RBCs are elastic bodies that may deform when subjected to external stresses. Under laminar high shear-rate flow (over 100-200 s⁻¹ according to [Baskurt \(2003\)](#)), RBCs tend to align and elongate in the direction of flow. On the other hand, at low shear rate, RBCs return to their round shape and freely rotate in the fluid.

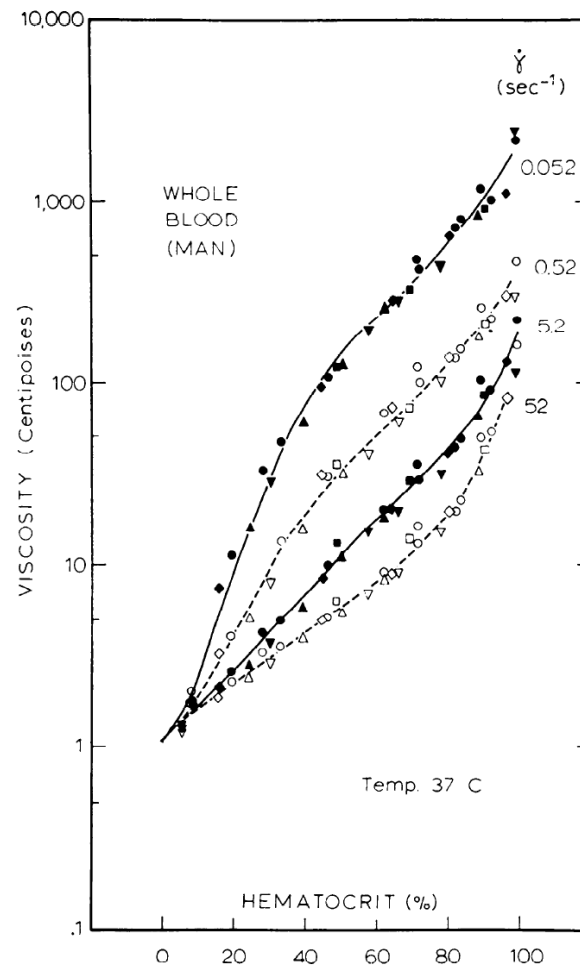


Figure 1.12: Viscosity at four shear rates with varying hematocrit of whole blood at 37°C. Blood was drawn from human veins and stored in tubes containing heparin to prevent coagulation. Ratios between plasma and RBCs were then artificially modified with man-made manipulations in samples to sweep hematocrit from 0 to 100% (Chien et al. (1966)).

- **Aggregation:**

At low shear rate RBCs aggregate as stack structure called "rouleaux" (figure 1.13. left). Rouleaux can align and connect each other, thus forming a rigid network in the fluid that appears to "resist" flow. Under this state, blood exhibits high viscosity. When shear rate increases and stress is applied to this rigid structure, rouleaux tend to progressively deaggregate. The rigid structure is broken, cells progress as independent elements in the fluid and blood viscosity lowers (figure 1.13. right). The level of aggregation strongly depends on the composition of suspending medium. For instance, fibrous proteins in plasma favor aggregation. Modification of the medium (due to pathologies, lifestyles or environment factors) impacts the aggregation process of RBCs.

A significant experiment was conducted by Chien (1970) to appreciate those two mechanisms. He investigated the role of RBCs deformability and aggregation. Comparison between modified blood solutions was achieved to highlight distinctly RBCs deformabil-

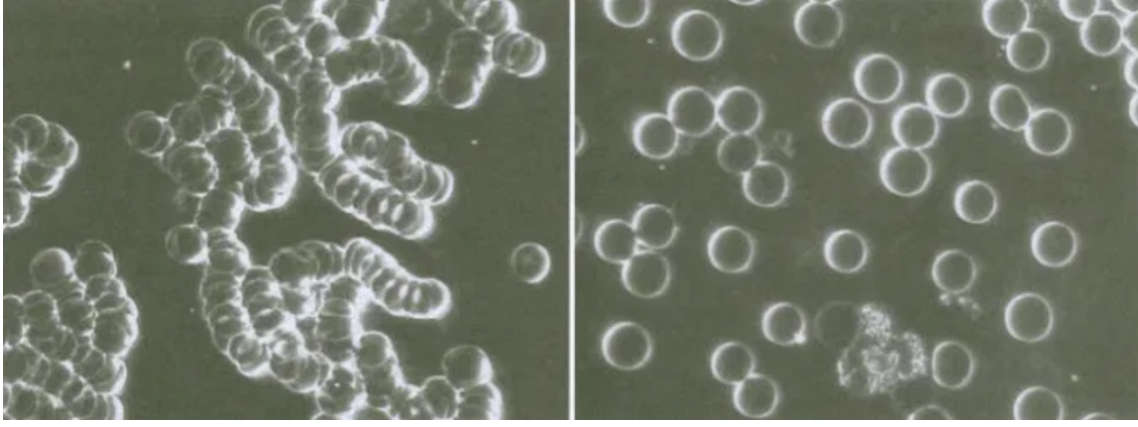


Figure 1.13: (Right) Red blood Cell geometry, (Middle) RBCs aggregated state named "rouleaux", (Left) RBCs in deaggregate state (Image from Live Blood Online). RBC typical size: 6-8 μm .

ity and aggregation impact on blood shear-thinning property. To that purpose, hardened RBCs were used to limit deformability on one side and albumin-Ringer solution was used to prevent aggregation on the other side. The results of the experiment are described in figure 1.14. Both modified RBCs resulted in attenuation of shear-thinning property and modification of the overall viscosity.

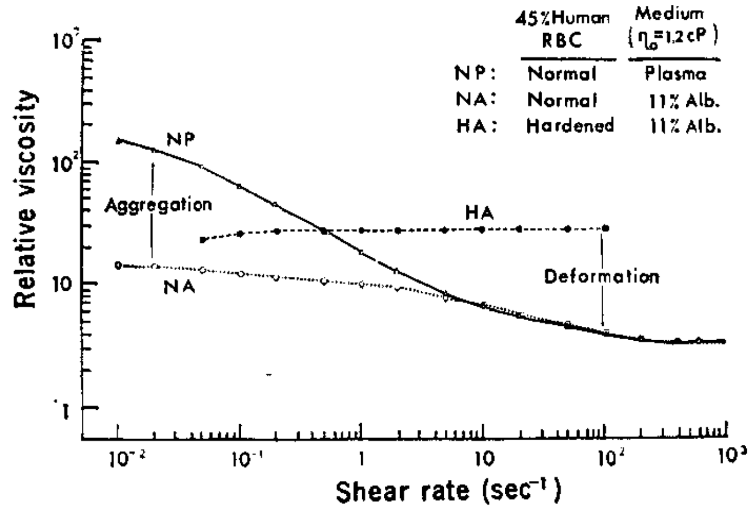


Figure 1.14: Relative viscosity with varying shear rate for three 45% human RBCs solutions: normal RBCs in plasma (NP), RBCs in albumin-Ringer (NA) and hardened RBCs in albumin-Ringer (HA), at 37°C (Chien (1970)).

Although shear-thinning property is well described (Thurston (1979); Chien et al. (1966); Chien (1970)) blood is a complex fluid which rheological properties may vary depending on sex (Zupančič Valant et al. (2011)), age (Long et al. (2005)), lifestyle and pathologies (Baskurt (2003)). This dependency results in a wide range of viscosity profiles. As a consequence, there is no absolute model for blood viscosity. One may only approach a general description of the shear-thinning curve of human blood with a range of accessible values.

Mathematical models

Generalized newtonian models well describe blood shear-thinning viscosity. Two assumptions are set: the fluid is homogeneous and its viscosity only depends on shear rate. In addition, instationary inertia forces are neglected as in Newtonian models. These blood viscosity models arise from experimental measurements on human blood with a rheometer achieving shear rate step-like ramps and waiting for stationary flow conditions at each step. Most of these viscosity models reach limit values for zero (μ_0) and infinite (μ_∞) shear rate. It implies that the fluid tends to a newtonian model at shear rates extrema. Several generalized Newtonian models can be mathematically represented by the following equation

$$\mu = \mu_\infty + (\mu_0 - \mu_\infty)f(\dot{\gamma}). \quad (1.1.5)$$

A non exhaustive list of functions $f(\dot{\gamma})$ is given in table 1.2 with corresponding constants. λ is a time constant while n , m and a are dimensionless constants (Galdi et al. (2008)). Each model is plotted in figure 1.15 and compared to experimental data on human blood from Thurston (1979); Chien (1970) and Zupančič Valant et al. (2011).

Table 1.2: Generalized Newtonian models for blood with constants $\mu_0 = 0.056$ Pa.s and $\mu_\infty = 0.00345$ Pa.s (Galdi et al. (2008))

<i>Models</i>	$f(\dot{\gamma})$	<i>Material constant for blood</i>
Powell-Eyring	$\frac{\sinh^{-1}(\lambda\dot{\gamma})}{\lambda\dot{\gamma}}$	$\lambda = 5.83$ s
Cross	$\frac{1}{1+(\lambda\dot{\gamma})^m}$	$\lambda = 1.007$ s , $m = 1.028$
Modified-Cross	$\frac{1}{(1+(\lambda\dot{\gamma})^m)^a}$	$\lambda = 3.736$ s, $m = 2.406$, $a = 0.254$
Carreau	$(1 + (\lambda\dot{\gamma})^2)^{(n-1)/2}$	$\lambda = 3.313$ s, $n = 0.3568$
Carreau-Yasuda	$(1 + (\lambda\dot{\gamma})^a)^{(n-1)/a}$	$\lambda = 1.902$ s, $n = 0.22$, $a = 1.25$

1.1.4.4 Other rheological properties

Viscoelasticity

Viscoelastic fluids are characterized by their ability to store and release energy. This ability is provided by RBCs deformability and 3D branched micro-structures which gives viscoelasticity to blood (Galdi et al. (2008)). Oscillatory test can be implemented with a rheometer to assess viscoelasticity which is reflected by a time shift between applied deformation and measured stress. Experimentally, a fluid is subjected to constant frequency

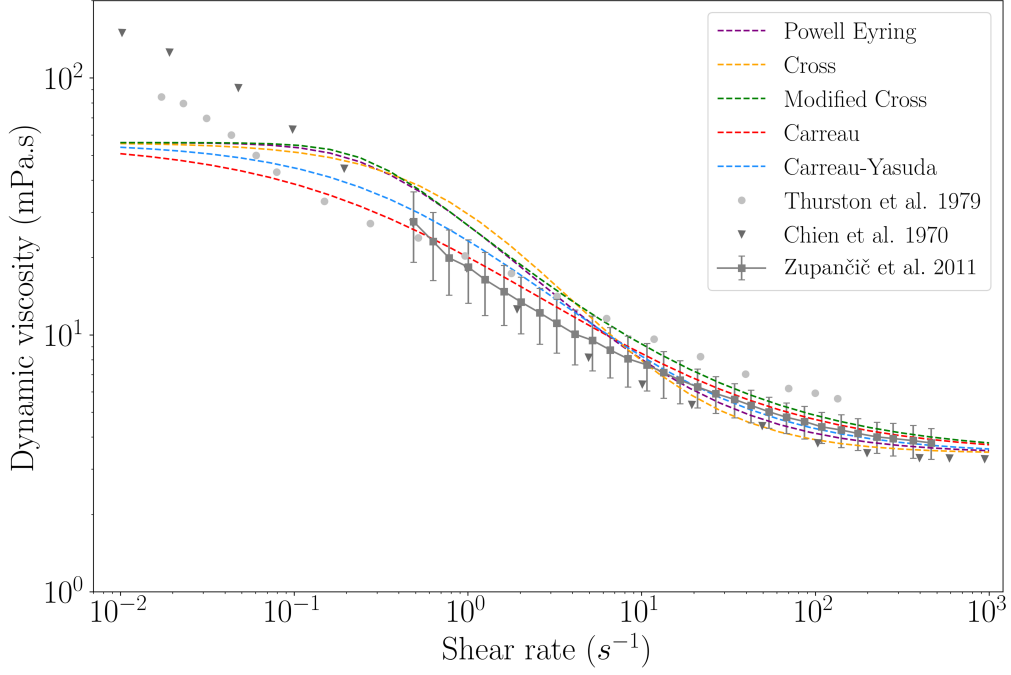


Figure 1.15: Generalized Newtonian models from Table 1.2. Reference parameters come from a 25 years old female donor (Ht% = 40% and $T = 23^\circ\text{C}$). Blood viscosity measurements were achieved with a Couette rheometer and shear rate sweeps between 300 and 1000 s^{-1} (Galdi et al. (2008)).

oscillations $\gamma(t) = \gamma_0 \sin(\omega t)$. When steady state is reached, an oscillatory stress $\tau(t)$ is measured and defined as

$$\tau = \tau_0 \sin(\omega t + \delta). \quad (1.1.6)$$

For small deformation, previous equation can be decomposed in the following manner,

$$\tau = \gamma_0 (G' \sin(\omega t) + G'' \cos(\omega t)), \quad (1.1.7)$$

where G' is the storage modulus and G'' is the loss modulus. The relation for G' and G'' is defined with a factor δ that represents the phase shift between applied displacement and stress

$$\tan \delta = \frac{G''}{G'}. \quad (1.1.8)$$

A complex viscosity μ^* is defined as $\mu^* = \mu' + i\mu''$ with

$$\mu' = \frac{G''}{\omega} \quad (1.1.9)$$

and

$$\mu'' = \frac{G'}{\omega} \quad (1.1.10)$$

Thurston and Henderson (2006) conducted experimental measurements of μ' and μ'' using blood samples with 22% and 44%Ht (figure 1.16, left). This study also emphasizes

the impact of measurement methodology on results and rheometer geometries. Indeed they conducted the same viscoelasticity determination in 1 cm tubes, microtubes and porous medium and showed some disparities in measurements of μ' and μ'' on blood samples with 22% and 44% hematocrit (figure 1.16, right). It is suggested that those changes mostly influence the dynamic of microstructures organization and RBCs deformability and thus, on viscoelastic behavior. These conclusions were made by measuring viscosity, elasticity, relaxation time, yield stress while imposing different shear conditions to control aggregation and deaggregation processes. When extrapolating from those results, one may expect that viscoelasticity is different in the context of arterial flow. Thus, special care should be taken when comparing experimental data from rheometers and *in vivo* behavior.

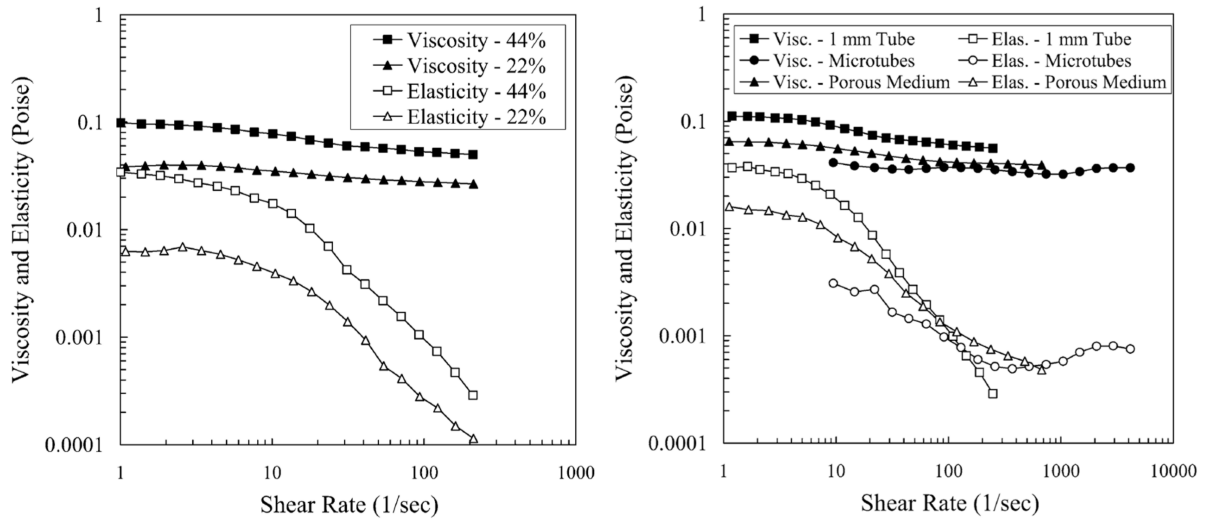


Figure 1.16: Viscosity and elasticity on blood samples with adjusted hematocrit to 22% and 44%. (Left) Measurements were achieved in 0.10 cm oscillatory tubes at 2 Hz, (Right) measurements comparison in 0.10 cm tube, microtube and porous medium [Thurston and Henderson \(2006\)](#).

Compared to the previously cited generalized Newtonian models that only focus on the shear-dependent viscosity, more comprehensive mathematical models allow to describe viscoelasticity, yield stress and thixotropy (Herschel-Bulkley, Maxwell, Phan-Thien-Tanner, etc.). These models are not presented as they will not be implemented in this work. They are often used in numerical simulation studies ([Menut \(2017\)](#); [Caballero and Laín \(2015\)](#)).

Every *in vitro* and *in silico* hemodynamical study has to build or to choose a model for blood rheology to represent blood. As for vessel wall models, depending of the scale of observation and the type of blood vessels, different simplifications are made to represent blood. This ranges from simple Newtonian to complex Phan-Thien-Tanner models. But it has to be kept in mind that representing all the complexity does not guarantee relevant models and can even be counterproductive. A large majority of experimental and numerical studies on aorta blood flow represent blood as a Newtonian fluid. This representation can be questioned and is discussed in the next section by not only considering blood rheology but a larger system depending on blood, vessels and flow conditions.

1.2 Hemodynamical flows

Blood flow is a complex topic at the crossroads of fluid mechanics, material science and continuum mechanics. Hemodynamics refers to the study of mechanisms and factors governing blood flows and the solid structures it goes through (Secomb (2016)). The previous section highlighted that blood rheology depends on the surrounding environment including flow conditions and piping system. As a matter of facts, hemodynamical flows are led by rheological behaviors of both blood vessels as an active piping system and blood itself as a complex conveyed fluid. Physiological and biological factors also influence formally described blood and vessels properties and can significantly modify flows.

This section provides an overview of the hemodynamical flow theories from fluid mechanics to solid mechanics applied on simplified models. In that way, we will introduce mathematical and physical concepts applied to hemodynamics, and highlight three main specificities of such flows : periodicity, non-Newtonian properties and wall compliance. The section describes global flow properties and does not focus on local properties with microstructures interactions which would imply biological, physiological and mechanobiological studies (Kim et al. (2017); Dahl et al. (2010)) which are out of scope for this study.

1.2.1 Basic concepts : pressure and flow distribution

The fundamental level of hemodynamics, is the study of pressure and flow distribution in the cardiovascular system (Secomb (2016)). In this study, "flow" refers to the motion of the conveyed fluid (blood) and "pressure" refers to the hydrostatic pressure. Along the vascular tree, pressure varies from one location to the other, thus giving rise to pressure gradients. The force that drives flow from point to point is the pressure gradient (Fung (1993)). Electric circuits analogies can be introduced to model these hemodynamics concepts. The vascular tree is represented by a circuit transporting a current I , corresponding to a volume flow rate Q . It is associated with a voltage V (electric potential difference), corresponding to the pressure difference ΔP between two points. These two points delimit the vascular part along which the intensity is transported. Ohm's law states that, for a resistive element R , the relation between voltage across the element and current is given by $R = V/I$. In the context of hemodynamics, Ohm's law introduces the concept of the viscous flow resistance of blood vessels R with the relation,

$$R = \frac{\Delta P}{Q} \quad (1.2.1)$$

where ΔP is the pressure difference (also called driving pressure or perfusion pressure) along the vessel. This relation is valid if we suppose the flow not to vary with time (the flow is supposed to be stationary). Under ideal physiological conditions, the vessel resistance does not depend on flow rate and pressure, it is only dependent on vessel geometry and blood viscosity. Electric circuit relations between series and parallel resistance still apply on peripheral blood vessels as depicted in figure 1.17.

This simplified electric model, allows to understand the main features of the cardiovascular system. Pressure differential generated by the heart pumping leads to flow motion in

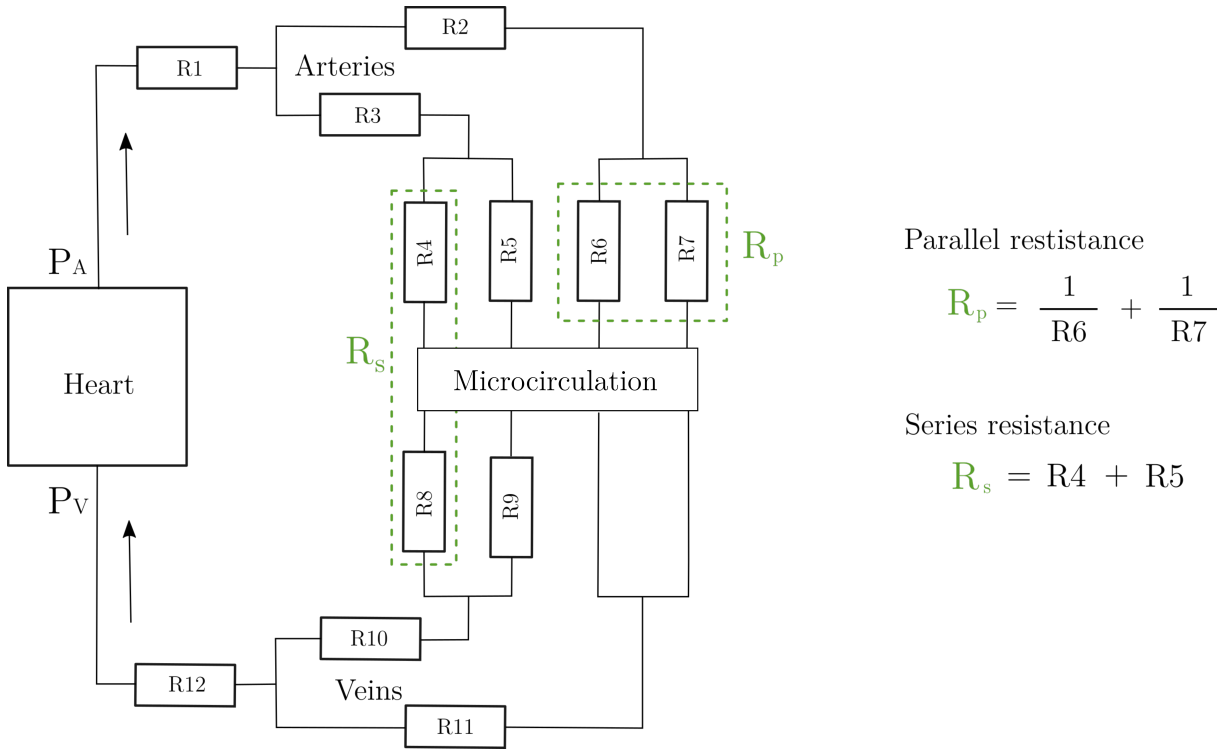


Figure 1.17: Electric circuit analogy for the vascular tree. P_A and P_V stand for arterial pressure and venous pressure respectively. Adapted from [Secomb \(2016\)](#).

the arterial tree (resistance circuit). On one hand, an increase of the resistance in a vessel segment, in small capillaries or due to vessel occlusion (thrombus), induces a lower flow rate that also affects peripheral vessels. On the other hand, a decrease of the resistance — in large vessels or due to vessels dilatation (aneurysm) — results in higher flow rate. Thus, the force that drives flow is the pressure gradient while the force that resists flow is the viscous flow shear force on blood vessels. Furthermore, those forces fluctuate along the arterial tree, through the cardiac cycle and with physiological conditions.

This resistance network modeling the vascular system is limited as it does not take into account time dependency of flow, pressure and resistance. Moreover, it does not represent what happens "in" the fluid and "in" the arterial walls. Indeed, it is a global model and complex local interactions are not represented. More elaborated models ([Abdi et al. \(2015\)](#)) such as inductance and capacitors circuits allow to represent those more complex behaviors. Here, we have confined ourselves to the schematic resistance representation to illustrate the notions of pressure and flow distributions.

1.2.2 Pressure wave propagation

When blood is expelled from the heart, a pressure wave is produced by left ventricle (LV) and travels through the arterial tree. Every level of that tree will not receive the wave at the same time. As this pressure pulse travels, it generates a negative pressure gradient that accelerates the fluid along its traveling path. This wave propagates faster than the flow and results in a delayed cardiac cycle waveform along the arterial tree. As an example systole is observed earlier in the ascending aorta than in the abdominal aorta which is

further from the heart (from where the pulse is emitted). Pressure wave velocity (PWV) is the velocity at which the pulse wave travels a given distance between 2 sites of the arterial tree. For healthy patients, PWV ranges from 4 to 10 m.s⁻¹ (van Elderen et al. (2011); Devos et al. (2015); Devos et al. (2017)).

In essence, the original wave from LV can reflect on obstacles such as arterial bifurcations and go backward the arterial tree. Thus, measured arterial pressure at a certain moment corresponds to the superposition of this original wave and many reflected waves as shown in figure 1.18. This superposition results in the amplification of the local pressure. The more we go down in the arterial tree, the more bifurcations, and thus, the more reflection sites are. Consequently, depending on the distance from the LV, an arterial section will receive more or less in-phase original and reflected waves. As an example, we may consider a simple model with LV, the aorta and a bifurcation (figure 1.18). Close to LV (far from the reflection site) the reflected wave returns after systole (original wave's peak) and thus, contributes to the increase of the diastolic pressure. Far from LV (close to the reflection site) the original and reflected waves are more in-phase. The local pressure is increased at systole and remains low during the diastolic phase.

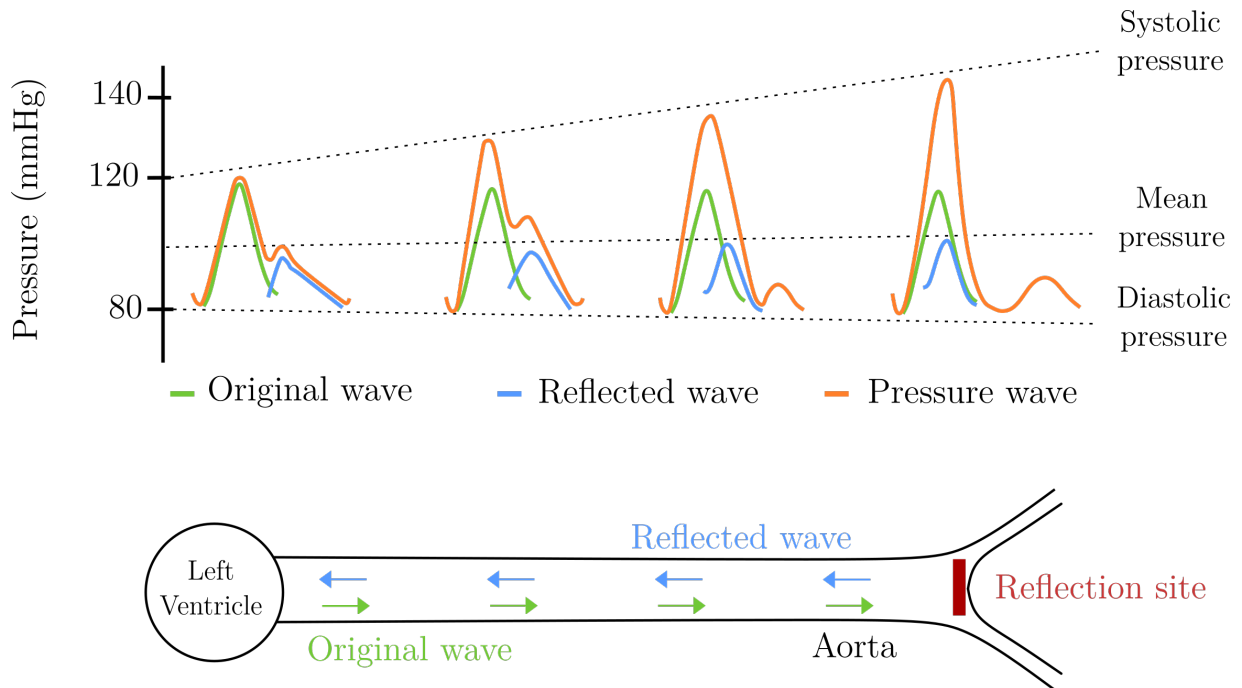


Figure 1.18: (Up) Original and reflected pressure waves superposition resulting in a total pressure wave. (Down) Representation of the vessel with a single reflection site. Adapted from Rachid (2018).

It is interesting to note that the shape of pressure profile strongly depends on the pulse wave propagation and reflections. These ones depend on material geometry and properties such as wall stiffness (calcification), obstructed areas (thrombosis), etc. Indeed, abnormal pressure profile is a good indicator of cardiovascular pathologies (Rachid (2018)) and can be measured with simple US-doppler examination on patient.

1.2.3 Fluid mechanics governing equations

Now the notions of pressure and flow distributions along the arterial tree were defined, mathematical models can be implemented. In this section fluid mechanics principles are applied to simplified models representing vessels and blood flow. Navier-Stokes equations are adapted to hemodynamical conditions (Galdi et al. (2008)) including non-Newtonian fluid behavior and pulsatile flow (non-stationary conditions).

From now on, the following mathematical notations are adopted: bold type is used to indicate a first order tensors (vector), double bars for a second tensor and the Einstein summation convention is adopted. We are working with Cartesian coordinates and tensors are relative to a fixed orthogonal basis (e_1, e_2, e_3) .

Let us consider an incompressible isothermal flow. The fluid is considered as a continuous material with density ρ . The second viscosity term is neglected by assuming the validity of the Stokes relation. The flow is described by the Navier-Stokes constitutive equations consisting of the mass conservation,

$$\frac{\partial \rho}{\partial t} + \nabla(\rho \mathbf{v}) = \nabla \mathbf{v} = 0 \quad (1.2.2)$$

and the momentum conservation,

$$\rho \frac{\partial \mathbf{v}}{\partial t} + \rho (\mathbf{v} \cdot \nabla) \mathbf{v} = \nabla \cdot \bar{\bar{\boldsymbol{\sigma}}} + \mathbf{f}_v, \quad (1.2.3)$$

where \mathbf{v} is the velocity and \mathbf{f}_v represents body forces acting on the fluid such as gravity. $\bar{\bar{\boldsymbol{\sigma}}}$ is the total stress tensor described as a sum of normal and shear forces,

$$\sigma_{ij} = -p \delta_{ij} + \tau_{ij}, \quad (1.2.4)$$

with p is the isotropic normal pressure, δ_{ij} is the Kronecker symbol and τ_{ij} is called the viscous stress tensor. This last one depends on the kinematic of the flow and on the rheological properties of the fluid.

For Newtonian flow, there is a linear relationship between viscous stress tensor and rate-of-strain tensor,

$$\tau_{ij} = \mu \dot{\gamma}_{ij}, \quad (1.2.5)$$

with the fluid viscosity μ and shear rate $\dot{\gamma}_{ij}$ defined as

$$\dot{\gamma}_{ij} = \left(\frac{\partial v_i}{\partial x_j} + \frac{\partial v_j}{\partial x_i} \right). \quad (1.2.6)$$

The momentum conservation equation 1.2.3 for newtonian flow is

$$\rho \frac{\partial \mathbf{v}}{\partial t} + \rho (\mathbf{v} \cdot \nabla) \mathbf{v} = -\nabla(p) + \mu \Delta \mathbf{v} + \mathbf{f}_v. \quad (1.2.7)$$

For non-Newtonian flows, viscosity depends on other factors such as shear rate. Generalized Newtonian models are often used to characterize this shear rate dependence by redefining τ_{ij} as a function of apparent viscosity which depends on rate-of-strain tensor $\dot{\boldsymbol{\gamma}}$,

$$\tau_{ij} = \mu(\dot{\gamma}_{ij}) \dot{\gamma}_{ij}. \quad (1.2.8)$$

In order to build up a constitutive equation, the dependency on $\dot{\boldsymbol{\gamma}}$ must respect the fact that the constitutive equation does not depend on the coordinate system. It is achieved using the invariants of the tensor. The three invariants of the rate-of-strain tensor are defined as

$$I = \dot{\gamma}_{kl}, \quad II = \dot{\gamma}_{kl}\dot{\gamma}_{lk}, \quad III = \dot{\gamma}_{kl}\dot{\gamma}_{lm}\dot{\gamma}_{mk}. \quad (1.2.9)$$

For incompressible fluids, the mass conservation equation sets $I = \nabla \cdot \mathbf{u} = 0$. Moreover when the flow is assumed to be shear-dominated III is often neglected. Therefore, II is the only non-zero invariant and the magnitude of shear rate tensor is

$$\dot{\gamma} = \sqrt{\frac{1}{2}II} = \sqrt{\frac{1}{2}\dot{\gamma}_{kl}\dot{\gamma}_{lk}}, \quad (1.2.10)$$

where $\dot{\gamma}_{lk}$ is defined as in equation 1.2.6. Finally, the momentum equation for generalized Newtonian flow is

$$\rho \frac{\partial \mathbf{v}}{\partial t} + \rho (\mathbf{v} \cdot \nabla) \mathbf{v} = -\nabla(p) + \Delta(\mu(\dot{\gamma})\mathbf{v}) + \mathbf{f}_v. \quad (1.2.11)$$

Generalized Newtonian models for blood were described in section 1.1.4.3 and can be implemented in the term $\mu(\dot{\gamma})$ of equation 1.2.11. Bear in mind that it is a global flow representation. As an example, more complex system such as FENE-P model can be introduced to take into account polymer conformation that generates viscosity variations as a function of shear rate (Cocconi et al. (2017)). In the present work the generalized Newtonian laws for viscosity is sufficient.

1.2.4 Flow characterisation using dimensional analysis

For Newtonian fluids, the Navier-Stokes equations can be written as dimensionless equations with the following dimensionless variables,

$$x_i^* = \frac{x_i}{D}, \quad p^* = \frac{p}{\rho V^2}, \quad v^* = \frac{v}{V}, \quad t^* = \frac{t}{T}, \quad (1.2.12)$$

where x_i^* are the spatial coordinates, D is the characteristic length (diameter for pipe flows), V is the flow mean velocity and T the characteristic time of the flow. In the case of oscillatory flow, T is the period of oscillations. Body forces are neglected and dimensionless Navier-Stokes equations are

$$\frac{\alpha^2}{Re} \frac{\partial \mathbf{v}^*}{\partial t^*} + (\mathbf{v}^* \cdot \nabla) \mathbf{v}^* = -\nabla p^* + \frac{1}{Re} \Delta \mathbf{v}^* \quad (1.2.13)$$

$$\nabla \cdot \mathbf{v}^* = 0,$$

with the Reynolds number

$$Re = \frac{VD\rho}{\mu}, \quad (1.2.14)$$

and the Womersley α number for $\omega = \frac{2\pi}{T}$ (Comolet (1984))

$$\alpha = \frac{D}{2} \sqrt{\frac{\omega \rho}{\mu}}. \quad (1.2.15)$$

The Reynolds number is the ratio of the convective inertia forces and the shear viscous forces in the momentum equation (Fung (1993)). Under ideal conditions, it is used to characterize laminar and turbulent regimes. At low Reynolds number ($Re < 2000$), the flow is laminar thanks to non negligible viscous forces which tend to inhibit turbulence. At higher Reynolds number ($Re > 2000$), inertial forces take over and the flow becomes turbulent. Throughout the body, Re drastically varies from 1 in small arteriole to 3000 in the aorta. This variation indicates a wide range of flow characteristics in the arterial tree. Note that a non-Newtonian the Reynolds number is difficult to conceive because viscosity is not a constant and is shear-dependent. A common approximation is to use the shear-thinning fluid asymptotic viscosity at high shear rate as a reference viscosity (between 3 and 5 mP.s (Baskurt (2003))).

Vessel	Diameter (mm)	Mean velocity (m.s ⁻¹)	Re	α
Aorta	25	4 . 10 ⁻¹	2650	12.87
Arteries	4	2 . 10 ⁻¹	212	2.06
Arterioles	0.03	5 . 10 ⁻²	0.4	0.015
Capillaries	0.008	3 . 10 ⁻⁴	*	0.004

Table 1.3: Order of magnitude assessment of Reynolds and Womersley number along the arterial tree depending on vessels diameter and mean blood velocity. Calculated values correspond to a 75 beats-per-minute heart pulse, a blood density of 1060 kg.m⁻³ and a viscosity of 4 mPa.s. * non identified value. (order of magnitude from Physiology class of Barry Belmont from Michigan University, Belmont (2020)) .

The Womersley number is the ratio of the transient oscillatory inertia force to the viscous shear forces. Considering viscosity and density as constants along the arterial tree, the main variable factors are vessel diameter and heart beats. At large Womersley numbers ($\alpha > 10$ in large vessels and/or at higher frequency) oscillatory inertia forces dominate over viscous forces (Fung (1993)). The flow grows with a reduced amplitude of motion and a phase difference appears between velocity and the driving oscillating pressure gradient. Conversely, at low Womersley numbers (higher frequency and/or in small vessels) viscosity dominates. The velocity profile is similar to a Poiseuille profile regarding its shape at a specific instant. This profile amplitude is oscillating in phase with the driving oscillating pressure gradient. Velocity grows in phase with the pressure gradient.

These two numbers are mostly used for Newtonian flows. They can be adapted to generalized Newtonian models by using a relevant apparent viscosity and by ignoring the shear-rate dependence. Table 1.3 shows typical Reynolds and Womersley numbers along the arterial tree.

These numbers play a significant role to determine whether or not simplifications can reasonably be applied on the Navier-Stokes equations. Concerning the cardiovascular system, heart pulse frequency, vessel diameter, shear rates, blood viscosity and velocity are directly related to those numbers and provide different simplified Navier-Stokes equations depending on the location in the arterial tree.

1.2.5 Blood flow simplified models

This section provides a mathematical analysis of a pipe flow problem to model arterial flow. The aim is to appreciate the meaning of each hemodynamics characteristics such as instationary flow, fluid shear-thinning behavior, walls deformation, etc. The following study of the Navier-Stokes equations and dimensionless number on a simplified pipe flow system will give an overview of the complexity of hemodynamical flows. It also provides guidelines for physically reasonable simplifications for the resolution of the real arterial hemodynamics problem. The idea is to determine if features such as non-Newtonian properties or pulsatile frequency are essential or negligible to explain flow profiles. Indeed, many studies simplify blood models to Newtonian flow (Bonfanti et al. (2020); Büsen et al. (2017)) or neglect the pulsatile nature of arterial flows. In this section, we investigate the impact of each feature step by step.

Let us consider an arbitrary blood vessel as an infinite straight pipe with a radius R . The flow is assumed to be fully developed and the fluid to be incompressible with a density $\rho = 1060 \text{ kg.m}^{-3}$ (human blood approximate density). Cylindrical coordinates are used to describe the system as shown in figure 1.19. The discussed hypotheses and models are summed up in figure 1.20.

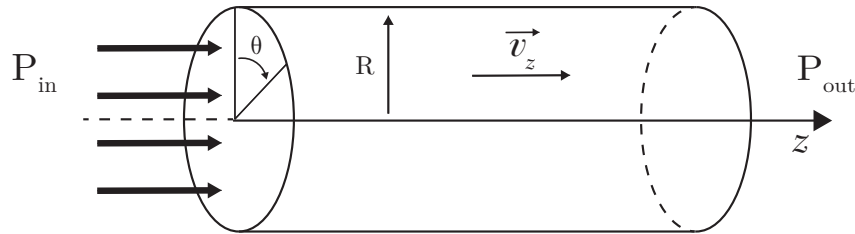


Figure 1.19: Pipe flow model with cylindrical coordinates

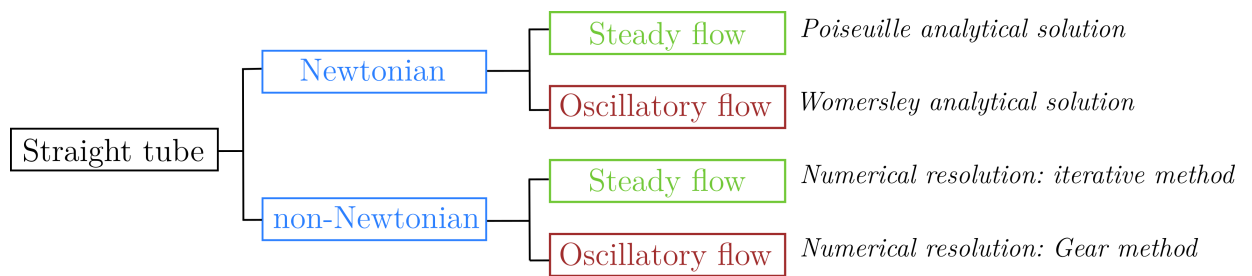


Figure 1.20: Overview of pipe flow hypothesis and corresponding solutions and/or resolution methods for the next paragraphs.

Steady Newtonian and non-Newtonian pipe flow: viscosity distribution

For incompressible steady flow under laminar condition, the pressure and velocity can be simplified, thanks to the cylindrical symmetry and mass conservation equation:

$$p(r, \theta, z, t) = p(r, z, t) \text{ and } \mathbf{v}(r, \theta, z, t) = v_z(r, t)\mathbf{e}_z.$$

For Newtonian flow under laminar condition, the Poiseuille analytical solution (Poiseuille (1840)) to Navier-Stokes equation 1.2.7 describes the flow velocity as a function of the pressure gradient along axis z , pipe radius R and viscosity μ .

$$v_z(r, \theta, z) = v_z(r) = -\frac{R^2}{4\mu} \frac{dp}{dz} \left(1 - \frac{r^2}{R^2}\right). \quad (1.2.16)$$

Note that the velocity runs parallel with z axis and only depends on the radius of observation r . A zero velocity is imposed along the wall $r = R$ while a maximum velocity appears at the pipe centerline $r = 0$. Moreover, shear-rate can also be calculated by deriving equation 1.2.16 and is defined as

$$\dot{\gamma} = \frac{\partial v_z(r)}{\partial r} = \frac{1}{2\mu} \frac{dp}{dz} r. \quad (1.2.17)$$

$\dot{\gamma}$ exhibit zero value at the centerline and a maximum value along the wall. If we assume that non-Newtonian steady pipe flows have similar profiles (Poiseuille), this shear rate property provides clues about the viscosity profile. For generalized Newtonian profiles, $\dot{\gamma}$ from equation 1.2.17 can be used. Thus, the viscosity is expected to be minimal along the wall where high shear-rates are observed. Conversely, maximal viscosity should be observed near the centerline where the shear-rate tends to zero.

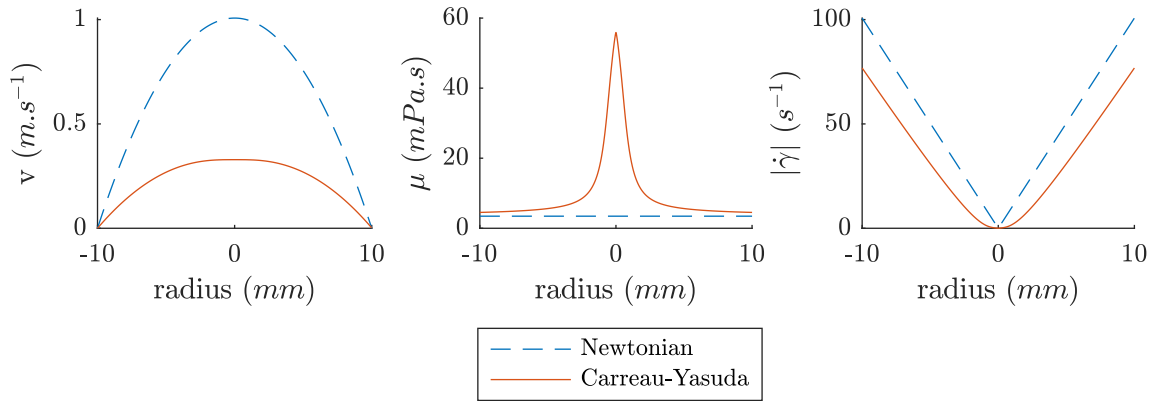


Figure 1.21: Pipe flow velocity profile for a 10 mm radius pipe for the Newtonian fluid flow. (Left), viscosity profile, (center) and absolute shear-rate profile, and (right) for a Newtonian ($\mu = 3.45$ mPa.s) and a Carreau-Yasuda fluid (refer to the model parameters in Table 1.2)

A numerical solution of Navier-Stokes equation for this pipe flow with a Carreau-Yasuda model is provided in figure 1.21. The computation was conducted with an in-house MATLAB program. The result was obtained with an iterative resolution of the

Navier-Stokes equation which was initiated with the Newtonian Poiseuille solution. The last one was set to reach a maximum velocity of 1 m.s^{-1} as a reference in a 10 mm diameter pipe (similar order of magnitude observed in human arteries). The notable difference with the Newtonian Poiseuille solution, is the flattening of the profile at the centerline. This outcome was expected since viscosity is supposed to increase near the centerline and thus, to resist the flow.

Unsteady newtonian pipe flow: Womersley velocity profile

Let us consider a periodic laminar pipe flow with a pulse $\omega = 2\pi/T$ where T is the period. The pressure gradient can be written as Fourier series,

$$\frac{\partial p(z, t)}{\partial z} = \mathcal{R}e\left(\sum_{k=0}^{\infty} c_k e^{ik\omega t}\right) \quad (1.2.18)$$

with i the imaginary number ($i^2 = -1$), Fourier coefficients c_k and $\mathcal{R}e$ the real part of associated complex number. The velocity also adopts the same form in accordance with the Navier-Stokes equations and is written as

$$v_z(r, z, t) = \mathcal{R}e\left(\sum_{k=0}^{\infty} v_k e^{ik\omega t}\right), \quad (1.2.19)$$

with the Fourier coefficients v_k . The Navier-Stokes equation is thus written with coefficient c_k and v_k as

$$\begin{aligned} \frac{\partial v_k}{\partial z} &= 0 \\ \rho i k \omega v_k &= -\frac{c_k}{\mu} + \mu \left(\frac{\partial^2 v_k}{\partial r^2} + \frac{1}{r} \frac{\partial v_k}{\partial r} \right), \end{aligned} \quad (1.2.20)$$

with $0 \leq k \leq \infty$. These linear equations admit an analytical solution called the Womersley solution ([Womersley \(1955\)](#)).

$$v_z(r, t) = -\frac{c_0 R^2}{\mu} \left(1 - \left(\frac{r}{R}\right)^2\right) - \frac{R^2}{\mu} \sum_{k=1}^{\infty} \mathcal{R}e \left(\frac{ic_k}{\alpha_k^2} \left(1 - \frac{J_0(\alpha_k \frac{r}{R} i^{\frac{3}{2}})}{J_0(\alpha_k i^{\frac{3}{2}})}\right) e^{i\omega t} \right). \quad (1.2.21)$$

The first term is the steady part of the solution which is similar to the Poiseuille solution. The second term consists of a zero order Bessel function J_0 and a coefficient α_k which is similar to the Womersley number, $\alpha_k = R\sqrt{\frac{k\rho\omega}{\mu}}$. Velocity profiles are shown in [figure 1.24](#) and [figure 1.25](#) for three different viscosities and four radii. In the present analysis, the constants were estimated from the literature such that maximal, minimal and in-between viscosities were taken from the Carreau-Yasuda model from [table 1.2](#) to cover the range of blood accessible viscosities ([1.22](#)). Similarly, radii from 1 to 30 mm were selected to represent the range of vessels diameters from the aorta down to the arterioles (refer to [table 1.1](#)). Finally, the pressure gradient was set as

$$\frac{\partial p(z, t)}{\partial z} = P_0 \cos(2\pi f t). \quad (1.2.22)$$

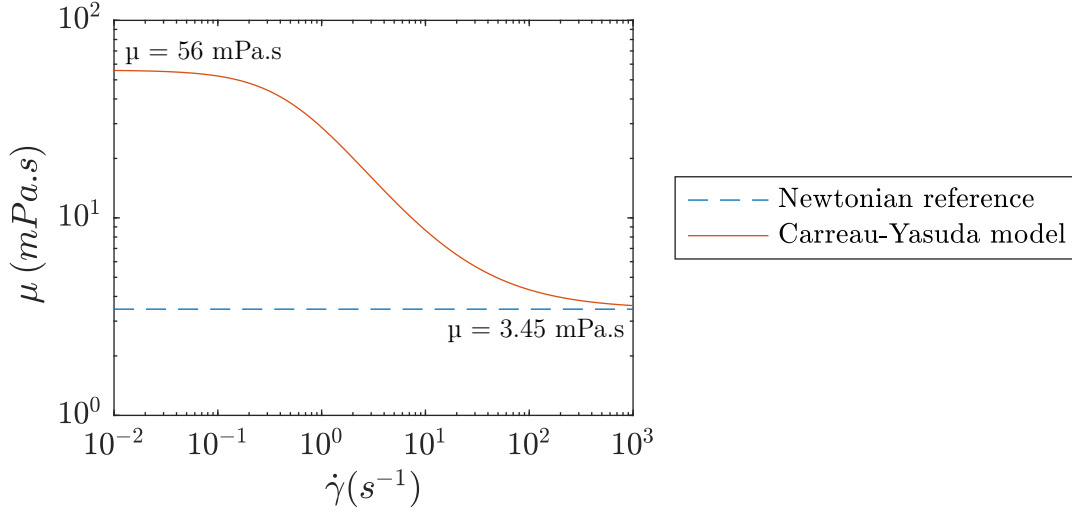


Figure 1.22: Viscosity references for the model

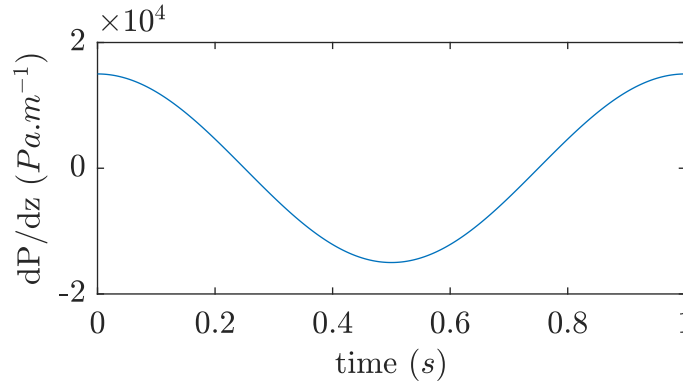


Figure 1.23: Pressure gradient profile.

with and $P_0 = 15000 \text{ Pa.m}^{-1}$ and $f = 1 \text{ Hz}$ for a oscillation period $T = 1 \text{ s}$ (1.23). The order of magnitude of the peak aortic pressure gradient is $15\,000 \text{ Pa.m}^{-1}$ (around 1 mmHg.cm^{-1}). This value was estimated from [Olson \(1968\)](#) and pressure gradient variations were simplified to a sinusoidal oscillatory signal over the cardiac cycle period T .

The more the viscosity increases and/or the radius decreases (small Womersley number), the more the velocity profile tends to a parabolic shape. These observations are consistent with the conclusions drawn with the dimensional analysis and the influence of the Womersley number in paragraph 1.2.4. The transient forces become less significant and the velocity profile tends to the typical parabolic shape observed in Poiseuille steady flows.

Many hemodynamical studies used this Womersley model by neglecting the non-Newtonian property of blood. Actually, the main quantities of interest for blood vessels concern near wall flows as they are essential to understand wall weakening mechanisms. In this region, the difference between Newtonian and non-Newtonian velocity profiles is less pronounced. However, this simplification is frequently questioned when considering more complex pipe geometries and tricky areas such as bifurcations, narrowing or curvature (discussed in subsection 1.2.6). As a consequence, an increasing number of research include generalized Newtonian pulsatile models for pipe flows ([Tabakova et al. \(2014\)](#)),

Boyd et al. (2007)).

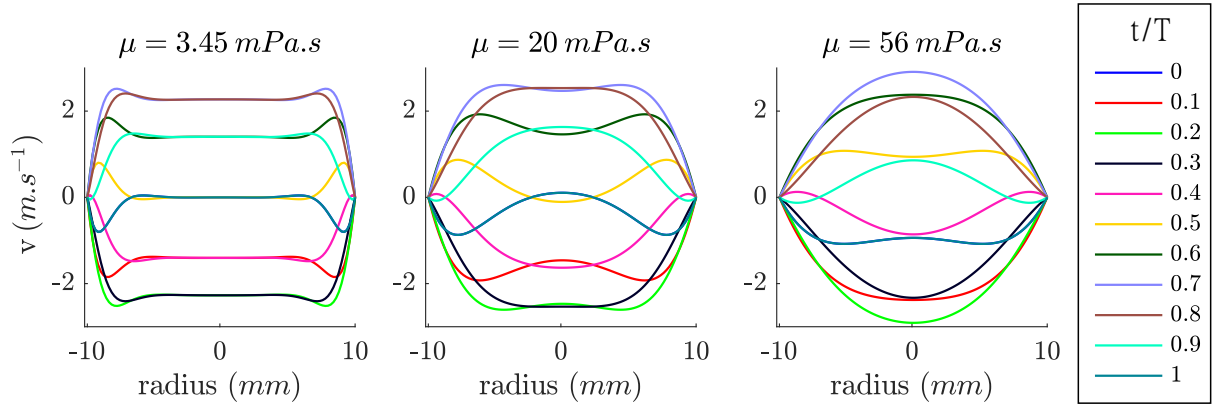


Figure 1.24: Womersley pipe flow velocity profile for a 10 mm radius pipe, oscillating pressure gradient and three different viscosities from left to right. Period of oscillations is $T = 1$ s and colors represent different instant of the oscillation.

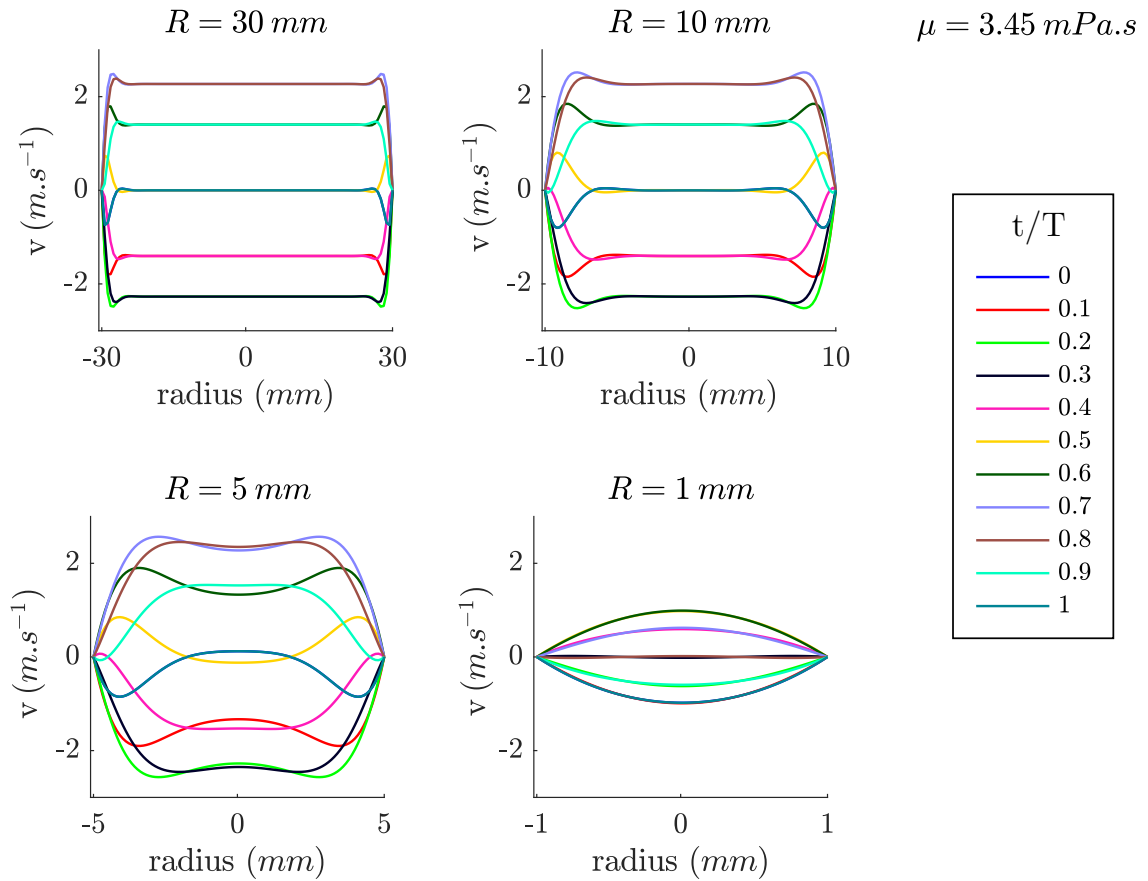


Figure 1.25: Womersley pipe flow velocity profile for a viscosity of $3.45 mPa.s^{-1}$, oscillating pressure gradient and three different pipe radius from left to right.

Unsteady non-Newtonian pipe flow

In the case of generalized Newtonian flow in a pipe, one may determine the velocity profile with numerical methods. The Navier-Stokes momentum equation can be simplified as,

$$\rho \frac{\partial \mathbf{v}}{\partial t} + \rho (\mathbf{v} \cdot \nabla) \mathbf{v} = -\nabla p + \Delta(\mu(\dot{\gamma})\mathbf{v}), \quad (1.2.23)$$

where volume forces such as gravity are neglected. As in previous cases, velocity is supposed to be oriented along the z axis with a cylindrical symmetry due to the pipe geometry. Moreover, the same pulsatile pressure gradient profile is adopted (1.2.22). The momentum equation becomes

$$\rho \frac{\partial v_z}{\partial t} = -\frac{\partial p}{\partial z} + \frac{1}{r} \frac{\partial}{\partial r} (\mu(\dot{\gamma})v_z), \quad (1.2.24)$$

where the viscosity term is described by a Carreau model which depends on the velocity gradient (see constants in table 1.2)

$$\mu(\dot{\gamma}) = \mu \left(\frac{\partial v_z}{\partial r} \right) = \mu_\infty + \frac{\mu_0 - \mu_\infty}{\left(1 + \left(\lambda \frac{\partial v_z}{\partial r} \right)^2 \right)^{\frac{1-n}{2}}}. \quad (1.2.25)$$

The velocity profile can be determined using Partial Differential Equation solving methods such as the Crank-Nicolson or Gear methods. As in previous cases, the velocity is supposed to be zero at the pipe walls and the velocity gradient is null at the pipe centerline.

A fifth order Gear method (Shampine and Reichelt (1997), Ordinary Differential Equation suite from MATLAB) was implemented on MATLAB to calculate the velocity profile in a pipe for a $T = 1$ s periodic pressure profile. Figure 1.26 shows results for a same system with the Newtonian Womersley analytical solution (solid lines) and Carreau solution solved with the Gear method (dashed lines).

The Newtonian and generalized Newtonian velocity profiles mostly differ at small pipe radius. The generalized Newtonian case shows flattened velocity profile with less abrupt curvature changes. Those differences are less pronounced at $R = 10$ mm than at $R = 1$ mm which supports the hypothesis of considering a Newtonian model beyond a certain pipe diameter, and thus for large arteries.

These simple models describe periodic non-Newtonian flows in a rigid tube and offer an overview of the influence of different flow parameters such as pipe diameter, viscosity properties, etc. on flow dynamics. With basic representation of the arterial system, complex behavior are already observed and provide clues for modeling hemodynamical flow depending on environment and conditions (diameter, pulse rate, Newtonian/non-Newtonian, etc). In previous models, walls were supposed to be rigid and we only provided fluid mechanics tools. In the next two sections, channel geometry and walls elasticity will be addressed as an additional element in the modeling process and bring additional complexity.

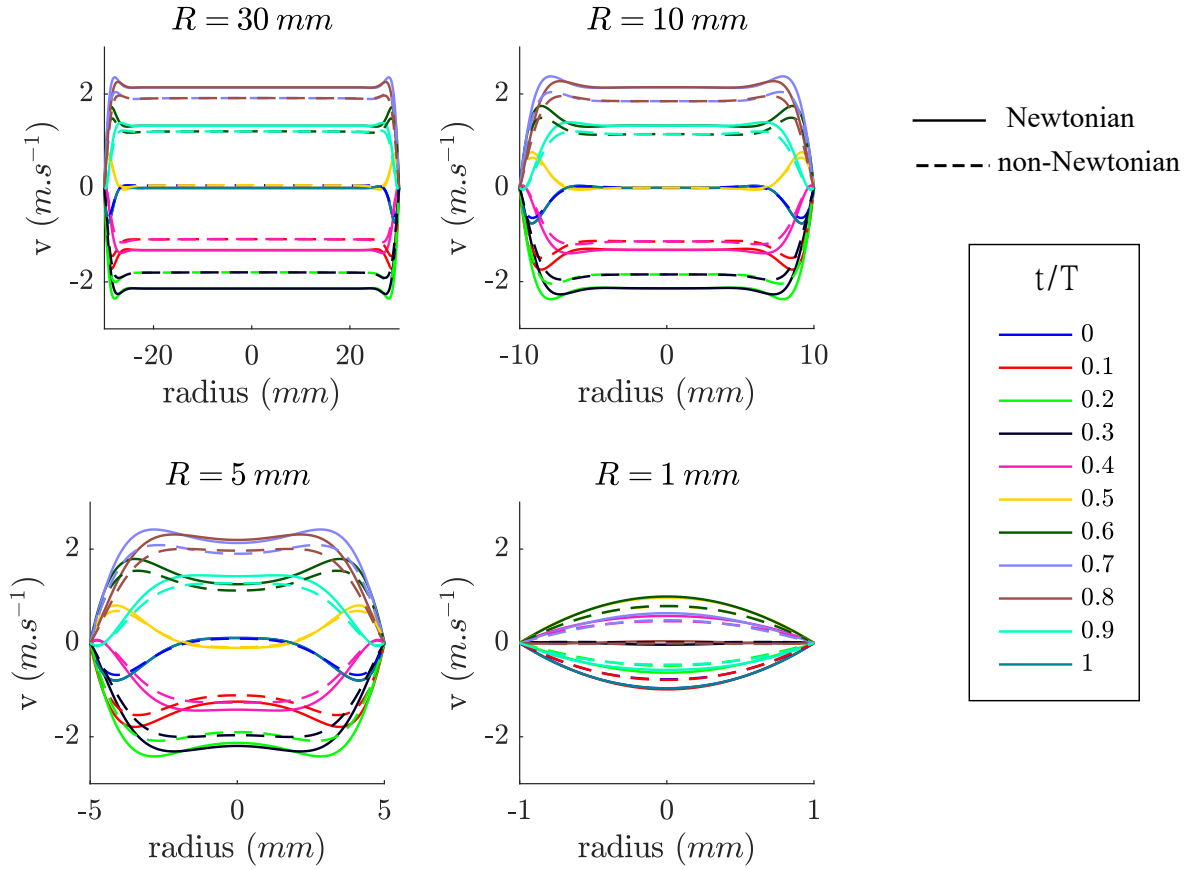


Figure 1.26: Newtonian Womersley (solid lines) and generalized Newtonian Carreau (dashed lines) pipe flow velocity profile for three different pipe radii under oscillating pressure gradient. Period of oscillations is $T = 1$ s and colors represent different instants of the oscillation.

1.2.6 Channel geometry and singularities

Many studies focus on the influence of geometry, irregularities and singularities on flow channels with Newtonian and non-Newtonian fluids. Diameter narrowing and planar expansion were investigated by Jung et al. (2004) and Neofytou (2006). These symmetrical channel geometry variations can lead to symmetry breaking, flow separation and swirling structure development. Jung et al. (2004) pointed out the development of asymmetrical flow in symmetrical channel geometry with a numerical model representing different degrees of stenosis (local channel diameter narrowing). Asymmetry appears beyond a certain percentage of stenosis (57% of channel narrowing). Neofytou (2006) highlighted the influence of flow Reynolds number on the transition from symmetrical to asymmetrical flow in channel with sudden expansion geometry and different Power-Law rheological model. Geometrical features combined with Reynolds numbers and rheological models appear to strongly influence flow distribution. It brings new flow features compared to simplified representations of arteries as straight tubes.

Numerical models of abdominal aorta aneurysm (AAA) equivalent to a channel with asymmetrical balloon shape-like expansion were implemented in Khanafer et al. (2006). Two types of pulsatile flow conditions (sinusoidal and physiological) and different AAA expansion degree were compared and exhibited clear differences between Newtonian and

non-Newtonian models. This study shows that flow distribution and swirling structures depend on three parameters: geometry, pulsatile flow conditions and fluid rheological model.

Finally, with a more realistic anatomical representation, [Prah Wittberg et al. \(2016\)](#) implemented numerical models of human aorta to study the influence of anatomical irregularities on flow patterns with a non-Newtonian model which included RBCs distribution. Normal, dilated, constricted and elongated aorta models were investigated and showed a clear influence of geometry on flow distribution, wall shear stresses and RBCs distribution. As an example, in this study, aorta diameter narrowing generated a jet-like flow. Noticeable swirling structures appear downstream from this irregularity (figure 1.27). Investigating those types of structure could provide clues on aortic flow mechanisms understanding related to geometrical features.

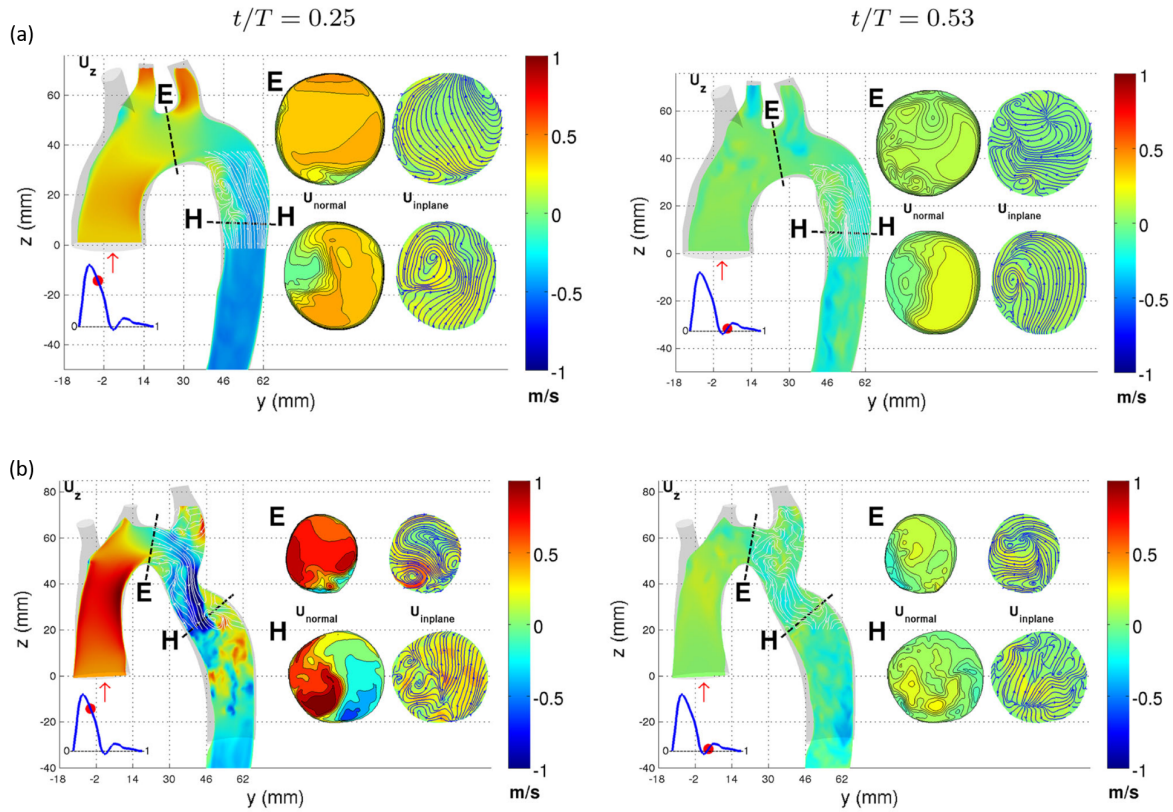


Figure 1.27: Velocity fields for normal (a) and constricted (b) thoracic aorta model from [Prah Wittberg et al. \(2016\)](#). Left and right columns correspond to two different cardiac cycle instants.

These studies showed that channel geometry clearly impacts hemodynamical flows at different scales depending on many features such as rheological model assumption, pulsatile flow conditions or Reynolds number. As a consequence, neglecting geometrical irregularities to simplify blood flow models may lead to inaccurate results and misinterpretations.

1.2.7 Compliant walls and Windkessel models

In previous models, walls were assumed to be rigid. However, aortic wall is compliant and plays a major role in hemodynamics. The Windkessel model allows to model the interaction between the propagating blood volume, the compliant aortic wall and peripheral vessels. The aorta is represented as an elastic chamber with a compliance C . Peripheral vessels are modeled as rigid tubes with a resistance R_p . Blood is forced into the system during systole and applies a transmural pressure on the aortic wall. The compliant wall allows volume expansion ΔV to compensate the increased pressure ΔP . The compliance is defined as

$$C = \frac{\Delta V}{\Delta P}. \quad (1.2.26)$$

Considering the electric circuit analogy from section 1.2.1, walls act as a capacitor that stores blood and energy during systole and then discharges it when pressure drops at diastole. The result is a dampening of blood pressure thanks to the volume expansion compensation. In addition, smaller peripheral vessels act as resistances. Indeed, their smaller diameter reflects a mechanical force which is opposed to blood flow (Comolet (1984)). These properties allow to represent the Windkessel effect with electrical circuit analogy and low pass filters. Figure 1.28 shows a 2-elements (compliance C and resistance R_p) Windkessel model. Addition of peripheral vessels/resistances at the entrance of the vessel can be modelled with more complex models such as 3 and 4 elements Windkessel.

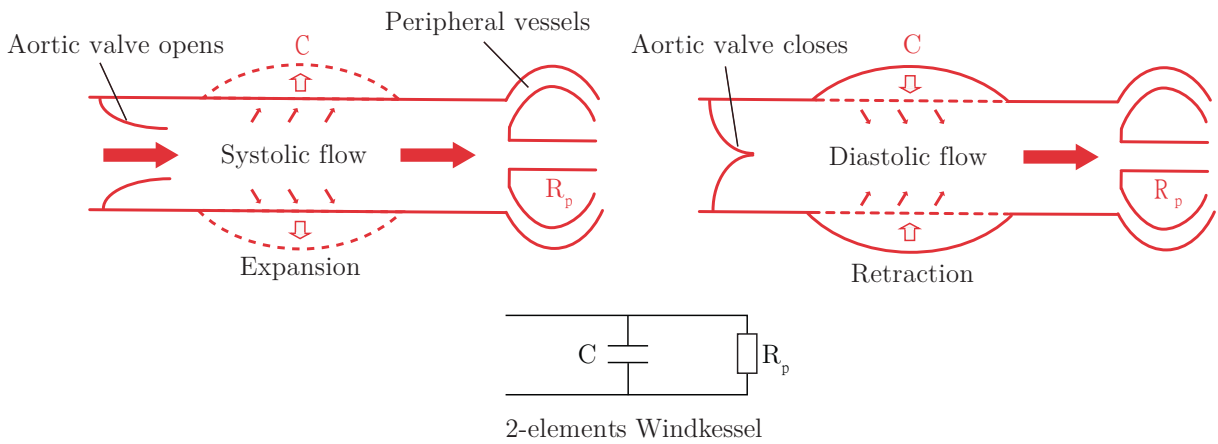


Figure 1.28: 2-elements Windkessel model representation.

This behavior highlights the joint role of aortic wall and fluid mechanics. The fluid motion impacts the solid walls by applying a certain stress, modifying the arterial lumen and thus, changing walls mechanical state. In turn, the aortic walls apply a certain stress on the fluid which modifies flow dynamics. The periodicity of arterial flow involves constant responses from the fluid to the solid walls and back again. Moreover, when considering the complex mechanical properties of both blood and arterial walls, their environment and interacting elements have a strong impact on their own behavior. Each system influence the other and cannot be addressed separately.

On one hand, the aortic wall behavior has been widely studied thanks to solid mechanics theories, experimental research and numerical simulations. On the other hand, blood flow dynamics has also been extensively investigated throughout the arterial tree. However, another difficulty is to combine both domains to accurately describe arterial hemodynamics. It is well known that non-Newtonian fluids and pulsatile flows exhibit specific properties regarding viscosity distribution, dampening effects and oscillatory velocity profiles. These properties become even more complex when the piping system has a tricky geometry and compliant walls. Hemodynamical behavior is considered as a major factor in the development of cardiovascular diseases. It is clear that vessels properties and geometry have non negligible interaction with blood flows. These make up an overall fluid/solid system within each element interacts with each other. Better knowledge of these flow systems could allow to understand, prevent and treat pathologies but requires complex modeling and measurements tools. The way hemodynamical flows impact diseases and vice versa is discussed in next section.

1.3 Effects of pathologies on hemodynamics (and vice versa)

1.3.1 Aorta pathologies

Atherosclerosis is a condition where arteries become narrowed and stiffer because the vessel lumen is occluded by the build-up of a plaque. The plaque is composed of fat, cholesterol, calcium and other blood substance that accumulate on the arterial wall (Rognoni et al. (2015)). The development of plaque can lead to arterial wall weakening, tears and/or occlusion. Partial occlusion of the lumen is called sclerosis and can result in a short supply of oxygen and nutrient to the irrigated organs (figure 1.29a).

Sometimes, the plaque ruptures and becomes a trap for clotting agents such as platelets. Platelets build-up contributes to the increase of the occlusion. Total occlusion of the vessel is called thrombosis and can completely stop blood supply to the irrigated organs. In some cases, the break of the build-up mass can generate clot that travels around the body and cause life threatening conditions such as embolus.

Atherosclerosis is the leading cause of death worldwide and the major trigger of vascular diseases such as Aortic Aneurysm and Aortic Dissection (Pahwa and Jialal (2020)). Atherosclerosis appears to be prevalent in countries with a middle and high income population where longer life expectancy are observed. Barquera et al. (2015) highlighted strong correlation between Atherosclerosis Cardiovascular Disease (ACD), high body mass index, hypertension, glucose and cholesterol level. Developing countries have experienced increases in both ACD and enumerated risk factors. However, in most developed countries, mortality rate has dropped thanks to early diagnose, efficient medication and reliable surgical solutions. As an example, mortality decreased from 22% in 1950 to 6% in 2010 in UK for middle-aged men (35-69 years) (Herrington William et al. (2016)). Atherosclerosis disease can be treated with drugs, angioplasty and stenting surgery to chemically or mechanically reduce or remove the plaque and thus, restore the artery lumen.

Aortic aneurysm refers to a localized and permanent enlargement of blood vessels of at least 50% of its original size. Most aortic aneurysms are caused by stiffening of arterial wall combined with high pressure blood that can cause expansion, bulge, wall thinning and tears (figure 1.29b). A ruptured aneurysm causes life-threatening bleeding with mortality rate between 80 and 90% including 50% of death before reaching the hospital (Thomas et al. (2014)).

A multicentre aneurysm screening has shown that Abdominal Aortic Aneurysm (AAA) concerns about 5% of male over 65 years old (Thompson et al. (2012)). AAA is considered as a male-dominated disorder and only a few studies have investigated AAA in the female population. One of these studies showed that 0.74% of women over 60 years suffer from AAA (Ulug et al. (2016)). One of the treatments consists in deploying an endograft (stent graft) in aneurysm site to reinforce weakened walls and prevent rupture.

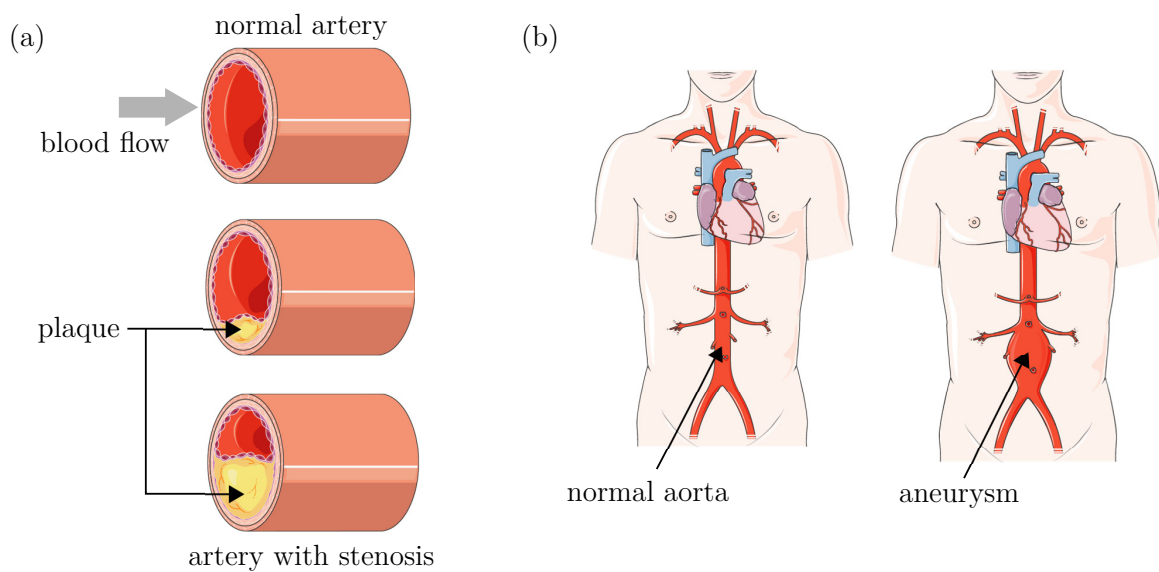


Figure 1.29: (a) Atherosclerosis and deposit of plaque, (b) aortic aneurysm with balloon shape enlargement of the abdominal aorta. Adapted from Servier Medical ART (smart.servier.com).

Aortic dissection (AD) is a condition in which the inner layer of the aorta tears. When blood surges into the tear, it can cause one or more layers to separate (dissect) resulting in the build-up of a "false" blood channel in between the dissected layers. Factors such as high blood pressure, atherosclerosis, presence of an aneurysm increase the risk of dissection. Two types of aortic dissections are identified in accordance with their location. Type A aortic dissection occurs in the ascending aorta while Type B aortic dissection appears in the descending aorta. According to the International Registry of Acute Aortic Dissection, a survey on 1417 AD patients showed 62.5% of Type A and 37.5% of Type B dissections (Tsai Thomas T. et al. (2006)). Both can have variable length false lumen including successive blood exit and re-entrance tears with the true lumen as shown in figure 1.30. The two aortic lumens are separated by a layer of tissue called the intimal flap (Criado (2011)).

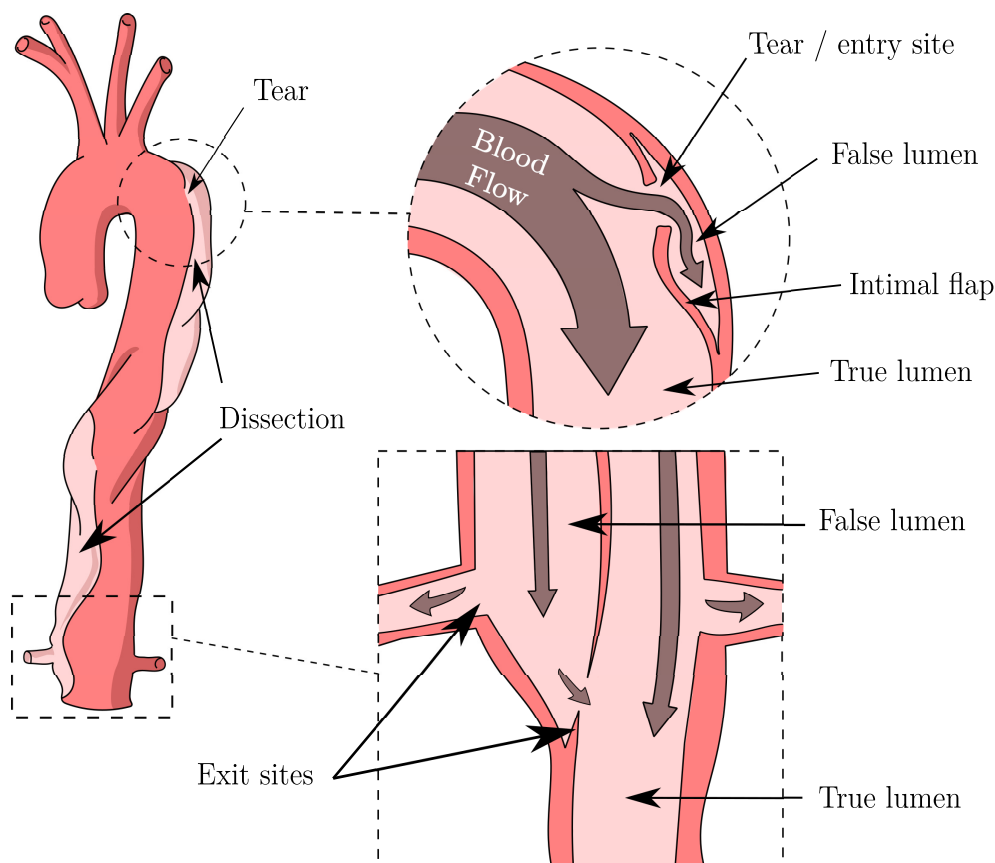


Figure 1.30: Aortic dissection with examples entry and exit sites

This condition strongly weakens aortic wall, disrupts blood flows and can cause multiple complications:

- Rupture of the aortic wall as its structure is weakened and thinned by the separation of layers.
- Circulation disturbances in the false lumen. Indeed, to ensure circulation in the false lumen, blood needs to enter through the entrance tear and leave through an exit toward the true lumen on other aortic branches. Sometimes, the exit is non-existent (blind pouch) or too narrowed to ensure proper circulation. When left untreated, it can result in stagnation and clotting of blood in the false lumen, growing of thrombosis and short blood supply to organs that connect the aorta at the location of the dissection (Singh and Mehta (2015); Shi et al. (2016)).
- Higher pressure in the false lumen due to the previously described circulation complication. Therefore, the false lumen can continue to expand and compress the true lumen and branches causing serious disturbance in the whole body circulation, aneurysm growing and higher risk of rupture (Shi et al. (2016)).

According to epidemiological studies, AD is also a male dominant condition with higher prevalence between 65 and 69 years old (Pacini et al. (2013)). In Iceland, a study from Melvinsdottir et al. (2016) on acute thoracic aortic dissection showed that 21.4% of patients who arrived at the hospital died within 24h and 30-day mortality reaches 45.2%

of patients. AD is rare (between 6 cases over 100 000 patients according to [Howard et al. \(2014\)](#)) and difficult to diagnose but is still a lethal condition. Therefore, an increasing number of studies focus on understanding and improving diagnosis and surgical procedures to limit AD mortality.

Endovascular aortic repair (EVAR) procedure or open surgery can be performed to restore flow in the most adapted lumen. These procedures are illustrated in figure 1.31. The "healthier" lumen could be the true or false lumen depending on the importance of peripheral vessels that are fueled by each channel. The complexity and length of a dissection may need more advanced grafting and stenting techniques. The main risk is to obstruct peripheral arteries with the graft and disturb organs blood supply. [Galvin et al. \(2016\)](#) describes a multi-technique procedure with graft sewing, covered stent graft and bar stent deployment (figure 1.32). This procedure was achieved to meet each AD section's characteristic. It is not a standard procedure but an interesting summary of the different techniques that can be performed on AD.

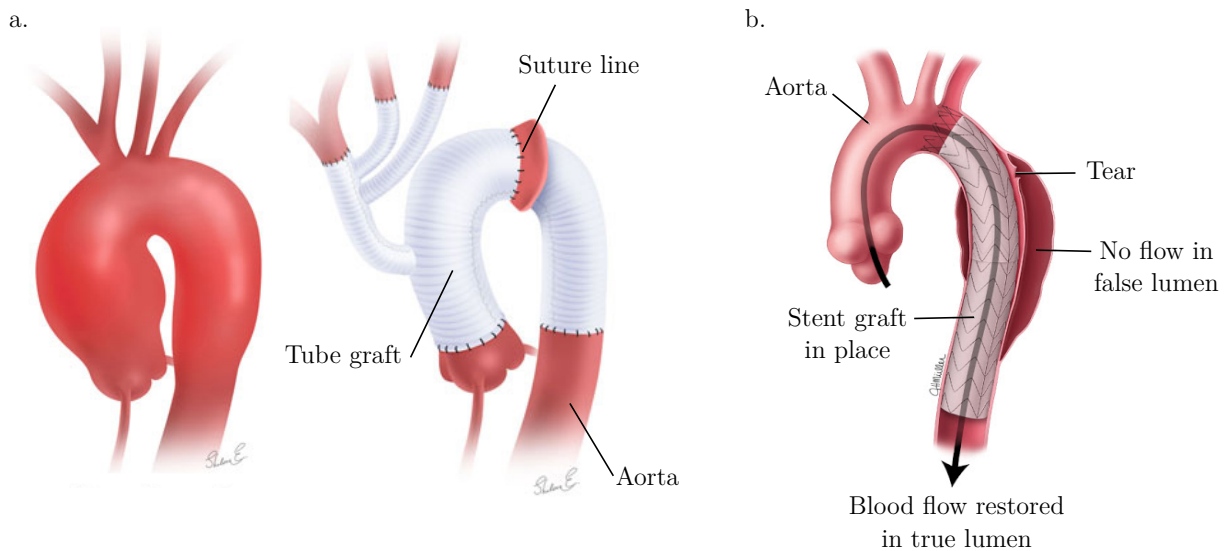


Figure 1.31: Aortic repair techniques, (a) open surgery of aortic replacement with sewed tube grafts, (b) Endovascular Aortic Repair with deployed stent graft in the true lumen and obstruction of the entry tear.

The constant increase of life expectancy goes along with a growing number of patients concerned by cardiovascular diseases. Atherosclerosis and aneurysms are widely documented while only a few large scale surveys focus on the prevalence, mortality and post-operative complications of AD. Aortic walls mechanical behavior and hemodynamical flows are believed to have a fundamental impact on the birth and growing of such pathologies. Surgeons, researchers and manufacturers keep developing new techniques and devices to improve understanding and monitoring of AD to guide surgical decision. To that extent, the following part will focus on hemodynamics studies that provide tools to analyze and treat cardiovascular diseases.

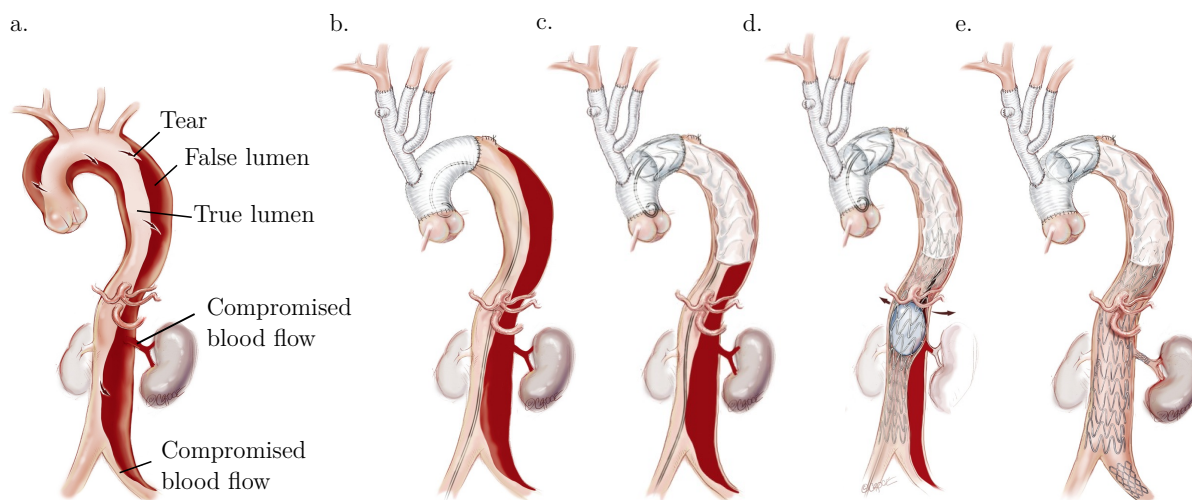


Figure 1.32: Aortic repair steps described in [Galvin et al. \(2016\)](#) (a) Aortic dissection depiction, (b) reconstruction of the aortic arch and branches with sewed tube grafts, (c) deployment of the covered stent graft in the descending aorta to obstruct the entry tear, (d) balloon-expanded metal bar stent along the descending aorta to rupture the flap, (e) completion of the surgery with branch stenting to restore blood flow in left renal and common iliac artery.

1.3.2 Hemodynamics : the key to understand diseases and develop treatments

Numerous hemodynamics studies have been conducted on blood vessels with the increase of cardiovascular diseases and development of medical imaging techniques. These studies have pointed out some hemodynamical features that could be related to aortic pathology outcomes. Some studies use the term "pathological flows" associated with "pathological geometries" to highlight the connection between fluid and structure in disease development.

Along the arterial tree and cardiac cycle, **flow distribution** widely fluctuates. Depending on walls geometry and compliance, localized preferred flow path, flow recirculation and/or stagnation areas are observed. These patterns mainly take place in regions of flow disturbance such as bifurcations, curvatures, and narrowing ([Davies \(2009\)](#)) that can be natural or caused by the presence of therapy devices (stents, bypass graft, etc.). When mapping cardiovascular diseases, their locations seem to be correlated with these atypical geometries and thus, with flow disturbed regions ([Davies \(2009\)](#); [Chiu and Chien \(2011\)](#); [VanderLaan Paul A. et al. \(2004\)](#)).

Endothelial cells cover the inner layer of the arterial lumen. **Wall shear stress** is the tangential force applied on endothelium by the flowing blood. It is a regulator of endothelial functions with a strong implication on endothelial cells remodeling, shape and orientation ([Fung \(2013\)](#); [Vlachopoulos et al. \(2011\)](#)). WSS depends on the cardiac cycle, vessel geometry and flow distribution among other things. It is therefore a spatiotemporal feature along the arterial tree and throughout time. Many studies have showed connections between wall shear stress distribution and local endothelial dysfunction that could result in disease outcome ([Moore et al. \(1994\)](#); [Pedersen et al. \(1999\)](#)). [Pedersen](#)

et al. (1999) highlighted a correlation between low and oscillatory shear stress with intimal thickening and thus, early stage of atherosclerosis development. Aneurysm growth and rupture also seem to be related to low shear stress regions (Arzani and Shadden (2015)). Indeed, low wall shear stress is believed to inhibit endothelium remodeling and favor plaque deposit which tend to weaken arterial walls and thus, enhance rupture risks. Although atherosclerosis process is well described, in the case of aneurysm it is difficult to say if the low wall shear stress causes the disease or the reverse (Sugimoto (2015); Boyd et al. (2016)).

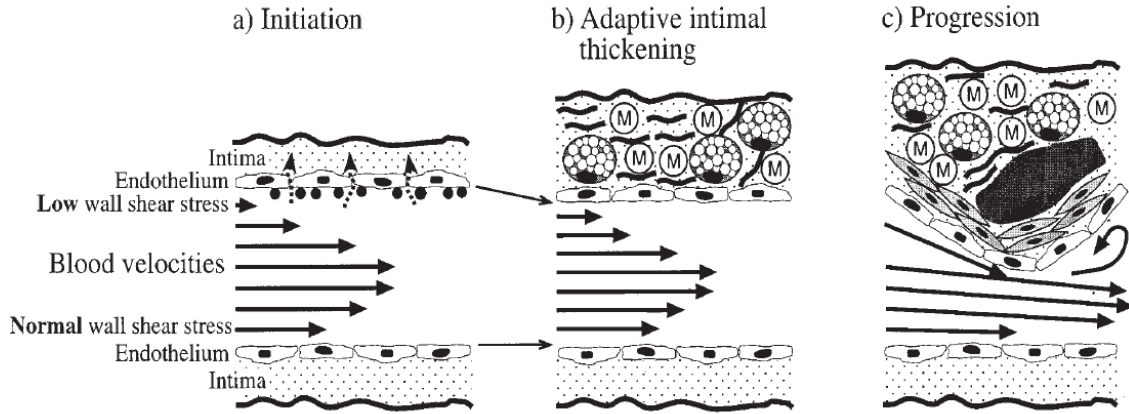


Figure 1.33: Atherosclerosis hypothetical process of initiation and growth of the plaque from Pedersen et al. (1999).

WSS distribution is associated with specific flow patterns including, recirculation, vortical and helical flow structures (Bürk et al. (2012)). These complex flows are difficult to visualize with available non-invasive medical imaging techniques because of limitations in spatio-temporal resolution. In recent years, the development of 4D-MRI (4 dimensional magnetic resonance imaging) provides detailed visualizations with 3-dimensional space and time resolved arterial flows. Bürk et al. (2012) analyzed aortic flow with 4D-MRI on patients with healthy and different abdominal aneurysm aortas. All of them presented vortical and/or helical flow patterns but with significantly higher intensities for patients with the most dilated aneurysm. This dilatation is also correlated with lower peak systolic wall shear stress. But once again, observations are often conducted on patients who have already developed the pathology. It allows to show correlations but not to conclude on the causes and mechanisms.

Most surgical treatments aim to restore healthy flows in arteries. As an example, stent graft deployment consists in redirecting flows in the true lumen for aortic dissections and restoring the lumen on stenosed arteries. Clearly identifying normal and abnormal flows would help improving treatments. To determine disease mechanisms, *in vivo* studies would require follow-ups on patients pre and post disease development or large scale studies on healthy versus pathological aortas. This type of study remains rare because of difficulties in implementation (volunteers, long term engagement and long term results).

To overcome these shortcomings, alternative approaches were developed to study hemodynamics by recreating artificial and numerical vascular systems. This can be

achieved experimentally with physical material and equipment or virtually by running numerical models. For those artificial representations, three main elements to consider are highlighted: aorta (material properties and geometry), circulatory loop (pressure, flow rates and pulses), and fluid (viscosity, elasticity, optical properties, etc.). Those items vary between studies and their representations are detailed for different approaches in the following sections with a main focus on aortic dissection.

1.3.3 From *in vivo* to *in silico* approach

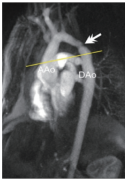



Approach	<i>In vivo</i>	<i>Ex vivo</i>	<i>In vitro</i>	<i>In silico</i>
Aorta :	 real	 real	 phantom	 numerical
Blood :	real	real or analog	analog	numerical
Flow Circulation :	real	mock loop	mock loop	numerical

Figure 1.34: Characteristics of the real and mock major elements to recreate aortic hemodynamical flow from the *in vivo* to *in silico* approaches (images from [Stankovic et al. \(2014\)](#), [Faure et al. \(2014\)](#), Elastrat aorta phantom, and [Bonfanti et al. \(2020\)](#)).

In vivo

In vivo studies are conducted on living human or animal patients. The great advantage is to have an accurate representation of human hemodynamics with real features. The main drawback is the limitation of measurement techniques. As the patient is alive, medical imaging techniques are mostly used to limit invasive methods. Those last ones, can not only affect measurement by disturbing physiological flow, but also involve more risky procedures for the patient. In most cases, *in vivo* hemodynamic data are collected from medical follow-ups of patients in hospitals. Traditional medical imaging techniques such as CT-scans, 4D-MRI and US Doppler are mostly used to monitor vessels walls shape, displacement and blood flows with or without pathologies. Physical quantities, such as wall shear stress, pressure, viscosity can then be calculated based on images and physical principles.

Depending on the object of study, *in vivo* data can be limited because of a lack of patients concerned with a pathology. As an example, [Liu et al. \(2018\)](#) conducted flow patterns analysis on only 16 patients with AD based on 4D-MRI and [Yang et al. \(2013\)](#) investigated AD flap motion with 49 patients enrolled. Both studies claim that their first limitation is the low number of patients and the limited number of exams they conduct on each patient. Furthermore long term studies also involve large variations between patients, monitoring techniques and operators. This makes it more difficult to draw reliable conclusions on a hemodynamic study with such experimental variations. As

a consequence, *in vivo* studies mostly refer to case studies on a single patient or large survey studies conducted on thousands of patients during many years.

One of the main reasons for the development of alternative techniques to *in vivo* experiments is to offer reproducible hemodynamics conditions and monitoring methods. This allows large scale studies to reach a statistical reliability. The other reason is to be able to use a wider range of monitoring and analysis techniques than traditional medical imaging that are limited in time/space resolution. Indeed, 4D-MRI is one of the most developed technique for blood flow analysis and offers a pretty fine time resolution of 20-60 ms with a poor spatial resolution of only 1-2 mm (Clough et al. (2012); Stankovic et al. (2014)). Super-resolved MRI are developing but are still very expensive and not commonly used in routine exams.

Ex vivo

Ex vivo experiments consist in collecting vessels from post-mortem human or animal subjects. The specimen is then studied outside the body with the use of artificial techniques to mimic relevant physiological conditions for the study. Those studies enlarge the choice of measurement techniques as the specimen is no longer in a living patient. Moreover, some anatomical parameters are partially preserved with tissue mechanical behavior, organ geometry or fluid properties when using real blood. However, physiological environment is not fully represented which can affect previously listed items (temperature, coagulation, de-oxygenated blood, tissue dryness, cells death, etc.).

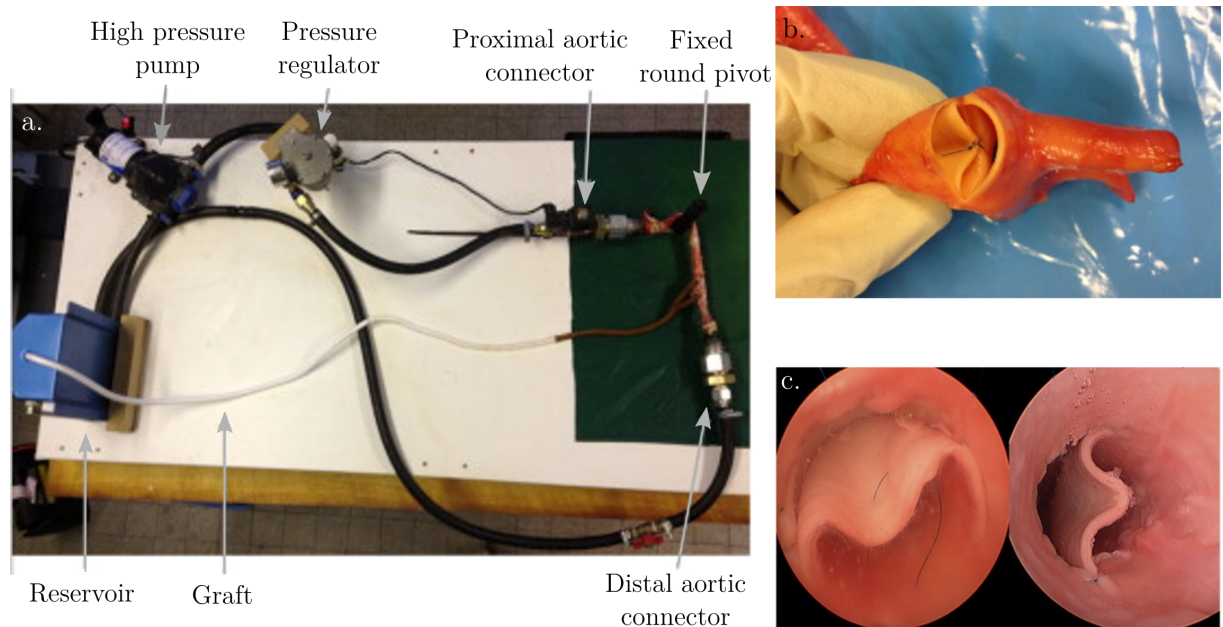


Figure 1.35: Experiments from Faure et al. (2014), (a) Benchtop pulsatile flow model, (b) opening the false lumen with intimal-medial layer detached from adventitia and (c) view of the entry tear from the video camera.

For example, Faure et al. (2014) focused on type B aortic dissection and on the influence of the tear region on the propagation of the dissection. They collected 20 non-

dissected human aorta on post mortem human subjects and artificially created the tear at different locations. Torn aortas were plugged on a circulatory mock loop with pulsed waveform imitating physiological flow rate and pressure. The circulating fluid was a Newtonian BMF (blood mimicking fluid) made of 30% glycerol and 70% water to set viscosity at 3.37 mPa.s. This value corresponds to the asymptotical viscosity of blood at high shear rate. Visualization of tear propagation was achieved with the insertion of a camera in the aorta lumen (figure 1.35). Post-procedural exam was conducted with a destructive method by cutting up aortas to evaluate the degree of dissection.

Some studies have focused on the efficiency of EVAR procedure for aortic dissection. [Canaud et al. \(2008\)](#) investigated different manufacturer stent fixations on pathological aortas. The artificial tears on collected aorta, the fluid, the circulation mock loop and optical observation tools were similar to the ones in [Faure et al. \(2014\)](#). In addition, [Zimpfer et al. \(2008\)](#) also performed EVAR on *ex vivo* porcine dissected aortas to compare four stent graft types. The circulatory mock loop system was more advanced with an artificial heart, a compliance chamber and peripheral resistances for the Windkessel effect. Moreover post surgical visualization was achieved with ultrasound imaging which is less invasive. After stent positioning, the residual flow in the false lumen of the dissection is studied with this technique.

Those techniques offer a better control on the reproducibility with the use of artificial mock loops. Nevertheless, their are still limited by the number of donors, variations in extracted samples, and usable monitoring and analyzing tools.

In vitro

In vitro studies are defined here as completely artificial experimental set ups. No specimen was collected from post-mortem subjects and every anatomical part and physiological condition were artificially replicated. The studied blood vessels are often represented by a physical models called "phantoms". These phantoms are designed to emulate vessels properties with different levels of realism (geometry, mechanical properties, etc.). This type of approach offers a wide panel of measurement techniques as the setup can be designed and adapted in accordance with measuring tools. Some used classic medical imaging tools such as MRI and ultrasounds while others preferred fluid mechanics traditional techniques such as Particle Image Velocimetry (PIV). Moreover, compared to *in vivo* and *ex vivo* approaches, reproducibility and large scale statistical studies can be achieved faster and more easily. Nevertheless, artificial organs, flow loops and fluids are often highly simplified representation of the complex anatomical and physiological environment. Therefore, numerous precautions must be taken when extrapolating results to living organisms. Two experimental *in vitro* studies on aortic dissection are described below.

[Rudenick et al. \(2013\)](#) analyzed hemodynamics on an idealized AD phantom with true and false lumen. A circulatory mock loop with pulsatile pump was designed and connected to a series of silicone AD phantom with different entry tear locations. A Millar catheter was introduced to assess pressure, a traditional ultrasound probe was used to measure wall displacement while Doppler ultrasound probe was used to assess flow rates. The circulating fluid was a Newtonian fluid - water - with graphite powder as contrast

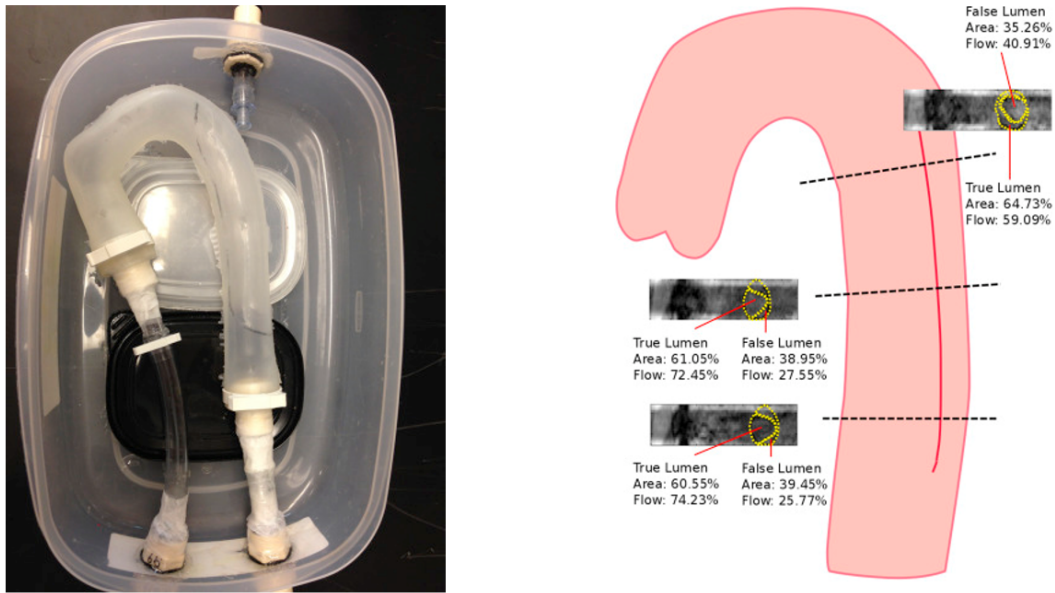


Figure 1.36: Aorta silicone phantom and location of observed plane sections from Birjiniuk et al. (2015).

agent.

Birjiniuk et al. (2015) used PC-MRI on his *in vitro* circulatory mock loop with silicone thoracic aorta phantom (figure 1.36). The phantom proportions were based on a patient scan. The fluid was a Newtonian BMF made up of a glycerol and water. Visualization was achieved with PC-MRI (phase-contrast MRI) and Wall Shear Stress (WSS) were then mathematically computed.

Furthermore, in traditional fluid mechanics, different optical techniques allow to assess flow in vessels. Those techniques can be adapted for *in vitro* hemodynamical studies, thanks to customizable benchtop experiment designs.

Many studies have used Particle Image Velocimetry (PIV) and Particle Tracking Velocimetry (PTV) to investigate hemodynamical flow vortices in aorta phantoms. Indeed, these non invasive optical techniques are high resolution flow visualization methods that allow to observe small and rapid hemodynamical features. They are implemented by replicating blood flows in an aorta phantom and tracking tracers displacements in the fluid to assess the flow. The main constraint about PIV and PTV is to design transparent elements to ensure optical accesses for visualization of tracers. It involves transparent aorta phantom and transparent working fluid. This transparency property can be difficult to combine with other essential mechanical properties such as aorta elasticity and compliance, fluid non-Newtonian properties, etc. Many studies have focused on designing those features to match PIV and PTV requirements in terms of fluid and aorta phantom as shown in figure 1.37.

In the field of PIV, Deplano et al. (2014) and Najjari and Plesniak (2016) (figure 1.38) used this technique on aorta phantoms to investigate vortices in tricky geometries such as Abdominal Aorta Aneurysm (Deplano et al. (2014)), curves aortic cross (Najjari and Plesniak (2016)) or micro vessels (Anastasiou et al. (2012)). Those three studies used non-Newtonian fluids with similar properties to blood thanks to water, glycerol and

xanthan gum mixtures.

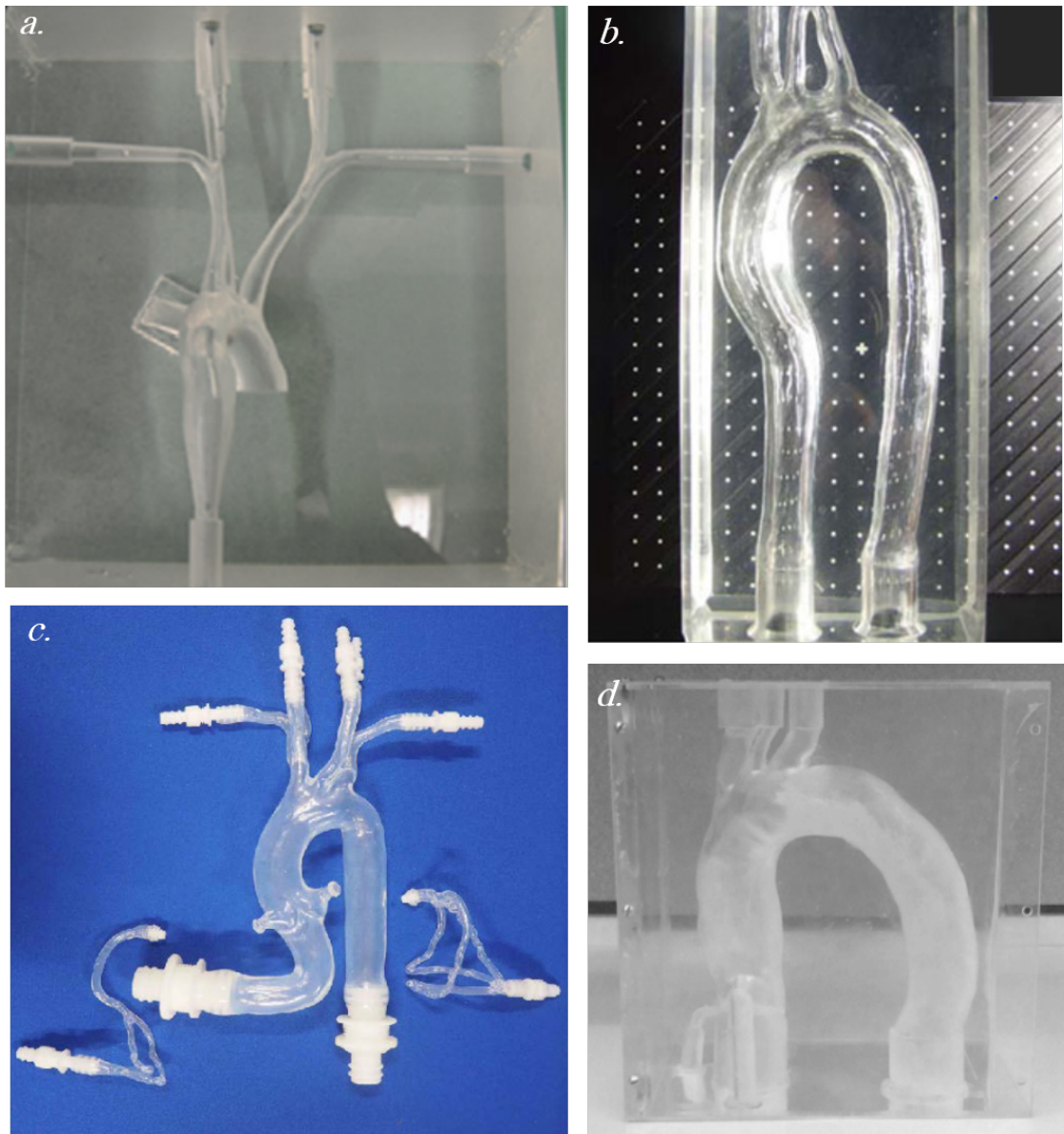


Figure 1.37: Aorta silicone phantoms from a. Büsen et al. (2015) for stereo PIV experiments, b. Gülan et al. (2012) for PTV c. Elastrat (T-S-N-001 2nd version) used in Rachid (2018) with 4D-MRI and d. Fernandes et al. (2019).

About 3D-PTV, Gülan et al. (2012) published a very detailed study on the implementation of this technique to study ascending aorta flow. This technique quickly provides 3D flow fields with a system of multiple cameras and will probably reach an important position in future publications.

Finally, only a few studies have combined fluid mechanics and solid mechanics experimental techniques. Indeed, some of them focused on flows while others focused on aortic wall displacements. Geoghegan et al. (2010) presented a method to assess both flows and wall displacements on a vessel phantom thanks to PIV and wall displacement tracking. However, as compliant wall phantoms are very rare in the literature, very few studies can investigate both flow and wall response on the same experiment.

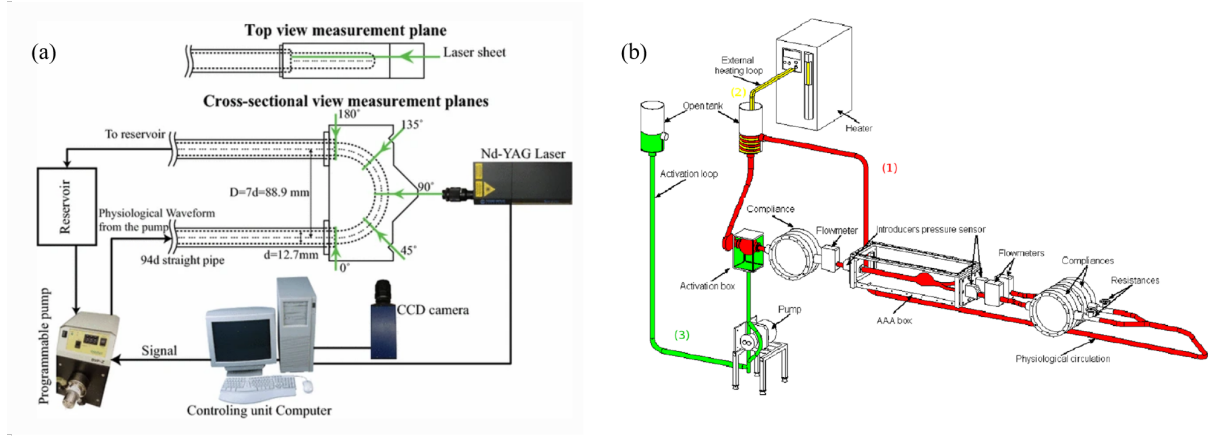


Figure 1.38: (a) [Najjari and Plesniak \(2016\)](#) experimental set up with circulatory mock loop, aorta phantom and PIV system, (b) [Deplano et al. \(2014\)](#) experimental set up with circulatory mock loop recreating different physiological features including compliance, resistance, temperature, etc.

In silico

In silico studies involve numerical simulations, CFD, FSI and other modeling methods. This technique enables hemodynamics investigation with full control and visualization of flow parameters. Geometry, material properties, flow rates and pressure can be set to study impact of each parameter on hemodynamics. Moreover those items can also be simultaneously monitored during a simulation. Compared to the previously described methods, numerical simulations are more relevant to conduct parametric studies as the model can be easily and rapidly customized.

However, the challenge in numerical simulations is to build an accurate model. Indeed, every parameter, law of physics and physiological environment are implemented by the simulation designer. The latter needs to make judicious choices to fit realistic living organism while maintaining a level of complexity that can be handled by a computer. Wrong choices of representation or mistakes can rapidly lead to misinterpretation of results. Therefore simulations must always be compared to physical experiments (*in vivo*, *ex vivo* or *in vitro*) and cannot be separated from previously described approaches.

Numerical simulation are very promising for understanding hemodynamical flow ([Cheng et al. \(2010\)](#); [Cheng et al. \(2014\)](#); [Ben Ahmed et al. \(2016\)](#); [Bonfanti et al. \(2019\)](#)) and for testing patient specific treatments or predict the evolution of their pathologies ([Altnji et al. \(2013\)](#); [Perrin et al. \(2016\)](#)).

Computational Fluid Dynamics (CFD) methods implement fluid dynamics laws and tools to assess flow in rigid walls modeling. Therefore, they do not directly model the motion of aortic walls and flap in the case of AD. However, implementing Windkessel models as output conditions allows to indirectly model the walls compliance and peripheral vessels resistance ([Menut \(2017\)](#); [Bonfanti et al. \(2017\)](#)). Another method consists in implementing Fluid Structure Interaction (FSI) models. FSI makes the connection between fluid mechanics for the flow and solid mechanics for wall motions. Both fluid and walls influence the behavior of the other and the modeling requires to take into account this

interaction. FSI appears to be the most relevant method but its greatest limitation is the difficulty to implement interactions which involves significant computation time, storage and cost (Alimohammadi et al. (2015)).

As an example, Karmonik et al. (2011) achieved a Computational Fluid Dynamics (CFD) study on aortic dissection pre and post treatment with stent graft to evaluate the graft influence on wall shear stress and pressure. Mouktadiri (2013) investigated catheter guidewires and aortic walls mechanical properties with different degrees of calcification to fuel a finite element model. This model was used to simulate guidewires introduction in the aorta and evaluate deformations.

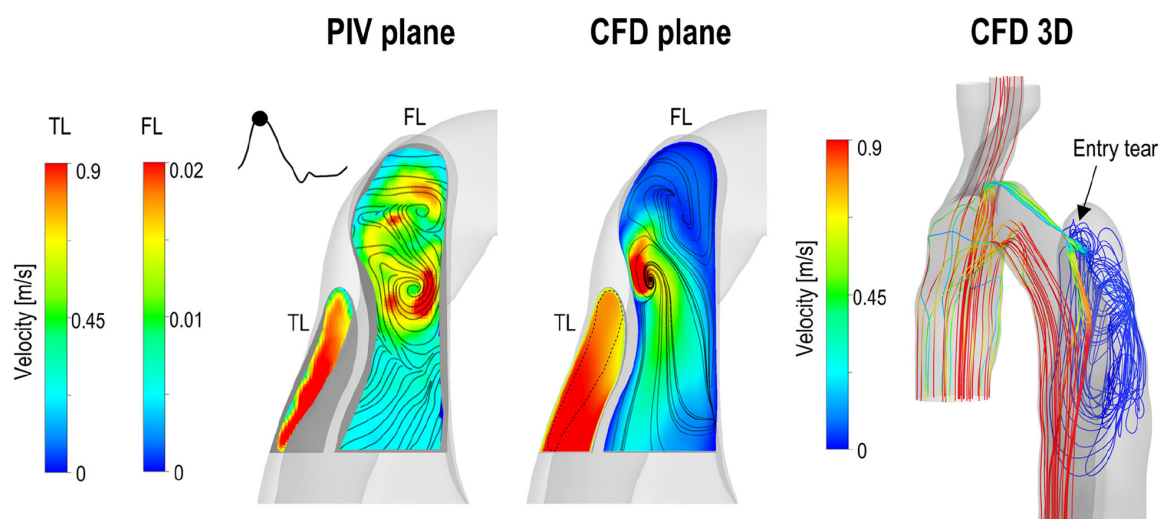


Figure 1.39: Comparison between *in vitro* PIV measurement and CFD simulations on an AD model in Bonfanti et al. (2020).

Regarding aortic dissection, only a few studies focused on simulating treatments for this pathology. Most existing studies present numerical models to better understand the hemodynamics of untreated AD (Cheng et al. (2010); Cheng et al. (2014); Ben Ahmed et al. (2016)). Fluid-Structure interaction AD models are developing (Alimohammadi et al. (2015); Bonfanti et al. (2018)) but stay difficult to implement due to highly complex modeling and geometry (true lumen, false lumen, flap, etc.).

Finally, two main research teams have combined *in vitro* and *in silico* studies on aortic dissection. The first one concerns the *in vitro* phantoms study of Rudenick et al. (2013) and the numerical simulations of Soudah et al. (2015). They used a simplified AD model with two straight parallel tubes to investigate different scenarios of tears in the flap. Although the model is very simple, the combined *in vitro/in silico* approach on AD has never been investigated that far.

The second study comes from Franzetti et al. (2019) circulatory mock loop for AD phantom (with PIV technique) and Bonfanti et al. (2020) numerical simulations (CFD) on the same AD model. This study confronts *in vitro*, *in silico* and *in vivo* data to validate their models and showed consistent matching between the three approaches. Figure 1.39 shows comparison between experimental PIV and CFD simulation flow distribution on an AD plane. The two main limitations of this study are the rigid walls hypothesis (on the physical phantom and numerical model) and the Newtonian fluid hypothesis (for the

in vitro working fluid and numerical blood model). The main difficulties come from the *in vitro* setup which is not easy to implement with non-Newtonian fluid and the challenge of manufacturing compliant wall phantoms.

1.3.4 Our trends in the *in vitro* approach

Each of the previously described approach has drawbacks and advantages. The strength of hemodynamical flow studies comes from their combination and inter-confrontation of these methods as one can fill the gaps of an other. *In vivo* data are essential as they come from the object of study : human body. *In vitro* studies allow to recreate an artificial environment without the drawback of managing human organs. It allows to implement flow assessment tools with more flexibility and higher resolutions. Moreover, a well-designed experimental setup can provide reliable experimental reproducibility and therefore, consistent statistical results to draw conclusions on observed flows. These are essential parameters to better describe aortic flows and thus, understand, diagnose and prevent aortic pathologies.

In this study, we have chosen to develop a benchtop experiment to investigate blood flows in the aorta and on aortic dissection models. Our collaboration with the cardiovascular department of the Hospices Civils de Lyon allows us to fuel our design and compare our results to *in vivo* data. The main constraint of traditional medical imaging tools is the low **time and space resolutions** which does not allow to fully describe and understand flow distribution on AD. Therefore, we have chosen to use **Particle Image Velocity** — a high-resolution flow visualization technique — to complete this gap. This optical technique is only feasible with *in vitro* but not with *ex vivo* experiments as it requires the design of specific fluid and aorta phantom with transparent properties.

Moreover, limitation of the literature experiments are addressed including the **Newtonian vs non-Newtonian** approximation, the design of a mock loop that **supports non-Newtonian fluid** and the use of **compliant wall phantoms** with **realistic geometry**.

Finally, these data are confronted with AD numerical models that are developed in parallel with another PhD thesis ([Pan \(2021\)](#)) as complementary works. This confrontation is achieved on aortic dissection cases to evaluate potential numerico-experimental applications on pathologies understanding.

1.4 Conclusion

Hemodynamical flows were addressed with special focus on the conveying vessels and the conveyed fluid. The aorta is a complex organ regarding morphological and mechanical characteristics which makes it an active piping system that interacts with blood, adapts physiological conditions and that may be damaged with age or altered physiological environment. Blood is also a complex fluid which can be seen as a non-Newtonian fluid at first approximation and with fluid mechanics point of view. This non-Newtonian property comes from the interactions of RBCs responding to shear conditions. Vessels and blood interactions result in hemodynamical flows that are pulsatile, non-Newtonian

and that propagate in an elastic system. Many studies have shown the role of hemodynamics in arterial disease development including atherosclerosis, aneurysm and aortic dissection. Therefore, understanding these flows have become a public health challenge as cardiovascular diseases is the leading cause of death in developed countries. In order to understand, analyze and treat those diseases, the scientific community has adopted different approaches from *in vivo* to *in silico* studies to investigate aortic flows on healthy and pathological cases. Each approach has drawbacks and advantages but above all, they are complementary. In this context, we have chosen to develop an *in vitro* benchtop experiment to mimic arterial circulation with biofidelic features: compliant aorta phantom with realistic geometry, blood mimicking fluid and pulsatile pressure/flowrate conditions. The following chapters describe the experimental process concerning the design of the bench, its evaluation and simplification hypothesis testing. The final scope is to investigate case studies on pathological cases of aortic dissection with confrontation to *in silico* models (other PhD work in parallel). The long term scope is to develop a tool for analyzing and treating aortic pathologies.

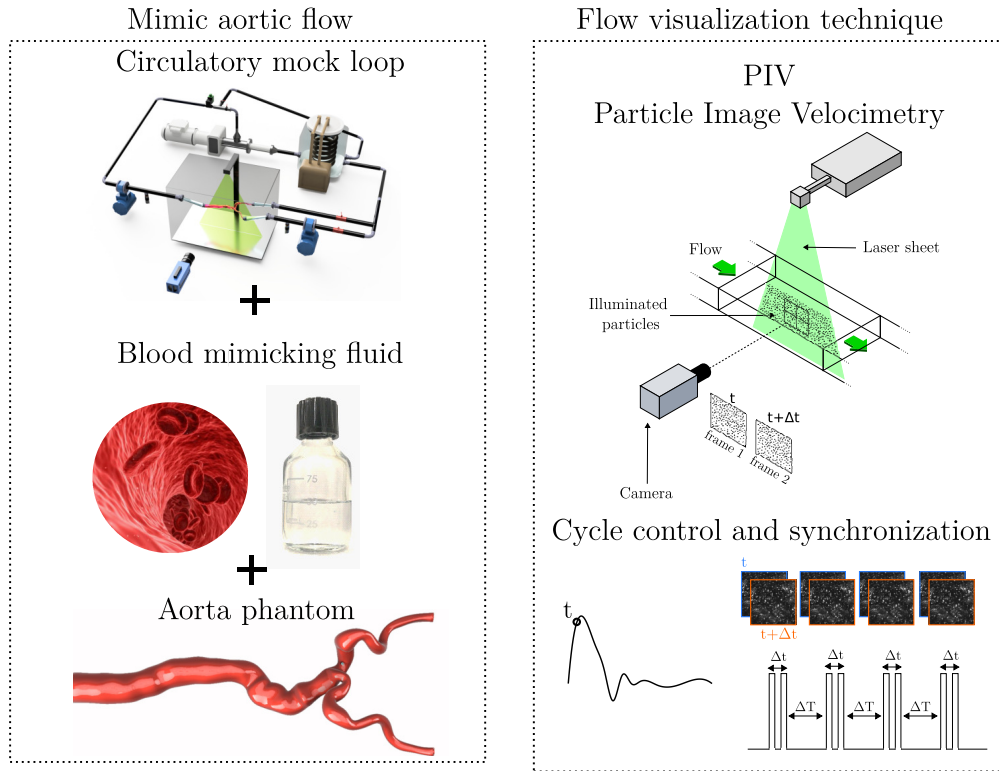
In vitro setup : how to mimic and assess aortic flows ?

Contents

2.1	Background	58
2.2	Circulatory mock loop	58
2.2.1	Mock loop setup	58
2.2.2	Pulsatile flow control : waveform and reproducibility	61
2.3	Particle Image Velocimetry	63
2.3.1	Principle	63
2.3.2	Implementation on the experimental setup	67
2.4	Aorta phantoms	71
2.4.1	Phantom properties	71
2.4.2	Geometry reconstitution	73
2.4.3	Manufacturing technique	74
2.4.4	Compliant phantom: Young's modulus	75
2.4.5	Refractive indexes	76
2.5	Blood mimicking fluid	76
2.5.1	Composition and target properties	77
2.5.2	Non-Newtonian BMF in the literature	79
2.5.3	Fabrication and viscometry	80
2.5.4	Results	81
2.5.5	Discussion and limitations	88
2.6	Conclusion	89

Abstract

An aortic flow simulator was designed to investigate hemodynamical flows in aorta phantom. The setup is made up of three elements: a circulatory mock loop, a blood mimicking fluid, and an aorta phantom. All those components are artificial and were manufactured and designed with an adapted degree of biofidelity. The technique of Particle Image Velocimetry was implemented to visualize flows in the phantom with a high resolution (below $1 \times 1 \text{ mm}^2$). The aorta phantom was manufactured with silicone injection and molding techniques to obtain a model with a patient-specific geometry and compliant walls with a realistic elasticity. Finally, a fluid with shear-thinning properties is fabricated with a mixture of xanthan gum, glycerin, water, and NaCl to mimic blood shear-dependent properties and managing its optical properties for PIV requirements. The simulator is driven by an in-house program for real-time control and monitoring in addition to cardiac cycle synchronization with PIV measurements.



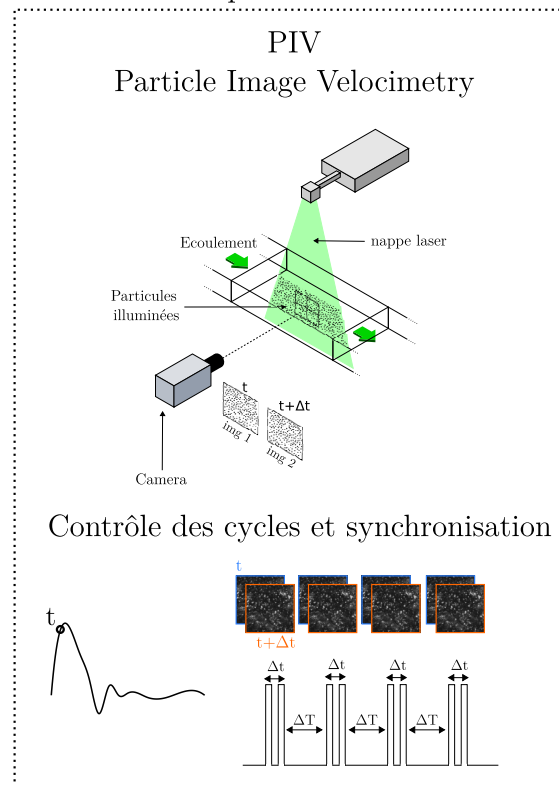
Résumé

Un simulateur d'écoulement aortique a été conçu pour étudier l'hémodynamiques dans un fantôme d'aorte. Le montage est composé de trois éléments : une boucle circulatoire, un fluide imitant le sang et un fantôme d'aorte. Tous ces composants sont artificiels et ont été fabriqués et conçus avec un degré de biofidélité adapté. La technique de Particle Image Velocimetry a été mise en place pour visualiser les écoulements dans le fantôme avec une haute résolution (inférieure à $1 \times 1 \text{ mm}^2$). Le fantôme d'aorte a été fabriqué avec des techniques d'injection et de moulage de silicone pour obtenir un modèle avec une géométrie patient-spécifique et des parois souples avec une élasticité réaliste. Enfin, un fluide avec des propriétés rhéofluidifiantes est fabriqué avec un mélange de gomme de xanthane, de glycérine, d'eau et de NaCl pour imiter la viscosité du sang et maîtriser ses propriétés optiques pour satisfaire aux exigences de la PIV. Le simulateur est piloté par un programme LabVIEW pour le contrôle et la surveillance en temps réel des cycles imposés, des débits et des pressions. De plus, la synchronisation des cycles cardiaques imposés avec les mesures PIV est assurée.

Reproduire les écoulements aortiques



Technique de visualisation



2.1 Background

This chapter presents an aortic flow simulator which is made up of 3 main elements : a circulatory mock loop, a blood mimicking fluid and an aorta phantom. The goal is to replicate aortic circulation with only artificial components and with an adapted degree of biofidelity. A flow visualization technique — PIV — is set up to visualize flows in the aorta phantom with high time and space resolutions. Each part was designed with respect of its own and of the other elements requirements. In existing *in vitro* studies, rigid aorta models and Newtonian working fluid are often used and thus, neglecting fluid-structure complex interaction between vessels walls and non-Newtonian fluid flows. To investigate these features, the present study focuses on phantom compliance and blood mimicking fluid non-Newtonian properties.

In the first two sections, the circulatory mock loop and PIV technique are presented. The circuit function is to emulate pulsatile flowrate and pressure in the aorta phantom associated with a real-time controlling, monitoring and recording data device. The mock loop has to accommodate the aorta phantom, convey and preserve the working fluid and provide optical access for a PIV equipment. The latter is programmed to ensure synchronization with the driven mock loop flow pulses. It allows to correlate imposed conditions and observed flows. Secondly, the blood mimicking fluid was designed to emulate some blood rheological behavior and more specifically its shear-thinning property. Regarding the large scale of the aorta, we focus on the macroscopic rheology and the fluid overall viscosity (not at the RBCs interactions scale). Finally, aorta phantom were manufactured to reproduce patient-specific geometries. The goal is to design transparent phantoms (for PIV) with compliant walls and realistic mechanical elasticity to mimic *in vivo* vessels walls - flow interaction. This chapter describes the experimental process developed to build this aortic flow simulator with special focus on the design of each element. The main picture is given for a reference silicone abdominal aorta phantom. Other types of phantoms are presented in the last chapter and will be adapted on the present chapter designed parts.

2.2 Circulatory mock loop

The circulatory mock loop is an experimental setup designed to mimic and monitor aortic hemodynamical flow. The aim is to recreate adaptable physiological pulsatile flow conditions, accomodate an aorta phantom, implement real-time controlling and monitoring devices on a benchtop experimental setup.

2.2.1 Mock loop setup

The circulatory mock loop was designed with four main requirements:

1. recreate pulsatile flowrate and pressure conditions to mimic the arterial circulation,
2. ensure cycle reproducibility,
3. preserve the fluid non-Newtonian properties,

4. provide optical access for flow fields visualization (PIV)

The experimental bench is designed to host a central element: the aorta phantom. As explained in the previous chapter, our goal is to manufacture a phantom with realistic geometry and compliant walls to represent the interactions between the pulsatile flow and aorta walls. The detailed phantom manufacturing is addressed in section 2.4 of this chapter. The following sections describe the benchtop experiment design that will host the phantom.

The setup is made up of three flow loops : (i) the aorta loop where pulsatile flow is imposed in the phantom, (ii) a by-pass loop to bring back extra flow to a reservoir, and (iii) a cooling loop to control the working fluid temperature. (i) and (ii) operate with the working fluid (blood mimicking fluid) and (iii) is a water loop for cooling purposes. The two fluids travel in independent systems and do not mix.

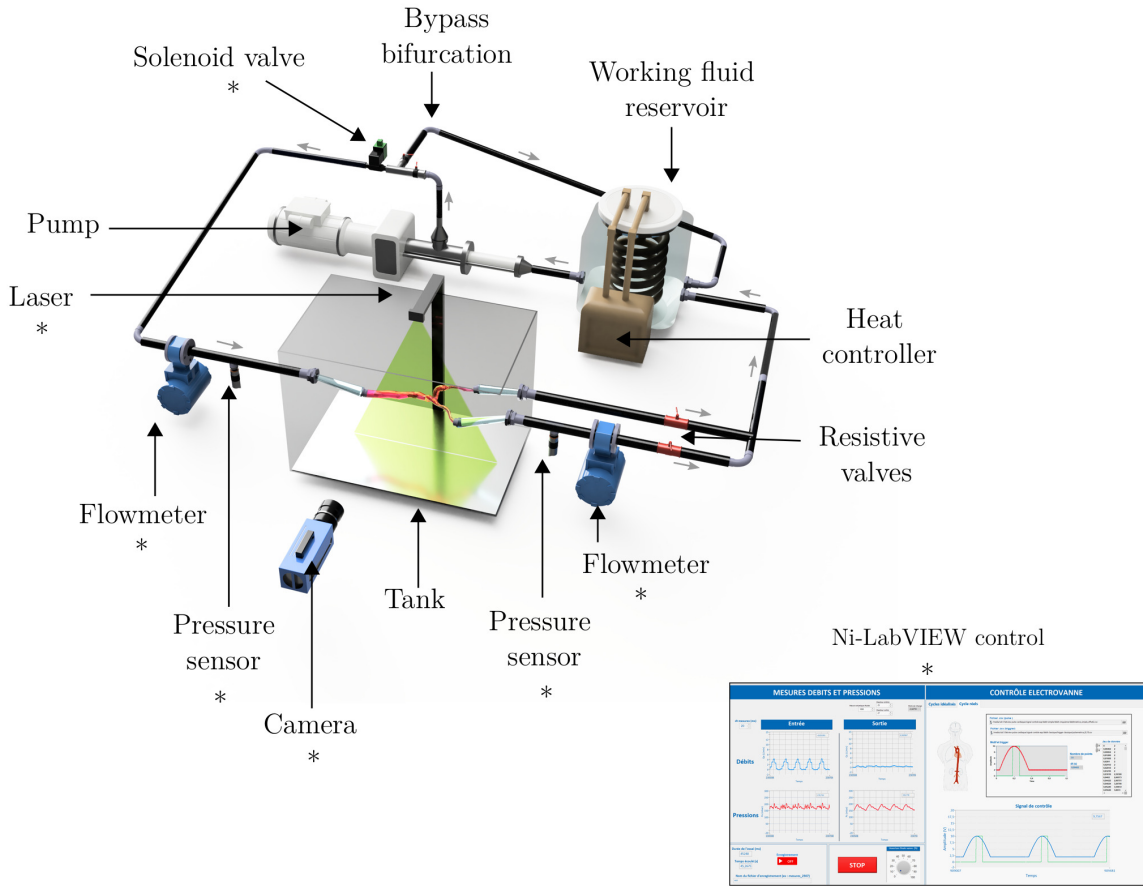


Figure 2.1: Experimental setup with abdominal aorta configuration. Custom made software interface is depicted on the left and (*) indicates devices controlled with the NI-LabVIEW system.

The setup is illustrated in figure 2.1 and corresponds to a compliant abdominal aorta phantom experiment configuration¹. The aorta circulation consists of successive elements

¹Later in the manuscript other phantoms (thoracic aortas) will be used on the simulator. Mock loop adaptation will be given at that time. For now, we focus on the abdominal aorta configuration.

which loop the working fluid between the reservoir and the aorta phantom. The reservoir contains a blood mimicking fluid and is connected to a pumping system. The latter pumps the fluid with continuous flowrate. A proportional solenoid valve (Posiflow 302, ASCO Numatics) controls the pulsatile flow into to aorta loop thanks to successive valve openings and closings (systole and diastole). Extra flow is redirected to the reservoir by a by-pass bifurcation to prevent pump instabilities when the solenoid valve closes (diastolic phase).

In the aorta loop, inlet and outlet magnetic flowmeters (Rosemount 8700, Emerson) and pressure sensors (PN 2298, IFM electronic) monitor flows. These devices are located in straight rigid PVC-U tubes (inner diameter 15 mm) with a sufficient length of 150 mm between devices to ensure flow stabilization and entrance length (equivalent to a length/diameter ratio of 10). A custom-made LabVIEW 2017 (National Instrument) program and a real-time operation controller (CompactRIO 9035, National Instrument) were implemented to operate the simulator. This LabVIEW system controls the solenoid valve and records data from the flowmeters and pressure sensors with a time resolution of 20 ms. It also ensures synchronization with the PIV system.

Downstream of the two iliac arteries, ball-valves are used to emulate peripheral vessels resistance. The closing degree of valves allows to set a certain pressure level in the aorta phantom otherwise it would tend to atmospheric pressure due to the communication with the open reservoir. In this configuration, no compliant Windkessel chamber is required. In the literature, it is common to add such system to dampen the flow signal and adjust pressure but most of these studies were conducted on rigid phantoms ([Bonfanti et al. \(2020\)](#); [Franzetti et al. \(2019\)](#); [Deplano et al. \(2007\)](#)). In our case, the phantom compliance was sufficient to recreate the flow dampening effect. The aorta phantom is immersed in a rectangular tank containing a fluid with refractive index properties. These optical features are detailed in the next sections. Immersing the phantom also applies a certain pressure on the aorta which depends on the tank filling height. This technique is a very simplified representation of internal organs pressure on the aorta. But this feature is essential otherwise the phantom diameter would expand too much with overdilatation when subjected to physiological pressures. Thus, the system operates with realistic vessel wall displacements in accordance with the imposed physiological pressures range.

Finally, the cooling loop is made up of a tap water tank, a chiller (TK 1000, TECO) and a cooper cooling coil. The coil is immersed in the working fluid reservoir to allow heat exchange with the working fluid and prevent communication between the working and the cooling fluids. The working temperature was set at 25 ± 2 °C and [figure 2.2](#) shows temperature control along an experiment with and without the cooling device. With no temperature control, a two hours experiment comes with a 13.2 °C rise in the working fluid. The pump functioning brings heat to the system and the heat controller allows to stabilize this temperature.

The working fluid is a water-glycerol solution containing xanthan gum polymers to mimic blood non-Newtonian behavior. Xanthan gum is sensitive to shear which risks breaking the polymer chains. This process affects the shear-thinning properties of the solution that can be damaged by commonly used pumping systems such as gear or piston pumps. [Deplano et al. \(2014\)](#) addressed this issue by controlling the contractile motion of

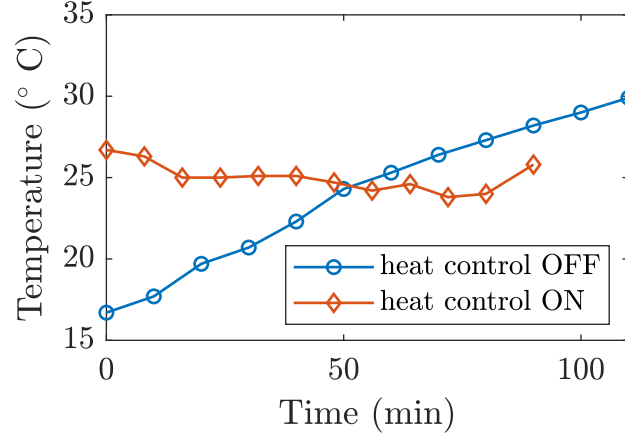


Figure 2.2: Temperature versus time measurements during similar experiments with and without heat control.

an artificial ventricle to "push" the BMF in the main loop. In the current study, the use of a pumping system with a progressive cavity (Eco-Moineau-C, PCM) allows to minimize shear on the working fluid and prevent from breaking polymer chains. The use of an external cooling loop also minimizes working fluid damaging risks because it does not loop again through any cooling circuit pump. Heat exchanges are ensured by the fluid interface with the copper coil and thus, without mechanical stress on the fluid.

2.2.2 Pulsatile flow control : waveform and reproducibility

The experimental set-up was designed to accommodate different shapes of aorta phantom geometry (thoracic, abdominal, with or without the iliac arteries etc.) and thus requires different pulsatile flow setups. The current description is given for the abdominal aorta with the iliac arteries configuration.

In this example, the solenoid valve was programmed to recreate the global flowrate waveform from [Cheng et al. \(2003\)](#) MRI data in the infrarenal region on human subjects under resting conditions. Figure 2.3 shows inlet flowrate and outlet pressure measured during an experimental trial with 6000 cycles. The mean and maximum inlet flowrates were equal to $Q_{mean} = 1.70 \pm \text{L.min}^{-1}$ and $Q_{max} = 5.80 \pm 0.37 \text{ L.min}^{-1}$ respectively. The cycle period was set at $T = 0.800 \text{ s}$. Outlet diastolic and systolic pressures vary between $P_{diast} = 90.09 \pm 2.67 \text{ mmHg}$ and $P_{syst} = 139.23 \pm 3.60 \text{ mmHg}$ during a cardiac cycle (in accordance with clinical data from [Olson \(1968\)](#) and [Pagoulatou and Stergiopoulos \(2017\)](#)). These results are provided with standard deviation on the 6000 cycles (shaded areas on 2.3). Mean inlet and [Cheng et al. \(2003\)](#) reference flowrate for abdominal aorta are depicted in figure 2.4. Note that the mock loop magnetic flowmeters are located on a rigid PVC pipe section and cannot record negative flowrates. Therefore, the actual flowrate in the compliant aorta phantom downstream of the flowmeter can have a different shape. The aim of this inlet monitoring is to set a global suitable amplitude, pulse period and consistent systolic/diastolic duration ratio. The precise aorta flowrate waveform will be evaluated with measured velocity fields from PIV in the aorta phantom (presented on PIV results in chapter 3). In the aorta phantom, backflow and diastolic are expected to

be more intense than the one observed on the flowmeter (in a rigid tube section) due to the wall compliance action on flow.

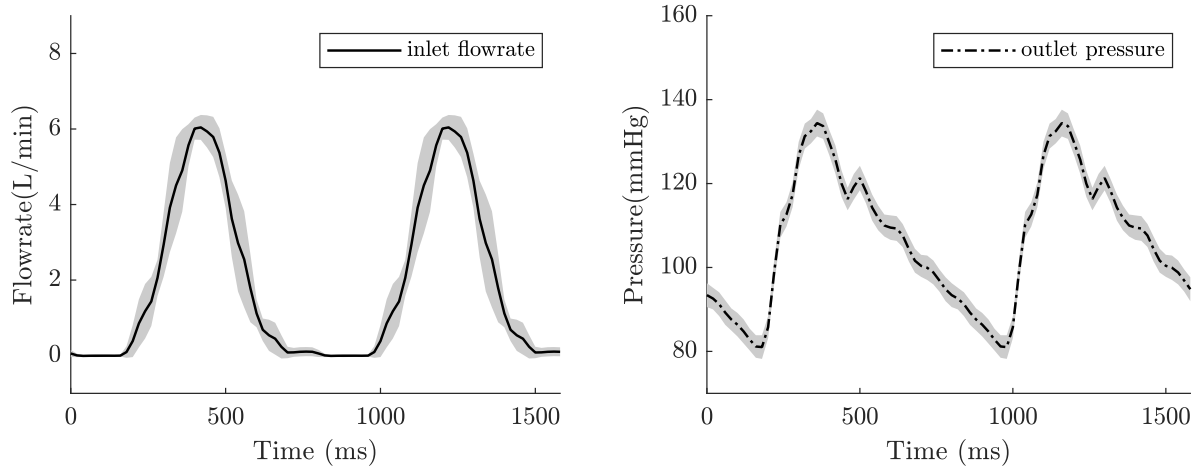


Figure 2.3: Inlet flowrate (left) and outlet pressure (right) waveforms for 2 successive cycles. Solid and dashed line are mean waveforms based on 6000 cycles (equivalent to one experimental trial) and shaded areas represent standard deviation.

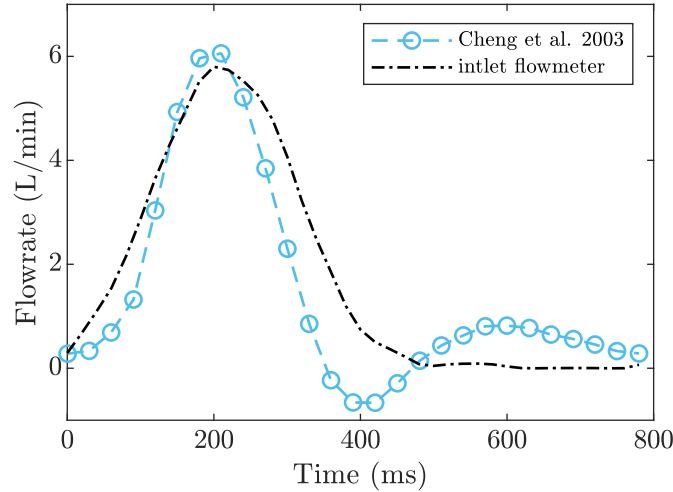


Figure 2.4: Inlet flowrate and flowrate reference from [Cheng et al. \(2003\)](#).

For other configurations, the solenoid valve can be programmed to mimic other pulsatile flowrate waveforms based on table data. Thus, amplitude, frequency, offset can be chosen by the user to mimic different types of inflow conditions. Finally a testing mode was programmed to generate solenoid valve continuous, sinusoidal and square signals mainly for testing sensors responses. Series of tests were carried out to check sensors and a description of sensors characteristics, accuracy and response time is provided in Appendix B.

The mock loop allows to emulate physiological flowrates and pressures with real-time control and monitoring. The setup enables to conduct series of experiments with consistent cycles reproducibility, temperature stability and fluid preservation. A NI-LabVIEW programming was implemented with a custom made program. The script not only controls the mock loop but also incorporates synchronization tools for the PIV measurements. The purpose is to obtain velocity fields in the aorta phantom for specific cardiac instants. Therefore, this process requires accurate synchronization between PIV imaging and controlled cardiac cycles with the solenoid valve. The next section details the functioning of the PIV technique and implementation on the mock loop.

2.3 Particle Image Velocimetry

Particle Image velocimetry (PIV) is the metrology technique implemented to assess flow velocity fields in the aorta phantom. This optical technique provides instantaneous high spatio-temporal resolution flow velocity fields. This section describes PIV general principles, implementations and experimental requirements. The way PIV is adapted to the mock loop setup is addressed regarding optical access to the flow, synchronization with the cardiac cycle and fluid/particle properties.

2.3.1 Principle

PIV emerged in the 80's and has become a essential flow visualization technique in the field of fluid mechanics ([Brookshier and Tarbell \(1993\)](#); [Boutier \(2012\)](#)). This optical technique provides local instantaneous flow velocity in a 2 dimensional plane with 2 components (2D-2C). The stereo-PIV allows to obtain 3 velocity components thanks to a pair of camera but this extension is not used in this work. PIV is considered as a non-invasive technique that requires optical access to the flow to visualize particles/tracers. Depending on the applications, those particles are naturally present or have to be seeded in the fluid. The rise of laser technologies, image processing and high-definition time-resolved cameras have boosted PIV implementation in laboratories and industries. It includes a wide range of applications with different scales such as aircraft wind tunnel for aeronautics ([Scarano et al. \(2015\)](#); [Bardera et al. \(2019\)](#)), *in vitro* cardiovascular studies ([Yazdi et al. \(2018\)](#); [Deplano et al. \(2016\)](#); [Büsen et al. \(2017\)](#); [Bonfanti et al. \(2020\)](#)), and microfluidic ([Lima et al. \(2006\)](#); [de Winter et al. \(2021\)](#)).

PIV consists in measuring the displacement of particles which were present or seeded in the fluid to act as tracers. When the flow is activated, a laser illuminates those particles and a camera captures their position at successive instants in the same illuminated area. The fluid velocity is then computed based on particle displacement between 2 successive instants corresponding to two successive snapshots. Velocity fields can be calculated by dividing the displacement by the time interval between these instants. Directly associating imaged particle displacements to the actual fluid velocity requires some experimental cautions and mathematical assumptions that are addressed in this section.

Cross-correlation

PIV provides instantaneous velocity fields based on groups of particles displacements. For an instant t , the camera records two frames of the target area at two instants: t (frame 1) and $t + \Delta t$ (frame 2). The image is split into sub-images called interrogation windows (2.5) which do not contain a single particle but a cloud of particles. The aim is to determine the most probable displacement of each interrogation window between frame 1 and frame 2 by identifying the group of particles from their previous and to their new position. To do so, displacement candidates are tested. Each interrogation window in frame 1 is shifted with $\mathbf{D}=(dx,dy)$ displacement and compared with corresponding interrogation window in frame 2. Each initial displacement possibility is computed with a cross-correlation algorithm applied between frame 1 and frame 2 to evaluate the most probable displacement. The cross-correlation coefficient is calculated pixel by pixel as

$$C_{corr} = \sum_{x,y} I_1(x,y) + I_2(x + dx, y + dy) \quad (2.3.1)$$

where I_1 and I_2 are image intensity from frame 1 and frame 2 respectively. The better $I_1(x,y)$ and $I_2(x + dx, y + dy)$ match for a specific shift (dx,dy) , the higher C_{corr} is. Figure (2.5) shows a correlation graph for different shifts along x and y axis. The shift (dx,dy) with the highest correlation coefficient (correlation peak) gives the interrogation window displacement $\mathbf{D} = (dx,dy)$. The process is repeated for each interrogation window to draw the instantaneous velocity field on the whole area of interest. At the end, the size of interrogation windows and shifts give the spatial resolution of the velocity field (Boutier (2012)).

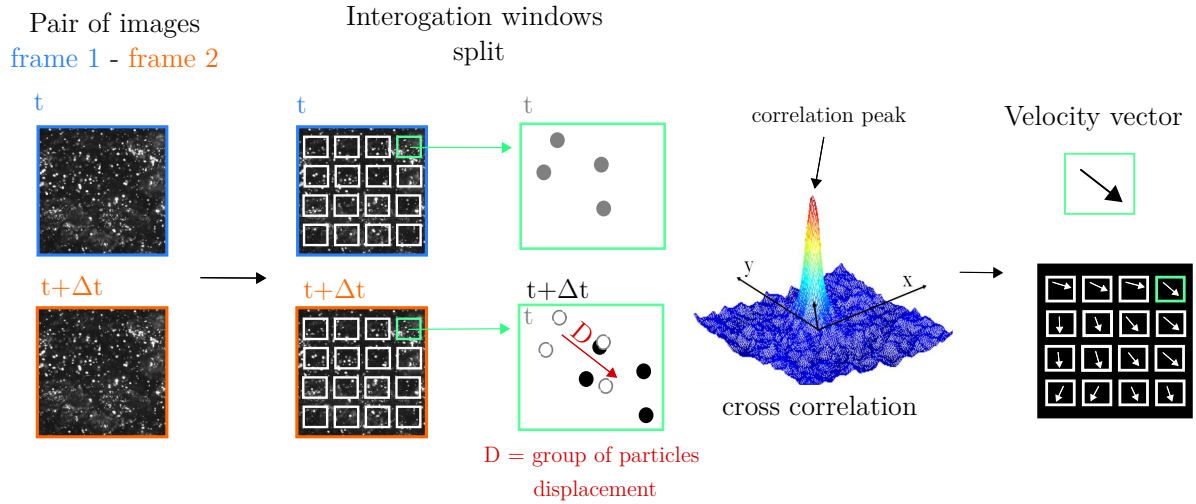


Figure 2.5: Process of cross-correlation on a pair of images. The correlation peak indicates the most probable displacement of particles between frame 1 and frame 2.

In practice, further computation are achieved to better identify the correlation peak location and estimate displacement probability. It can include noise peaks comparison, sub-pixel shifts, the use of non-square interrogation window etc. Moreover, large series of N images of the same flow may be needed to perform cross-correlation. It allows to reach a

statistical convergence of calculated velocity fields. Depending on the observations (mean flow, turbulence, vorticity) more or less images computation allows to conduct statistical analysis.

Capturing particles images : spatial configuration

A typical two-dimensional two-components PIV (2D-2C-PIV) set up is presented in figure 2.6a. The term "2D-2C" refers to the calculation of velocity in a 2D plane (xy) with 2 components u_x and u_y . The 2D plane thickness corresponds to the laser sheet thickness which is typically around 1 mm. It is applied in conditions where the main flow displacement — and thus, particle displacements — occurs in this 2D plane (xy). This technique is adapted for channel flow such as aortic phantom flow with rather straight geometry. The use of a laser sheet allows to only illuminate a 2D plane in the flow. The particles that cross this lighted plane are visible to the camera while backward and forward particles are not. This technique allows to focus on a specific flow 2D plane and track particles that are flowing in it. It is not adapted to strongly 3 dimensional flows where too many out-of-plane particle displacements would occur and thus, would not be visible for the camera and increase the noise in cross-correlation.

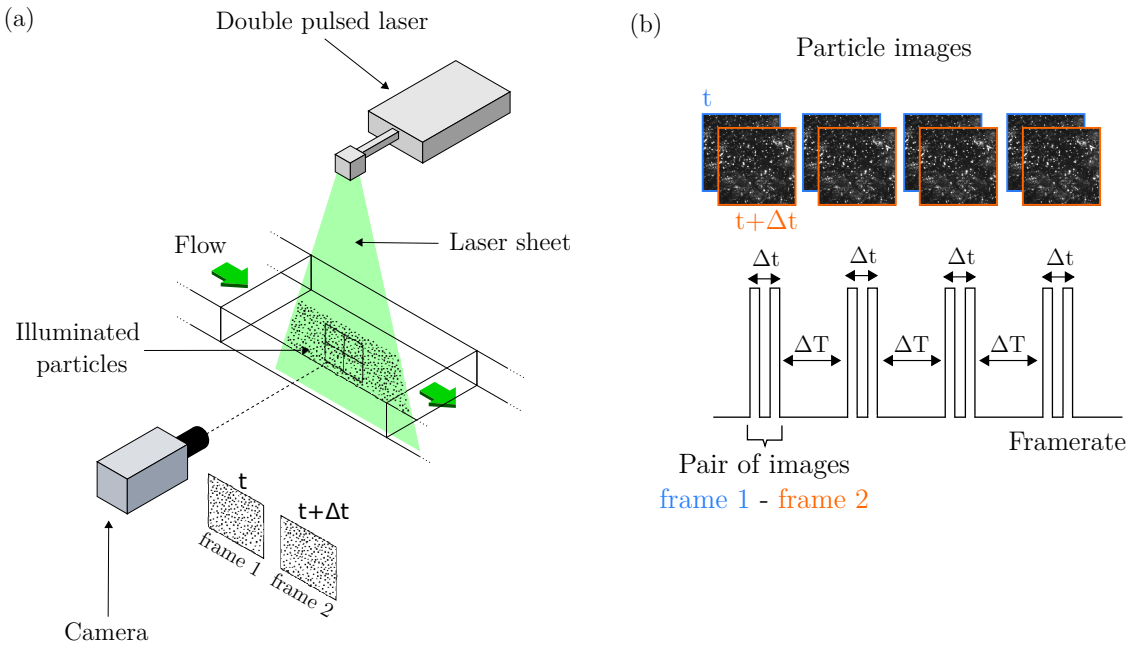


Figure 2.6: (a) Typical 2D-2C PIV setup, (b) double frame PIV principle and imaging framerate. Δt is the time lapse between two images of a pair and ΔT is the time laps between two pairs.

Temporal setup and framerate

Double-frame PIV works with pair of images to calculate the velocity field at an instant t_i . Displacement is thus calculated on the two images of a pair but not in between

pairs (figure 2.6b). Δt refers to the time lapse between 2 images of a pair at t_i . ΔT is the one between two pairs of images t_i and t_j ($i \neq j$). Regarding imaging framerate, particles are flowing with a certain velocity and a camera takes snapshots of their position. Two successive snapshots need to be close enough in time (short time-lapse Δt) to see the same cloud of particles in the image window. Otherwise, the tracking cannot be achieved because of lost and out-of-view particles. But these snapshots also need to be taken far enough in time (long enough time-lapse Δt) to observe a sufficient displacement between images. Otherwise two identical pictures are taken and a zero displacement is calculated. As a result, Δt has to be carefully set by taking into account the flow velocity.

Imaging fast flow can result in blurred image of particles when the camera shutter is too slow. This is the reason why laser pulses are often used to freeze the particle motion in the camera view. The short laser pulse acts like a photographic flash. Double pulsed lasers allow to implement double-frame PIV by emitting 2 successive pulses with time lapse Δt . A typical pulse duration is in a 5 to 10 ns range while Δt is usually between 1 ms to 1 s. Standard PIV systems can reach a maximum 10 Hz frame rate which corresponds to $\Delta T = 100$ ms. This technique relies on synchronization between laser pulses and camera imaging. Most PIV systems come with a synchronization unit to ensure timing control and this is the case in our experimental bench.

Particles size and density

Flow field calculation is based on the assumption that particles follow the flow. Choosing particles for a certain flow measurement is not trivial. They have to meet requirements to match fluid and flow features regarding shape, density and size. The Stokes number (equation 2.3.2) enables to evaluate if a particle is adapted or not to carry out PIV on a flow and is expressed as

$$St = \frac{1}{18} \frac{\rho_p D_p^2 U_0}{\mu L}, \quad (2.3.2)$$

where ρ_p is particle density, D_p is particle diameter (with an hypothesis of spherical particles), U_0 is flow mean velocity, μ is the fluid dynamic viscosity and L is a flow characteristic length. Stokes number is an evaluation of the particle characteristic time over fluid characteristic time ratio. Appropriate tracers should have a short response time compared to the fluid's one ($St < 1$). This property is often validated by choosing particles with a density close to the fluid's one as heavy particles tend to sediment in the fluid while light ones fleet.

In addition, particle size is essential to provide clear images on the camera sensor and to conduct cross-correlation. The image of one particle should be encoded on at least 2 to 3 pixels to enable sub-pixel displacement computation (Boutier (2012)). The size of the field-of-view and the camera sensor resolution impose the choice of particle size.

Finally, the number of seeded particle must be considered with precaution. On one hand, too few particles result in unfilled areas where no displacement can be calculated. On the other hand, too many particles can generate light scattering effect and noisy images. A commonly used criteria is : at least 10 particles for an interrogation window.

Thus, the seeding quantity needs to be adapted to particle size, imaging area, camera resolution and flow characteristics.

2.3.2 Implementation on the experimental setup

Device characteristics

Particle Image Velocimetry technique is implemented on the experimental bench to acquire velocity fields in the aorta phantom under pulsatile flow. The standard region of interest (ROI) is focused on the aorta phantom and has an area of about 70x50 mm. The working fluid was seeded with 20 - 50 μm fluorescent particles (PMMA-RhB, $\rho_p = 1190 \text{ kg.s}^{-3}$, LaVision). They were illuminated by a 1 mm thick laser sheet emitted by a double-pulsed Nd:YAG laser (nanoPIV, L120-20PIV, $\lambda = 532 \text{ nm}$, Litron laser). An Imager sCMOS camera (2560 x 2160 pixels, Imager sCMOS CLHS, LaVision) is equipped with a 60 mm lens (Nikkor, NIKON) and synchronized with the laser pulses to capture pairs of images with a time interval Δt .

In the worst case scenario, the Stokes number can be calculated for these PMMA particles with equation (2.3.2). Constant quantities were set as $U_0 = 1 \text{ m.s}^{-1}$, $\mu = 3 \text{ mPa.s}$ (blood lowest viscosity in arterial flow conditions), $L = 3 \text{ cm}$ (aorta approximate diameter) and equation (2.3.2) results in $St \in [10^{-6}; 10^{-5}]$ which validates the choice in particles. These constants correspond to the orders of magnitudes of quantities reported in the literature that were presented in chapter 1.

Optical access

Optical access to the aortic flow is ensured by the transparency of the fluid and the aorta phantom. The phantom is immersed in a tank with flat Plexiglas surfaces. The camera is located outside the tank and focuses on a ROI in the aorta phantom. Between the particles that were seeded in the flow and the camera sensor, light has to cross 6 different media : working fluid, aorta phantom walls, tank fluid, tank Plexiglas, air and camera lens (figure 2.7). As light passes the interface between media with different refractive index, it will be refracted depending on incident angles (Snell-Descartes law).

As a result, the light that travels from the particles to the camera sensor are subjected to successive light deviations due to successive media interface crossings. The consequences are errors when locating particles on camera snapshots. A method to avoid or correct those deviations has to be found to properly locate particles. A first solution would be to insert a calibration plate in the aorta phantom prior to the experiment to compute necessary geometric corrections. These corrections would then be applied to PIV images to obtain real particles locations. This technique is highly difficult to implement in the aorta phantom that has a tortuous shape and compliant moving walls. Inserting, maintaining and positioning a calibration plate in this geometry under pulsatile flow turned out impossible. Therefore, optical tricks involving refractive index matching are implemented.

Firstly, to minimize optical distortions, the camera sensor, the tank flat surface and the laser sheet are aligned in parallel planes thanks to a set of laser levels. Secondly, to

imposed by the solenoid valve. As an example, the user may want to only image flow at the systolic peak on "n" successive cycles. Then, imaging has to be triggered at this specific instant for each of the n successive cycles.

To synchronize imaging trigger and cardiac cycle, 2 sets of datastream are generated with the same time resolution and output rate. They are created with a custom made Python program. The first set controls the solenoid valve cyclic openings/closings while the second set triggers the imaging process (figure 2.8). The two datastreams are processed and output simultaneously by the NI-controller. The output signal toward the valve is a 0-10 V analog voltage while the trigger signal is 5 V TTL (transistor-Transistor logic). Prior to the experiment, a bank of datastreams is created to define accessible trigger instants.

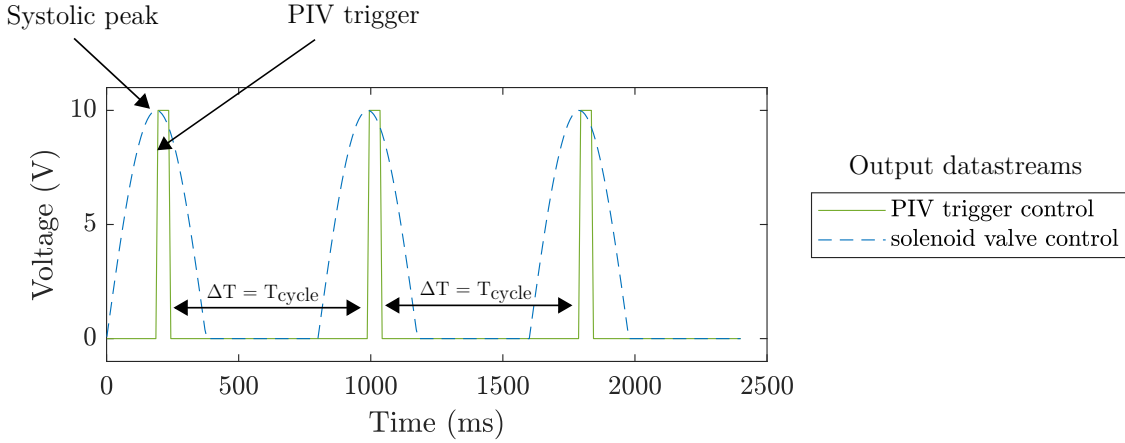


Figure 2.8: Example of the 2 sets of datastream to trigger PIV at the systolic peak imposed by the solenoid valve on 3 successive cycles. The first laser pulse and image of a pair is triggered at the square signal uprise as a TTL (Transistor-Transistor Logic) trigger.

Flow velocity strongly varies along the cardiac cycle. The interval Δt between two snapshots is adapted to the imaged cycle instant to ensure consistent particle displacement between each pair of images. Δt varies between 3 ms (at systole) and 15 ms (at diastole) depending on the location in the aorta and the time in the cycle. This method ensures reliable image correlation in post-processing². For each instant, a series of 500 to 1000 images are shot at the exact same instant in the cycle. It is achieved through 500 to 1000 cycles. It involves measuring a single cardiac instant at each experimental trial to set the right Δt which is a fixed parameter. Thus, k successive experimental trials have to be ran to image a single ROI at k different cardiac instants (figure 2.9).

Duration

In the current study, the flow follows a cyclic pattern. This pattern is analyzed by observing the same cycle instant k on a succession of n cycles. The number n of reproduced cycles has to be large enough to reach statistical convergence of computed velocity fields.

²In the literature, most studies shoot the whole cycle with the same Δt (Deplano et al. (2014); Bonfanti et al. (2020)). It can lead to higher measurement uncertainties and a lowering cross-correlation quality throughout the cycle.

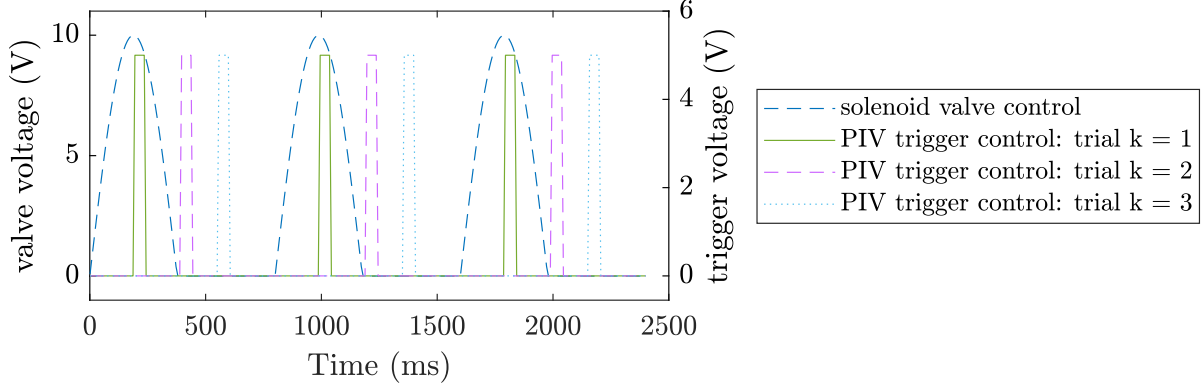


Figure 2.9: Example of trigger datastream to image 3 different cycle instants. The same experiment as to be re-run 3 times with the PIV trigger datastream that corresponds to the target cycle instant. For each trial, $\Delta T = T_{cycle}$ while Δt can be fixed by the user depending on the flow velocity.

This number depends on the quantity of interest. 100 pairs of images are usually sufficient to calculate mean flow quantities while 1000 pairs of images are generally required to study turbulence (Boutier (2012)). As an example, to analyze $k = 12$ cycle instants on a targeted region with $n = 500$ images each and cardiac cycle period $T = 0.800$ s, the experiment has to run on 6000 cycles (80 minutes). The experimental duration is quite long compared to a cardiac cycle. This is the reason why cycles reproducibility, temperature control, and fluid rheological properties preservation are carefully set up and monitored as described in previous section concerning the circulatory mock loop (section 2.2.1).

The implementation of PIV on the circulatory mock loop is adapted to cyclic cardiac conditions, aorta phantom geometry and optical properties. To ensure reliable cross-correlation and velocity field computations of the simulated aortic flow, optical access and light distortions have to be carefully considered. Designing a complete mock loop allows to adapt each feature for the use of such optical metrology method. It involves transparent tank, flat surface, optical access, solenoid valve/PIV imaging synchronization and suitable setup control and reproducibility. The most difficult part is to design an aorta phantom and a blood mimicking fluid (BMF) that are transparent with compatible RI (refractive index) for PIV. Indeed, the aorta phantom and the BMF also have their own requirements regarding mechanical and rheological properties. These ones are not always compatible with the transparency criterion for PIV. The next two sections describe how BMF and phantom were fabricated to meet all these characteristics which affect PIV measurement quality.

2.4 Aorta phantoms

In vitro hemodynamics studies require physical representation of arteries called artery **phantoms**. These models are designed with more or less complexity regarding material properties or geometry from simple rigid tubes to CT-scan based replica with compliant walls. Our goal is to design an aorta phantom with a patient-specific geometry and compliant walls with realistic mechanical properties. Even though geometrical and mechanical features play a non negligible role in hemodynamical flows (refer to chapter 1), such phantom have rarely been investigated (Büsen et al. (2015); Büsen et al. (2017)) on circulatory mock loop. The main reasons are difficulties in manufacturing this type of aorta models. This section focuses on the process of designing and evaluating an abdominal aorta that will be hosted in the circulatory mock loop.

As depicted in chapter 1, the aorta is a highly complex geometrical and morphological structure. Therefore modeling simplification for *in vitro* setups are to be addressed in accordance with the required degree of biofidelity and measurement techniques for this study. Two types of models are targeted:

- **A silicone compliant wall abdominal aorta** : this model matches our requirements for this study with compliance and transparency. It is used for the *in vitro* benchtop design, validation and a comparative study between Newtonian and non-Newtonian blood mimicking fluids (chapter 3). Silicone is the ideal material for PIV experiments because of its transparency. It is also a good candidate to mimic aortic wall compliance. The previously described mock loop was designed with this reference phantom. The design and evaluation of this model are described in this section.
- **Rigid and compliant 3D printed aortic dissections** : these models are used for case studies based on patients *in vivo* data and comparison with numerical studies (chapter 4). 3D printing allows rapid prototyping (48h) with limited cost compared to casting and silicone injection technique. It would be useful for rapidly manufacturing a patient aorta and testing it on the *in vitro* setup for surgery training and stent graft testing. However, difficulties in manufacturing such complex geometries involved sacrificing some phantom properties. To our knowledge, the combination of good transparency and compliance on a same phantom is hardly compatible with currently available 3D printing techniques. Therefore, we have chosen to test both rigid and compliance AD models with their limitations. Due to the complexity in designing such phantoms, AD models will be addressed in chapter 4 in the AD case study description. However, the phantoms general design process, requirements and tricky points described in this section apply to any phantom that can be hosted in the mock loop.

2.4.1 Phantom properties

The *in vitro* circulatory mock loop was designed to study human aorta hemodynamics with or without pathology such as aortic dissection which has a significant patient-specific

nature. Accordingly, our goal is to reach a certain degree of biofidelity and to implement phantoms with patient-specific geometry and compliant walls. The following paragraphs describe the process that led to the manufacturing of an aorta phantom and the next items detail the requirements and properties for our phantoms.

- **Patient-specific aorta geometry** : the *in vitro* simulator was designed with the idea of studying aorta pathologies such as aortic dissection that are highly geometry-specific pathologies. The shape, lengths, location of entry/exit sites on the aorta and the flap defines flow distributions (refer to chapter 1 section 1.3.1 for pathologies). Idealized shape models would only provide a general picture of flows and pressure distribution which is not sufficient to analyze such aortic conditions. It is therefore more appropriate to design a patient-specific model at life-size to represent the geometry complexity of such pathologies and facilitate confrontation with *in vivo* data. Among the long term objectives, the simulator will be adapted for surgery training which also demands for patient-specific life-size models.
- **Simplified geometry to main branches** : because of *in vitro* setup limitations, a certain degree of simplification has to be implemented. *In vivo*, aortic hemodynamics is not only limited to the aorta. For instance, the heart, peripheral vessels, the capillary bed are some of surrounding elements that affect aortic flows (compliance, resistance, pressure waves, etc.). However, one may not represent a complete artificial human cardiovascular system (at least in 2021). Therefore, we have chosen to represent the aorta and some main branches for the phantom. It involves the iliac arteries for the abdominal aorta model. The influence of the rest of the anatomical environment is represented with mechanical hydraulic elements on the mock loop (described in section 2.2.1). These elements allow to mimic global constraints on the aorta (external load), dampen the flowrate and pressure signals etc.
- **Transparent material** : the use of PIV – the optical method for flow visualization – involves optical access to the flow. The transparency of the phantom material is therefore a critical necessity for our assessment. Later in the essay, we shall see that this property is the most restrictive regarding available materials and manufacturing techniques.
- **Homogeneous material** : as depicted in chapter 1, the aortic wall is an heterogeneous material with different mechanical properties depending on layers and orientation. However, in this *in vitro* study as for the numerical simulations, the material is supposed to be homogeneous. The phantoms are manufactured with a single material with a constant wall thickness of 2 mm. It ensures a good knowledge of the refractive index to manage PIV images distortion and index matching of the BFM. It also guaranties proper control of the wall mechanical response along the phantom. This homogeneity hypothesis is a limitation in biofidelity as the aorta mechanical behavior is not accurately represented. Phantom manufacturing process and 3d printing are constantly developing with promissing techniques to match the anisotropic and multi-layers aortic structure (Brunette et al. (2004); Pazos et al. (2010)). But for now, we confine ourselves to the material homogeneity hypothesis.

- **Rigid and compliant models** : both rigid and compliant wall phantoms are used in this study. A compliant model, is of course, more representative of an *in vivo* model as wall displacement and fluid-solid interactions are part of the hemodynamic behavior. A compliant phantom with elastic properties close to a human one is used for the setup validation and a comparative study for Newtonian and non-Newtonian BMF. Regarding the aortic dissection study, due to difficulties in manufacturing a transparent model with such complex geometry, both rigid and compliant models were investigated with more or less transparency. In any event, both rigid and compliant models can be used for numerical simulation step-by-step validations from CFD to FSI. These last points will be addressed latter in the AD case study chapter (chapter 4).

2.4.2 Geometry reconstitution

Aorta geometries are extracted from CT-scans provided by the clinicians in Hospices Civils de Lyon, Hopital Louis Pradel. In the case of CT-scans, the blood domain is reconstructed first as it appears clearer on the scan sliced images thanks to contrast agents. The CT-scan provided for a patient with aortic dissection are shown in figure 2.10 with focus on the aortic dissection region. The wall domain is then reconstructed as the negative body of the blood domain. The hypothesis of constant wall thickness is applied on walls.

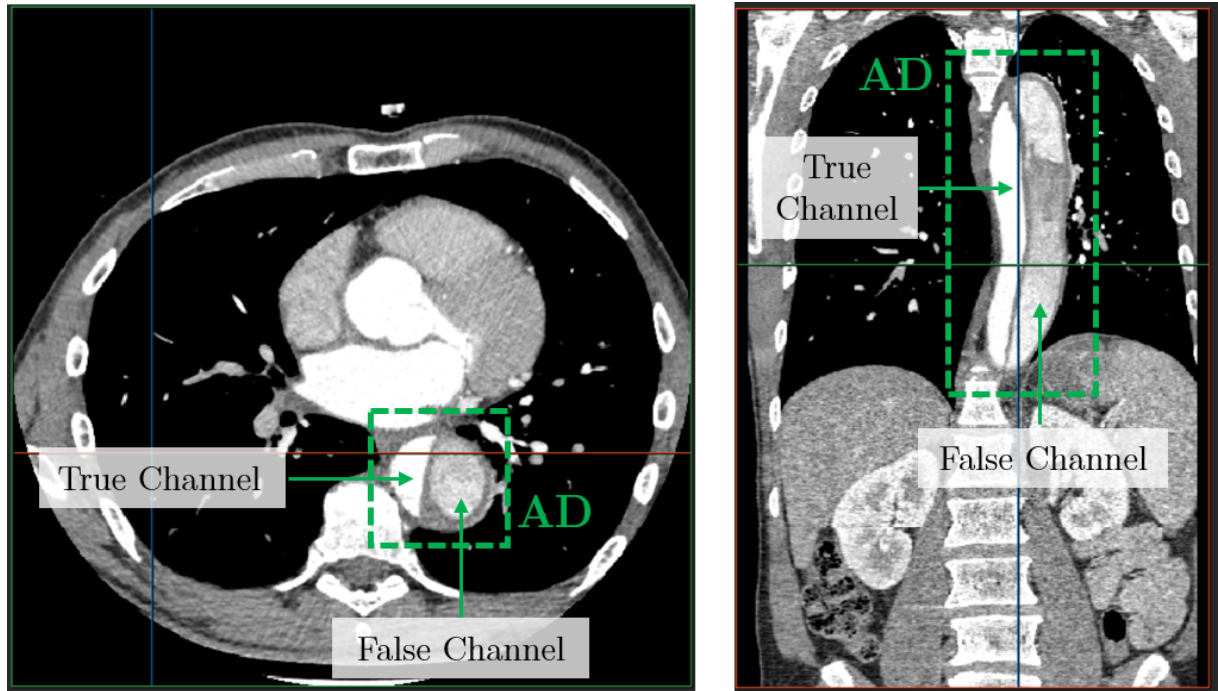


Figure 2.10: CT scan with (Left) the transverse plane and (Right) the frontal plane of the thoracic region for patient with AD. True and false lumen are indicated on the aorta.

Segmentation and surface interpolation of the blood domain is performed with the semi-automatic tool Simpleware Scan IP 2017 (Synopsis, CA, USA). Manual adjustments are performed to remove artifacts and some peripheral vessels emerging from the aorta which will not be represented on the final phantom. The wall domain is then reconstructed

and meshed with STAR-CCM+ 12 (Siemens). A 2 mm wall thickness is applied on the 3D model. The fully reconstructed AA model (abdominal aorta model) and an AD (aortic dissection) model are presented in figure 2.11. Now, the next step consists in obtaining a physical model of these 3D reconstruction to conduct flow visualization on the circulatory mock loop with PIV.

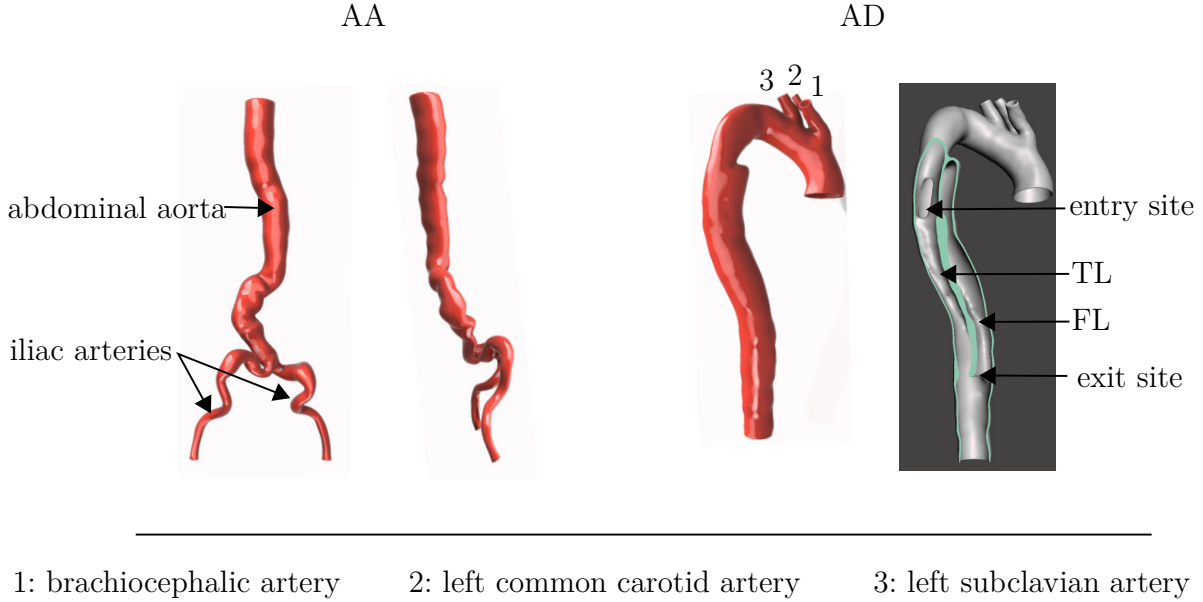


Figure 2.11: (a) abdominal aorta reconstitution (b) aortic dissection reconstitution (corresponds to the patient presented in figure 2.10).

2.4.3 Manufacturing technique

The present AA model is a replica of an abdominal aorta with the iliac bifurcation. It was fabricated with cast manufacturing technique by Segula Technologies. The phantom was constructed with silicone that was shaped with a male (internal surface) and a female mold (external surface). The resulting phantom is a clear silicone rubber model with a soft surface. The exact silicone material reference could not be communicated by the manufacturer.

This silicone injection technique provides phantoms that meet our requirements, especially the clear material property for PIV measurements. The model thickness homogeneity was evaluated by cutting and measuring a sacrificial phantom. The wall thickness was 2.19 ± 0.42 mm. Three identical AA phantoms were manufactured with this technique.

Unfortunately, we did not find any manufacturer who could design a mold for a silicone phantom of an aortic dissection. Our patient specific geometries with the parallel lumens and the flap were too complex for the cast design and the extraction of the silicone model once shaped. This technique could only be applied to single lumen aorta model such as the AA one. Therefore, we have tested other techniques including 3D printing for manufacturing AD that will be addressed in chapter 4. However, The previously described process of reconstitution is still valuable for building 3D models of aortas that

can be implemented for the numerical simulation and even for 3D printing.

For now the next section focuses on silicone AA model. This phantom has to be evaluated regarding elasticity with young's modulus assessment and refractive index (two important features for realistic wall behavior and PIV optical access).

2.4.4 Compliant phantom: Young's modulus

The previously designed AA model has compliant walls and its elasticity has to be evaluated to estimate whether or not it is a good candidate to mimic human aorta. Mechanical tensile tests were conducted on the model to evaluate its Young's modulus (E). These tests were conducted by Laurie Portero, a master student in the context of an internship. As mentioned previously, 3 identical AA phantoms were manufactured. One of them was sacrificed for tensile tests combined with Digital Image Correlation (DIC). For more details on the digital image correlation technique refer to [Yoneyama \(2016\)](#) (DIC principle) and to [Palanca et al. \(2016\)](#) (applications to biomechanics). Results are presented on table 2.1 for phantom samples cut in the longitudinal ($n = 8$ samples) and radial direction ($n = 2$ samples). Young's modulus were calculated with both tensile force/jaws displacements detected by machine and DIC computation.

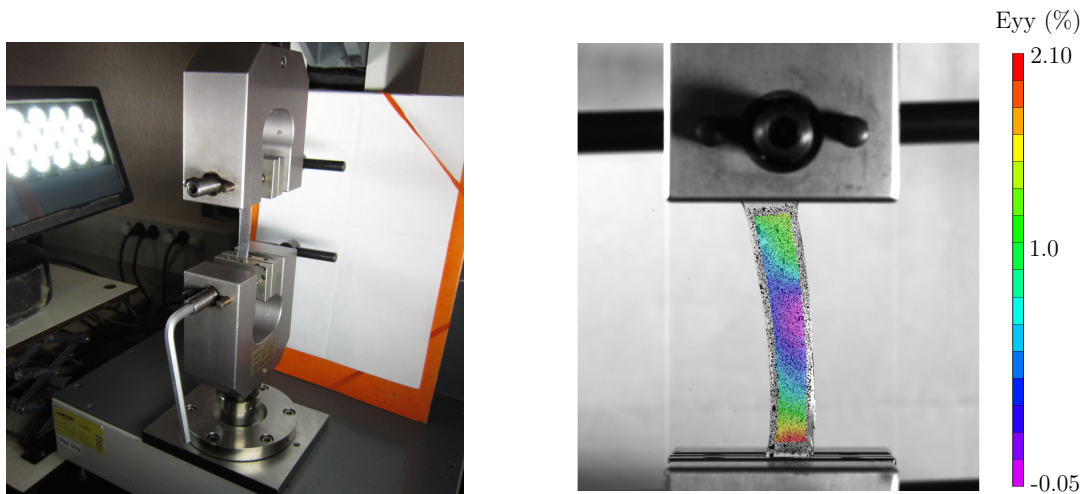


Figure 2.12: Tensile tests and digital image correlation on a silicone AA phantom sample.

Table 2.1: AA phantom Young's modulus (E) calculated from tensile tests. Mean and standard deviation are indicated for the tensile test conducted on "n" samples on both specimen orientations.

	Longitudinal specimen ($n = 8$)	Radial specimen ($n = 2$)
E (MPa) - machine	0.47 ± 0.07	0.78 ± 0.06
E (MPa) - DIC	0.53 ± 0.07	0.91 ± 0.12
Error	10%	14%

The young's modulus were measured with a low number of sample. Note that a phantom was scarified to conduct those tensile tests and because of the limited phantom number and samples we could not conduct more experiments. The longitudinal specimen elasticity value will be retained as the phantom elasticity. The radial specimen elasticity value is given for information but is not sufficiently reliable due to the limited number of samples (only 2). However, the elasticity value is still in the range of human aorta.

2.4.5 Refractive indexes

Finally, optical information on the AA phantom are required to optimize the PIV setup. Measuring the refractive index (RI) of solids with complex geometry is a difficult task. For the compliant silicone phantom, the material shape cannot be inserted in an abbe refractometer for a direct RI measurement. We only have 3 shaped AA models with this material. Therefore, indirect RI measurement technique is used by immersing the phantom in solutions with different RI until they match. When the model appears transparent in the solution, the match between the solution and the phantom RI is achieved. The solution RI is then measured with an abbe refractometer at 25°C (NAR-1T, Atago). The refractive index was evaluated as 1.402.

The phantom satisfies our requirements concerning transparency (attached to PIV constraints), elasticity and geometry for biofidelity. The use of silicone injection technique allowed to obtain a clear transparent silicone model which is essential for the implementation of PIV. The refractive index was quantified and will serve as the targeted index for the blood mimicking fluid design.

2.5 Blood mimicking fluid

The use of human blood for *in vitro* experiments involves tricky procedures including ethic, health regulations and difficulties in obtaining large volumes. Moreover, the add of chemicals to prevent coagulation, a non-physiological temperature and the lack of oxygen may disturb the fluid properties and thus result in unreliable measurements. Eventually, real blood opacity limits optical applications. Optical instruments may require fluid specificities such as transparency and optical index matching for Particle Image Velocimetry (PIV). To that extent, studies have focused on designing **blood analogues**, also called **blood mimicking fluids (BMF)**, to meet both the rheological behavior of blood and the measuring device requirements (Najjari et al. (2016); Yousif et al. (2011)).

In the present study, we focus on the non-Newtonian shear-thinning property to emulate human blood behavior with custom optical properties. Actually, the PIV technique demands a transparent working fluid for PIV particles optical access. Moreover, RI matching of the fluid and the phantom is achieved to ensure reliable PIV measurements and minimize optical distortions. This section describes the fabrication of a BMF that meets these criteria and the quality controls that are carried out to inspect if the fluid can be handled in the experimental setup (pump's shear damaging, temperature alteration, optical properties etc.).

2.5.1 Composition and target properties

A wide range of liquids offer custom viscosity, elasticity, stability and refractive index possibilities. But when simultaneously considering all those features, the list of relevant liquids is drastically shortened and different products have to be mixed (Najjari et al. (2016); Yousif et al. (2011); Anastasiou et al. (2012)). Most commonly used BMF are **glycerol** solutions in **de-ionized water** to match viscosity. The non-Newtonian property is ensured by **xanthan gum** or **polyacrylamide (PAA)**. Both components provide similar viscosity but different elastic behavior. Besides, most *in vitro* experiments involve blood vessel phantoms with transparent material such as glass for rigid models, PDMS, and silicone for compliant models. When implementing optical measurement methods, index matching between the fluid and the phantom material is needed to prevent optical distortions. Thus **NaI**, **NaSCN** or **KSCN salts** are added to adjust refractive indexes even though they are known to alter fluid shear-thinning behavior. Each component interacts with each other and their own properties cannot be considered isolated.

Transparency and temperature stability

PIV is implemented to assess flow velocity fields. Therefore the BMF needs to be transparent and to meet shear-thinning behavior. Those blood physiological properties (at 37 °C) should match at the room temperature (25 °C) for the BMF to avoid using a complex temperature regulation system. The previously cited ingredients allow to fabricate a transparent solution. However, their rheological and optical properties may vary with temperature and need to be checked in the experimental range of temperature (25 ± 2 °C).

Viscosity and viscoelasticity

In non-Newtonian applications, the two most commonly used substances to mimic blood viscosity are glycerol and xanthan gum. Glycerol is added to deionized water to increase the overall viscosity while xanthan gum is used to provide shear-thinning and elastic behavior to the solution. Both allow to obtain transparent solutions as long as the polymer concentration is low (under 400-500 ppm). Xanthan gum is a well established polymer in agribusiness and cosmetics industry. This polysaccharid is produced by the bacterium *Xanthomonas Campestris* and provides strong shear-thinning properties with only small amount in solutions (< 1 %). Other studies have investigated aqueous polyacrylamid (PAA) to replace xanthan gum. This polymer provides appropriate shear-thinning properties but elasticity is much higher than blood's one. PAA model is out of range regarding viscoelasticity and oscillatory conditions (Mann and Tarbell 1990). It will not be considered in the current study.

Xanthan gum characteristics

Xanthan gum is a high molecular weight polysaccharid consisting of a backbone and side chains (2.13). The molecule conformation impacts the solution viscosity and shear-thinning properties. Two different conformations are observed: ordered and disordered (Whitcomb and Macosko (1978); Garcia-Ochoa et al. (2000); Zhong et al. (2013)). For the ordered conformation, molecules are arranged in stable and organized helical structures

which increase the solution viscosity (resistance to flow). For the disorder conformation, molecules adopt more flexible and extended coil structures which decrease the solution viscosity. Depending on the applied shear-rate, xanthan molecules may adopt different conformations and transitional states which affect the solution viscosity. In some aspects, this conformational change resembles the RBCs behavior described in chapter 1. Xanthan gum is therefore a good candidate to mimic blood shear-thinning property.

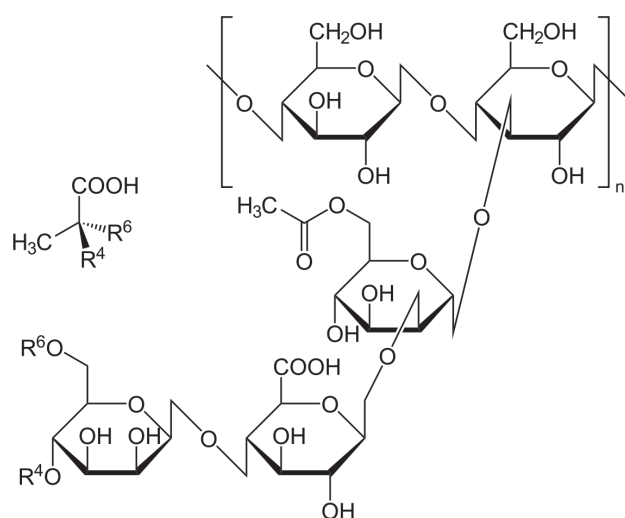


Figure 2.13: Molecular structure of xanthan gum

In addition, the solution concentration, temperature, ionic and molecular interactions influence the general structure of the polymer and thus, solution rheological properties (Whitcomb and Macosko (1978); Garcia-Ochoa et al. (2000)). First, increasing xanthan gum concentration non-linearly increases the absolute viscosity and shear-thinning slope because of stronger inter-molecular interactions (Zhong et al. (2013)). Moreover, salt concentration is known to influence xanthan gum viscosity (Whitcomb and Macosko (1978)). It is a polyelectrolyte polymer which is sensitive to the presence of ion. Zhong et al. (2013) investigated the influence of ionic strength on high and low concentration xanthan gum solutions. At high concentration (>1000 ppm), addition of NaCl ionic salts increased the solution viscosity and shear-thinning degree. Conversely, at low concentration (< 200 ppm), a decrease in both properties was observed. This behavior is explained by xanthan molecule, its conformational changes and the modifications of inter-molecular interactions in the presence of salt (Zhong et al. (2013)). In the present study, a maximum xanthan concentration of 400 ppm is tested to design the BMF. Indeed, Deplano et al. (2014) reported that xanthan concentrations over 400 ppm alter the mixture transparency and become turbid which makes PIV measurements delicate. Note that the use of salt to adjust the RI is expected to decrease the solution viscosity and shear-thinning degree. The influence of the concentration, salts, temperature and molecule degradation on solutions are studied in the scope of designing and preserving our BMF.

2.5.2 Non-Newtonian BMF in the literature

A large number of hemodynamics studies have used BMF to mimic blood viscosity with the Newtonian or non-Newtonian assumption. With the Newtonian assumption, water-glycerol solution are commonly used to match human blood high shear-rate asymptotic viscosity (between 3 and 4 mPa.s) (Yousif et al. (2011); Büsen et al. (2015); Bonfanti et al. (2020)). With the more realistic non-Newtonian assumption, xanthan gum is added to the previous mixture to obtain a shear-thinning property as in human blood (Yazdi et al. (2018)). Some of these studies have used optical flow visualization techniques on vessel phantoms which require index matching. Figure 2.14 shows five different xanthan gum BMF from the literature with two reference viscosity measurements for human blood (Chien (1970), Thurston (1979)). As an example, Najjari et al. (2016) investigated xanthan BMF with the influence of NaI, NaSCN and KSCN salts to adjust the refractive index. This study offers a range of ingredient proportions to match phantom RI from 1.372 to 1.495 in accordance with human blood shear-thinning degree. Campo-Deaño et al. (2013) compared xanthan gum solutions with alternative components. In this last study, XG and PAA were used for their shear thinning properties while dimethyl sulfoxide (DMSO), hyaluronic acid and sucrose for viscosity and refractive index adjustment. Both studies specifically target PDMS blood vessels phantoms that are silicone based material.

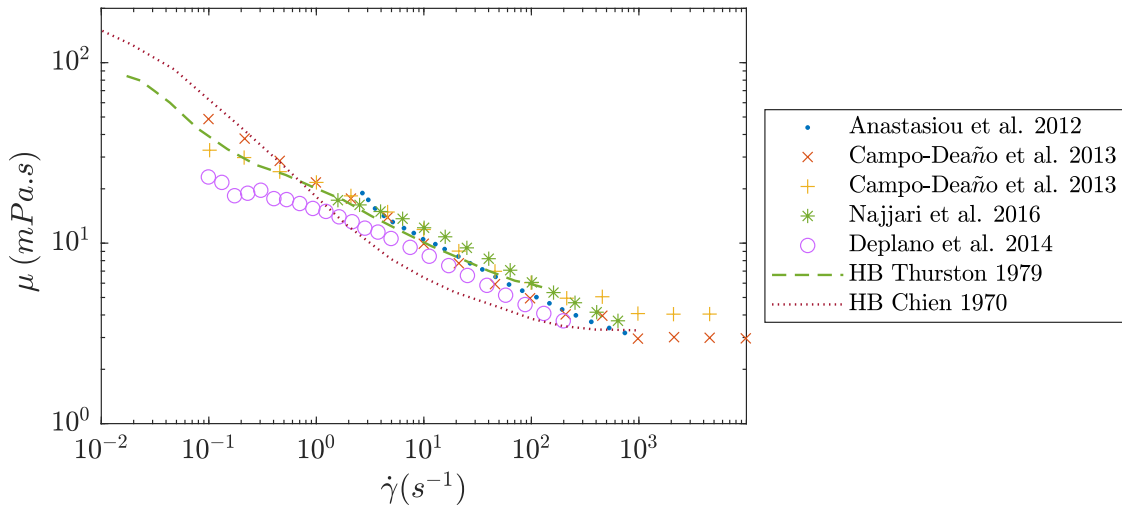


Figure 2.14: Viscosity of blood mimicking fluid under shear rate sweep measurements from the literature. Solutions were made with a mixture of xanthan gum and glycerin (or equivalent) in different proportions. Results were extracted from Campo-Deaño et al. 2013 (symbol (x) = XG - DMSO solution, symbol (+) = XG - sucrose solution), Deplano et al. (2014) (XG - Gly - sodium salt), Anastasiou et al. 2012 (XG - Gly solution) and Najjari et al. 2016 (XG - Gly - KSCN solution).

These BMF studies indicate that xanthan gum and sodium salts are particularly well adapted to the design of blood analogs with RI requirements for silicone phantoms. For this section, we focus on the silicone AA phantom for refractive index matching and BMF design. As mentioned earlier, other phantoms (for aortic dissection) will be manufactured with 3D printing. These models have a different refractive index that cannot be matched

with the technique described in this section.

2.5.3 Fabrication and viscometry

In the present study, the fluid is designed using four main components : **water**, **glycerin** (4813, Oleon), **xanthan gum** (Keltrol, CP Kelco) and **NaCl**. In addition to their interesting rheological properties, these components are not expensive, have low toxicity and are readily available. Then, the question arises of using deionized water or tap water when considering the need for large volume of fluids (tank and reservoir can host about 150 L). In this section, all the presented solutions were fabricated in small quantities (100 mL) with de-ionized water for the only purpose of rheometry and RI measurements. [Zhong et al. \(2013\)](#) reported a significant decrease in the shear-thinning degree when using tap water (from the city of Richland, USA) instead of de-ionized water. In the current study, similar test were conducted with tap water (from the city of Villeurbanne, France) and no differences were noted within the investigated rheological scale. For convenience, large volume of solutions for the circulatory mock loop (30 L) are prepared with tap water and measurements are conducted to check if properties match their de-ionized water equivalent solution. In what follows, the results from tap water solutions will be explicitly stated in figure captions.

The solutions are prepared by first mixing glycerol and xanthan gum in a flask. In fact, it is much easier to dissolve xanthan gum in glycerol than in water thanks to limited polymer agglomerations. Moreover, moderate stirring and heating (30°C) facilitate mixing. Then, deionized water is added to the solution and goes in magnetic stirring for 12 hours (one night). High xanthan gum concentration solutions (over 100 ppm) are directly prepared with the target concentrations. The xanthan powder is weighed with a 1 mg precision balance. Less concentrated solutions (under 100 ppm) are prepared by diluting a higher concentration mother solution. The solutions are tested the day after preparation. The mixture proportions are given in percentage by weight (%wt) for water, glycerin and NaCl while the xanthan gum concentration is given as parts-per-million (ppm).

Different proportions were tested to approach the viscosity profile of human blood. Tested proportions ranges were defined using the BMF compositions from the literature: between 50 and 400 ppm for xanthan gum concentration, and between 80/20 %wt and 60/40 %wt for water/glycerin proportions.

The viscosity measurements were carried out with a MCR 302 Anton Paar rheometer with a cone-plate CP50-1 configuration (50 mm diameter and 1° angle). Dynamic viscosity is assessed for shear-rates ranging from 1000 down to 0.01 s⁻¹. At low shear-rates (between 0.01 and 0.1 s⁻¹), solution viscosities below 10 mPa.s are out of the rheometer measurement range. Therefore, plot comparisons involving below 10 mPa.s are presented in a 0.1-1000 mPa.s range even though measurements were conducted in a wider range.

Every solution was tested 3 times with 3 different samples from a flask or the reservoir. Every, presented plot represent mean viscosity curve from the 3 samples. When comparing multiple viscosity measurements from a same solution, a mean difference of 1% is observed at 1000 s⁻¹ while, the mean difference is of 22% at 0.1 s⁻¹. This is due to the decrease of rheometer precision when lowering shear-rates. For reasons of visual clarity, viscosity error bars are not represented on every plot but note that viscosity measurements standard

deviation decreases from about 1% at 1000 s^{-1} to 22% at 0.1 s^{-1} . Additional details on the BMF fabrication steps and rheometer setup for viscosity measurements are available in appendix C.

2.5.4 Results

Overview of component interactions

First tests were carried out to identify each components influence on the solution overall viscosity. Figure 2.15 shows how glycerol, xanthan gum and NaCl modifies the solution properties. Viscosity versus shear-rate measurements were conducted on similar water-glycerol ratio solutions (figure 2.16). The addition of glycerol to water leads to an increase in viscosity to reach human blood asymptotic high-shear rate viscosity (3 - 4 mPa.s). The obtained fluid remains Newtonian. The shear-rate property is brought up by xanthan gum (200 ppm here). High shear-rate viscosity ($>1000 \text{ s}^{-1}$) tends to the water-glycerol base value while low shear-rate viscosity is 50 times higher. In these lower ranges, the viscosity curve seems to reach a "plateau" which is also observed on human blood. Finally, the addition of NaCl to the solution while respecting water-glycerol ratio clearly decreases the shear-thinning degree and the viscosity at very low shear rates. The "plateau" at low-shear rate does not appear anymore in the observed shear range and the overall viscosity is decreased.

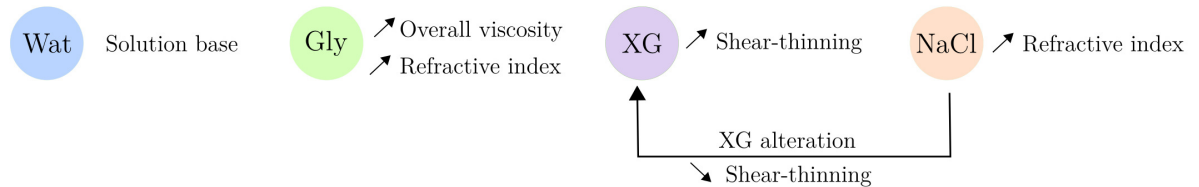


Figure 2.15: Schematic view of the influence of BMF components on the solution properties.

Let's not forget that the fluid RI needs to match the aorta phantom one (about 1.4). The use of salts is essential to reach this RI even though it alters shear-thinning properties. In this case, the Wat-Gly Xg solution has an RI of 1.372 while the one with NaCl has an RI of 1.399. A balance between NaCl and xanthan gum concentration has to be found to optimize both properties: RI and shear-thinning viscosity. These results validate previously described observation from the literature (Najjari et al. (2016)). In the next paragraphs, a more precise view of components influences is shown with different proportions of each ingredient. The purpose is to design a relevant BMF but not to conduct a large scale parametric study on glycerol-xanthan-NaCl solutions. Therefore, out-of-range concentrations regarding human blood viscosity ranges are not tested. The next sections investigate each ingredient influence on solution viscosity by varying one component concentration at a time.

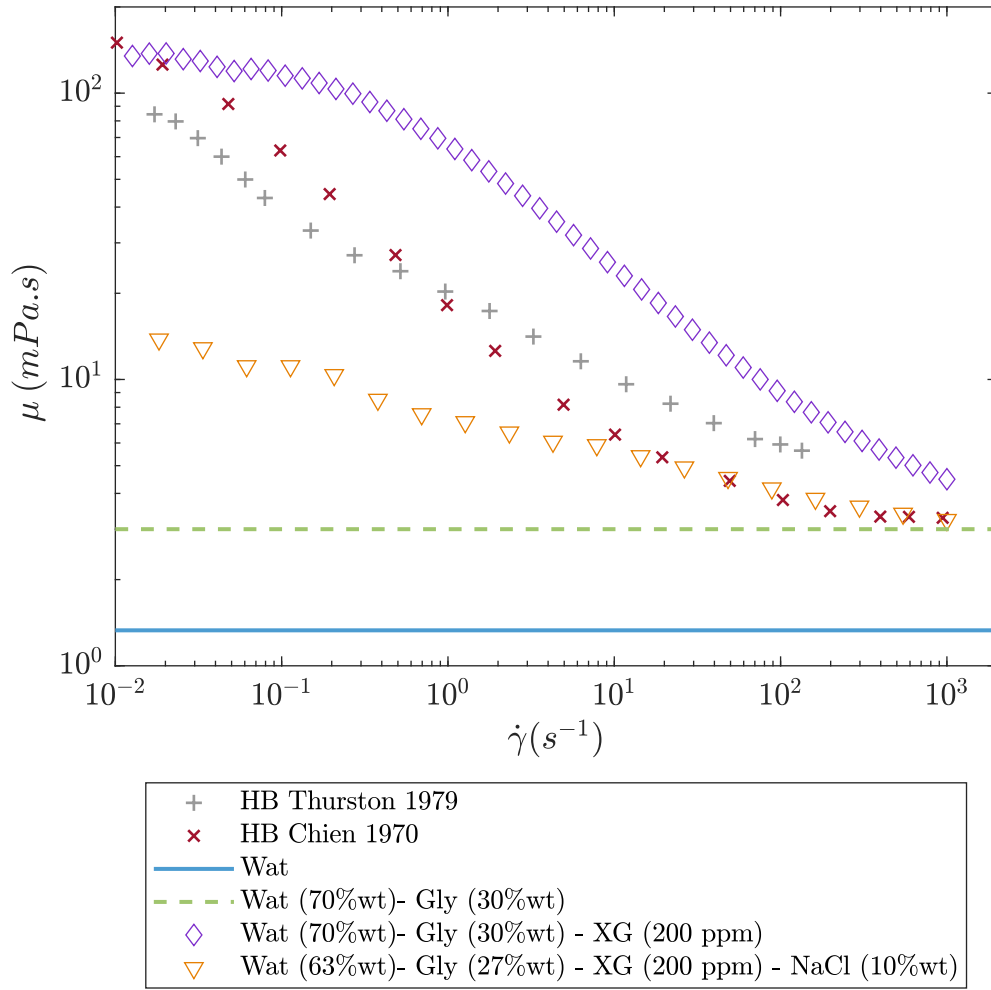


Figure 2.16: Viscosity versus shear rate measurements on the BMF to highlight the influence of each component on viscosity and shear-thinning properties. Wat = water, Gly = glycerin, XG = xanthan gum - NaCl = sodium chloride. Human blood viscosity data from [Thurston \(1979\)](#) and [Chien \(1970\)](#) are shown as references.

Dynamic viscosity versus shear-rate

Glycerol influence: In a water-glycerol-xanthan solution with constant xanthan concentration, the variation of glycerol-water proportion leads to a modification in shear-thinning degree. As shown in figure 2.17, a 10% increase of glycerol concentration results in an increase of high-shear rate viscosity while the one at low shear rate seems unchanged. When mixed to xanthan, glycerol does not only modify the overall viscosity but also share-thinning behavior. This process mostly takes place at high shear-rates and seems to fade when shear-rate decreases.

Xanthan gum influence: The same method was applied to a constant water-glycerol ratio solution with varying xanthan gum concentrations (from 20 to 400 ppm). Figure 2.18 shows the increase in overall viscosity and shear-thinning degree with increasing xanthan concentration. At low shear-rates ($<1 \text{ s}^{-1}$), all the solutions seem to exhibit a lowering in shear-thinning slope which suggest an early stabilized viscosity plateau.

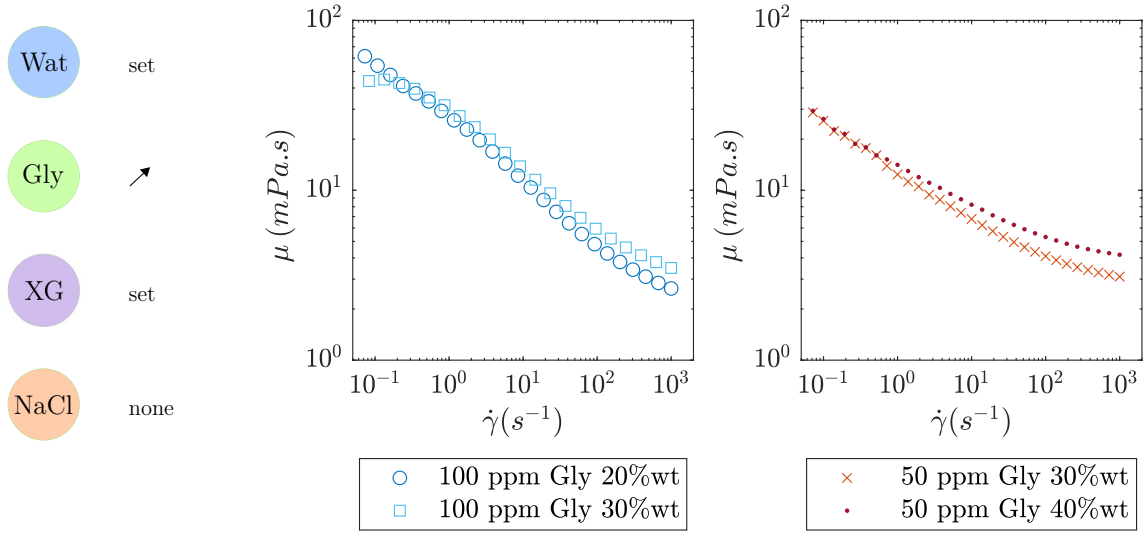


Figure 2.17: Dynamic viscosity versus shear-rate measurements on designed BMF candidates. The graph shows the influence of glycerol concentration on solutions with fixed xanthan concentrations (50 ppm and 100 ppm) and without NaCl.

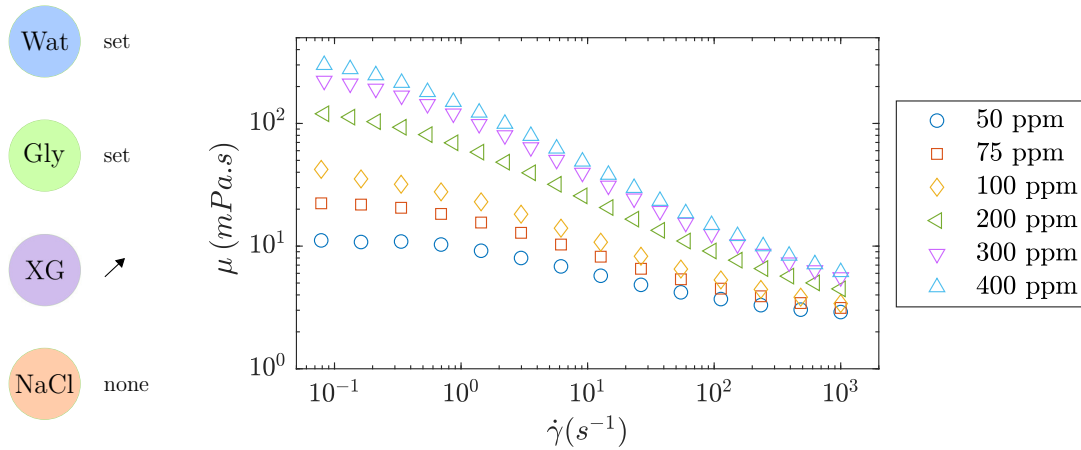


Figure 2.18: Dynamic viscosity versus shear-rate measurements on designed BMF candidates. The graph shows the influence of xanthan gum concentration on solutions with fixed water-glycerol concentrations (Wat 70%wt- Gly 30%wt) and without NaCl.

Refractive index and NaCl

Finally, constant water-glycerol-xanthan ratio solutions were measured for different NaCl concentrations to show the influence of salts on RI and viscosity. Four initial 100 g mixtures of Wat 70%wt, Gly 30%wt and 100 ppm were prepared. In each of these solutions, different quantities of NaCl are added : 0 g, 10 g, 20 g, and 23 g. The refractive indexes are indicated in table 2.2 and viscosity measurements on 2.19. Adding NaCl results in an increase in RI and a decrease in overall viscosity and shear-thinning degree. Moreover, NaCl solutions show a slight increase in viscosity curve slope at low shear-rate and do not

indicate any plateau. Thus, the viscosity curve is different from its salt-free equivalent not only regarding slope but also concerning curvature. Table 2.2 also shows water-NaCl and water-glycerol solution to underline the fact that both glycerol and NaCl allow to increase RI. A balance between these components enables to adjust RI while minimizing the impact on shear-thinning degree.

Solution	Wat	Gly	XG	NaCl	RI
A	100 % _{wt}	-	-	-	1.333
B	-	100 % _{wt}	-	-	1.472
C	83% _{wt}	-	-	17% _{wt}	1.362
D	70% _{wt}	30% _{wt}	-	-	1.372
E	70% _{wt}	30% _{wt}	100 ppm	-	1.372
F	70% _{wt}	30% _{wt}	100 ppm	+ 10g	1.384
G	70% _{wt}	30% _{wt}	100 ppm	+ 20 g	1.399
H	70% _{wt}	30% _{wt}	100 ppm	+ 23 g	1.402

Table 2.2: Refractive indexes for different water-glycerol-xanthan-NaCl solutions.

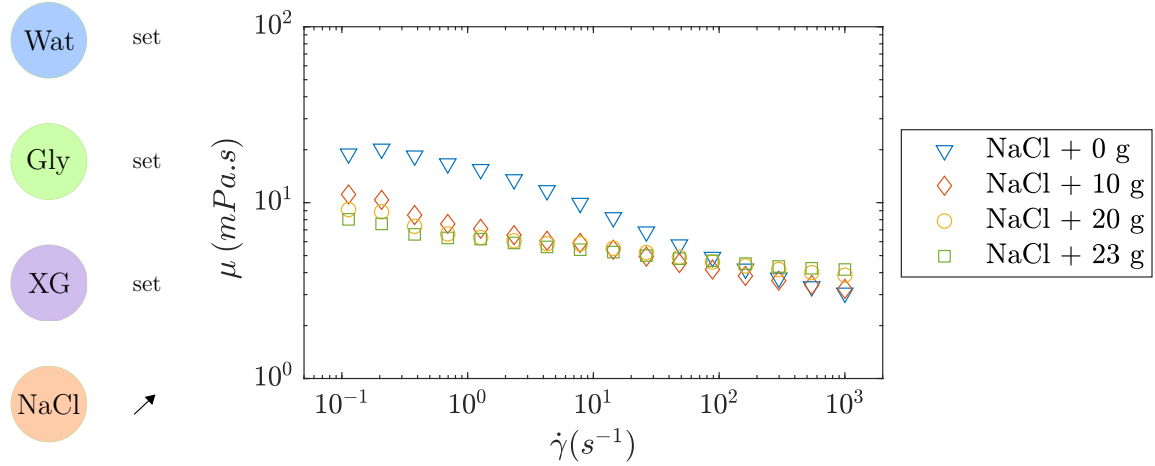


Figure 2.19: Dynamic viscosity versus shear-rate measurements on designed BMF candidates. The graph shows the influence of NaCl concentration for solutions with fixed water-glycerol-xanthan concentration (Wat 70%wt- Gly 30%wt ratio and XG 100 ppm).

To illustrate the importance of RI matched BMF and aorta phantom, figure 2.20 shows the silicone abdominal aorta phantom in BMF with different RI. A grid is placed backward from the phantom and magnets maintain the phantom at the bottom of the tank. Index examples are given from low RI water to the higher RI BMF (solution A, C, D and H from table 2.2). RI were measured with an abbe refractometer at 25°C (NAR-1T, Atago). With these observations, the target RI for the fluid is confirmed at 1.402 to minimize optical distortion and makes the phantom practically invisible when immersed in the fluid.

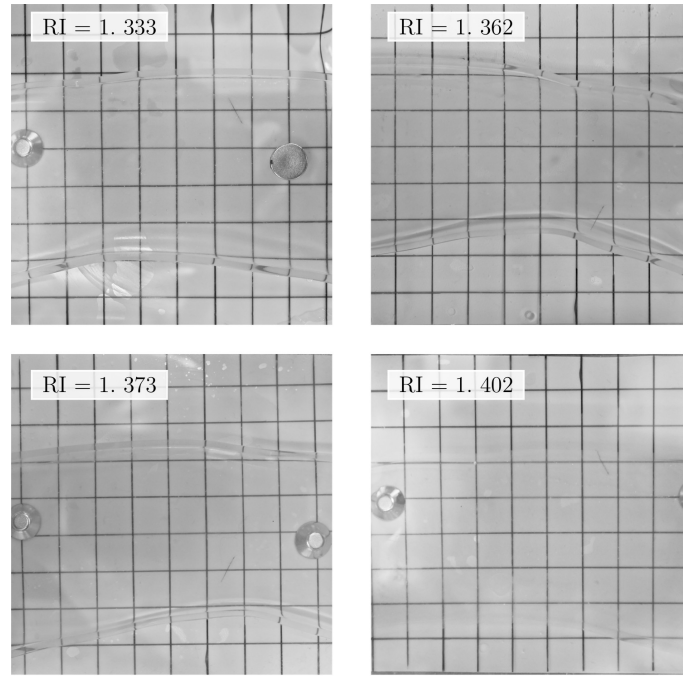


Figure 2.20: Illustration of refractive index matching with the BMF and aorta phantom. The latter is immersed in a tank containing BMF with different RI. A grid in the bottom of the tank allows to see distortions mainly on the phantom diopters with strong curvature. RI = 1.402 is set as the target BMF RI to match the phantom one.

Optimal BMF formulation

Now components characteristics influences on overall solution viscosity and optical properties were investigated, an optimal BMF was designed. Its composition is : 55.6%wt of water, 37%wt of glycerin, 7.4%wt of NaCl and 200 ppm of xanthan gum. The obtained fluid density is of $1\,146\text{ kg.m}^{-3}$ and the RI of 1.399. An equivalent Newtonian fluid was fabricated with 55.6%wt of water, 37%wt of glycerin and 7.4%wt of NaCl. It exhibits the same density and RI as the non-Newtonian version. Its viscosity is equal to 3.9 mPa.s to approach high-shear rate asymptotical viscosity of the non-Newtonian BMF.

This Newtonian fluid has two purposes: serve as a reference working fluid for flow comparison with the non-Newtonian fluid and act as index matching fluid for the tank that contains the aorta phantom. In fact, xanthan gum is difficult to mix and deteriorates over time. The only function of the tank fluid is to apply a certain pressure on the aorta model, match the phantom material refractive index and minimize optical distortions. Therefore, the tank fluid does not need any shear-thinning properties. For convenience purpose, this Newtonian version of the BMF is used as a RI matched fluid in the tank.

Viscosity versus shear-rate measurements are presented in figure 2.21 with a reference human blood (HB) viscosity curve from [Thurston \(1979\)](#) at 45%Ht. At low and high shear-rates extrema, a good approximation of viscosity values is obtained with the BMF compared to the human blood reference. The fluid has a shear-thinning behavior with a viscosity ranging from 5.2 to 95.9 mPa.s in the investigated shear-rate range (1000 to 0.01 s^{-1}). Differences in viscosity curve slopes and curvatures are observed between BMF and HB. The HB curve exhibits less variations in slope with an almost linear relationship

between viscosity and shear-rate. However, the main objective is to design a BMF with shear-thinning properties in the range of human blood viscosity. The presented formulation appears adapted to conduct *in vitro* experiments with a good approximation of human blood rheological behavior and adjusted RI. Note that the reference curve from [Thurston \(1979\)](#) is not universal as human blood shear thinning degree can be influenced by age, sex, etc. ([Long et al. \(2005\)](#)). Unfortunately, to the authors knowledge, there is no precise blood viscosity measurement for large panel of population with different conditions. We have chosen to take the results from [Thurston \(1979\)](#) as a reference because the measurement methodology and patients characteristics are well reported.

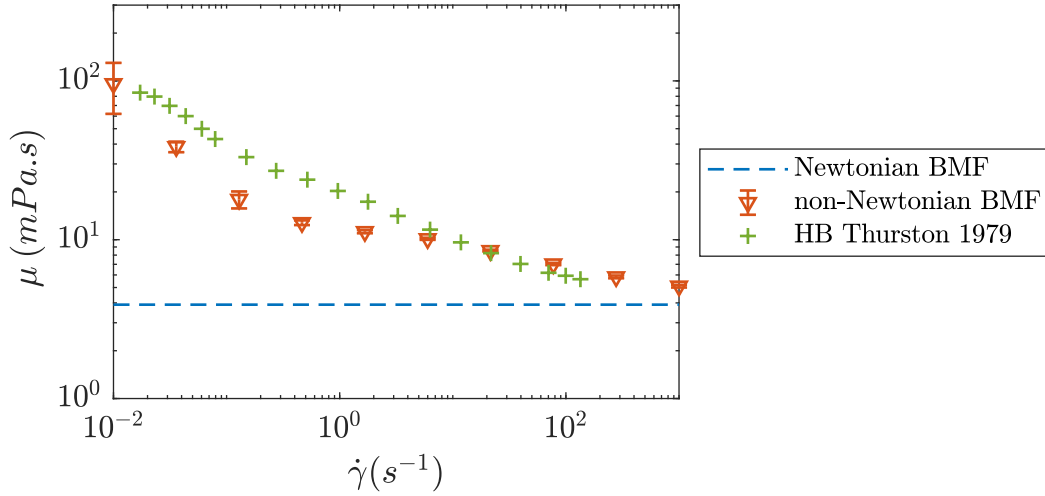


Figure 2.21: Viscosity measurements of the optimal non-Newtonian BMF. References for human blood dynamic viscosity from [Thurston \(1979\)](#) are shown and the reference Newtonian BMF is a water-glycerol-NaCl equivalent of the non-Newtonian version ($\mu = 3.9$ mPa.s)

Stability over time and temperature variations

To check if the BMF can be implemented on the experimental setup, it has to fulfill some requirements imposed by the mock loop. The latter works in a temperature range from 23 to 27 °C and risks of damaging xanthan gum molecules still exists. It is necessary to ensure constant working fluid properties during an experiment. Firstly, the BMF was measured with the viscometry tests described in previous sections at 3 different temperatures: 23, 25 and 27 °C ([2.22](#)). No main differences between viscosity values were detected. The fluid is thus, considered as stable in the mock loop working temperature range. Secondly, a four hours experiment of continuous BMF pumping and looping in the mock loop was carried out to follow polymer degradation. In practice, it corresponds to the longest duration of an experimental trial with the mock loop. Samples were collected in the working fluid reservoir at different instants after pumping started (1h30, 2h30, 3h30 and 4h) and then, tested on the rheometer at 25 ± 2 °C. As for temperature measurements, no noticeable degradation were observed on the working fluid after 4 hours of pumping. Note that these samples were collected during a PIV experiment which allowed to set up the synchronization system in parallel without wasting BMF. Therefore, the working fluid

was seeded with particles. The presence of particles in the samples measured with the rheometer may explain the slight differences of viscosity values at low-shear rate. In fact, these viscosity measurements are more representative of the BMF in working conditions which is supposed to contain PIV particles.

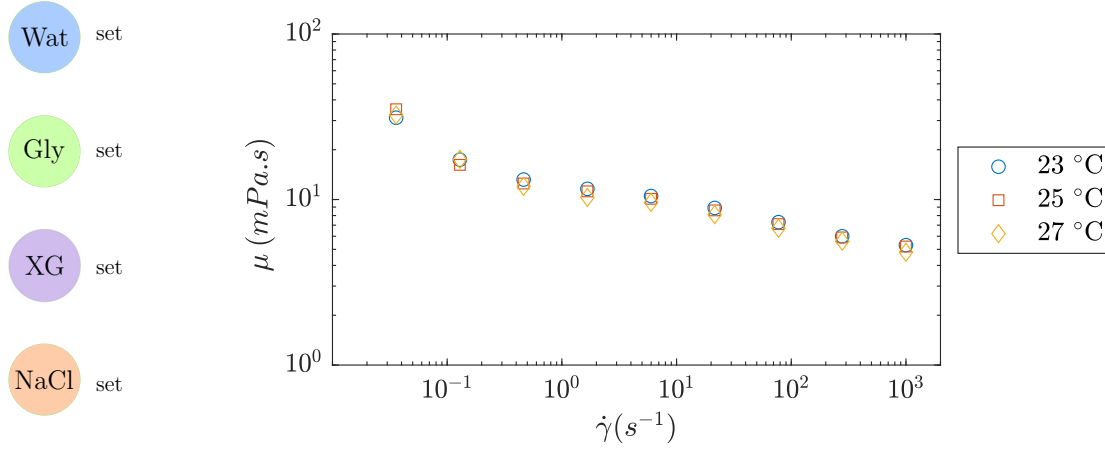


Figure 2.22: Dynamic viscosity versus shear-rate measurements on designed BMF candidates. The graph show the influence of temperature for solutions with fixed water-glycerol-xanthan-NaCl concentration (optimal BMF formulation). Temperature was tested in a range 25 ± 2 °C which corresponds to the mock loop experimental conditions.

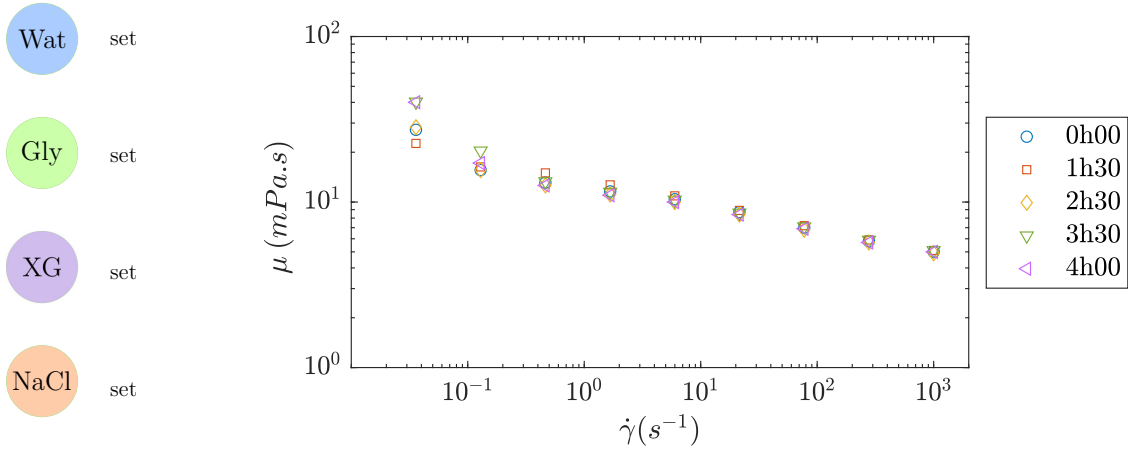


Figure 2.23: Dynamic viscosity versus shear-rate measurements on designed BMF candidates (optimal BMF formulation). BMF samples were collected in the reservoir throughout a 4 hours experiment with continuous looping on the mock loop. No degradation of the fluid shear-thinning properties were observed.

2.5.5 Discussion and limitations

The fabricated non-Newtonian BMF exhibits similar properties to human blood regarding shear-thinning behavior. However, there are some limitations in BMF measured dynamic viscosity.

Firstly, the range of accessible shear-rates is limited with the cone-plate rheometer, especially in the lower range. The device offers a good precision at shear-rates between 0.1 and 1000 s^{-1} but accuracy drops below 0.1 s^{-1} . Similar tests were conducted with a couette rheometer configuration below 0.1 s^{-1} , but results were as poor. Therefore, this measurement technique does not allow to study viscosity within this lower range of shear. Other types of rheometers allow to study this domain but in return, the high shear-rate domain precision decreases. Practically, knowledge of blood rheological behavior is also limited at very low shear-rates. The present references for HB viscosity were taken from studies which investigated the same range of shear-rates probably also because of rheometer limitations. Thus, hypothesis are formulated regarding out-of-range shear-rates. Many studies showed that HB reaches a Newtonian like plateau and viscosity tends to stabilize at very high (1000 s^{-1}) and very low shear-rates (0.01 s^{-1}) (Merrill and Pelletier (1967)). The viscosity shear-thinning behavior mainly occurs in the middle shear-rate range (0.1 to 1000 s^{-1}). The high viscosity limit is estimated around 100 mPa.s and the lower one around 3 mPa.s (Baskurt (2003)). Xanthan gum solutions are good candidates to replicate this plateau viscosity (especially at low shear-rates) but could not be measured in the present study. In line with xanthan gum studies from the literature with similar concentrations, our BMF should not exceed the 10^2 mPa.s order of magnitude in the low shear-rate domain (Najjari et al. (2016); Brookshier and Tarbell (1993); Whitcomb and Macosko (1978)). Regarding the upper shear values, the measured shear-rates (1000 s^{-1}) correspond to the maximum order of magnitude observed in human aortas (Sakariassen et al. (2015) and estimated from Cheng et al. (2003) with shear stress and blood viscosity).

Secondly, as mentioned in chapter 1, cone-plate rheometer shear conditions are different from aortic flow conditions. To remain in the same *ex vivo* conditions, the presented results on the BMF were compared with HB viscosity measurements carried out with rheometer. However, *ex vivo* measurements may not be directly applied to *in vivo* conditions (Baskurt (2003)). As an example, Thurston and Henderson (2006) investigated influence of flow geometry and viscometry tubes media on blood viscoelastic measurements and noted slight differences. *In vivo* active response of arterial walls and geometry bring influence RBCs mechanical solicitations and thus fluid viscosity. These processes are believed to be more important in small vessels and microvascular networks (same characteristic length than independent RBCs and rouleaux structures) but secondary in large arteries such as the aorta (Baskurt (2003)).

Finally, viscoelasticity was not investigated because of limitation in the rheometer oscillatory mode. Viscoelastic coefficients G' and G'' values are too low for the device precision. However, xanthan gum was chosen among other shear-thinning polymer for its limited viscoelastic contribution. Najjari et al. (2016) studied xanthan gum BMF viscoelastic properties under oscillating strain rate sweeps. Similar trends between HB and BMF are observed which comforts the use of xanthan polymer to fabricate such fluids.

A BMF was designed to mimic human blood shear-thinning properties and fulfill circulatory mock loop experiment requirements. It includes RI matching with the aorta phantom and preserved fluid properties along time and temperature variations. A rheology study was conducted on solutions containing water, glycerol, xanthan gum and NaCl to analyze each component's influence of the solution viscosity properties. An optimal BMF was designed with these ingredients to find a balance between faithful dynamic viscosity compared to human blood and RI matching for PIV measurements. The BMF RI is calibrated to match the silicone phantom of an abdominal aorta that will be used on the mock loop for PIV measurements.

2.6 Conclusion

An aortic flow simulator was designed with the purpose of mimicking and measuring physiological flows in an aorta phantom with fully artificial elements. The simulator is made up of 3 main elements : a circulatory mock loop, a blood mimicking fluid and adaptable aorta phantoms. A flow visualization technique — PIV — is implemented on this experimental bench to assess flows in the aorta phantom. The use of this technique involves optical access on the mock loop and transparency criteria on the working fluids and on the aorta phantom. The circulatory mock loop function is to recreate pulsatile flowrates and pressure as in the arterial circulation with accurate cycle frequency, amplitude and waveform. The blood mimicking fluid was designed to mimic the blood's shear thinning behavior while maintaining an acceptable refractive index to ensure reliable PIV computation. The fluid is a mixture of water, glycerin, xanthan gum and sodium iodine. Finally, an aorta phantom was manufactured with patient specific geometries. This AA silicone model has compliant walls and is the ideal aorta replica for such measurements regarding material transparency and Young's modulus. Unfortunately, the same technique and material could not be used for AD models because of their complex geometry. 3D printing techniques are much less limited by complex geometry models but is highly limited with available materials. Those 3D printed phantom will be presented in chapter 4 in the aortic dissection case study. However, the present chapter process still applies to those phantoms. All these elements make up the aortic flow simulator that can accommodate different shapes of aorta phantom (AA, AD, and other diseases), different types of fluid (Newtonian vs non-Newtonian BMF) and emulate different waveforms in cardiac cycles. Each element has its limitations in biofidelity regarding simplification : homogeneous mechanical properties, phantom geometry, fluid rheology (limited to the global viscosity behavior) and mock loop (restricted to the aortic circulation). We also neglect other vessel and organ influences (upstream, downstream and around the aorta). Knowing these limitations, next chapters focus on the experiments that were conducted on this experimental bench to observe and evaluate the influence of working fluid properties, phantom geometry, presence of pathologies, etc.

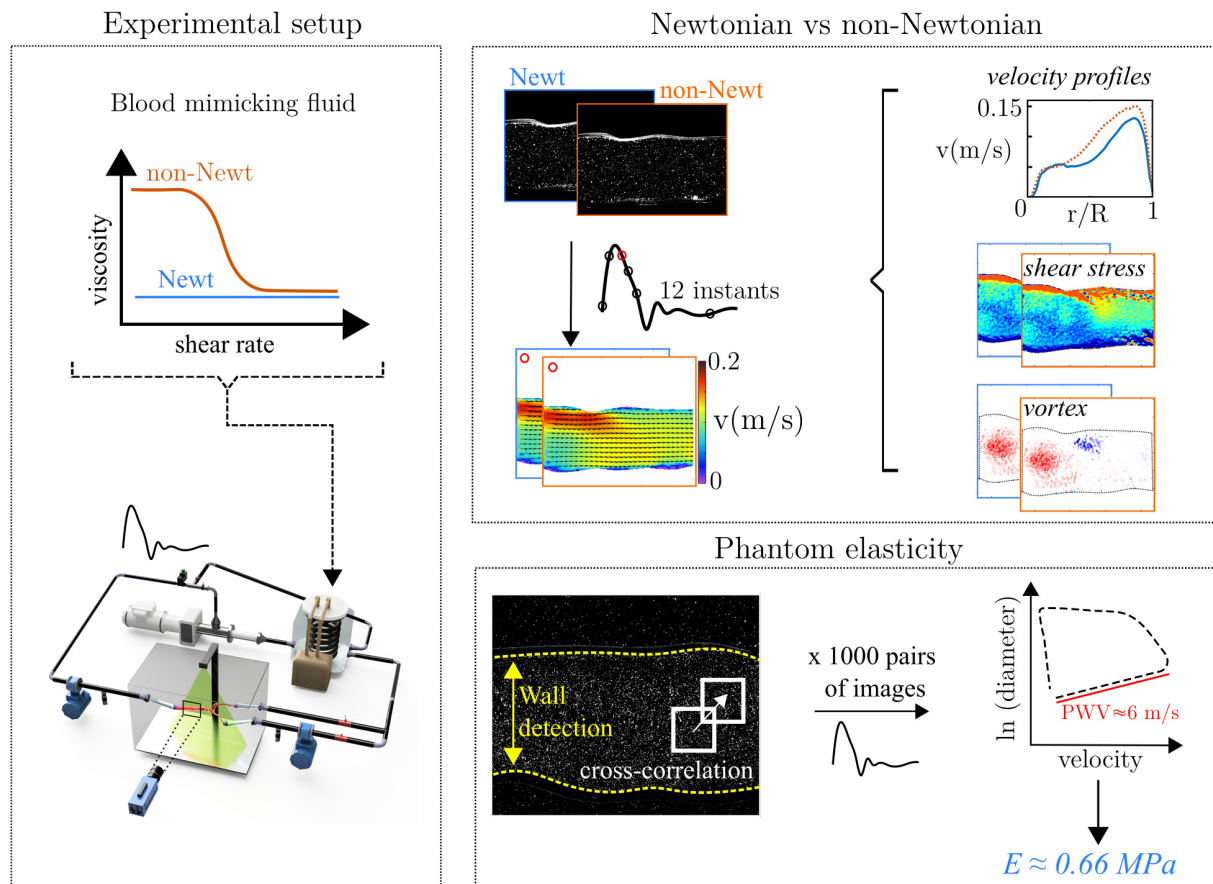
Abdonimal aortic flow with Newtonian and non-Newtonian blood mimicking fluid

Contents

3.1	Background	94
3.2	Materials and methods	96
3.2.1	Experimental setup	96
3.2.2	PIV measurements	98
3.2.3	Image post-processing	99
3.3	Newtonian vs non-Newtonian BMF: flow analysis	101
3.3.1	Wall displacement	101
3.3.2	Inflow conditions	101
3.3.3	Flow distribution	104
3.3.4	Vortex tracking	107
3.3.5	Shear rates and shear stresses	110
3.4	Discussion	113
3.4.1	Related geometry flow distribution	113
3.4.2	Limitations	114
3.4.3	Newtonian versus non-Newtonian representation	115
3.5	Phantom performances : pressure wave velocity and elasticity	116
3.5.1	The lnD-V method	116
3.5.2	PWV and elasticity evaluation with PIV	117
3.5.3	Limitations	121
3.6	Conclusion	122

Abstract

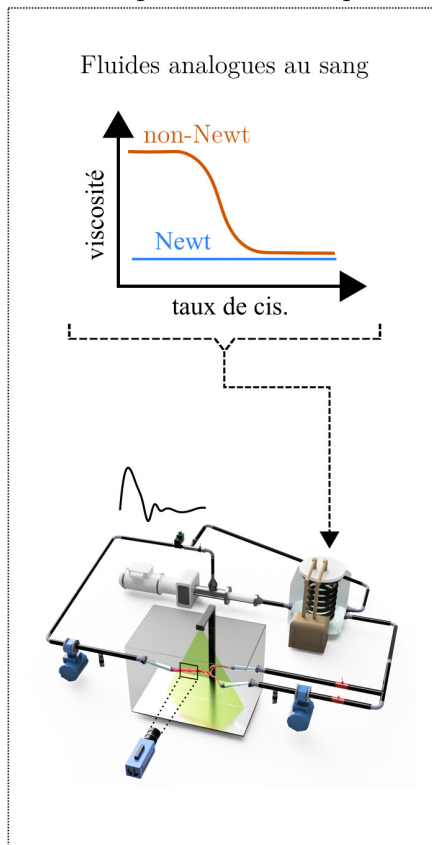
The developed circulatory mock loop is tested on an abdominal aorta phantom with a realistic geometry and compliant walls. Newtonian and non-Newtonian blood mimicking fluids are often considered equivalent in *in vitro* mock loop experiments for large arteries. However, these are mostly carried out in simplified aortic models with rigid walls. In the present study, a comparison between Newtonian and non-Newtonian blood analogues is achieved on the current mock loop under pulsatile conditions and with our more realistic abdominal aorta phantom. Velocity profiles, shear stresses and vortex rings trajectories highlight stronger preferential flow path and asymmetries in the non-Newtonian case. These features are observed in diameter narrowing region of the phantom due to natural curvatures of the model (not related to a pathology). In those types of complex geometry phantom, the Newtonian assumption appears unsuitable as it underestimates the complexity of flow distribution, extreme shear stress regions and wall shear stress magnitude (twice lower in the Newtonian case). In the context of understanding disease mechanism this simplification may lead to misinterpretation of risky areas. The non-Newtonian BMF is thus adopted for the mock loop. Finally, these experiments are used to evaluate the mock loop and phantom performances regarding cycle-to-cycle reproducibility, phantom wall mechanical response to pulses, pressure wave velocity and material elasticity. These features are quantified and appear in good accordance with *in vivo* data which makes the bench an interesting *in vitro* tool to mimic and analyze aortic flows with the scope of studying pathological cases.



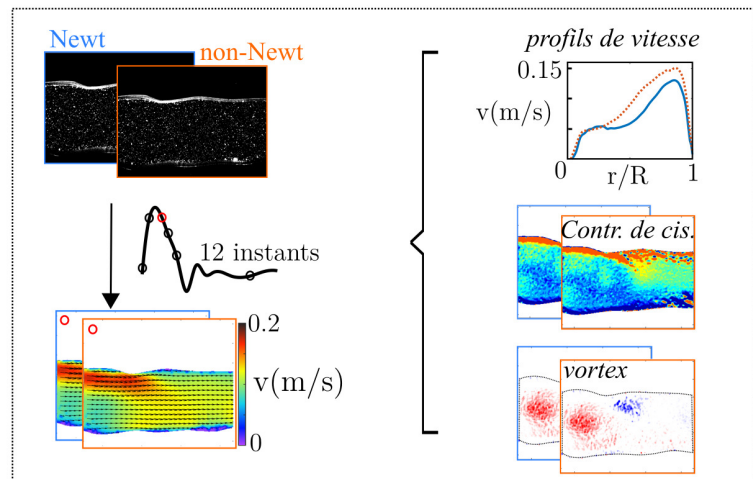
Résumé

Le simulateur d'écoulement aortique est testé sur un fantôme d'aorte abdominale dont la géométrie est réaliste et les parois souples. Les fluides analogues au sang Newtonien et non-Newtonien sont souvent considérés comme équivalents dans les expériences de simulateur *in vitro* sur les artères de large diamètre. Néanmoins, ces expériences sont le plus souvent réalisées sur des modèles simplifiés de tubes droits à parois rigides. Dans cette étude, une comparaison entre fluide Newtonien et non-Newtonien est menée sur le banc expérimental et sous conditions d'écoulements pulsés dans notre modèle d'aorte plus réaliste. Les profils de vitesses, les contraintes de cisaillement et les déplacements de tourbillons montrent des chemins préférentiels d'écoulements et des asymétries plus marqués dans le cas non-Newtonien. Ces phénomènes sont observés dans une région du fantôme avec réduction du diamètre due aux courbures naturelles de l'aorte (non pathologiques). Sur ce type de géométrie, l'hypothèse Newtonienne semble inadaptée car elle sous-estime la complexité de la distribution des écoulements et des contraintes de cisaillements ainsi que l'amplitude des contraintes aux parois (deux fois plus faible dans le cas Newtonien). Dans le contexte de la compréhension des mécanismes conduisant aux maladies cardiovasculaires, cette simplification peut notamment conduire à une mauvaise interprétation des zones à risques. L'hypothèse non-Newtonienne est donc adoptée pour le banc expérimental. Enfin, ces expériences sont utilisées pour évaluer les performances du banc concernant la reproductibilité cycle-à-cycle, la réponse mécanique du fantôme aux écoulements pulsés, la vitesse de l'onde de pouls et l'élasticité du matériau. Ces aspects sont quantifiés et semblent en accord avec les données *in vivo*, ce qui fait du banc un outil *in vitro* intéressant pour reproduire et analyser les écoulements aortiques dans l'optique d'étudier des cas pathologiques.

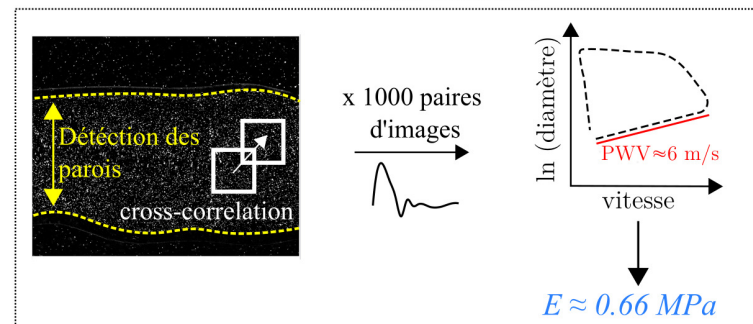
Experimental setup



Newtonien vs non-Newtonien



Elasticité du fantôme



3.1 Background

Over the past decade, aorta hemodynamics studies have grown considerably with the purpose not only of improving treatments but also of preventing disease by understanding their development mechanisms. Vortical flows, wall shear stresses, and modification of vessel wall mechanical properties are among the main factors that could explain the results of aortic diseases such as aneurysm and aortic dissection (Bürk et al. (2012); Kolipaka et al. (2017)). *In vivo*, these characteristic investigations have shown some limitations regarding invasive measurement methods, and insufficient spatial and temporal resolutions of medical imaging techniques. To overcome these limitations *in vitro* and *in silico* approaches were developed to recreate hemodynamical environments while controlling physiological conditions, circulating fluid, and aorta material properties. *In vitro* studies allow the use of high-resolution flow visualization techniques with fewer restrictions than invasive measurement probes and the ability to conduct reproducible experiments. Particle Image Velocimetry (PIV) (Deplano et al. (2007); Najjari and Plesniak (2016); Büsen et al. (2017)) and 3D-Particle Tracking Velocimetry (Gülan et al. (2012)) have been used in hemodynamics studies to provide high spatial resolution (under $1 \times 1 \text{ mm}^2$) to complement *in vivo* observations. In the case of blood flow *in vitro* simulators, the main difficulty is to recreate aortic flows with complex features: realistic aorta geometry, aortic wall compliance (Deplano et al. (2007)), blood non-Newtonian behavior (Deplano et al. (2014); Walker et al. (2014)), and faithful pulsatile flow conditions (Thirugnanasambandam et al. (2021)). Each of these characteristics plays a major role in hemodynamical flows. The challenge lies in combining them in a single experiment.

Many circulatory mock loops have been designed to emulate human circulation (Kung et al. (2011); Thirugnanasambandam et al. (2021)) and recent research mainly focuses on improving biofidelity of *in vitro* simulators with patient custom features. Franzetti et al. (2019) and Bonfanti et al. (2020) developed an *in vitro* circulatory mock loop for aortic dissection investigations and compared it to numerical simulations. Their aorta geometry was extracted from Computed Tomography scans (CT) and custom Windkessel models were implemented to meet the patient's *in vivo* conditions. In addition, their aorta phantom was a rigid model and the working fluid was a Newtonian blood analog. A large majority of *in vitro* (and *in silico*) studies used a Newtonian representation for blood and did not consider the shear-thinning behavior (Yousif et al. (2011); Büsen et al. (2017)) claiming that blood Newtonian assumption is acceptable in large vessels such as the aorta. Deplano et al. (2014) analyzed the influence of shear-thinning properties on vortex rings propagation in an idealized model of aortic aneurysm. They showed that the Newtonian fluid tended to overestimate vortex ring velocity and travel distance compared to the shear-thinning case. Non-Newtonian blood analogs are therefore, more reliable to realistically mimic aortic hemodynamical flows, at least in certain specific geometries and conditions.

In vitro studies with non-Newtonian blood analog are emerging but most of them are conducted on idealized and rigid models such as curved channels (Najjari and Plesniak (2016)) representing the aortic arch or straight partially occluded tubes for stenosed arteries (Walker et al. (2014)). Realistic aorta models with compliant walls are still lacking

while these features could make the difference in biofidelity. This lack is mainly due to the difficulties in manufacturing such models when considering geometry complexity, material waterproof, need for transparency for optical techniques, and mechanical properties (Yazdi et al. (2018)). Usable materials and manufacturing options are limited to some silicone molding techniques (Hütter et al. (2016); Büsen et al. (2017)) and a few 3D printing resins.

Table 3.1: Summary of *in vitro* arterial flow studies with specific features regarding phantom geometry, wall properties, and blood mimicking fluids.

Newtonian BMF		
Geometry/Walls	Rigid	Compliant
Idealized - Standardized	Deplano et al. (2007)	Deplano et al. (2007)
	Walker et al. (2014)	Kung et al. (2011)
	Najjari and Plesniak (2018)	Deplano et al. (2014)
		Najjari and Plesniak (2018)
Anatomical	Stamatopoulos et al. (2011)	
	Schirmer and Malek (2007)	Gölan et al. (2012)
	Bonfanti et al. (2020)	Büsen et al. (2017)
	Franzetti et al. (2019)	Thirugnanasambandam et al. (2021)
	Zimmermann et al. (2021)	Zimmermann et al. (2021)
Non-Newtonian BMF		
Geometry/Walls	Rigid	Compliant
Idealized - Standardized	Gijsen (1999)	
	Schirmer and Malek (2007)	
	Anastasiou et al. (2012)	Deplano et al. (2014)
	Walker et al. (2014)	Deplano et al. (2016)
	Najjari and Plesniak (2016)	
Anatomical	x	x

To the author's knowledge, no study has combined *in vitro* **pulsatile flow mock loop**, **patient-specific aorta phantom**, **compliant walls**, and **non-Newtonian blood mimicking fluid** (table 3.1). Some of the previously cited studies investigated the impact of experimental features simplification and showed the necessity of realistic geometries and fluid-wall interactions brought by the compliance (Deplano et al. (2007); Perktold et al. (1994); Zimmermann et al. (2021)). The **non-Newtonian fluid necessity** is however more controversial as contradictory results emerged from different studies (Deplano et al. (2014); Bonfanti et al. (2020)). To address these shortcomings, a circulatory mock loop was designed to mimic aortic pulsatile flows in a compliant aorta phantom with an anatomically accurate geometry. A blood mimicking fluid with shear-thinning

properties was used to replicate blood viscosity. It was compared with a reference Newtonian blood analog (design described in chapter 2). In this chapter, flow velocity fields were assessed with PIV technique for different cardiac cycle instants. Analysis of velocity profiles, shear rate, and shear stress distributions highlight the differences between Newtonian and non-Newtonian fluid flows in an aortic region with slight diameter variation (14.4% narrowing). Finally complementary results on wall displacements and responses to pulsatile flows allow to evaluate the compliant phantom performances and limitations. The goal is to address two main questions regarding the mock loop performances :

- Are the Newtonian and non-Newtonian BMF equivalent in this type of hemodynamical flow study ?
- How does the designed compliant silicone phantom behave under pulsatile flow ?

3.2 Materials and methods

3.2.1 Experimental setup

In this chapter, the experimental setup is the same as the one described in chapter 2. Two Regions of Interest (ROI) in the aorta phantom are chosen to analyze flow and wall displacements under pulsatile conditions (figure 3.1). The aim is to recreate physiological conditions regarding flowrate and pressure thanks to the mock loop setup. The solenoid valve was programmed to recreate the flowrate waveform from [Cheng et al. \(2003\)](#) (MRI data in the infrarenal region of human subjects under resting conditions). The targeted mean and maximum inlet flowrates were equal to $Q_{\text{mean}} = 1.70 \text{ L/min}$ and $Q_{\text{max}} = 5.80 \text{ L/min}$ respectively. The cycle period was set to $T = 0.800 \text{ s}$. Outlet pressure varied between 90 and 135 mmHg during a cardiac cycle. Two regions of interest are imaged with different purposes :

- **ROI_main** is the main region of interest for this study. It is located in the main trunk of the abdominal aorta in a region with slight "natural" geometrical features: a local narrowing in diameter of 14.4% and non-straight region in the longitudinal axis. Imaging this region avoids falling in the "straight tube" usual experiment and to take into account aortic shape on a healthy region. Note that the risk is to have some out-of-plane flow which cannot be fully described by 2D-2C-PIV.
- **ROI_down** is located downstream from ROI_main in a straighter region of the aortic trunk. This region was imaged as a reference straight area with limited out-of-plane flow compared to ROI_main. This region is used for flow/wall relationship investigations.

Two sets of experiments are conducted to compare BMF options. A first set was conducted with the Newtonian BMF while the second set was achieved with the non-Newtonian BMF. The two fluids design were described in chapter 2 and figure 3.2 shows fluid viscosity characteristics. The fluid flows comparison is achieved in ROI_main and depending on the conclusion on each fluid's relevance, following experiments will be carried

out with the more suitable one. The ROIs, PIV equipment configuration and experimental goals are illustrated in figure 3.1 and described in table 3.3. To ensure consistent fluid flows comparison, the two sets of experiments are conducted under the same inflow conditions and PIV imaging parameters. Experimental reproducibility is addressed in the following parts to quantify uncertainties of computed flow fields.

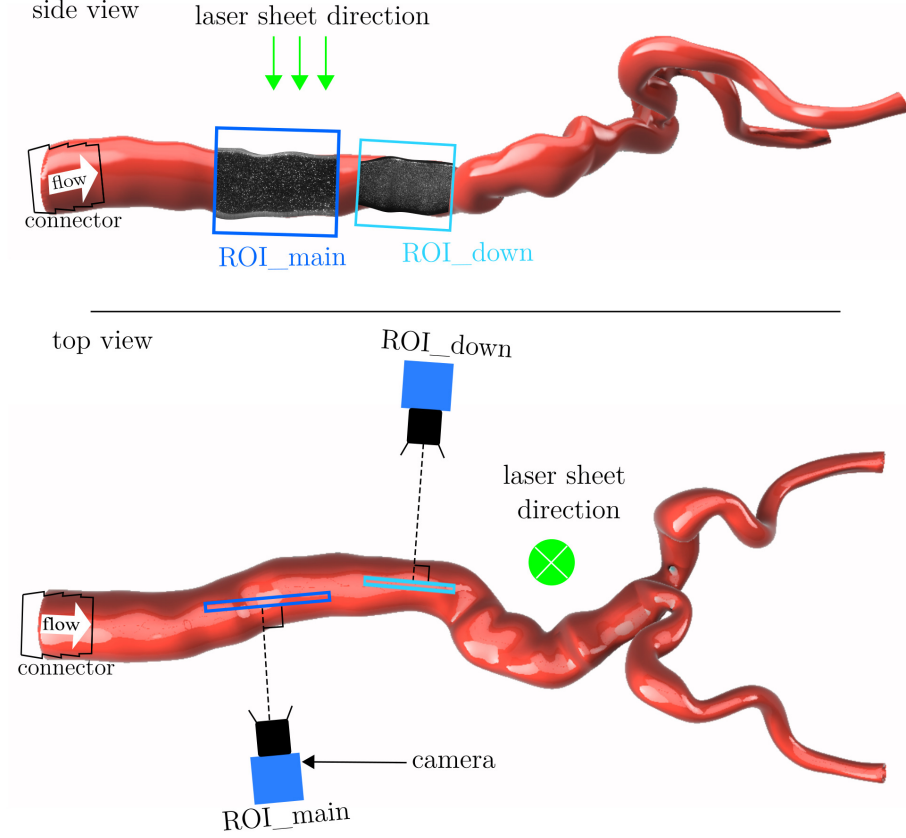


Figure 3.1: Top and side view of the aorta phantom with the two ROI.

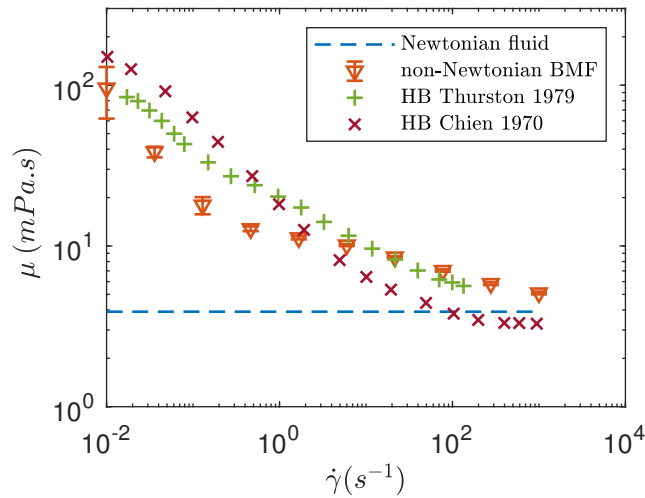


Figure 3.2: Measurement of dynamic viscosity as a function of shear rate for the Newtonian and the non-Newtonian fluids. Comparison with human blood references from [Thurston \(1979\)](#) and [Chien \(1970\)](#).

3.2.2 PIV measurements

PIV imaging is achieved with the setup and characteristics described in chapter 2. Two types of measurements are conducted :

- **Synchronized imaging with fixed instants in cycle:** this mode allows to adjust PIV imaging with particular position in the imposed cycle by the solenoid valve. As described in chapter 2, for each targeted cycle instant a series of N images are shot at this exact instant to compute velocity fields with a good statistical convergence. The limitation of this synchronized mode is the large number of cycles that have to be reproduced to shoot the N images for each targeted cycle instant. The frame frequency is also limited in the synchronization mode. Parameters and imaged cycle instants are provided in table 3.2.

Table 3.2: PIV synchronization parameters to image 12 cycle instants (ROI_main).

Cycle instant “k”	1	2	3	4	5	6	7	8	9	10	11	12
Cycle time (ms)	0	50	100	150	200	250	300	350	400	500	600	700
Δt (ms)	5	3	3	3	3	4	5	6	6	7	8	4
Number of acquired images/cycles	500	500	500	500	500	500	500	500	500	500	500	500
Total number of acquired cycle/images	6000											

- **Random imaging along cycles:** this mode allows to shoot images with a framerate up to 10 Hz (every 100 ms). Images are thus, randomly shot throughout cycles and synchronization is not ensured. Still, this mode gives clues on flow patterns with successive snapshots closer in time. Each snapshot velocity field is computed individually with no statistical treatment.

Table 3.3: ROI corresponding experiments configurations.

ROI	ROI_main	ROI_down
Location	Aortic trunk (slight narrowing and curvature)	Aortic trunk (straight region)
Objectives	Compare Newtonian and non-Newtonian fluid flows	Compute wall displacements and PWV
BMF	Newtonian non-Newtonian	non-Newtonian
PIV mode	Synchronized	Random

3.2.3 Image post-processing

Wall detection and masks

As the phantom walls are compliant, the ROI area varies throughout the cardiac cycle. Therefore, special image processing has to be applied to take into account this ROI change. First, image post-processing consisted in detecting the phantom compliant wall positions for each image. Walls were detected and tracked with threshold and morphological closing algorithms thanks to an in-house MATLAB script. When focusing on one cardiac cycle instant, data were averaged on the N images of each cycle instant to obtain the corresponding average wall positions. This script provides aorta walls coordinates and inner and outer diameter variations throughout the cardiac cycle.

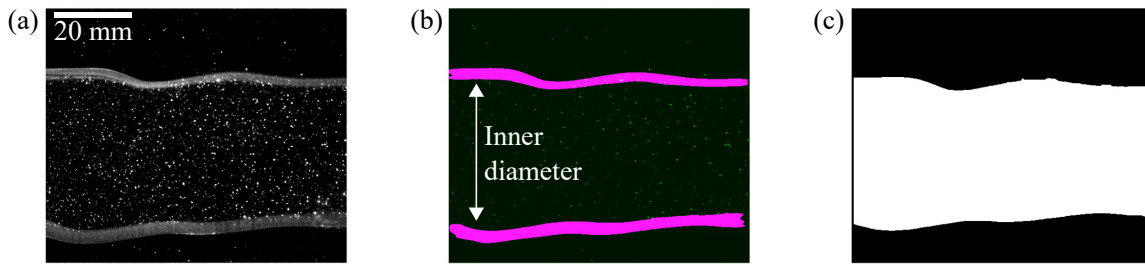


Figure 3.3: Example of wall detection and masking steps for one PIV image. (a) Particles image with enhanced contrasts to highlight the phantom walls, (b) wall detection with thresholding to select walls gray scale value, (c) corresponding generated binary mask for cross-correlation. The definitive mask for each cycle instant is a mean mask of the N images per instant.

In addition, the script generates binary masking images for each cardiac instant based on average wall position. The purpose is to isolate the ROI by activating pixels inside the aorta phantom (where particles flows, white area) and by de-activating phantom walls and the dark background (figure 3.3). These masks are then used to limit the cross-correlation computation to the ROI without calculating on walls and background with the correct ROI for each cycle instant.

Cross-correlation and vector fields accuracy

Images are then processed with Davis 10 software (Davis10 (2017), LaVision) to compute vector fields. Images are masked out with the pre-computed masks as described above to deactivate non-interesting pixels: background and vessel walls. Image cross-correlation is performed with a multipass method on the non-masked area limited to the aorta lumen. The first pass is achieved with a initial 64x64 pixels interrogation window with an ellipsoid weight (long axis in the flow main direction x) and without overlap. The second and third pass consist of 32x32 pixels interrogation windows with a round Gaussian weight and 75% overlap. For each field, missing vectors (less than 1% of computed vectors) are filled up with a polynomial interpolation algorithm and a 3x3 smoothing filter is applied. The

final resolution of vector fields is $0.95 \times 0.95 \text{ mm}^2$ (about 0.6% of the aorta cross-sectional area in the ROI). 400 images are needed to reach velocity field statistical convergence in the worth case scenario (figure 3.4). When considering mean velocity fields from a whole set of 500 images to ensure statistical convergence, velocity uncertainties are provided in table 3.4. In figure 3.4, the evolution of the mean velocity is represented on the whole ROI (left) and on a specific interrogation window of the ROI as a function of N. N is the number of images that were taken into account to compute the mean velocity.

Finally, vector field post-processing is performed with a custom MATLAB script to compute and analyze quantities of interest (shear rate, shear stress, swirling strength, etc.).

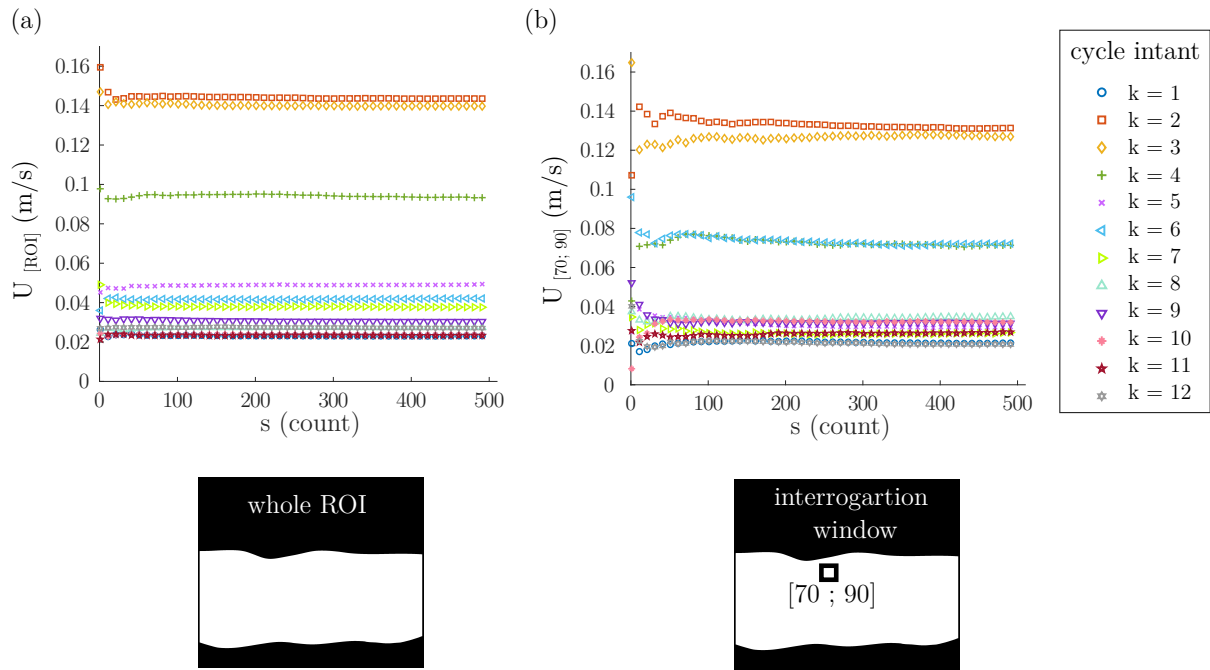


Figure 3.4: Statistical convergence graph of mean velocity per cycle instant "k" (a) in the whole ROI and (b) in an interrogation window (coordinates $[x_{\text{window}}; y_{\text{window}}] = [70; 90]$). In the whole ROI, 50 to 100 images are required to reach velocity statistical convergence. In the interrogation window, from 200 to 400 are needed depending on the cycle instant. s (count) is the number of images taken into account for mean velocity calculation.

Table 3.4: Mean and maximum uncertainties computed on the whole set of PIV images. Maximum error corresponds to the worth case error among the interrogation windows.

Fluid flow	Mean error (m/s)	Maximum error (m/s)
Newtonian	7.10^{-4}	5.10^{-3}
Non-Newtonian	8.10^{-4}	4.10^{-3}

3.3 Newtonian vs non-Newtonian BMF: flow analysis

3.3.1 Wall displacement

Thanks to the wall detection algorithm, the mean diameter for each of the 12 cycles instants was computed. Table 3.5 shows both fluid experiment diameter characteristics. The minimum diameter is observed at $k = 0$ (0 ms), while the maximum diameter is observed at $k = 6$ (250 ms). According to [Sonesson et al. \(1994\)](#), the observed range of diameter changes (here 0.92 ± 0.10 mm for the Newtonian and 1.2 ± 0.15 mm for the non-Newtonian experiment) are consistent with a 53 - 69 years old male patient. Indeed, having a phantom with realistic stiffness as described in chapter 2 does not guaranty realistic wall displacement under physiological pulsatile flow conditions. Therefore, these results in wall displacement throughout a cardiac cycle comfort the choice of silicone material to mimic the aorta in such circulatory mock loop.

Table 3.5: Diameters from PIV images for the Newtonian and the non-Newtonian fluid flow experiments.

	Newtonian (n = 500)		Non-Newtonian (n = 500)	
	Mean (mm)	Standard deviation (mm)	Mean (mm)	Standard deviation (mm)
Minimum diameter (D0)	31.03	0.04	34.21	0.06
Maximum diameter	31.95	0.06	35.42	0.09
ΔD along cycle	0.92	0.10	1.20	0.15

3.3.2 Inflow conditions

To make a comparison between the Newtonian and the non-Newtonian fluid flow experiments, inflow conditions should be sufficiently similar so flow differences could be attributed to fluid choice and not to experimental instabilities or lack of reproducibility. It concerns inter-experimental and intra-experimental conditions stability and cycle-to-cycle reproducibility. Flow conditions control comparison was achieved between the Newtonian and non-Newtonian experiments with a consistent match between flowrates, pressure, peak Reynolds (equation 3.3.1) and Womersley (equation 3.3.2) numbers (table 3.6).

$$Re_{peak} = \frac{\rho D_{peak} V_{peak}}{\mu} \quad (3.3.1)$$

$$\alpha = D \sqrt{\frac{\omega \rho}{\mu}} \quad (3.3.2)$$

D_{peak} and V_{peak} are the mean aorta diameter and velocity at the systolic peak, D is the aorta mean diameter throughout a cycle, and $\omega = 1/T$ is the pulse period. Viscosity μ is taken as equivalent high shear rate viscosity in the non-Newtonian case (highest shear-rate viscosity measured with the rheometer, $\mu = 5.2 \text{ mPa.s}$). The cycle-to-cycle mean and standard deviation quantities were calculated over the 6000 cycles recorded along the PIV measurements (figure 3.5). ¹.

Table 3.6: Newtonian and non-Newtonian flow experiment parameters. Reynolds and Womersley numbers were calculated with equivalent viscosity at high shear rate for the non-Newtonian case (asymptotic viscosity). The peak Reynolds number was calculated with systolic peak diameter and velocity data. Data are provided with their standard deviations computed over the 6000 cycles.

	Newtonian	Non-Newtonian	Difference
Density, ρ [kg.m-3]	1146	1146	0 %
Viscosity, μ [mPa.s]	3.9	5.2	33.3 %
Flow conditions			
Mean inlet flowrate, $Q_{\text{in mean}}$ [L/min]	1.69 ± 0.44	1.73 ± 0.44	0 %
Maximum inlet flowrate, $Q_{\text{in max}}$ [L/min]	5.57 ± 0.30	5.80 ± 0.37	3.96%
Min outlet pressure, $P_{\text{out min}}$ [mmHg]	89.58 ± 2.40	90.12 ± 2.67	0.60%
Max outlet pressure, $P_{\text{out max}}$ [mmHg]	139.46 ± 2.87	139.23 ± 3.60	0.16 %
Peak Reynolds number, Re_{peak}	1200 ± 2	1129 ± 2	6.2 %
Womersley number, α	15.3	14.6	4.8 %

Note that the flowmeters only integrate positive flowrates which do not allow to visualize the backflow and diastolic phases. Moreover, there is a time lag between observed inlet and ROI pulse (70 cm distance) due to the transit time of the pulse. The aortic wall compliance generated backflows that were observed on the PIV images but not with the inlet flowmeter. Therefore, aorta ROI flowrate was estimated with PIV measurements, the aorta diameter variations along the cycle, and the hypothesis of a circular cross-section (figure 3.6). The systole magnitude was consistent with inlet flowmeter measurements

¹These 6000 (12*500) cycles correspond to the 12 cycle instants successively measured with 500 images each. As explained in chapter 2, the synchronization mode works by taking one image per cycle. A total of 6000 successive cycles are thus needed to measure the 12 instants.

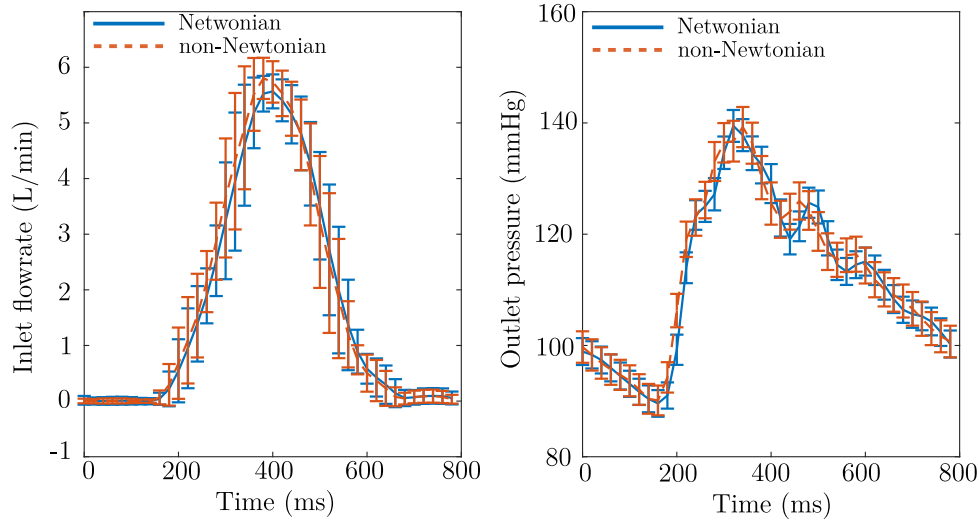


Figure 3.5: Newtonian and non-Newtonian experiments flowrate (left) and pressure (right) conditions. Lines represent mean values calculated throughout the 6000 successive cycles of the PIV imaging process for each fluid flow experiment. Error bars correspond to the standard deviation at each point throughout the 6000 cycles (cycle-to-cycle reproducibility). Data were recorded every 20 ms and the cycle period is $T = 800$ ms.

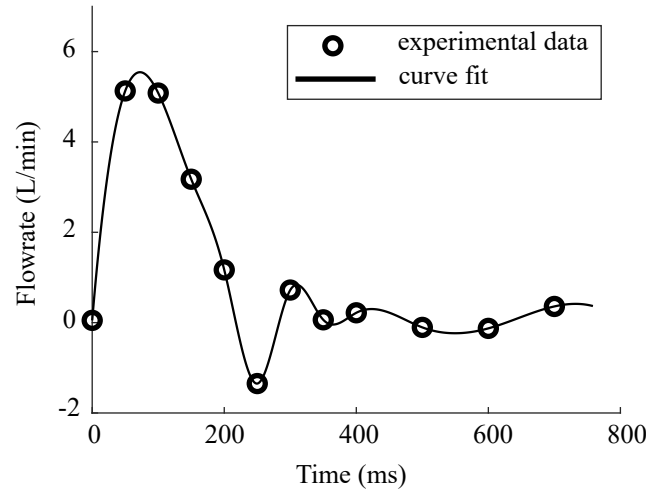


Figure 3.6: Estimation of flowrate in the aorta ROI from PIV velocity fields and aorta diameter. The circles correspond to PIV image recorded instants. This time the diastolic phase is visible compared to figure 3.5 because the computation is not limited by the flowmeter abilities. In this case PIV allows to visualize negative flow and does not integrate the signal over time.

(figure 3.5). The cycle is the reference cycle regarding time and phases for the following analysis as it corresponds to observations in the ROI.

Slight differences are observed between the two experiments inflow conditions and in cycle-to-cycle reproducibility. A large number of cycles and PIV images are needed to

reach statistical convergence of computed velocity fields and thus, decrease uncertainty which are satisfying for the current experiments. Now errors were quantified, we may analyze differences between fluid flow experiments and determine whether or not these differences are attributed to experimental uncertainty.

3.3.3 Flow distribution

PIV images were computed to draw mean velocity fields at specific cycle instants for both fluid flow experiments. Comparison between these maps allows to highlight similarities and differences in the Newtonian and the non-Newtonian cases in the same ROI with comparable inflow and boundary conditions.

Velocity fields and profiles for the Newtonian and non-Newtonian BMF are presented at 4 distinct cycle instants numbered with k indexes ($k = 2, 4, 6, 10$): near systolic peak, systole deceleration, backflow transition, and diastole (figure 3.7). The complete set of velocity fields for the 12 cycles instants that were chosen to describe the cycle, is provided in appendix D. Here, we have chosen to focus on 4 representative cycle instants. The computed fields provide a general overview of flows while profiles give a more detailed view which allows to quantify similarities and differences. Thus, velocity profiles are drawn for three locations (profiles a, b, and c) of the aorta phantom ROI (figure 3.8). We observe that both flows exhibit the same velocity trends with a strong asymmetry. At first glance, the non-Newtonian fluid flow showed higher velocity extrema on profiles. To evaluate the mean difference between the two profiles, a normalized root mean square error is calculated with equation 3.3.3.

$$NRMSE = \frac{\sqrt{\sum_{i=1}^N (u_{x,i}^{newt} - u_{x,i}^{non-newt})^2}}{\sum_{i=1}^N \frac{u_{x,i}^{newt} + u_{x,i}^{non-newt}}{2}} \quad (3.3.3)$$

with $u_{x,i}^{newt}$ and $u_{x,i}^{non-newt}$ Newtonian and non-Newtonian velocity profiles respectively. N is the number of points on the profile line ($N = 100$). This error is normalized by the mean velocity between Newtonian and non-Newtonian profiles at each specific instant k .

Note that the observed difference exceeds the uncertainty of velocity fields provided in table 3.4. Therefore, fluid flow velocity profiles differences cannot be attributed to the computed velocity errors. The velocity difference was particularly high at the diastolic phase (higher than 200% difference) where a flatter profile is observed for the Newtonian case. When analyzing velocity fields for the same 4 cycle instants (figure 3.7), a high-velocity path is observed at $k = 2$ and $k = 4$ for both fluid flows. This preferred trajectory seems to be directed by the aorta curvature on upper wall ($y/D = D$ on profiles figure 3.8) with a narrowing in diameter (path arrow on maps figure 3.7). This narrowing corresponds to a decrease of 14.4% in diameter compared to the ROI entrance. Backflow is observed on $k = 6$ and seems to oppose this high-velocity path resulting in a low axial velocity region. At post-systole ($k = 6$ and $k = 10$), a preferred backflow path arises along the lower wall in figure 3.7 ($y/D = 0$ on profiles figure 3.8). Finally, swirling structures appear near the top wall. During diastole, these structures are pushed down by the higher velocity path

for the non-Newtonian fluid while their displacement is limited in the Newtonian case. The next section focuses on quantifying those observations with vortex locations, travel distances and velocities.

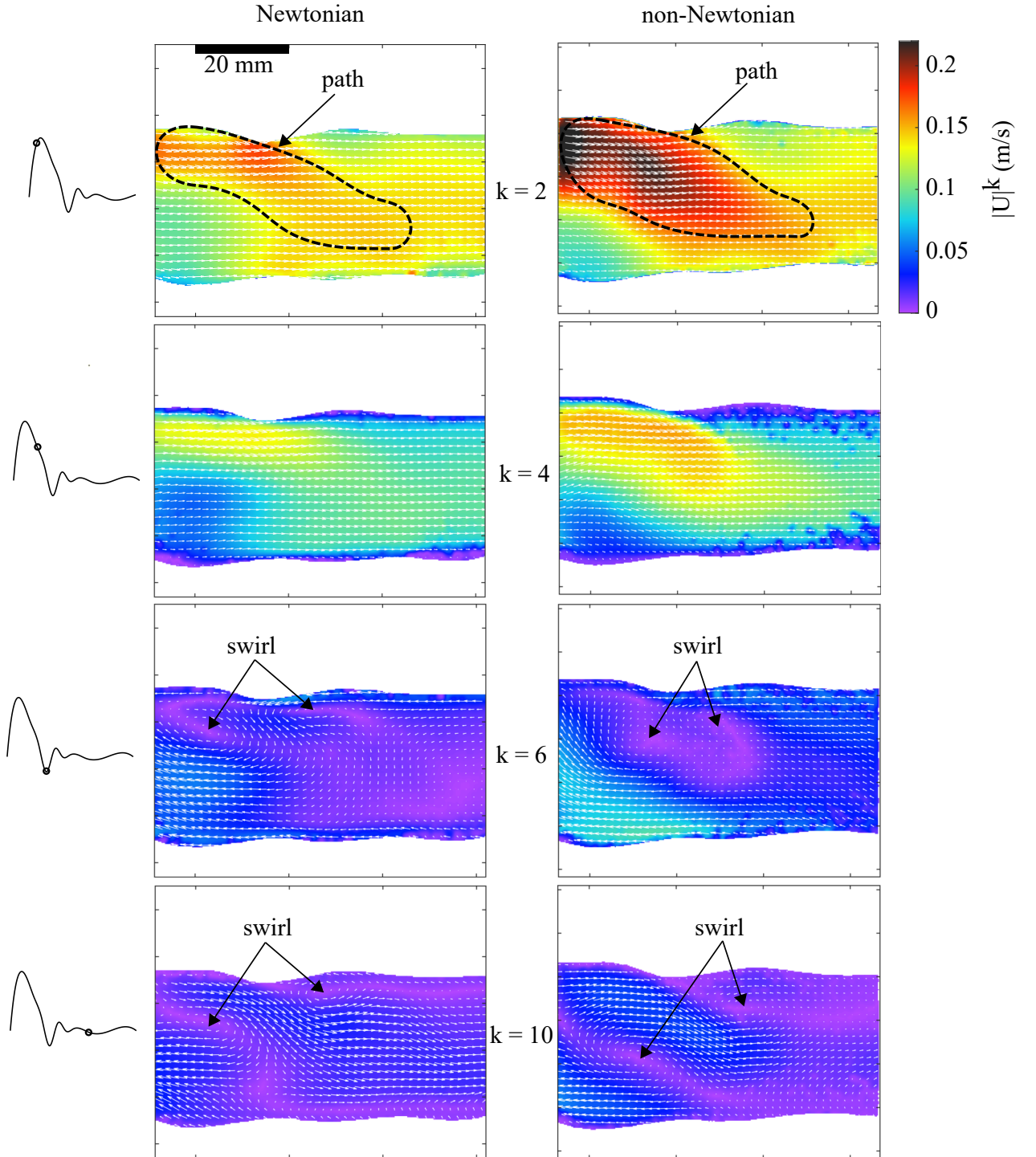


Figure 3.7: Velocity fields for the Newtonian (left) and the non-Newtonian (right) fluids at four cycles instants ($k = 2, 4, 6$ and 10). Each instant field is a mean velocity field from the 500 PIV images at the corresponding instant.

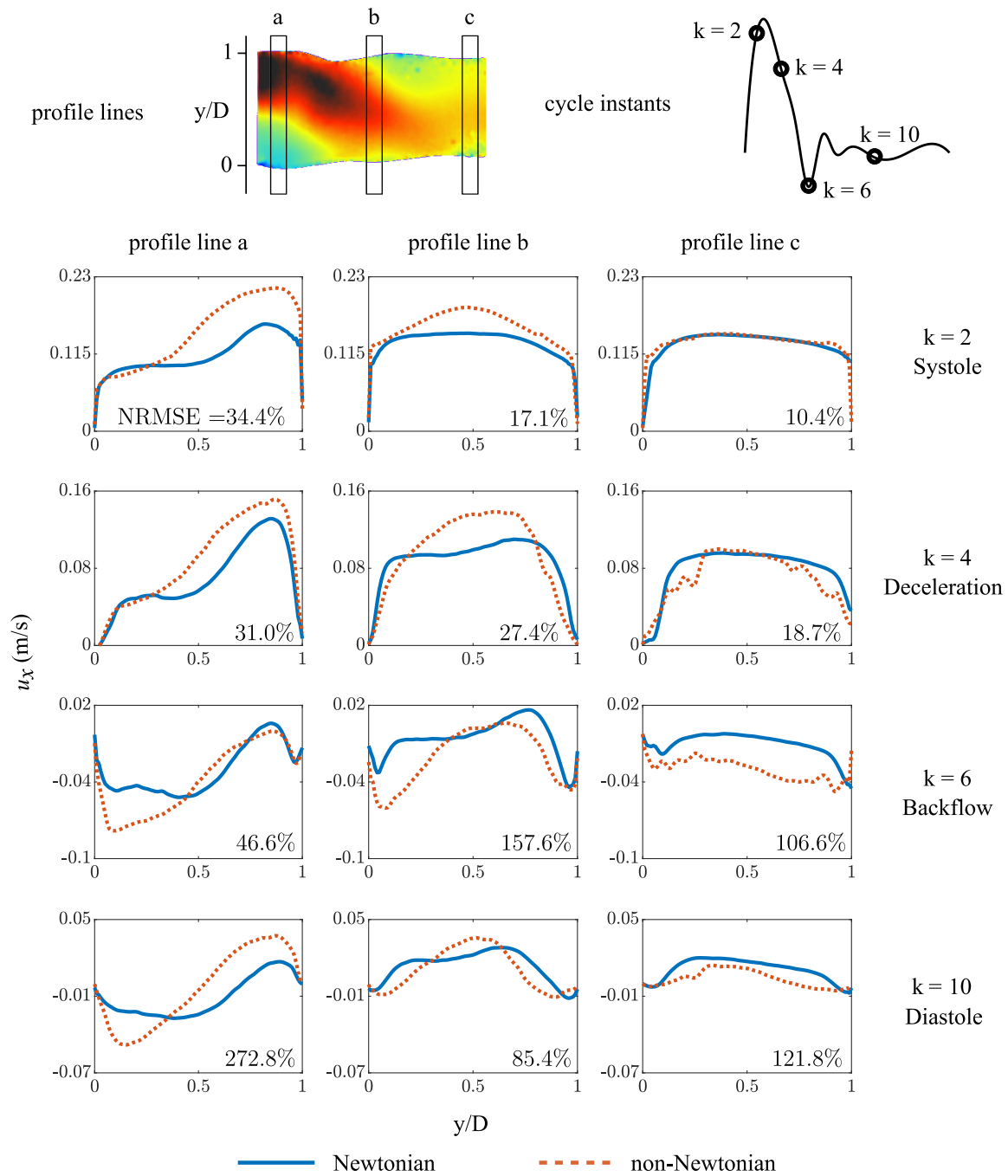


Figure 3.8: Velocity profiles for the Newtonian and non-Newtonian fluids at three locations of the aorta ROI. Corresponding instants are drawn on the flowrate curve. The circles correspond to recorded instants with PIV images. Normalized root mean error from equation 3.3.3 is indicated at the bottom right side of each profile. Each velocity profile is computed on 500 PIV images shot at the same instant.

3.3.4 Vortex tracking

In both fluid flow experiments, swirling structures are observed near the upper wall. They do not emerge and travel the same way in the Newtonian and in the non-Newtonian experiments. To detect and track them, swirling strength is computed thanks to the method described in [Chen et al. \(2018\)](#) (first proposed in [Zhou et al. \(1999\)](#)). This technique has proven to be efficient in wall turbulence flows and is applied here in the 2D plane ROI_{down}. The goal is to identify common characteristics and differences in vortices behavior between the two fluid flow experiments. Swirling strength λ_{ci} is defined as the imaginary part of complex eigenvalues of the velocity gradient tensor. It is a good indicator of rotational flow to detect vortices. In this case, direct computation of the vorticity quantity did not provide satisfying results on the detection and precise location of the swirling structures because of shear flow. This point is discussed with more details on the λ_{ci} and vorticity methods in appendix E. Therefore, we choose to use the swirling strength method ([Chen et al. \(2018\)](#)).

Let us consider the plane XY as the PIV imaged plane with Z the normal axis. The quantity Λ_{ciXY} from equation 3.3.4 is calculated on the whole ROI to locate swirling patterns. λ_{ci} is related to the intensity of swirling structures but does not provide information about the rotational sens. Therefore, we use the sign of the vorticity ω_z to determine the vortex rotation sense ([Tomkins and Adrian \(2003\)](#); [Chen et al. \(2018\)](#)).

$$\Lambda_{ciXY} = \lambda_{ciXY} \frac{\omega_z}{|\omega_z|} \quad (3.3.4)$$

Each map results from the mean velocity field computed on the 500 images of the corresponding instant. Two major vortices are clearly identified in the ROI: a central vortex rotating in the clockwise direction ($\Lambda_{ciXY} > 0$) and a near-wall vortex rotating in the counter-clockwise direction ($\Lambda_{ciXY} < 0$). Figure 3.9 shows Λ_{ciXY} maps for all the 12 imaged instants with PIV in the non-Newtonian case. A similar map is obtained for the Newtonian case (not shown here). An in-house MATLAB script is programmed to locate the two vortices throughout the cardiac cycles (figure 3.10).

Now vortices positions are defined for the imaged cycles instants, their displacement along x and y axis can be computed. The positions X and Y are mathematically expressed as a relative position to the initial x_0 and y_0 position of the first detected swirl on the ROI of each category (clockwise Newtonian, counterclockwise Newtonian, clockwise non-Newtonian, etc.). The common characteristic between the two experiments is that two vortices develops in the ROI. An each cardiac cycle, a counterclockwise vortex emerges from the upper wall when leaving the diameter narrowing region while more central vortex appears at the ROI entrance. In the two fluid flows, the vortices generated at each cycle seem to persist during two successive cardiac cycle. Their displacements follow the same tendencies with a decrease in the Y axis and an increase in the X axis (figure 3.11). Finally, based on these displacements, vortex velocities can be computed knowing the time lapse between each imaged cycle instant (figure 3.12). Every figure includes the flowrate curve for 2 successive cycles to help locating trajectory data in the cycle phases.

The main limitation of this method is that it is particularly efficient when vortices are strictly normal to the 2D plane. Out-of-plane vortices leads to intensity underestimation

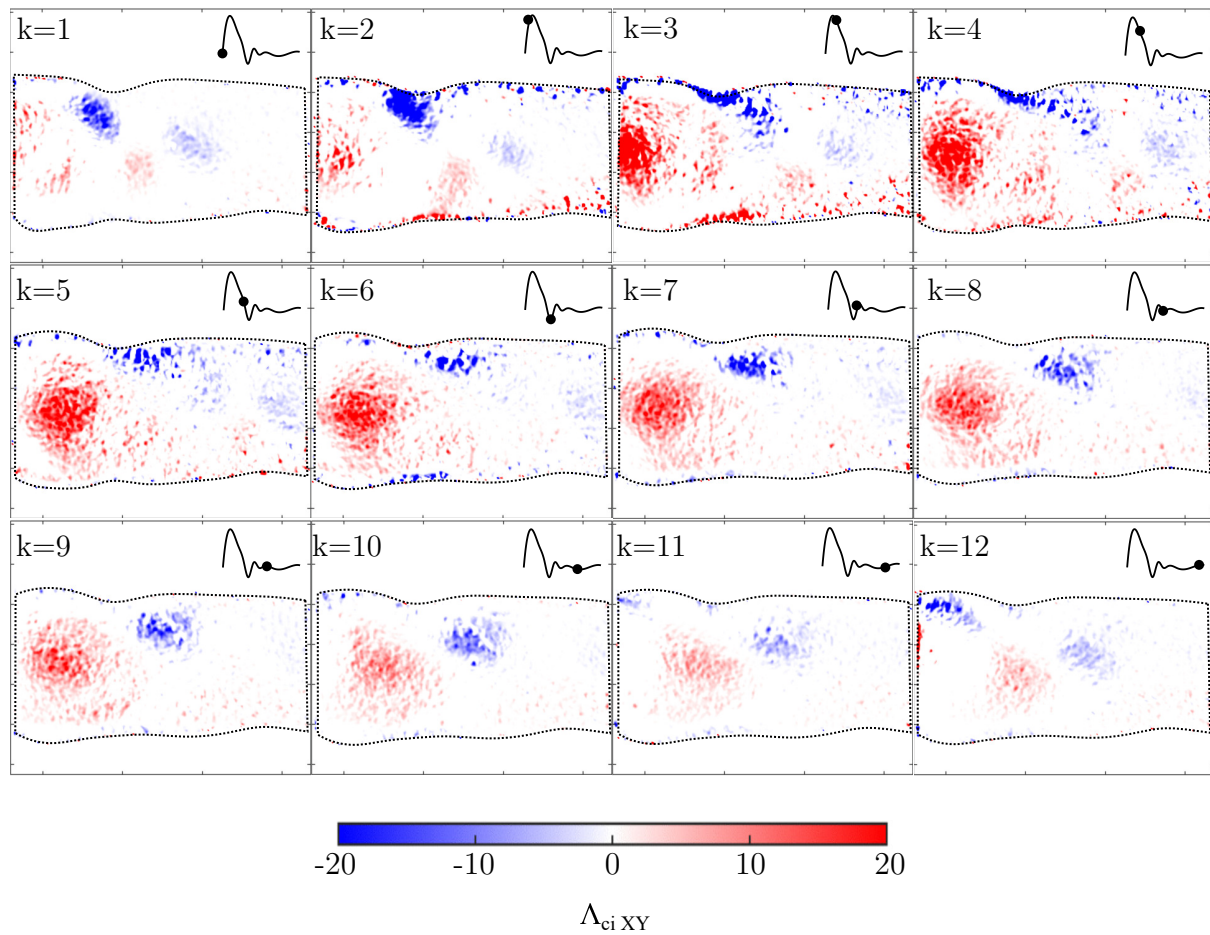


Figure 3.9: Λ_{ciXY} maps for all the 12 imaged instants with PIV in the Newtonian case.

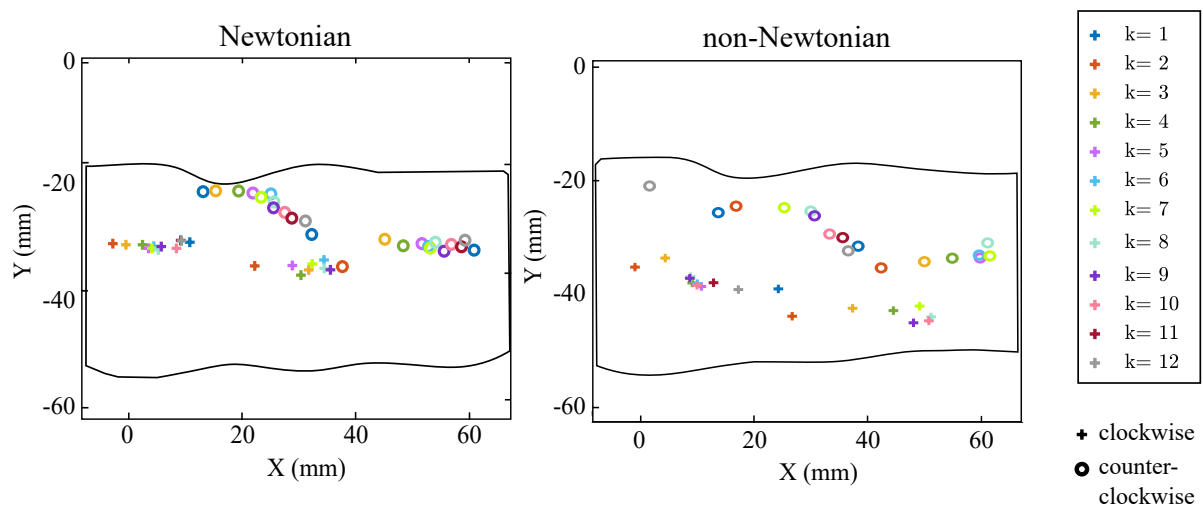


Figure 3.10: Location of vortices centroids throughout the cardiac cycle for the Newtonian and the non-Newtonian fluid flow experiments. k indicated the cycle instant corresponding to the centroid location. Each generated vortex appear to persist in the ROI during two successive cardiac cycles.

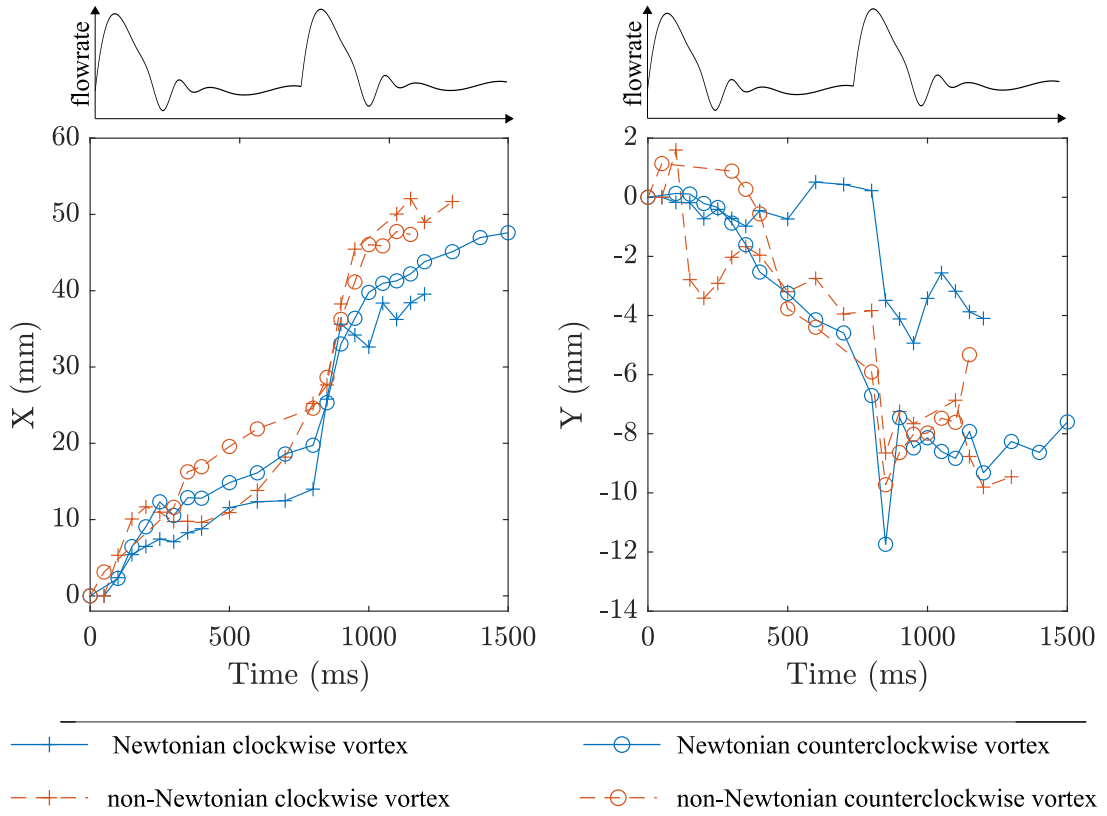


Figure 3.11: Vortices trajectory tracking on X and Y axis throughout time. The detected vortex rings always persists along two successive cardiac cycles. Data are provided for each vortex rotation direction and fluid flow experiment (Newtonian vs non-Newtonian.)

and location loss during tracking. Due to the complex geometry of the phantom, 3D and asymmetrical flows, it is probably not the case here. However, the idea here is not to quantify vortices intensity and displacement as a comparison to *in vivo* data but to compare the two fluid flow experiments that were carried out with similar inflow conditions, assessed with the same methods and analyzed with the same computation process.

For both experiments, vortex trajectories follow the same tendencies except for the clockwise vortex in the Newtonian case. It is much less deviated on the Y axis (4.9 mm from initial position) and follows a much straighter trajectory along the X axis. The non-Newtonian one is deviated of 9.8 mm (twice higher). This difference is not surprising when considering velocity maps in figure 3.7 where a higher velocity path is observed in the non-Newtonian case and marked by the dashed area. This path seems to push down flow toward negative Y axis direction with higher intensity than in the Newtonian case.

Regarding the vortex velocities, magnitude are similar to the fluid flow velocities with noticeable increase at the systolic peak of the second cycle. Vortex velocities show oscillations throughout the cycle in both cases. Deplano et al. (2014) showed that less oscillations are observed in the Newtonian case compared to a shear thinning BMF in an aneurysm model. In this last article, the flow quiet remained in-plane with an idealized symmetrical model which allows better tracking of vortices. We cannot draw the same conclusion here since displacement in the third dimension was not computed. The visible

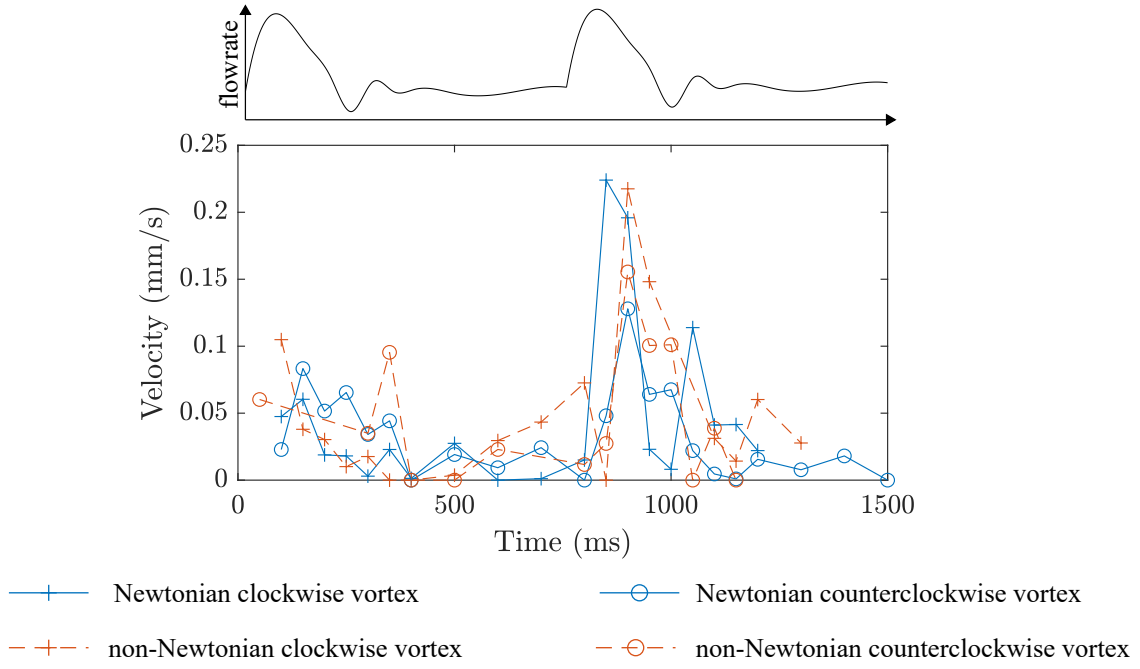


Figure 3.12: Vortices velocity throughout time. The detected vortex rings always persists along two successive cardiac cycles. Data are provided for each vortex rotation direction and fluid flow experiment (Newtonian vs non-Newtonian.)

oscillation could be an artifact due to displacement in the third dimension direction. We may not conclude with the current 2D-images. Furthermore, we may notice a slight phase shift in velocity for the non-Newtonian case when considering the systolic peak at $t = 900$ ms. A phase shift was also observed in previously cited article [Deplano et al. \(2014\)](#) between Newtonian and non-Newtonian vortex (observed in circulation strength intensity).

It can be stated that the two vortices paths vary between the two experiments (Newtonian vs non-Newtonian). Any differences in pattern, phase shift and travel distance may induce differences in interpreting risky areas, endothelial stimulation and platelet deposit when extrapolating to the *in vivo* environment ([Jesty et al. \(2003\)](#); [Schoepfoerster et al. \(1993\)](#)). Vortex patterns can also be related to shear distributions differences in both fluid flow. The next sections focus on shear quantities evaluation.

3.3.5 Shear rates and shear stresses

Finally, shear related quantities are computed, analyzed and compared to highlight differences in both fluid flow experiments. Concerning previously described flow distribution and vortices displacements discrepancies, different shear rate and shear stress patterns are expected.

It appears that due to the aorta geometry, certain preferential flow paths are amplified in the non-Newtonian case. To investigate these path consequences, the shear rate is calculated (equation 3.3.5) and is shown in figure 3.14 for the 4 representative instants ($k = 2, 4, 6$ and 10).

$$\dot{\gamma} = \frac{\partial u_y}{\partial x} + \frac{\partial u_x}{\partial y}. \quad (3.3.5)$$

For the non-Newtonian fluid, corresponding viscosity maps are computed with shear rate dependent viscosity $\mu(\dot{\gamma}_{\text{norm}})$ data from the rheology study (figure 3.2) and the shear-rate $\dot{\gamma}_{\text{norm}}$ from equation 3.3.6. Shear stress is then calculated with equation 3.3.7 and presented in figure 3.14. In the Newtonian case, viscosity is a constant $\mu(\dot{\gamma}_{\text{norm}}) = \mu_{\text{newt}} = 3.9 \text{ mPa.s.}$

$$\dot{\gamma}_{\text{norm}} = \sqrt{\frac{\partial u_y}{\partial x}^2 + \frac{\partial u_x}{\partial y}^2}. \quad (3.3.6)$$

$$\tau_{ss} = \mu(\dot{\gamma}_{\text{norm}}) \cdot \dot{\gamma}. \quad (3.3.7)$$

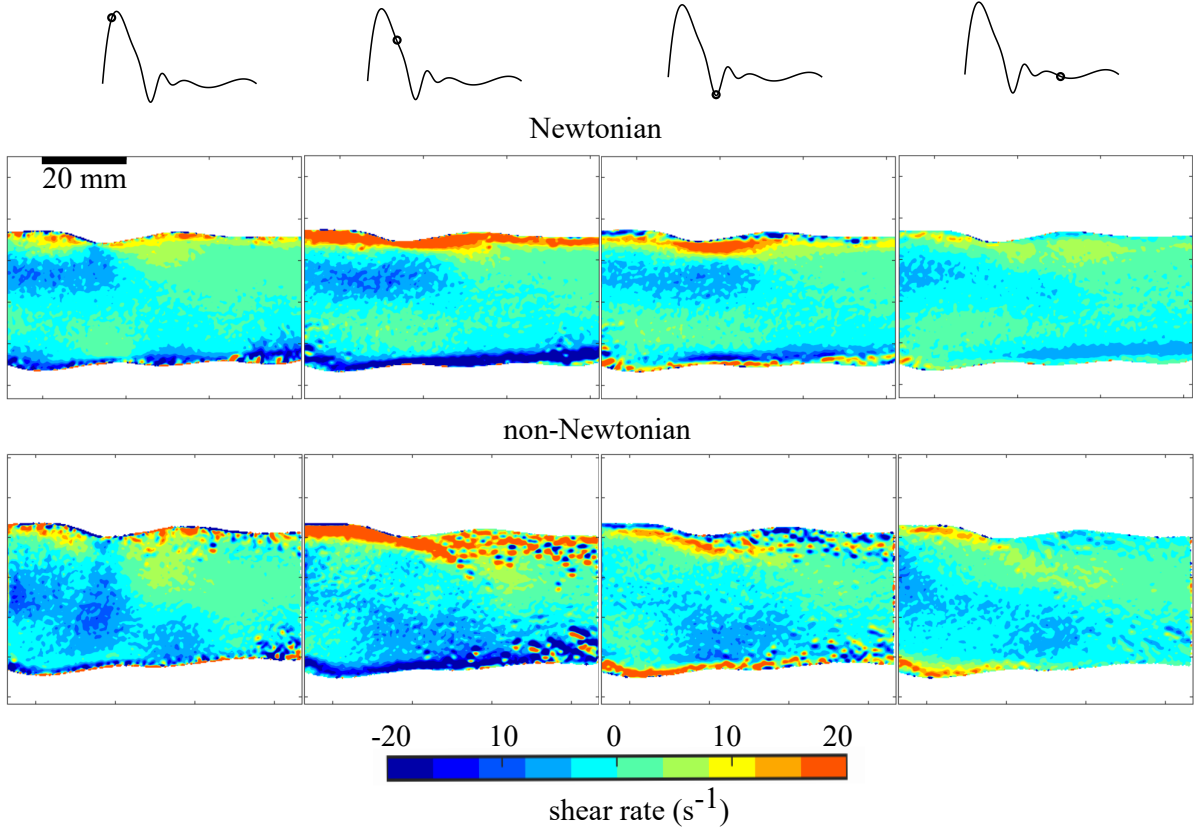


Figure 3.13: Shear rate maps for the Newtonian and non-Newtonian fluid experiments at four cycle instants $k = 2, 4, 6$ and 10 .

The shear stress is plotted for the 12 cycle instants (figure 3.15). Mean shear stress (integration on the whole ROI) and wall shear stress (WSS) are presented as absolute terms. A WSS per instant is evaluated as a mean shear stress $\mu(\dot{\gamma}_{\text{norm}}) \cdot \frac{\partial u}{\partial y}$ on a near-wall layer (5% of aorta diameter thick layer along the upper and lower walls). On the whole ROI, shear stress is about three times higher for the non-Newtonian fluid than for Newtonian fluid. $|\text{WSS}|$ is twice higher for the non-Newtonian BMF with a maximum and

average shear stress of 0.23 Pa and 0.071 Pa respectively while they are of 0.11 Pa and 0.035 Pa for the Newtonian fluid. Since the non-Newtonian fluid equivalent viscosity (at high shear rate) is 33.3% higher than the Newtonian fluid one, global higher shear stress values are expected. However, the 100% increase and shear distribution discrepancies in the ROI could not be attributed to this shift in overall viscosity.

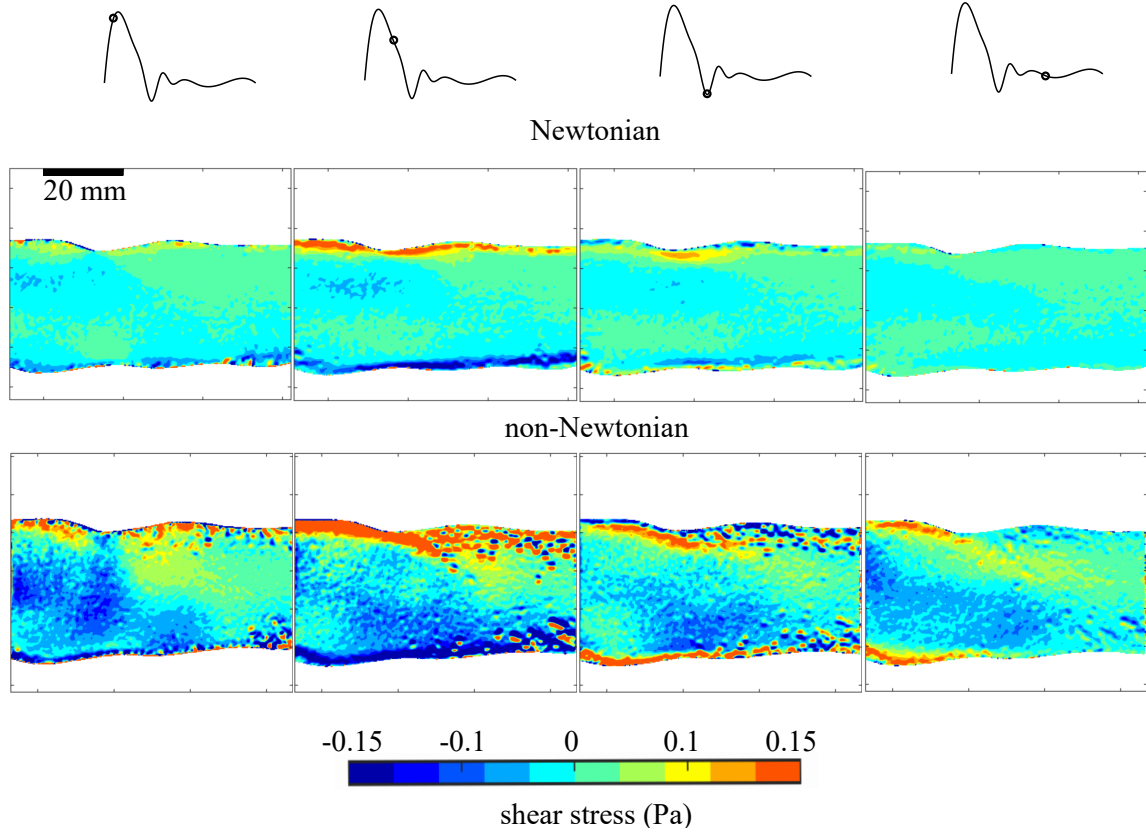


Figure 3.14: Shear stress maps for the Newtonian and non-Newtonian fluid experiments at four cycle instants $k = 2, 4, 6$ and 10 .

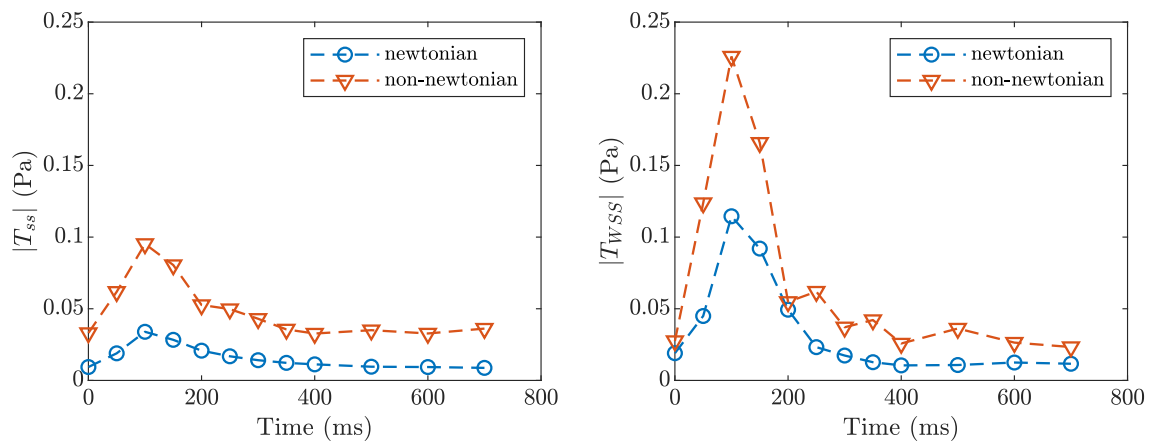


Figure 3.15: (Left) Shear stress absolute term calculated on the aorta ROI1 versus time, (Right) wall shear stress on a 5% of aorta diameter thick layer along the upper and lower walls versus time.

As expected, higher shear rates and shear stress are observed near walls. More chaotic

shear patterns are observed in the non-Newtonian case downward the diameter narrowing regions. In both cases, higher intensity shear rate is observed in regions corresponding to the vortices path described in previous section. It corresponds to a straighter trajectory in the Newtonian case (dark blue area in the upper region) and a downward path in the non-Newtonian case (dark blue area descending to the lower wall).

3.4 Discussion

3.4.1 Related geometry flow distribution

The analysis mainly focused on the four previously described instants which represent very distinct cardiac cycle phases (systolic peak, deceleration, backflow, and diastole). One of the main observations on velocity field maps was the upper wall flow jet-like deviation in the narrowed region at systole. Recirculation paths appeared on the opposite wall at diastole. These flow patterns were observed in [Prahl Wittberg et al. \(2016\)](#) where aorta geometry irregularities influence on flow were studied with numerical simulation on a non-Newtonian blood flow (with rigid walls aorta model). A local reduction of the diameter induces a deflected flow jet in the curvature direction which persisted downstream of the narrowing. These results also showed chaotic flow, vortical motions, and higher wall shear stress around the section narrowing. In the current study, this effect was amplified for the non-Newtonian case. [Jung et al. \(2004\)](#) and [Neofytou \(2006\)](#) studied the development of asymmetric flows that were specific for non-Newtonian fluid flows. They showed that these asymmetries appeared downstream from the singularities and were amplified when Reynolds number increases (>500). Moreover, [Amornsamankul et al. \(2007\)](#) investigated the influence of non-Newtonian fluid characteristics on flow patterns in symmetric and asymmetric tube geometries and highlighted similar velocity profiles when comparing Newtonian and non-Newtonian fluids. In our non-Newtonian experiment, the maximum Reynolds number at systole was $Re_{peak} = 1129$ which could explain the amplified asymmetry in the aorta ROI.

In the present study, measured T_{WSS} remained in the lower range of *in vivo* measurements in healthy aortas in the non-Newtonian case ([Kolipaka et al. \(2017\)](#); [Cheng et al. \(2003\)](#)). Note that PIV image resolution and the missing velocity third dimension component can lead to an underestimation of velocity gradients ([Tokgoz et al. \(2012\)](#)). Therefore, the calculated shear stresses give clues on distribution and evolution along the cycle but cannot be directly compared with *in vivo* absolute values. Appendix F provides an overview of cross correlation parameters influence on computed velocity gradients depending on interrogation window size and overlap.

Many numerical studies were conducted on smaller arterial systems (femoral, coronary, etc) and showed that Newtonian representations underestimate WSS compared to non-Newtonian models ([Apostolidis et al. \(2016\)](#); [Weddell et al. \(2015\)](#)). Numerous studies on large arteries showed that the Newtonian assumption is acceptable ([Caballero and Laín \(2015\)](#); [Iasiello et al. \(2017\)](#)) but most of them were conducted on simplified and idealized geometries. The previous observations on increased flow asymmetry for non-Newtonian fluid came with higher shear stress values and different patterns while inflow

conditions and measuring methods were similar. The complete 2D map of shear stress is given as a comparative flow structure for the two fluid flow but the WSS is more relevant in the context of pathology investigations. However, in both cases (shear stress map and WSS) results question the Newtonian assumption (as equivalent to non-Newtonian in large arteries) at least in this type of more complex geometry with compliant walls.

3.4.2 Limitations

Rheology limitations

The non-Newtonian working fluid was designed to approach human blood shear-thinning viscosity. Human blood reaches a viscosity plateau at low shear rates. The designed BMF did not reach this plateau and thus, did not well mimic human blood in this lower range of shear rate. It would result in an overestimation of viscosity at low shear rate (<0.01 mPa.s) which could question shear stress results. Moreover, other rheological properties such as viscoelasticity were not explored in our xanthan solution (Campo-Deaño et al. (2013); Najjari et al. (2016)). Brookshier and Tarbell (1993) showed that xanthan gum was a good candidate to mimic blood viscoelasticity compared to other polymers. In this study, more complex rheometric devices are needed to explore low shear rates and viscoelasticity (oscillatory and capillary rheometers).

PIV limitations

In addition, a 3D visualization technique (slices of stereo-PIV) could provide information on the 3rd dimension to better estimate velocity gradients and thus wall shear stress. Indeed, velocity gradient are underestimated by both the resolution of PIV treatment (interrogation windows size) and the missing third dimension due to the choice of a 2D visualization technique (2D-PIV).

Mock loop setup limitations: vortex rings

The observed vortex rings were used as a comparative element between the Newtonian and the non-Newtonian experiments regarding their location, displacement and velocity. The exact same setup regarding geometry, inflow conditions and phantom positioning were applied in both experiments which make the fluid comparison possible. But where does this rotational flow come from ? The upper wall one seems to emerge from the upper wall curvature, but the central swirling structure do not have a clear origin. Imaging the entrance region with the mock loop connector to the phantom suggested that the central swirl emerged from the connector transition. More precise visualizations of connectors transition flow are addressed in the next chapter on AD phantom cases. In the current experiment, the central swirl cannot be attributed to phantom geometry flow but can still be used as a comparative element since inter-experimental conditions are the same.

Reproducibility

The reproducibility of the measurement can be questioned regarding the positioning of the phantom and the laser sheet at the exact same position between experiments. Regarding the phantom positioning, markers were drawn on the fixed connectors of the tank and on the transparent aorta model. Each time, we position the phantom, the marker are

used to put it in the same position. However, since the phantom is flexible it can be difficult to reach the exact same position each time because of possible model twist. Second the laser sheet positioning is achieved with the help of cross-liner lasers (Cross 90, Stanley) which were fixed on the laser/camera structure. Matching the laser sheet with the fixed laser liner allows to always align it the same way on the phantom. The mismatch could occur when superposing the two laser line of about 1 mm thickness (reference liner and PIV laser) but should not be higher than a few hundred of micrometers. A High Precision Motorized Stage Systems (Edmund Optics) allows to move the laser sheet and the camera in a translational motion along the phantom. The fact that the laser head and the camera are both moving on the same frame prevents from breaking the parallelism (camera sensor and laser sheet) which was adjusted prior to the experiment. It is set to image the aorta section at the maximum of its diameter. The repeatability of the motorized system positioning is below $3\text{ }\mu\text{m}$.

3.4.3 Newtonian versus non-Newtonian representation

In the literature, a wide range of *in vitro* studies use the Newtonian representation for their BMF. In most cases, the working fluid are often designed with water-glycerin solution to reach the high-shear rate asymptotical viscosity of human blood (about 3 - 4 mPa.s). As shown in the dimensional analysis from chapter 1, section 1.2.4, this assumption is acceptable when considering the Navier-Stokes equation terms contribution. The viscosity term is negligible compared to the other which questions the relevance of a non-Newtonian model. However this mathematical demonstration corresponds to a highly simplified model of straight pipe tube flow. Indeed, most *in vitro* experiments from the literature, are actually conducted in straight pipes with symmetrical flows.

There are two major studies on non-straight pipes which compare Newtonian versus non-Newtonian BMF in artery phantoms: Walker et al. (2014) and Deplano et al. (2014). Deplano et al. (2014) studies an idealized aneurysm model which can be treated as a divergent pipe problem while Walker et al. (2014) focused on partially occluded channel to mimic stenosis. Both of them observed major differences in the two fluid flows. It concerns flow distribution, vortex ring travel, shear rate, shear stress, pressure drop, turbulent shear stress, etc.

In the current study, the analysis was focused on flow distribution, vortex ring travel, shear rate and shear stress. Strong similarities between fluid flows were observed but slight differences appeared often in accordance with Deplano et al. (2014) work. The major one in the higher intensity and more chaotic shear stress patterns observed in the non-Newtonian case. Shear stress patterns is known to have a strong influence on aortic diseases with endothelial stimulation of cells, platelet activation and deposition (Lu et al. (2013); Jesty et al. (2003); Schoephoerster et al. (1993)). Regarding our observations, the Newtonian representation seems to dampen and underestimate shear stresses in the aorta phantom. Lower shear stress areas are higher risk regions where endothelial cells are less stimulated (Pedersen et al. (1999)). Underestimating shear would result in overestimating risks as low wall shear stress regions are targeted as risky areas (refer to chapter 1 section 1.3.2). Moreover, vortex ring travel and shear stress differences may also influence the transport of platelets, activation and release location (Deplano et al. (2014)). The use of

a Newtonian representation (equivalent to the high-shear rate asymptotical viscosity of blood of about $3\text{-}4\text{ }\mu\text{m}$) then appears unsuitable to model the non-Newtonian behavior of blood as it is not equivalent in the present work ². In the context of analyzing and treating cardiovascular diseases the Newtonian BMF would result in misinterpretation of flows and thus of disease mechanisms and risks.

3.5 Phantom performances : pressure wave velocity and elasticity

Flow were studied in the phantom with the non-Newtonian component for the working fluid as a more "representative" fluid to mimic blood. But how is the phantom mechanical response relevant to emulate aortic wall behavior ? A first positive observation was that the wall displacements were in accordance with human aorta under similar pulsatile conditions. Moreover, the elastic modulus is in the range of the human ones. This section focuses on the evaluation of another criteria related to flow and wall behavior: pressure wave velocity (refer to chapter 1, section 1.2.2). This quantity is a good indicator of aortic wall stiffness and can be computed with traditional imaging methods such as US-doppler, catheter pressure sensors or 4D flow MRI (Houriez-Gombaudo-Saintonge et al. (2019)). One of these methods is applied on our compliant aorta phantom and the technique of PIV to estimate if computed PWV and arterial stiffness are realistic compared to *in vivo* data.

3.5.1 The lnD-V method

In vivo, aortic stiffness is associated with some pathologies. The measurement of pressure wave velocity (PWV) can be evaluated with non invasive techniques to find the elastic modulus. As depicted in chapter 1, section 2.4.4, pressure wave velocity is the velocity at which the blood pressure pulse travels through vessels. Two main techniques exist to evaluate PWV :

- **Transit Time method (TT method)**: consists in measuring the pressure pulse in two locations of the arterial tree. Knowing the distance between these two points and measuring the time required for the pulse to travel between these two points, PWV can be calculated by dividing the distance by the travel time. This method is mostly implemented by inserting invasive catheter-tip in the arteries at two different locations. The disadvantage is the invasive catheter which can disturb flow and artery geometry. Moreover, measuring the distance between the two points is not that trivial. 4D-MRI technique exists as non-invasive alternative but still requires more expensive and more complex equipment (van Elderen et al. (2011); Weber et al. (2009); Naidu et al. (2020)).

²Note that the goal is to compare a realistic shear-thinning fluid to mimic blood and the traditionally used Newtonian representation. Other Newtonian versions with potentially higher viscosity were not considered but could show different results (impact on Reynolds number, higher shear, etc.).

- **lnD-V method:** is a non invasive method based on the measurement of blood velocity and artery diameter change throughout cardiac cycle at only one location. *In vivo*, this method can be achieved with US-Doppler or 4D-MRI exams to obtain a regional assessment of arterial stiffness (Di Lascio et al. (2014); Negoita et al. (2018)). PWV is calculated thanks to a correlation between diameter change logarithm (lnD) and corresponding blood velocity (V). Compared to TT method, it requires a good time resolution to assess a large number of data along a cardiac cycle to obtain a reliable correlation. However, it is an easier and cheaper method than the TT one that can be implemented with conventional ultrasound machines. The method is described below.

The lnD-V method is non invasive and only requires to know the targeted vessel diameter change and flow velocity in one region. The PIV method described in the previous section allows to evaluate both variables. It is therefore an interesting setup to test for the evaluation of the phantom PWV. The method description comes from the study of Di Lascio et al. (2014) and emerges from the Bramwell-Hill equation (Bramwell and Hill (1922)). The reader can refer to those two studies for more details on the lnD-V method.

Local PWV can be calculated with the following equation 3.5.1:

$$PWV = \frac{1}{2} \frac{dV}{d \ln(D)} \quad (3.5.1)$$

with dV the velocity variation and dln(D) the change in natural logarithm of the vessel diameter D. This relation is only valid in unidirectional waves periods along the cardiac cycle. If reflective waves appear, the relation can no longer be applied. Methods to identify reflection-free periods in the cardiac cycle exist (Di Lascio et al. (2014)). A Wave Intensity Analysis (IA) allows to identify reflection-free period. Wave intensity can be calculated with velocity and diameter time derivation as in equation 3.5.2.

$$WI = \frac{dD}{dt} \frac{dV}{dt} \quad (3.5.2)$$

Studies have shown that backward waves have negligible effects on diameter and velocity variations at the two positive peaks of WI (Jones et al. (2002); Harada et al. (2002)). In most cases these peaks correspond to early and late systole. Locating one or the two phases allows to determine where backward wave contributions are negligible. In this study, we will focus on the early systole phase identification to compute PWV as it can be easily detected.

3.5.2 PWV and elasticity evaluation with PIV

The lnD-V loop techniques can be used on the compliant aorta phantom to estimate the material PWV (figure 3.16) and thus, the elasticity modulus. This value can then be compared to the young's modulus calculated from the destructive mechanical tensile tests and DIC methods.

To compute diameter change and velocity, the PIV measurements were achieved in ROI_{down} which is a rather straight region in the longitudinal axis (main flow direction).

It allows to avoid out-of-plane flow and capture reliable velocity fields magnitude in the targeted region. By contrast with the previous experiments (in ROI_main), synchronization of PIV imaging triggers with the solenoid valve was not achieved. The goal is to sweep successive cardiac cycles with high framerate to get pairs of PIV snapshots. For each snapshot, the velocity field (Davis 10, LaVision) and the corresponding diameter is calculated (MATLAB in-house program). PIV parameters are set to shoot 1000 pairs of images at a framerate of 10 Hz. The timelapse between two images of a pair was set at $\Delta t = 4000 \mu s$ to optimize cross correlation at the systolic phase which is the most relevant phase to compute PWV. Obtained velocity and diameter waveform are shown in figure 3.17.

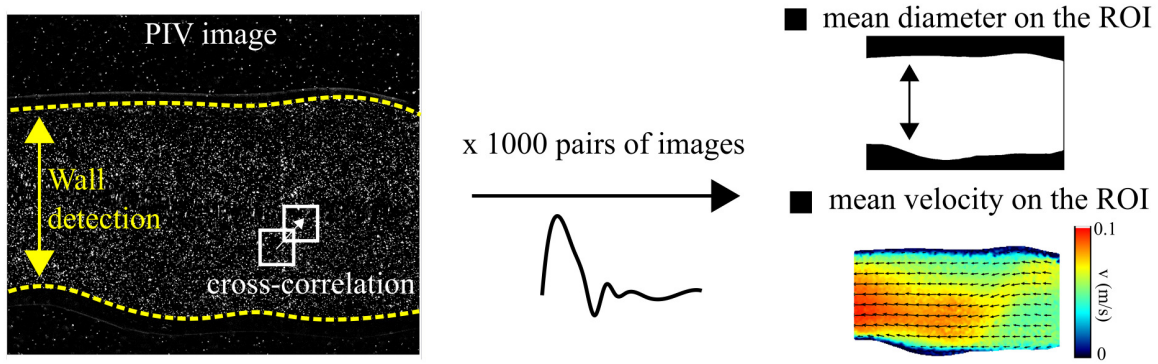


Figure 3.16: Illustration of the lnD-V method applied on PIV images. The inlet of the phantom is at the right side of the image. Refer to figure 3.1 for the PIV images orientation.

First, Wave intensity (WI) was computed with equation 3.5.2 to detect local maxima. The early systole maxima is clearly identified and indicated in red on the curve. This period is thus considered as reflection-free where diameter and velocity correlation can be computed to determine PWV.

Second, the lnD-V graph is provided in 3.19. The cycle shows similar shape as in Di Lascio et al. (2014) where the experiment was conducted on mice with ultrasound measurements. Data corresponding to early systole (reflection-free period identified with WI) are isolated and presented on figure 3.20. The linear regression slope gives the $\frac{d \ln(D)}{dV}$ factor. Computed PWV with equation 3.5.1 is of 5.92 ± 0.35 m/s. Uncertainty mostly comes from the diameter detection uncertainty. As images are not averaged throughout the cycle, each velocity and diameter point is computed on a single image. For the wall detection algorithm, it sometimes results in misinterpretation of wall position due to punctual light reflections, bubble, dust, fibers or particles circulating in the background of the ROI. A value of $PWV = 5.92 \pm 0.35$ m/s is in the range of abdominal aorta PWV for normal subject of about 50 years old (Devos et al. (2015); Grotenhuis et al. (2009)).

Finally, the phantom material young's modulus can be calculated thanks to the PWV. Equation 3.5.3 gives the relation between PWV and the material young's modulus E.

$$PWV = \sqrt{\frac{Eh}{\rho d}} \quad (3.5.3)$$

where h is the aortic wall thickness (2.19 ± 0.42 , refer to chapter 2, section 2.4.3), ρ

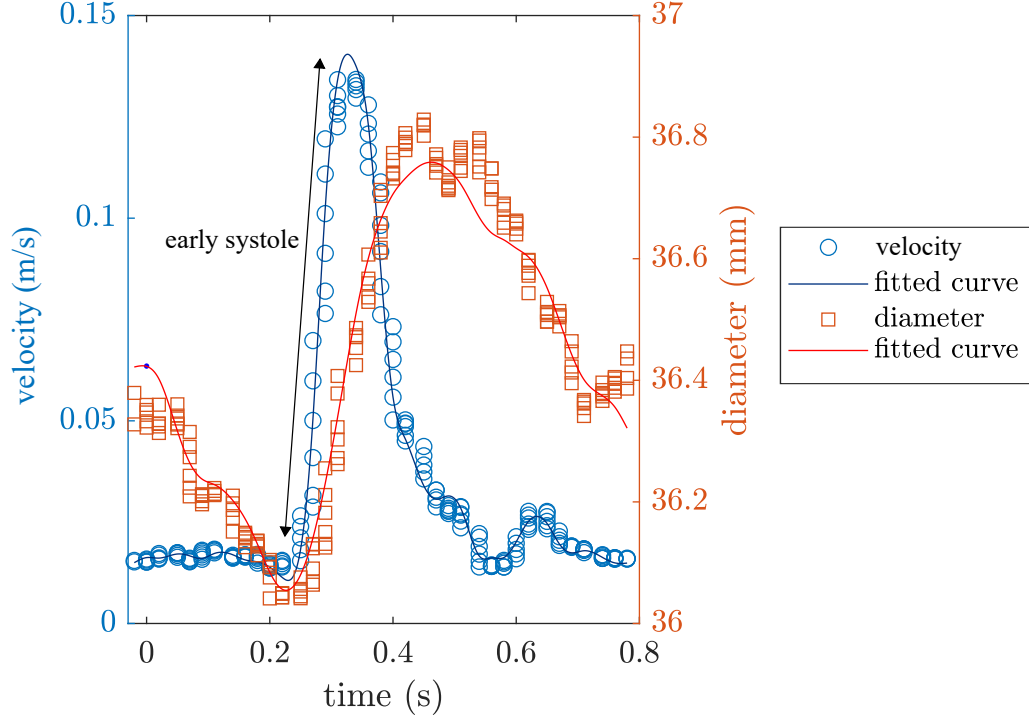


Figure 3.17: Mean diameter and velocity waveform in the aorta ROI_{down}. Raw data and fitted curves are shown. The velocity may appear low compared to *in vivo* data, note that this velocity is the mean velocity on the whole image. This is in accordance with the velocity data from [Cheng et al. \(2003\)](#) for healthy patients in the abdominal aorta.

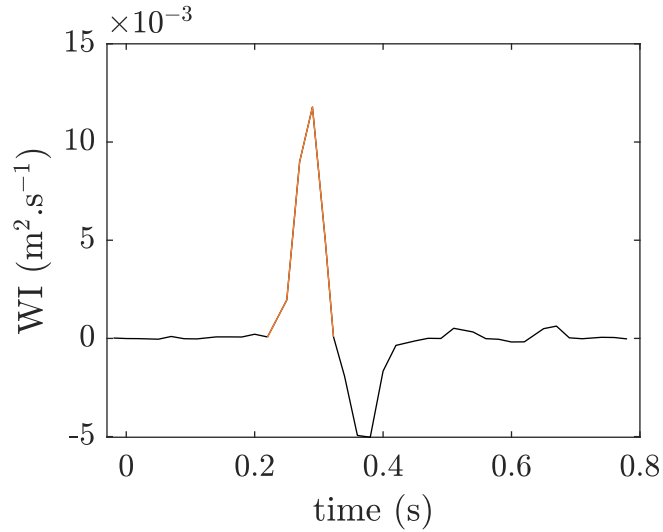


Figure 3.18: WI was calculated and a local maxima was identified. It corresponds to the systolic increase. Two secondary maxima emerge but will not be used for PWV computation.

is the conveyed fluid density (1146 kg.m^{-3}), and D aortic inner diameter. The diameter is set as the average diameter in ROI_{down} at early systole and is equal to 36.1 mm. As a result, the computed young's modulus is $E_{\text{lnD-V}} = 0.66 \pm 0.08 \text{ MPa}$. In most *in vivo* experiments, the use of these methods lack validation and comparison because no

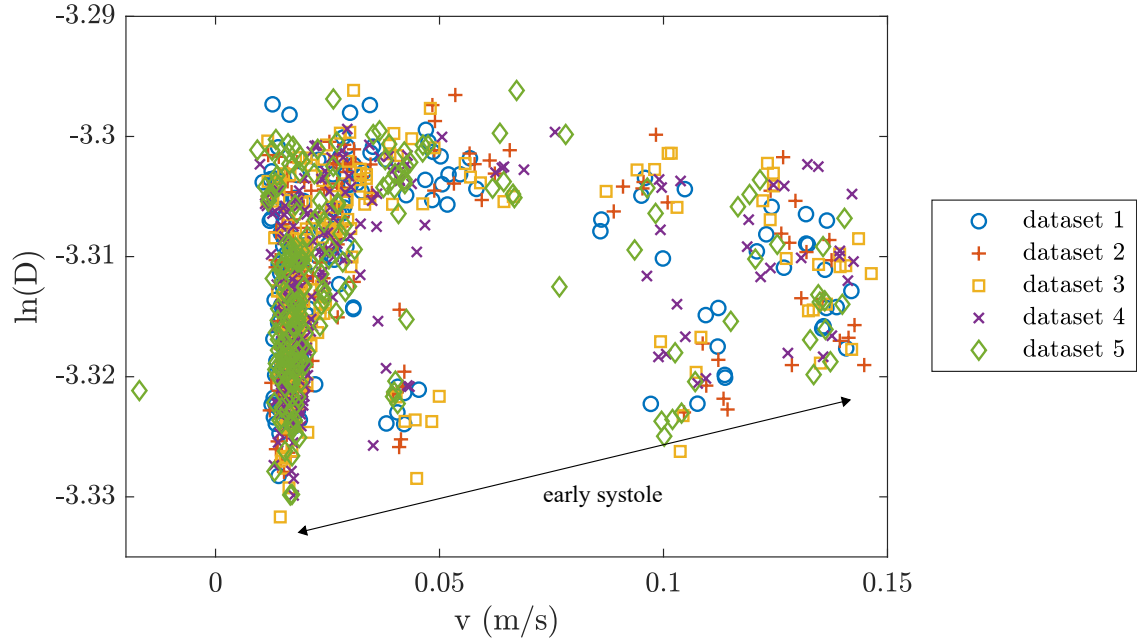


Figure 3.19: $\ln D$ - V loop graph for 5 datasets of 200 images each. Each dataset corresponds to PIV measurements in the same ROI2. Note that the main flow direction is from right to left since the camera orientation has changed for ROI_down imaging (refer to figure 3.1)

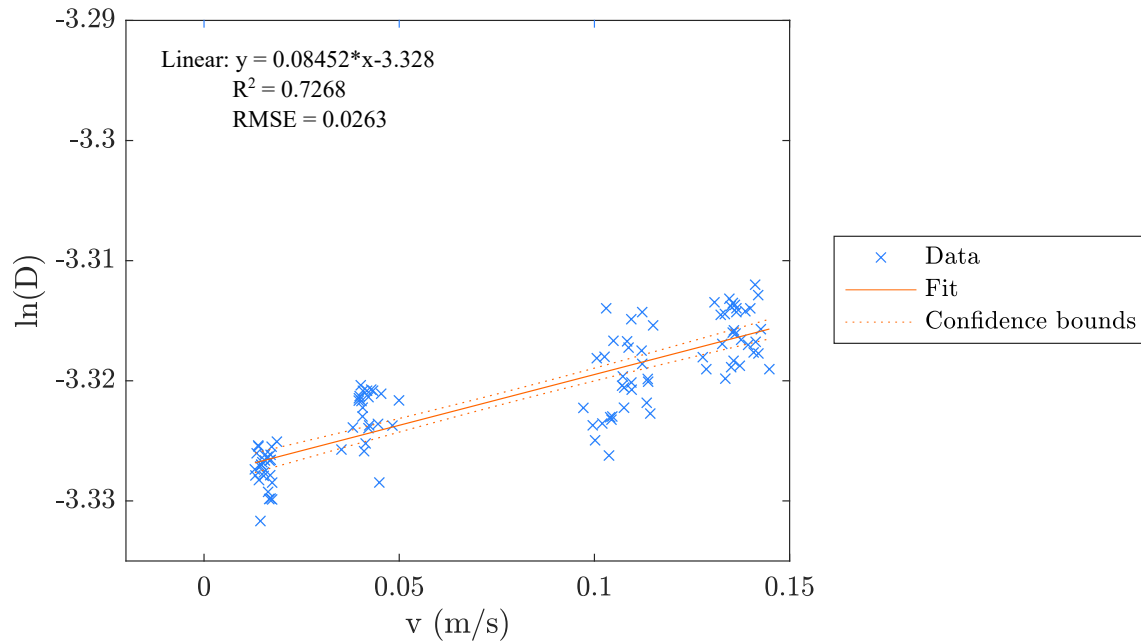


Figure 3.20: Curve fit on data corresponding to the increase in systole (109 images).

mechanical tests can be conducted on the patient. In our case, the phantom's young modulus was evaluated with tensile tests (refer to chapter 2, section 2.4.4) which revealed an elasticity of $E_{\text{tensile}} = 0.53 \pm 0.07$ MPa (figure 3.21). Considering the uncertainty in the two computed young's modulus, the values are consistent with each other.

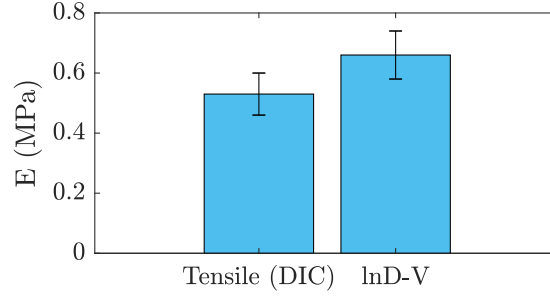


Figure 3.21: Young's modulus assessed with tensile tests and Digital Image Correlation (DIC) on samples of a sacrificial aorta phantom and the one computed with lnD-V non invasive and non-destructive method.

3.5.3 Limitations

The main limitation comes from the diameter detection. As explained previously, each point presented on the lnD-V loop corresponds to a single pair of images. Conversely with the experiments on Newtonian vs non-Newtonian fluids, neither diameter nor velocity fields reaches statistical convergence. Indeed, 500 pairs of images for a point on the cycle were needed in those previous experiments. As a consequence, in the present experiments, we count on a large amount of random data on the period of interest (early systole) to guaranty a reliable linear regression to compute the $\frac{d\ln(D)}{dV}$ coefficient. On a pair of images, the most difficult value to compute is the diameter, as punctual wall detection defects can occur due to the presence of foreign body and light reflection in the field of view (mostly in the background). The algorithm is based on grey scale value differences between the dark background and the lighter phantom. Strong disturbance on the background or micro-bubble deposit on the phantom surface can cause incorrect localization of the phantom's walls. These errors are largely compensated when averaging on a large number of images (as in the experiments in ROI_main) but remain in single pair of images computation (as in experiments on ROI_down).

In the current set of data, 1000 pairs of images were shot but only 109 of them were in the early systole period (10.9%). Two ways to improve the technique would be to shoot a larger number of data as a quantitative improvement or to optimize the wall detection algorithm as a qualitative improvement. This last technique appears wiser to minimize experimental duration and thus limit cycle reproducibility uncertainty, temperature variations, polymer degradation, etc.

The lnD-V method often lacks validation with traditional tensile test to measure material elasticity. Of course, this limitation comes from the impossibility to perform these tests *in vivo*. The current experiment on the aorta phantom is therefore an interesting comparison between lnD-V method to compute Young's modulus and traditional tensile test evaluation.

Further validation could be conducted with other techniques such as the TT-method. In the presented experimental bench it could not be directly applied with the inlet and outlet flowmeters of pressure sensors because they are located out of the phantom. Indeed, they are in rigid pipe tube sections which would not be representative of the phantom PWV.

3.6 Conclusion

The developed aortic flow simulator emulated reproducible flowrate and pressure conditions on an anatomically realistic compliant aorta phantom. The device was tested to compare Newtonian and non-Newtonian fluid flows under pulsatile conditions to mimic human blood. Both fluids are often considered equivalent in such *in vitro* experiments from the literature. However, to the author's knowledge no study has combined realistic geometry and compliant walls on a phantom with non-Newtonian fluid flow experiments. These features could make the difference in observed Newtonian and non-Newtonian flows.

As a result, both fluid flow experiments showed common trends regarding flow distribution, shear quantities and vortex ring travel. However, these were not strictly equivalent as the non-Newtonian fluid flow exhibited stronger preferred paths with higher velocity and flow asymmetry especially in the diastolic phase. These features were observed in a diameter narrowing region due to natural curvature of the phantom model. Therefore, it could explain why these are not observed in commonly used straight tubes models where both fluids are often considered equivalent.

Moreover, the non-Newtonian experiments revealed shear stress twice higher than in the Newtonian case. Two vortex rings were observed in the region of interest. Travel distance and velocities are similar in both cases. But the deviation on the aorta axial direction is stronger in the non-Newtonian case and in accordance with the direction and location of the more pronounced flow path and enhanced asymmetry.

All those observations tend to invalidate the hypothesis that Newtonian and non-Newtonian BMF models are equivalent for *in vitro* aorta fluid flow experiments, at least in phantoms with complex geometry and compliant walls. The Newtonian hypothesis tends to underestimate shear quantities and vortices contribution which could lead to misinterpretation of flow distribution and risky areas when considering disease mechanisms analysis. The non-Newtonian BMF will therefore be used for the mock loop as the working fluid for future experiments. The previously described experiments also allowed to highlight the accuracy and limitations of the designed mock loop regarding cycle-to-cycle repeatability, velocity fields uncertainty, phantom wall tracking errors etc.

Finally, phantom performances were evaluated regarding wall displacements, pressure wave velocity and elasticity. Wall displacements were in accordance with human subject measurements. Moreover, PWV evaluation was achieved with the lnD-V method to estimate the phantom material Young's modulus as a non-invasive and non-destructive method. The measures value of 0.66 ± 0.08 MPa remain in the range of human aorta elasticity and is in accordance with measured value with mechanical tensile test on an identical sacrificial phantom. Actually, this method has rarely been validated with mechanical tests on *in vivo* patients (human and/or animals). Therefore, the proposed method on *in vitro* phantom is an interesting alternative for the lnD-V technique evaluation. A way to continue this investigation would be to calculate the PWV in different locations along the phantom with different orientation of the PIV plane.

Now the experimental set up is validated and we are able to quantify its accuracy and limitations. The mock loop can be used to study flows in pathological phantoms. The goal is to visualize and analyze fluid flows in aortic dissection phantoms and make

a comparison with numerical simulations. These simulations can be used to improve surgery planning by emulating the surgical procedure and the mock loop is a relevant tool to validate those simulations.

Aortic dissection case studies

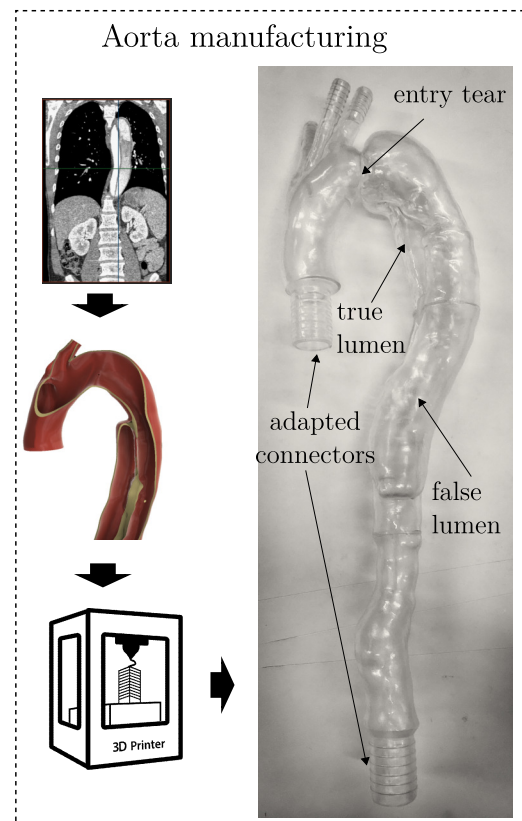
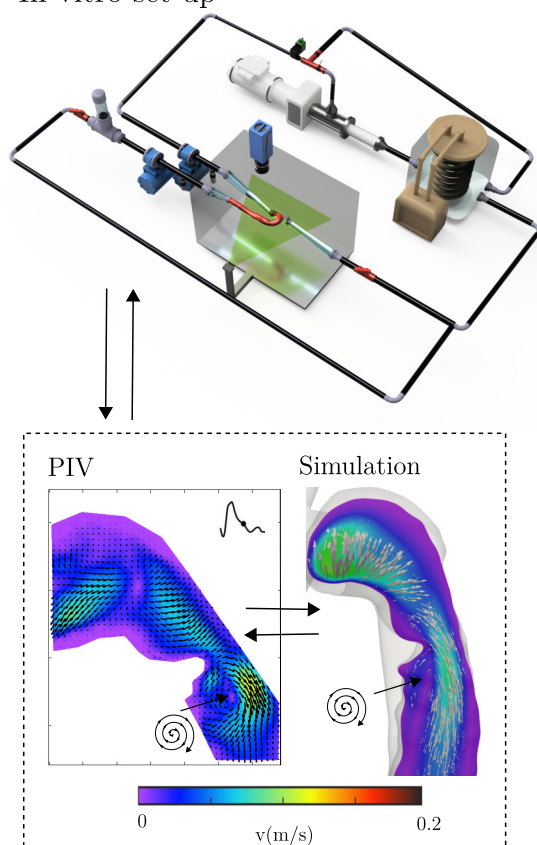
Contents

4.1	Background	128
4.2	Aorta phantoms	129
4.2.1	Phantom properties and geometry	130
4.2.2	3d printing testing approach	131
4.2.3	Refractive indexes	133
4.3	Materials and methods	136
4.3.1	Experimental setup	136
4.3.2	PIV measurements	138
4.3.3	Image post-processing	140
4.4	Flow analysis: AD1 case	141
4.4.1	Flow distribution	141
4.4.2	Vortices	145
4.4.3	Discussion and limitations	146
4.5	Flow analysis: AD2 case	147
4.5.1	Flow distribution	147
4.5.2	Shear quantities and vortices	148
4.5.3	Discussion	153
4.6	Comparison with numerical simulation: preliminary study	155
4.6.1	Simulation setup	155
4.6.2	Results and discussion	157
4.6.3	Limitations and perspectives	163
4.7	Conclusion	164

Abstract

An aortic dissection case study is conducted on aortic flow simulator. Two aorta models with aortic dissection and patient specific geometry were manufactured with a 3D printing technique. The resin provided rigid walls models with transparent properties. Experiments were conducted on the two models with a non-Newtonian blood mimicking fluid and pulsatile inflow conditions to mimic physiological flows. To deal with phantom walls rigidity a Windkessel model was implemented on the mock loop with a compliance chamber and resistive valves. Three regions of interest were imaged with tricky geometries on two aorta models. It includes the aorta entrance, the dissection entry tear and the false lumen. Velocity, shear and vorticity were computed on PIV images with variable cross-correlation quality depending on optical accessibility and phantom material surface state. The results were compared with numerical simulations conducted on the two same aorta models as a preliminary *in vitro-in silico* confrontation. Similar flow tendencies were observed on both models and differences appeared related to mismatch in outlet boundary condition between the experiment and the numerical simulation. Boundary condition optimization would be required to perfectly match both models setup. Finally, the 3D visualization offered by the numerical simulation brought new information on flow pattern which comforts the idea of using both methods as complementary tool for hemodynamical studies.

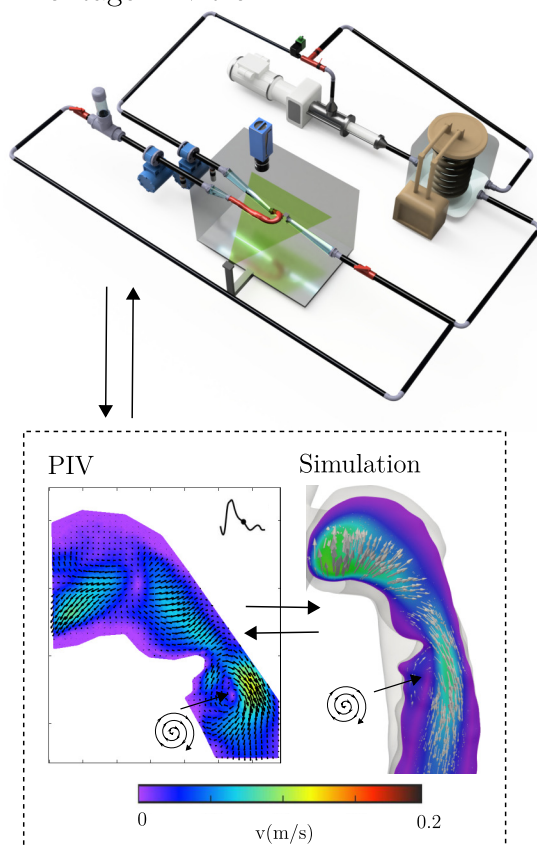
In vitro set up



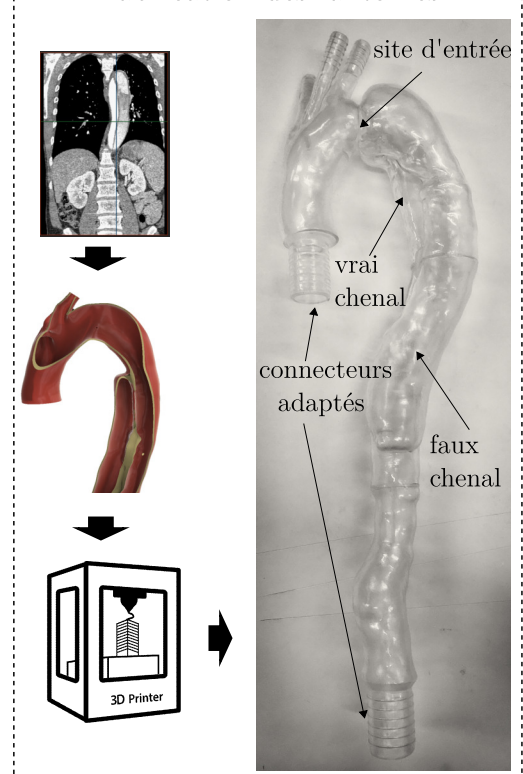
Résumé

Une étude de cas sur la dissection aortique a été réalisée grâce au simulateur d'écoulement sanguin. Deux modèles de dissection avec des géométries patient-spécifiques ont été fabriqués par technique d'impression 3D. La résine utilisée a permis d'obtenir des fantômes rigides avec parois transparentes. Sur les deux modèles, les expériences sont réalisées avec le fluide analogue au sang non-Newtonien et des conditions de débit et de pression pulsés pour imiter les écoulements physiologiques. Afin de compenser la rigidité des fantômes, un modèle Windkessel est ajouté au circuit grâce à une chambre d'amortissement et des valves de résistance. Trois zones d'intérêt ont été filmées (sur deux fantômes) par PIV menant à des corrélations d'images de qualité variable en fonction des accès optiques et de l'état de surface des fantômes. Les résultats sont comparés à des simulations numériques menées sur les deux mêmes modèles en tant que confrontation *in vitro-in silico* préliminaire. Des tendances similaires sont observées au niveau des répartitions des écoulements. Les différences semblent liées à la non-correspondance des conditions limites de sortie entre l'expérience et le modèle numérique. Une optimisation des conditions limites serait nécessaire pour obtenir une parfaite correspondance entre les deux approches. Enfin, la visualisation 3D offerte par les simulations numériques amène des informations supplémentaires sur la structure des écoulements. Cela conforte l'idée de combiner numérique et expérience en tant qu'outils complémentaires pour l'analyse des écoulements hémodynamiques.

Montage in vitro



Fabrication des fantômes



4.1 Background

Aortic dissection (AD) is a condition in which the inner layer of the aorta tears. When blood surges into the tear, it can cause one or more layers to separate (dissect). The consequence is the build up of a "false" blood channel in between the dissected layers. The true (original arterial path) and the false lumen are separated by the intimal flap. The more blood penetrates into the layers, the more the intimal flap can expand in the antegrade and/or the retrograde direction from the tear. AD is a life-threatening condition involving weakened arterial walls, risks of breaking, false lumen thrombosis and malperfusion of organs (Nienaber et al. (2016)). Therefore, an increasing number of studies focus on understanding and improving diagnosis and surgical procedures to limit AD mortality. As described in chapter 1, hemodynamics plays a major role in the development and progression of AD. Flow and pressure distribution, wall shear stress, and recirculation areas affect the false lumen expansion and thrombosis formation. Among the *in vivo* observations with 4D-MRI, false lumen stroke volume and velocity, helical flow and distal entry tears appeared correlated with AD rapid expansion (Clough et al. (2012)).

However, *in vivo* data collection are limited by traditional medical imaging techniques (resolution, availability, price, late diagnose, etc.) and invasive measurement tool capabilities. It is therefore difficult to conclude on mechanisms that drive AD. Even though, 4D-MRI and 4D-flow assessments have considerably increased the knowledge of AD development and treatment as an excellent time resolved and volumetric imaging tool (Clough et al. (2012); Chen et al. (2021)), some important quantities of interest such as pressure and WSS are still difficult to evaluate (Stalder et al. (2008); Petersson et al. (2012)). Alternative techniques with numerical simulation and *in vitro* experiments can generate even more precise visualizations, providing that emulated environments are realistic (Armour et al. (2021); Bonfanti et al. (2020)).

In vitro, *ex vivo* and *in silico* are thus developed to address the shortcomings of *in vivo* investigations (Alimohammadi et al. (2015); Armour et al. (2021); Pan et al. (2020); Bäuml et al. (2020)). These alternative approaches are mostly implemented to obtain better visualizations of AD flows and multi-analysis possibilities (flowrate, pressure, wall displacements, etc.) with physical *in vitro* models and numerical simulations (Soudah et al. (2015); Birjiniuk et al. (2015); Faure et al. (2014); Rudenick et al. (2013)). One of the most complete model was proposed by Franzetti et al. (2019) and Bonfanti et al. (2020) who implemented an *in vitro* mock loop validation for a CFD numerical study on an AD model with patient specific geometry and rigid walls. Boundary conditions are accurately represented with a complex network of multiple Windkessel models to emulate patient-specific inflow and outflow conditions. However, the physical and numerical models, both lack from a non-Newtonian representation for blood. Regarding the outcomes of chapter 3 experiments and other studies from the literature (Deplano et al. (2014); Walker et al. (2014)), this feature is non negligible to accurately represent hemodynamical flows especially in a complex geometry such as the presented patient-specific AD model. To the author's knowledge, no study has combined *in vitro* circulatory mock loop that mimics *in vivo* pulsatile flow conditions, non-Newtonian blood mimicking fluid and patient-specific

AD phantoms. The designed aortic flow simulator in this study can address these features.

The current project is developed in parallel with another thesis on CFD and FSI models of AD flows with surgical simulation implementing catheter progressions and stent graft deployment (Pan (2021)). Data are collected thanks to a collaboration with the Hospices Civiles de Lyon on patients with AD and regular follow-up. One of the objectives of the present *in vitro* aortic flow simulator is to confront and validate those numerical simulations with physical models of the same AD phantoms. This chapter focuses on the following items:

- Adapt the previously designed mock loop to AD study.
- Manufacture patient specific AD models that suit the mock loop and PIV requirements.
- Visualize flows in the AD models with PIV, flowrate and pressure assessments.
- Confront *in vitro* data to numerical simulations.
- Draw conclusions on AD flow specificities and on the relevance of such *in vitro* tool to investigate them.

4.2 Aorta phantoms

To investigate aortic dissection cases on the mock loop, new phantoms have to be designed. The goal is to create phantoms with the same performances as the AA silicone phantom. As mentioned in chapter 2 section 2.4.3, it is difficult to find a manufacturer who can create silicone aorta model with our AD patient-specific geometry. Unfortunately, silicone injection and molding technique could not be applied to complex geometries such as AD. This issue comes from impossibility to extract the internal molds from the model once solidified because of the tortuous true/false channel configuration, model bulges and cavities. Therefore, we have investigated 3D printing methods to manufacture AD models for the circulatory mock loop. These methods will be described in section 4.2.2.

In this section, we describe the design of some **rigid and compliant 3D printed aortic dissections**. These models are used for case studies based on patients *in vivo* data and compared with numerical simulations. 3D printing allows rapid prototyping (48h) with limited cost compared to casting and silicone injection technique. In addition, it would be useful to rapidly manufacture a patient aorta and test it on the *in vitro* setup for surgery training and stent graft testing. However, regarding the present situation of 3D printing technologies, difficulties in manufacturing such complex geometries involve sacrificing some phantom properties. To our knowledge, the combination of good transparency and compliance on a phantom is hardly compatible with currently available 3D printing techniques and resins. Therefore, we choose to test both rigid and compliant AD models knowing their limitations. The rigid models (even if less realistic) are still useful for CFD numerical results simulation which are built with rigid walls.

4.2.1 Phantom properties and geometry

The phantom properties were addressed in chapter 2, section 2.4.1. As a reminder, targeted phantom characteristics are : patient-specific geometry, simplified geometry to main branches, transparent material, homogeneous material, rigid and compliant walls.

In the case of 3D printing, the advantage is to easily manufacture patient-specific geometry. The most precise 3D printing techniques regarding resolution and surface quality are resins printers. They are based on photopolymerization of a UV-sensitive resin. The resin is solidified when subjected to UV-light with a spot-by-spot or layer-by-layer enlightenment system until the desired shape is obtained. Different processes and resins exist on the market with varying qualities. The one that are used for this study are presented in appendix G. Refer to this section for a more detailed description of each process.

Combining transparent and flexible materials is difficult to achieve with currently available printing technologies. A series of tests were thus conducted with different printing technologies and resins to meet all the previously cited phantom requirements.

Geometry reconstitution was achieved in the same way as described in chapter 2. Refer to section 2.4.1 for more details. Three AD models (AD1, AD2, and AD3) and the AA reference model are presented in figure 4.1. The following paragraphs describe the process that led to the manufacturing of four AD phantoms (corresponding to three geometries AD1, AD2 and AD3). The AA silicone phantom used in chapter 3 experiments serves as a reference as its optical and mechanical properties fulfilled most of the requirements regarding biofidelity and PIV imaging compatibility. All the models characteristics are summarized in table 4.1. Among the models, only AD2 and AD3 were provided with 4D-MRI. These data allowed to extract the *in vivo* flow velocity fields. For AD1, only the model geometry was accessible with CT scans. AD1 was only provided with the patient CT-scan, therefore without flow information.

Table 4.1: Overview of aorta phantoms used in the current study with manufacturing techniques and features (Polyjet and DLP (digital light processing) technologies are described in appendix G). In code names, CT = CT-scans, index "c" indicates a compliant model and "r" stands for rigid.

<i>Manufacturing technique</i>	Casting	3D printing			
<i>Geometry</i>	Abdom. aorta	Thoracic aortic dissection			
<i>Patient case</i>	AA	AD1	AD1	AD2	AD3
<i>Phantom ID</i>	AAc	TAD0r	TAD1r	TAD2r	TAD3r
<i>Matrrial/Resine</i>	Silicone (compliant)	VeroClear (rigid)	Orthoclear (rigid)	Orthoclear (rigid)	Orthoclear (rigid)
<i>3D printer</i>	-	Polyjet	DLP	DLP	DLP
<i>Young's modulus</i>	0.53 MPa	-	-	-	-
<i>Refractive index</i>	about 1.40	1.51 (Wolfe et 2018)	1.496	1.496	1.496
<i>Available in vivo data</i>	geometry CT	geometry CT	geometry CT	geometry CT+ 4D-MRI flows	geometry CT+ 4D-MRI flows

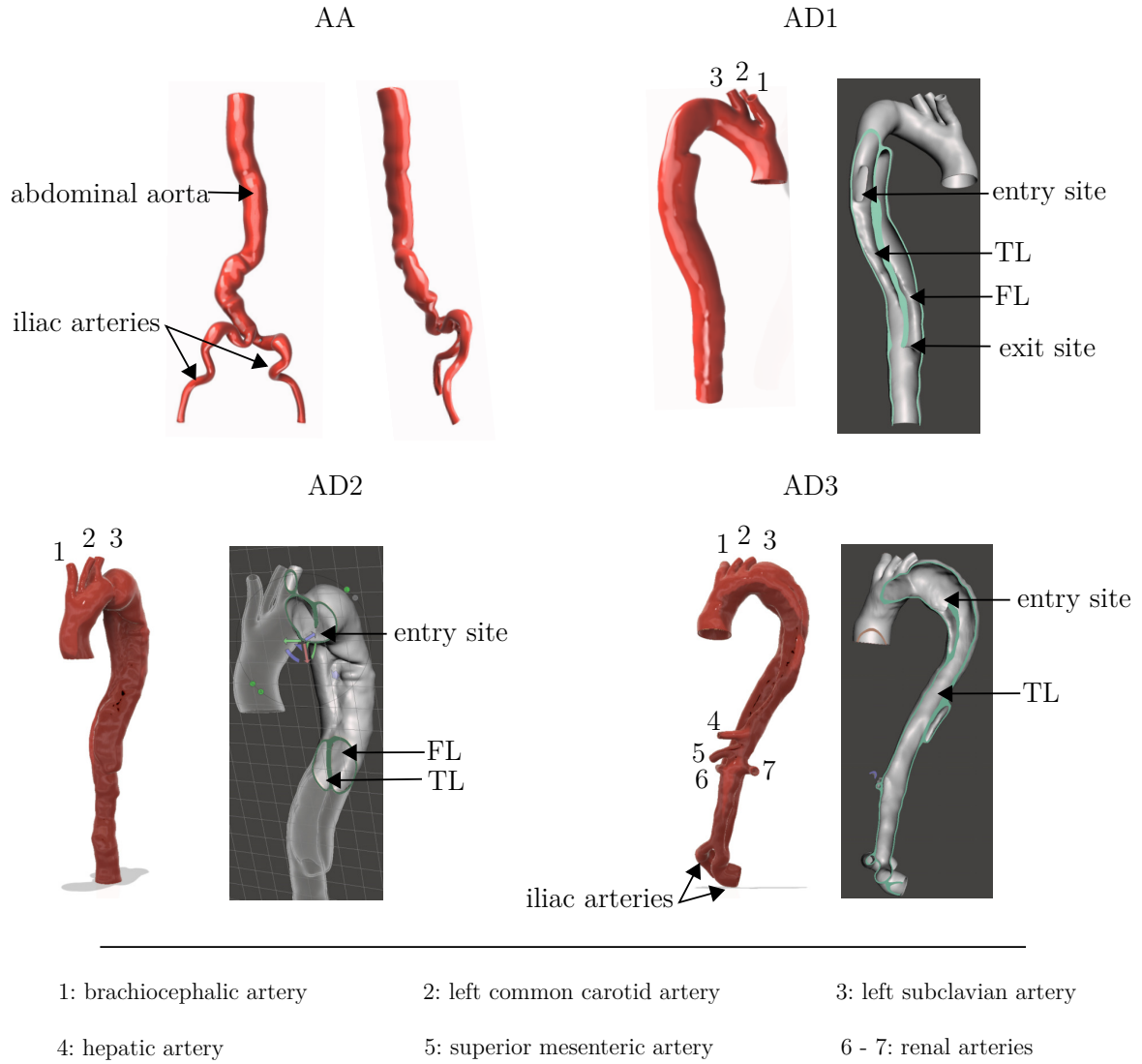


Figure 4.1: The four reconstructed and manufactured models. AA = abdominal aorta, AD= aortic dissection, TL = true lumen and FL = false lumen. The AA model was the one described in chapter 2 and 3 which serves as a reference regarding its mechanical and optical properties. AD1, AD2 and AD3 are aortic dissection cases that are targeted in this chapter 4. Their manufacturing is achieved with 3D printing.

4.2.2 3d printing testing approach

The testing approach for 3d printing transparent aorta models is described in the following steps. This approach is based on very qualitative appreciation criteria as it allows to quickly eliminate improper resin candidates with poor transparency or low mechanical resistance. Printed models observation and manipulation resulted on a shortlist of candidates that had good potential for being mounted in the circulatory mock loop (mechanical resistance) and PIV measurements (clear transparency). Once the shortlist established, more quantitative tests were conducted on the models to assess their mechanical and optical properties. Table 4.2 enumerates resin/printer candidates, the different companies or laboratory that printed the models and comparative qualitative appreciations of

transparency, resistance and flexibility. The testing approach steps are listed below and illustrated in figure 4.3.

1. **Selecting duo resins/printer candidates** capable of making compliant and transparent models. Some rigid resins were also selected for alternative solid model printing (also interesting for CFD comparison).
2. **Designing tube samples** with selected resins and techniques. Tubes were designed with a standard 25 mm inner diameter to fit the circulatory mock loop connectors. Thicker borders are designed to prevent cracks when clamping on the connectors.
3. **Qualitative estimation of transparency** to eliminate samples that are not suitable with PIV. The tube samples are immersed in the BMF with a refractive index of 1.40 (same BMF as for the silicone model). If the observer cannot read a ruler graduation through the model, it is eliminated from the candidate list.
4. **Mechanical resistance testing** under pulsatile flow. The sample tubes were mounted on the circulatory mock loop and submitted to a series of 50 cardiac cycles. Tubes that cracked or leaked during the trials were eliminated from the candidate list. The Siraya and Monocure3D tubes were very friable and cracked during mounting manipulation or at the very beginning of pressurization.
5. **Flow measurement with PIV** on the tube sample. It allows to eliminate samples with poor particle image quality and impossibility to conduct image correlation. It was observed that printing techniques processing with layers such as LCD (refer to table 4.2) produced models with visible layers. When capturing particle images with PIV, particles (20-50 μm fluorescent PMMA) appeared fragmented and/or with diffraction patterns. The printing layers (about 50 μm) seem to act as diffraction grating which significantly disturbed the image correlation process. This phenomenon was not observed with the polyjet models (refer to table 4.2) and is less pronounced with the DLP printed models (figure 4.2).
6. **Printing complete aorta models** with resin/techniques that passed all the tests. The targeted models correspond to the reconstitutions in figure 4.1.

Table 4.2 sums up the 3D printed models that were evaluated through the testings steps. Ultimately, two resin/printing technique pairs produced models with an acceptable transparency for PIV measurements : VeroClear/Polyjet and OrthoClear/SprintRay. Unfortunately both of them correspond to rigid printing resins. The TangoPlus resin with Asiga printer offered a good potential with an announced Young's modulus of 0.8 - 1.5 MPa (source: manufacturer) which is the range of human aorta elasticities. However, visible printed layers disturbed the cross correlation and the use of a coating to smooth the surface did not improve image quality. Moreover, regarding the size of the LCD printer, it would be difficult to print a full aorta model in one piece. It would need to be printed in 7 pieces and then bounded. Each bounding area resulted in local material non-homogeneity and alterations of the mechanical properties. Therefore, VeroClear/Polyjet and OrthoClear/SprintRay candidates were selected for printing full aortic dissection models based

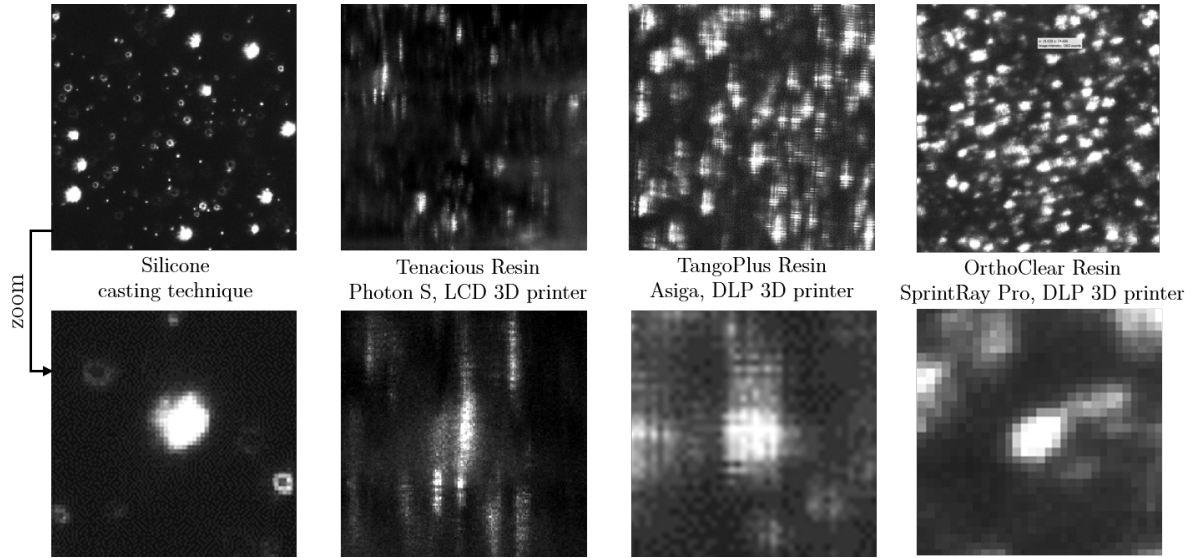


Figure 4.2: Image of particles with PIV trough 3 different models: the AA silicone phantom (high particle image quality), a Tenacious tube printed with LCD technology (poor quality), a TangoPlus tube with DLP technology (acceptable quality) and OrthoClear tube with DLP technology (good quality). All the tubes were immersed in the same BMF with the same particles and the same laser sheet illumination configuration.

on reconstruction from CT-scans. The available printer sizes allow to print the phantoms in two pieces. They were then bounded with epoxy glue for a perfect sealing. The region for bounding was pre-determined to avoid altering critical regions (entry exit sites, branches, etc.). Special care was taken to avoid roughness on the walls and to obtain a smooth surface. A total of four phantoms were obtained as announced in table 4.1 earlier in this section. Photos of AD1 and AD2 models are provided in appendix H. Complementary measurements on refractive indexes are then conducted to properly characterize them.

4.2.3 Refractive indexes

For the 3D printed models with Orthoclear resin, 3D cubes were also printed at the same time as the aorta models to fit the refractometer measurement cavity. This way, a direct RI evaluation is achieved. Prior the measurement, the cubes are polished with abrasive papers and successive finer steps (from P222 to P1000 grit). A similar process was achieved by the 3D model manufacturer to smooth the final phantoms. A final step consists in polishing the cube with a diamond suspension ($1 - 3 \mu\text{m}$) on a rotating disc pad to obtain a clear surface. The refractive index was evaluated as 1.496 which is much higher than the one set by the designed BMF and will demand for complementary optical corrections for proper PIV use (with calibration plate). Such high RI could not be matched with our standard BMF ingredients (refer to chapter 2 section 2.5.4).

The VeroClear resin is expected at $\text{RI} = 1.53$ (manufacturer data) but we've chosen not to use it for the experiments as the polyjet models have a grainy surface with a frosted glass effect. Orthoclear printing provides a much clearer material with an excellent surface quality thanks to the DLP printing technique.

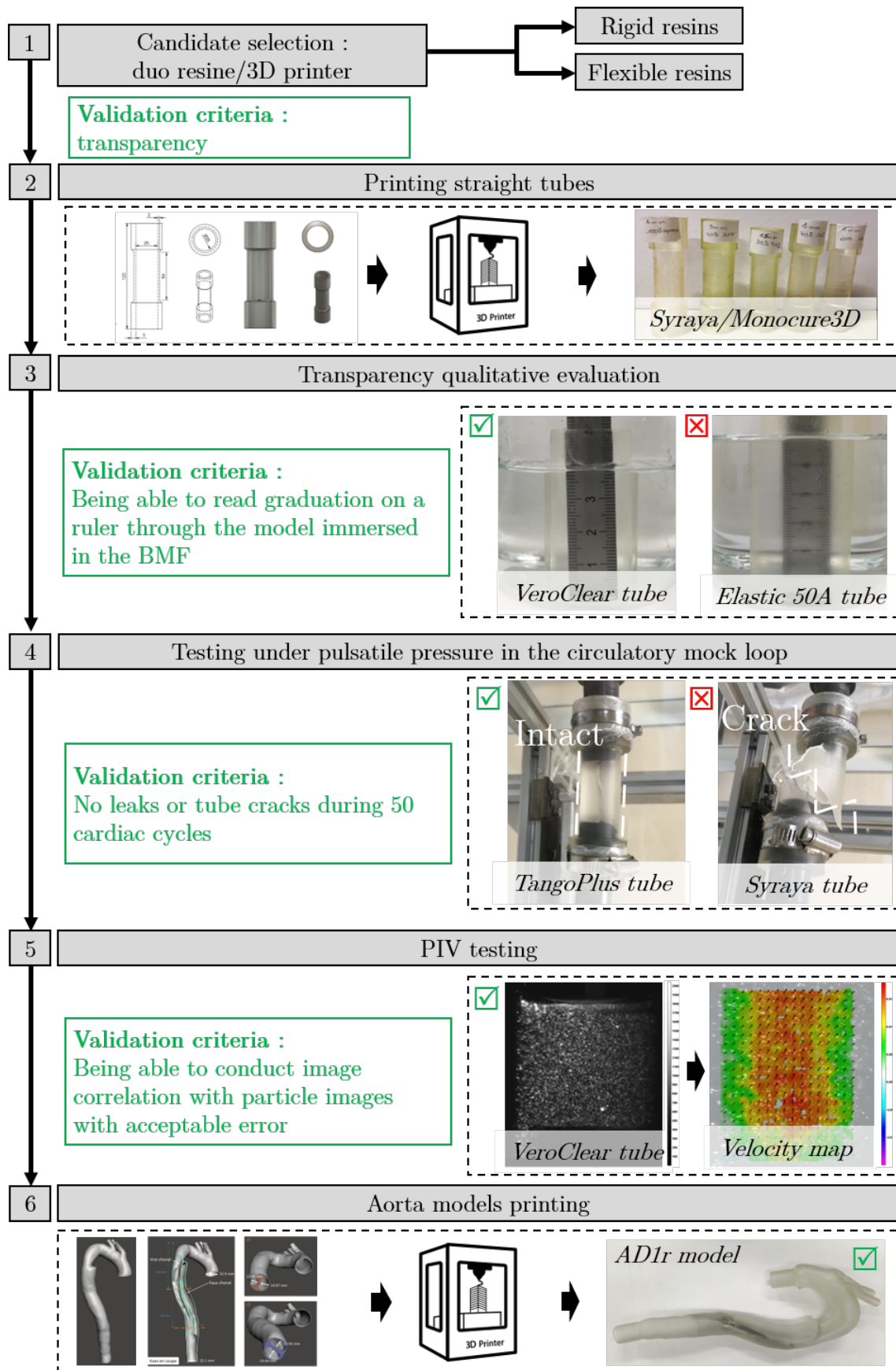


Figure 4.3: 3D printing resin selection approach for printing a complete aorta model. Steps are illustrated with resins that passed or failed the tests.

Table 4.2: Overview of tested resins and printers to design straight tubes that are tested on resistance to flow on the circulatory mock loop and qualitative scoring of material transparency from 1 to 5 (5 is the transparency level of our silicone molded model). The test step column indicates the step where the candidate was eliminated. (*) mixture of resins from 50-50%_{vol} to 70-30%_{vol}. (**) exact model not communicated.

Resin (manufacturer)	3D printer	Technology	Performed by:	Material resistance (qualitative)	Material transparency (qualitative)	Reached test step
Elastic 50A Resin (formlabs, USA)	form 2, formlabs	SLA	formlabs	Flexible and resistant	1/5	3
Flex 100, (Monocure 3D, Australia)	PhotonS, Anycubic	LCD	LMFA 3DRAION	Flexible and friable	1/5	3
3D Rapid Clear (Monocure 3D, Australia)	PhotonS, Anycubic	LCD	LMFA 3DRAION	Rigid and friable	1/5	3
Tenacious (Siraya Tech, USA)	PhotonS, Anycubic	LCD	LMFA 3DRAION	Rigid and resistant	3/5	4
Mix of Tenacious/ Monocure Flex*	PhotonS, Anycubic	LCD	LMFA 3DRAION	Flexible and friable	2/5	4
Veroclear, (Stratays, USA)	Polyjet, Strataysys	Material jetting	3DMEDLAB	Rigid and resistant	4/5	6
TangoPlus (Stratays, USA)	Polyjet, Strataysys +coating	Material jetting	3DMEDLAB	Flexible and resistant	1/5	3
TangoPlus (Stratays, USA)	Asiga, Kreos	DLP	3DMEDLAB	Flexible and resistant	3/5	6
OrthoClear (NextDent, Netherlands)	SprintRay Pro, SprintRay	DLP	3DMEDLAB	Rigid and resistant	5/5	6
Comparison with the silicone model						
Silicone (not communicated)	-	casting technique	Segula Technologies	Flexible and resistant	5/5	-

At the end of all those trials and processes to evaluate the compatibility with our PIV measurement, four AD phantoms with patient specific geometries were manufactured to be tested on the circulatory mock loop. Unlike the silicone compliant abdominal aorta model with a realistic young's modulus and excellent transparency, AD models could not be manufactured with the same technique because of their complex geometry (tortuosity and sinuosity). This non dissected model (AA silicone phantom from chapter 3) serves as reference model and is the best candidate to mimic aorta behavior and mechanical response to flow conditions in the simulator. The four other aorta phantoms were 3D printed with rigid resins and aortic dissection patient's geometry. A compromise had to be found between transparency and compliance in 3D printing techniques. Transparency is a non negotiable property as PIV measurements depend on it. We have chosen to have a less biofidelic representation of AD with rigid walls which remains valuable for validation of aortic flow CFD simulations (flow in a rigid walls domain).

4.3 Materials and methods

4.3.1 Experimental setup

To conduct the experiments on the AD models, the circulatory mock loop was adapted to deal with two new features of the phantoms: rigid walls and thoracic aorta geometry. Indeed, the location and number of branches lead to different circulation loops and connections.

The model geometry imposes modifications in inlet and outlet locations in the tank. The whole setup has been designed to adapt other artery configuration and each pipe and sensors can be easily moved with quick connectors. The new set up is presented in figure 4.4. Flowmeter and pressure sensors are located at the entrance and exit of the main aorta. No additional sensor were added for the three arteries emerging from the aortic arch. Flowrates will be deduced from inlet and outlet data. The laser now illuminates the phantom from the tank side while the camera images flow from the top of the tank. A Plexiglas panel is placed just above the tank fluid surface to avoid image distortions due to fluid surface oscillations during the experiment. This configuration makes it easier to image interesting planes such as those including aortic arch and dissection entry tears on all of the printed models.

Conversely with the compliant AA model, the dampening effect from the Windkessel theory cannot be ensured by the phantom itself. Indeed, the compliance of the AA phantom allows to dampen inflow conditions that were imposed by the solenoid valve to meet *in vivo* typical flowrate and pressure waveforms. It is characterized by a soften systolic phase, followed by a backflow phase and a diastolic phase resulting from restored energy by the phantom relaxation. In AD model cases, additional elements have to be implemented on the mock loop to mimic this dampening effect. Therefore, a compliance chamber is placed at the outlet of the phantom as shown on figure 4.4. As in previous experiments resistive valves are set at each outlet (aorta, left common carotid, brachiocephalic and left subclavian arteries) to emulate capillary bed resistance.

Solenoid valve programming, heat control in the reservoir and imaging process are kept

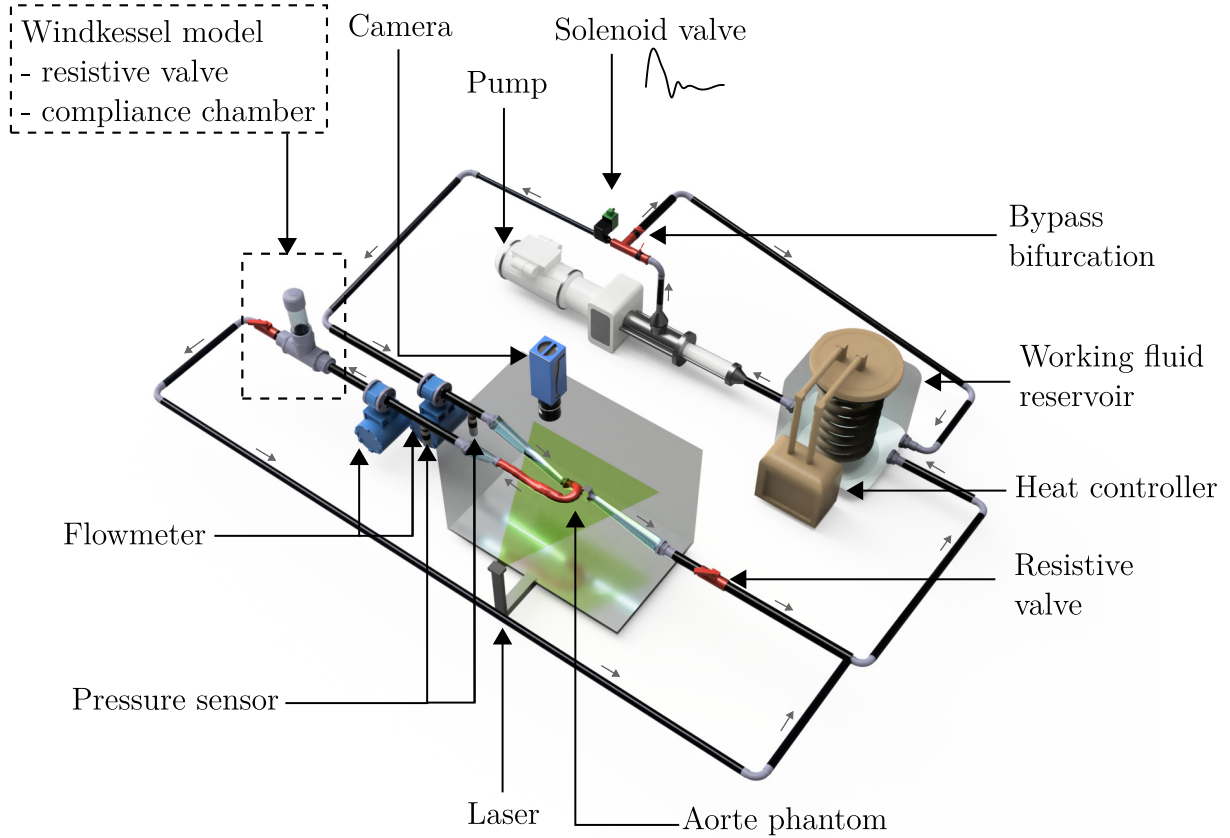


Figure 4.4: Experimental setup in the aortic dissection configuration. The global structure and elements are the same as in the experiments from chapter 3. A Windkessel compliance chamber model is added because the AD phantoms are rigid. The resistive valves are used to represent arteriolar and capillary bed resistances as in the configuration from chapter 3. The camera is placed on the top of the tank to easily image the aortic arch. The laser is therefore flashing from the tank side to illuminate a perpendicular plane to the camera axis.

the same as in previous experiments (chapter 3). The temperature variation throughout an experiment is in the range of 25 ± 2 °C. According to the conclusions from chapter 3 on Newtonian vs non-Newtonian BMF, we have adopted the non-Newtonian representation for the whole set of measurements in AD. The Newtonian version of the BMF is still used to fill up the tank where the phantom is immersed for optical continuity purposes.

A cardiac cycle with a period $T = 0.800$ ms is imposed thanks to the solenoid valve with a systolic peak flowrate of about 10 L/min. Resistive valves are partially closed to make 68% of the entrance flowrate go through the aorta and leave at the main exit. Therefore, 31% of the entrance flowrate is evacuated through the three aortic arch branches (figure 4.5). These distribution values are in accordance with clinical data from patients with AD2 and AD3 for whom we have 4D-MRI data. They also correspond to proportions in Bonfanti et al. (2020) on a patient with Type-B aortic dissection. Note that the delay between the inlet and the outlet waveform in figure 4.5 is not representative of the pulse propagation in the phantom. As shown on the setup design, series of rigid and compliant

tubes connect the phantom to the inlet and outlet flowmeters which are distant of about 1.5 m considering pipes length and the necessity to obtain established flow upward from sensors. A simple TT-method (refer to chapter 3, section 3.5.1) to compute PWV could not be applied on such multi-material piping system.

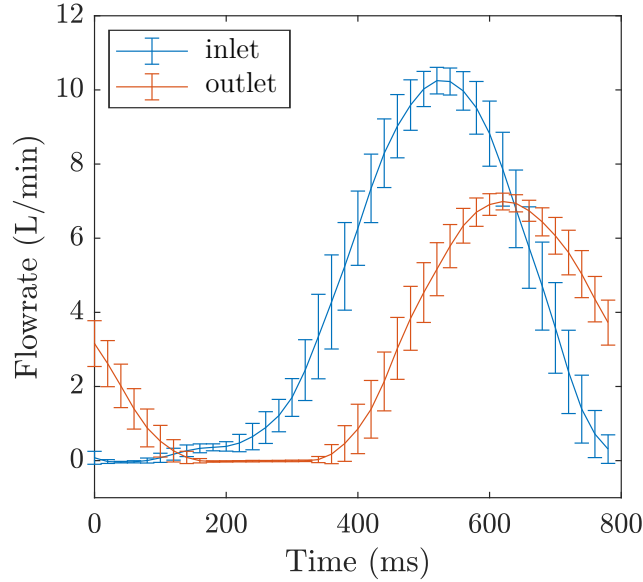


Figure 4.5: Inlet and outlet flowrate imposed in the mock loop for AD experiments. The mean and standard deviation are provided for 6000 successive cycles.

4.3.2 PIV measurements

Particle image velocimetry was conducted on two AD models (AD1 and AD2). These regions were chosen as critical locations of flow disruption in dissection cases including the true, the false lumen and the entry tear:

- **AD1:** two regions were imaged in the AD1 phantom. AD1_ROI1 is located at the dissection entry tear. The field of view contained the entry tear, true and false channel as shown in figure 4.6. This region does not provide clear view of the particles. Some reflections occurred on the intimal flap surface resulting in overexposed areas. Moreover, the surface quality is less smooth in this region and some particle images appeared blurry. A second region AD1_ROI2 was shot to visualize the entrance in the phantom and possible generated vortices due to the circuit connector. ROI2 has a less complex geometry with less optical deformations due to the phantom material surface.
- **AD2:** Only one region was imaged on AD2, it corresponds to the false channel view. This region offers a very clear surface with high quality particle images. A strong narrowing in diameter should provide interesting flow behavior regarding acceleration path and vortex formations (figure 4.7). Unfortunately, other regions could not be imaged with this phantom because it broke in the glued regions between the phantom two pieces.

In both phantom experiments, the particles, PIV equipment and process described in chapter 3 are implemented with the synchronization mode (solenoid valve/PIV synchronization). 12 cycle instants are targeted to describe the cardiac cycle. For each instant 500 pairs of images are shot to compute velocities and reach a good statistical convergence. Thanks to this technique, the time lapse Δt is set for each cycle instant as a large variety of flow velocities are observed throughout the cycle. This Δt adaptation enhances cross-correlation quality as each instant is treated separately with its own optimal parameters. Table 4.3 shows PIV imaging parameters and corresponding cycle instants.

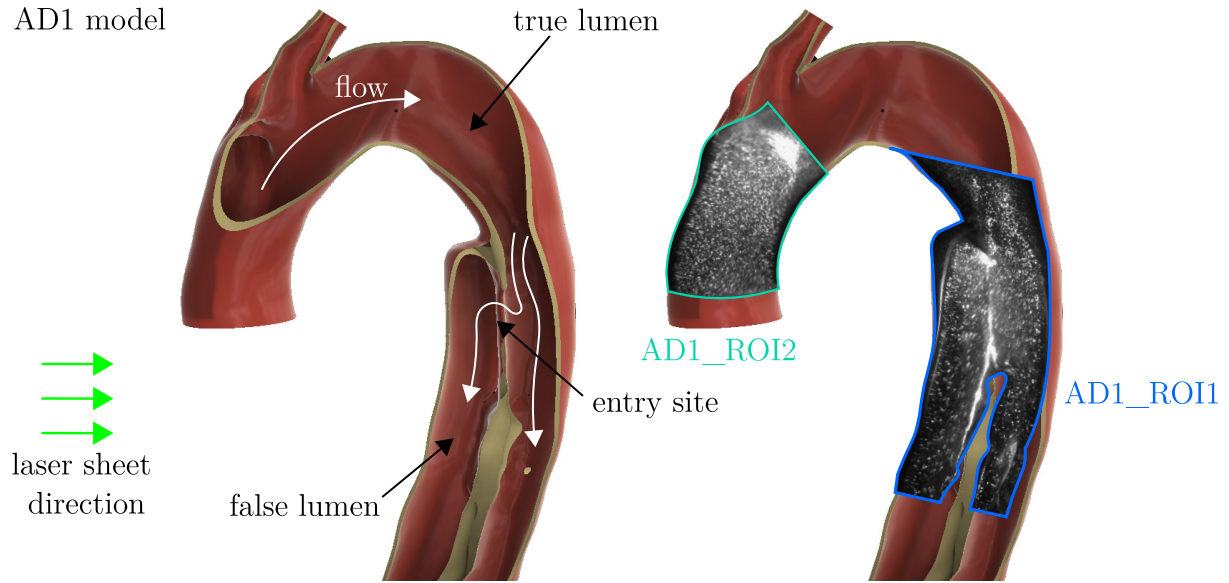


Figure 4.6: ROI for AD1 phantom. ROI1 includes both the true and false channel with the entry tear that communicates between them. ROI2 was imaged to have an overview of the phantom entrance flow which can be affected by the connector configuration.

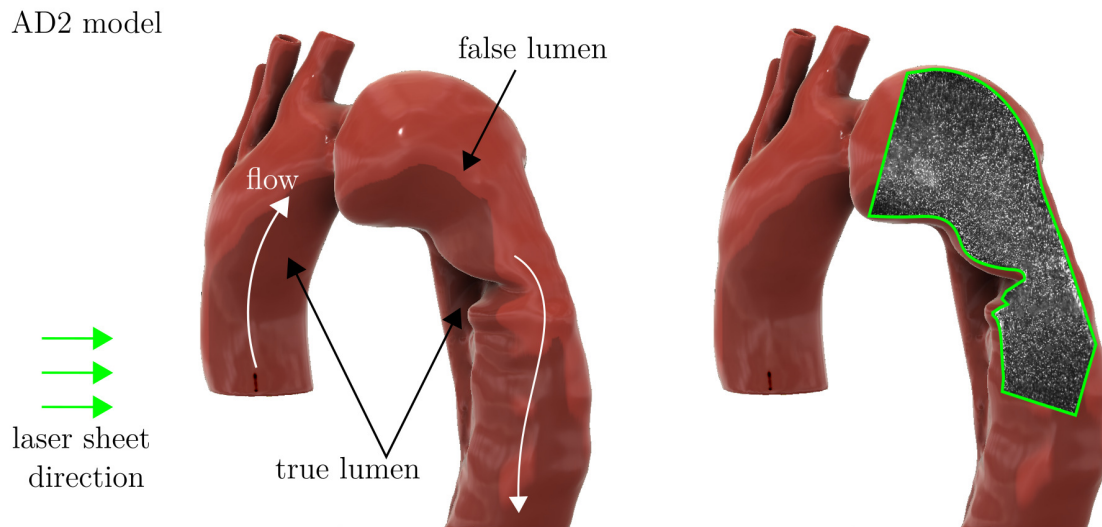


Figure 4.7: ROI for AD2 phantom. Only the false channel was imaged in a curved and strongly narrowed region. The entry tear is at the back of the imaged plane.

Table 4.3: PIV synchronization parameters to image 12 cycle instants throughout the cardiac cycle in all AD models. There is an exception for AD1_ROI2 where there are only 200 pairs of images per instant.¹

Cycle instant "k"	1	2	3	4	5	6	7	8	9	10	11	12
Cycle time (ms)	0	40	80	120	160	200	240	300	400	500	600	700
Number of acquired images/cycle	500	500	500	500	500	500	500	500	500	500	500	500
Total number of acquired cycle/image	6000											

4.3.3 Image post-processing

Images are then processed with Davis 10 software (Davis10 (2017), LaVision) to compute vector fields. In AD phantom cases, walls do not move anymore, therefore no wall tracking algorithm was applied to the images. Images are masked out with a geometric mask defined with a lasso tool on Davis 10 to deactivate walls and background pixels (out of the flow domain). Image cross-correlation is performed with a multipass method on the non-masked area limited to the aorta lumen (as explained in section 3.2.3). The first pass is achieved with a 64x64 pixels interrogation window with a round Gaussian weight. The second and third pass consist in 16x16 pixels interrogation windows for AD2 and 24x24 pixels windows for AD1, both with a round Gaussian weight and 75% overlap. For each field, missing vectors (less than 1% of computed vectors) are filled up with a polynomial interpolation algorithm and a 3x3 smoothing filter is applied.

Table 4.4: Information about PIV images and velocity fields post-treatment resolutions and uncertainties.

	AD1_ROI1	AD1_ROI2	AD2-ROI1
Field of view (mm x mm)	89.32 x 75.37	82.7 x 69.78	81.59 x 68.84
Pixel size (pixel/mm)	28.66	30.96	31.38
Interrogation window (pixel x pixel)	24 x 24	24 x 24	16 x 16
Interrogation window (mm x mm)	0.84 x 0.84	0.78 x 0.78	0.51 x 0.51
Mean velocity uncertainty (m/s)	2.10^{-3}	5.10^{-3}	1.10^{-3}
Max velocity uncertainty (m/s)	1.10^{-2}	2.10^{-2}	3.10^{-3}

The final resolution of velocity fields is expressed as the interrogation windows size (table 4.4). An example of statistical convergence graph focusing on an interrogation window near the narrowing area in AD2 is provided in figure 4.8. 400 images are needed to

¹less images were taken in this area as it was only shot for qualitative observation on the connector emerging flow. AD1_ROI1 was the main region of interest.

reach velocity field statistical convergence in the worst case scenario. When considering mean velocity fields from a whole set of 500 images to ensure statistical convergence, velocity uncertainties are calculated and provided in table 4.4. Mean velocity uncertainty corresponds to the mean uncertainty observed in all the computed instants while the maximum uncertainty corresponds to the worst error in an interrogation window among all the imaged instants. Finally, as in chapter 3 vector field post-processing is performed with a custom MATLAB script to compute and analyze quantities of interest (shear rate, shear stress, swirling strength, etc.).

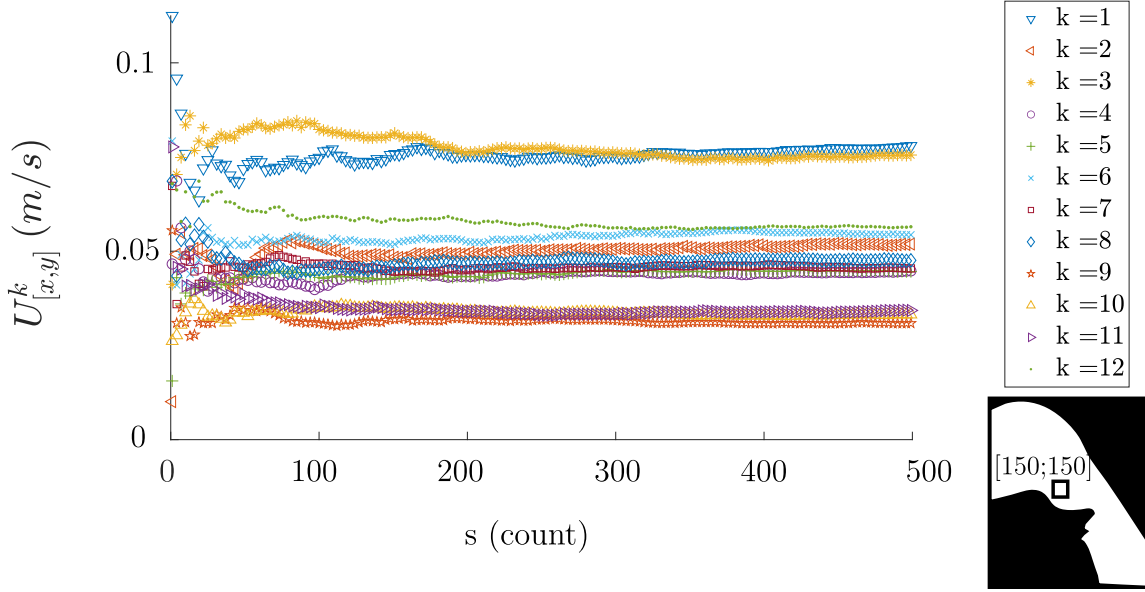


Figure 4.8: Statistical convergence graph in ROI1 from AD2 phantom. The velocity in interrogation window $[x; y] = [150; 150]$ indicated for every cycle instant depending on the number of images taken into account. These coordinates are provided as an example, other coordinates convergence graphs are similar. About 400 images are needed to reach statistical convergence in the worst case scenario.

4.4 Flow analysis: AD1 case

4.4.1 Flow distribution

The AD1 case was imaged with two regions of interest. The first one was located at the entry tear of the dissection (AD1.ROI1) and the second one at the entrance of the ascending aorta (AD1.ROI2). The two regions have different shapes with more or less optical access to conduct PIV.

AD1.ROI1

The dissection tear region was imaged such that the false and true channel were visible as well as the entry tear that communicates between them. Figure 4.9 shows the velocity

maps for a few instants. The other instants are not shown due to light disturbances showing up during the experiment and images poor quality.

The entry tear and the intimal flap were tricky regions to image as more pronounced curvatures and larger phantom wall thickness were applied to reach this complex shape. The apparent large thickness of the intimal flap is due to calcification of the patient's vessel. The phantom had a large separation between the two channels that generated a lot of light reflections for the PIV laser sheet. Those reflections were visible in the camera and induced overexposition. In the cross-correlation process these regions mostly correspond to purple areas where an almost null velocity was computed. This blind region is indicated by a white dashed area on $k = 7$ map (figure 4.9). Slight movement of the phantom depending on the cycle instant changed this blind zone due to different reflections on the flap. The presented results correspond to experiment where reflection did not prevent to compute velocities in this region. This is the reason why some cycle instants are missing from the results. We may not guaranty that the laser sheet was not distorted in this particular region. Results are provided with a high uncertainty on velocity fields (refer to table 4.4).

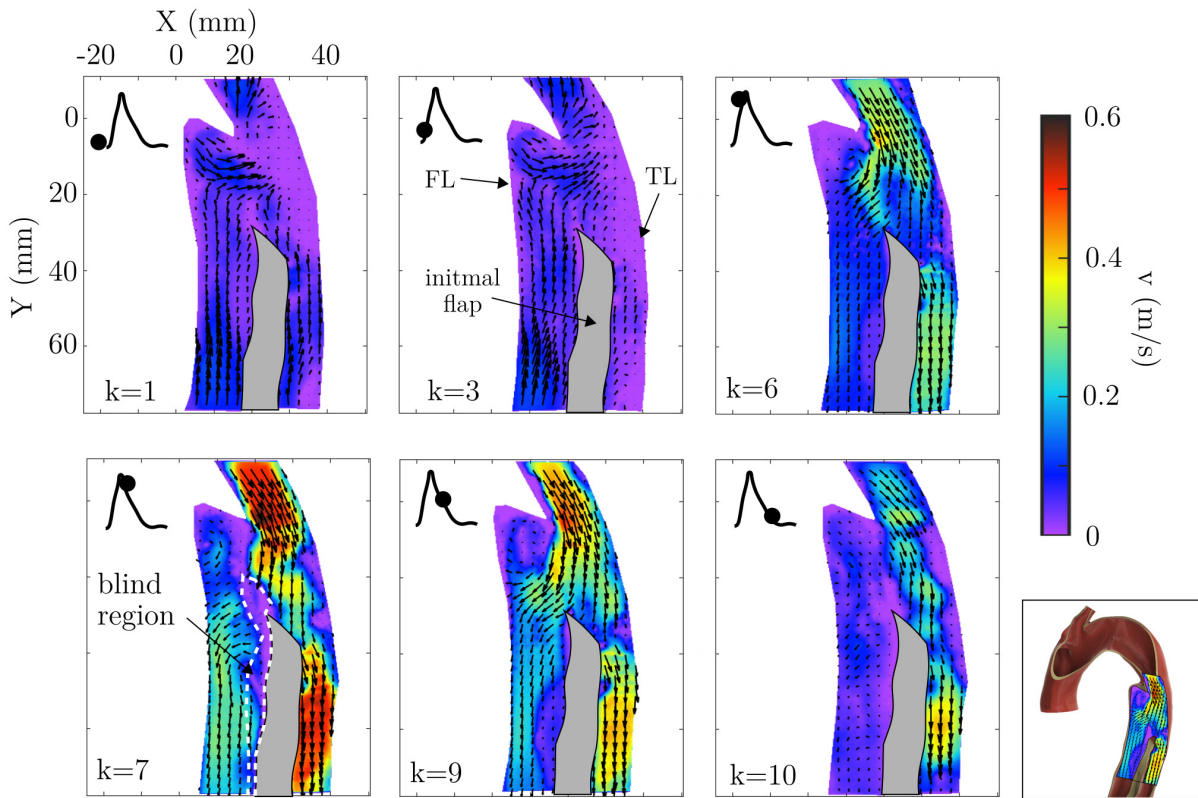


Figure 4.9: AD1_ROI1 velocity fields. Each field is the mean velocity field computed for 500 images at each instant. Arrows indicate the mean velocity field in the imaged plane. The bottom right image shows the ROI location in the aorta phantom.

Still, a global flow distribution analysis can be conducted on those images. The first interesting observation concerns differences in forward and backward flow phases. During

forward flow phases ($k = 4$ to $k = 10$), higher velocities are observed in the true lumen while in backward flow phases, the false lumen seems to take the lead to drive the fluid. Another interesting observation is that a swirling structure appears in the bulged region on the top of the false channel. It is clearly visible in $k = 9$ but can also be observed in $k = 1, 3, 6$ and 7 . Finally, we may notice that the near flap velocity field in the false lumen is particularly low in $k = 6, 7, 9$ and 10 . When looking at the CT-scan data the flap was suspected to be calcified because of its substantial thickness. This near wall stagnation area observed with PIV can be related to the deposit of plaque and thus thickening of the flap. Further investigation should be conducted to confirm this hypothesis such as wall shear stress analysis which is difficult to compute with the poor image quality in this region.

This description shows overall trends in flow distribution between the true and false channel. Because of the poor PIV images, it is difficult to conclude with further analysis. However, those trends will be compared to numerical simulations later in this chapter to confirm those observations.

AD1_ROI2

The entrance of the aorta was imaged with the purpose of visualizing inflow conditions in the phantom to investigate the risk of flow disturbance near the connector. Moreover, with this more simplistic geometry, we may evaluate if the phantom material is unadapted to PIV or if it is more related to geometrical features such as tricky optical diopter shape and surface quality as in AD1_ROI1 case. Velocity maps are provided in figure 4.10 for 11 cycle instants. The position in cycle is indicated at the top right of each map. The connector shape is represented on $k = 8$ map. We expect the transition between the connector and the aorta to generate flow disturbances and vortex ring development.

Throughout the cycle, the pulse ejection into the aorta entrance is visible from the early systole to the systolic peak ($k = 4$ to $k = 7$). A high velocity path emerges in the center of the entrance and pushes the fluid toward the left wall (external curvature of the aortic arch) with lower velocities on the right side (internal curvature of the arch). These distributions are the most pronounced in $k = 7$ and $k = 8$. Note that late systole is the cycle period where rapid changes in velocity fields occurs. The pattern in $k = 8$ is very different from $k = 9$, where the flow main orientation changes with the development of a swirling structure near the left wall. This rapid change in pattern was also observed in the abdominal aorta case from chapter 3 with complete velocity fields in appendix D (the transition from $k = 4$ to $k = 6$ in both Newtonian and non-Newtonian cases). In $k = 2$ and $k = 3$, velocities are oriented on the top left direction which corresponds to the brachiocephalic artery when referring to the global view at the bottom right of figure 4.10. It may suggest that, during lower velocity phases, the fluid tends to fuel aortic arch branches while during high velocity phases the fluid preferential path follows the aorta lumen. However, a more precise view of the arch branches would be needed to conclude but these ones are difficult to image due to limitations in optical access (obstructed by branches connectors).

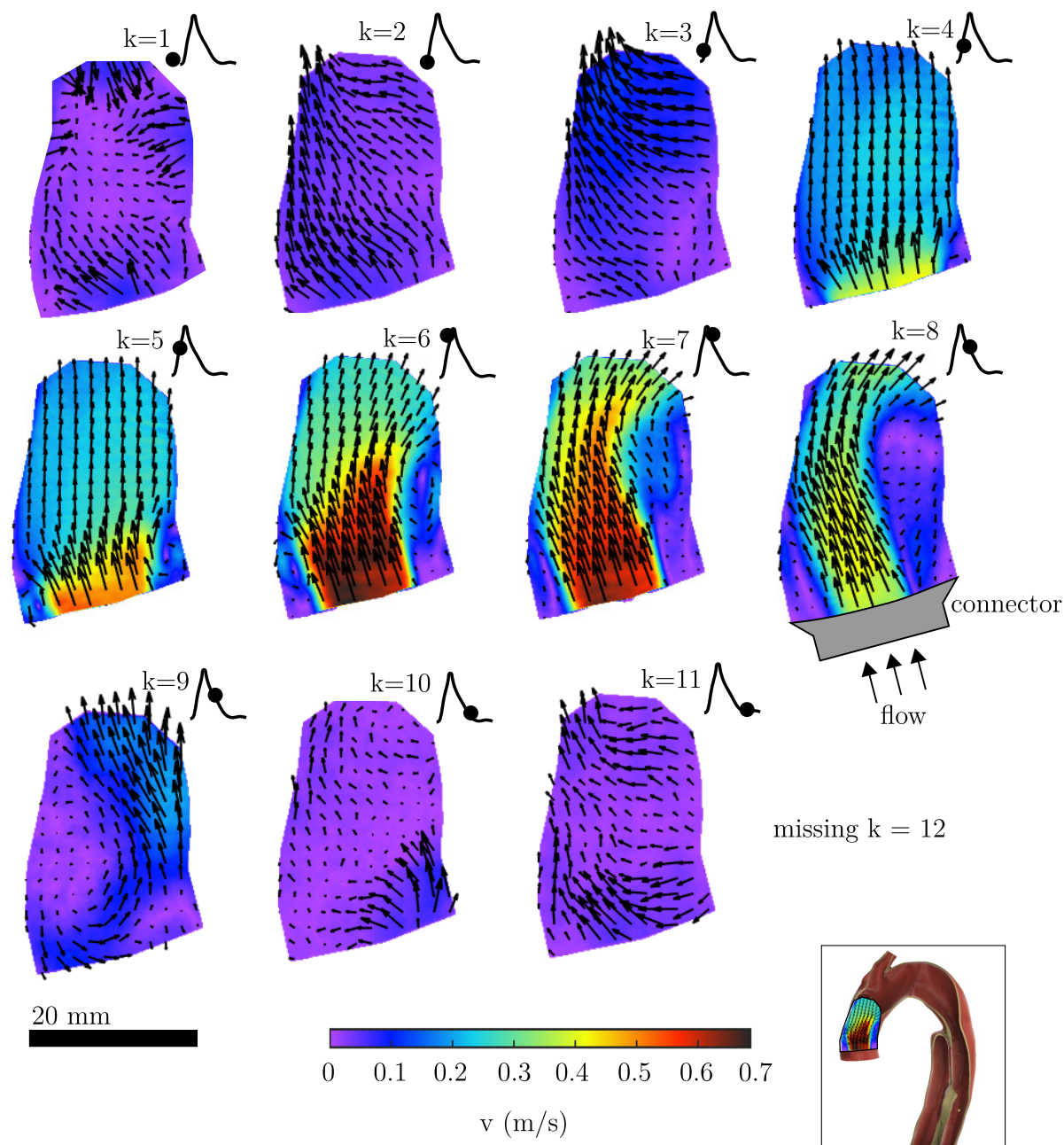


Figure 4.10: AD1_ROI2 velocity fields. Each field is the mean velocity field computed for 200 images at each instant.

4.4.2 Vortices

When zooming into the velocity fields obtained from PIV measurements, vortices develop at the entrance of the phantom on the two sides of the high velocity path. This pattern is typical of divergent pipe which corresponds to the shape of the connector/aorta transition. Maps with magnified velocity fields are shown in figure 4.11. To follow the vortex ring development, vorticity is computed and shown in figure 4.12. Vorticity is expressed as the Z direction vorticity (perpendicular axis to the imaged plane) and is computed with the definition from equation 4.4.1 applied on the discrete velocity fields. Before $k = 4$, no intense vorticity is observed in the ROI. From $k = 4$ to $k = 8$, a vorticity pattern emerges from the entrance of the phantom and rises up following the aorta longitudinal direction. At $k = 9$, the vorticity patterns dissipate. When comparing with the velocity fields maps (figure 4.10), the two vorticity pathes (blue and red) correspond to the borders of the high velocity path. It seems that this high velocity path generates vorticity in the near wall flow. Instant $k = 9$ also corresponds to the rapid change in velocity pattern which seems to dissipate vortices. For more details on the vorticity computation and comparison with the swirling strength criteria, refer to appendix E.

One of the questions raised by these vorticity patterns observation is : do the vortices come from the shape of the connector or from the pulsatile nature of the flow ? Indeed, the pulsatile flow generates alternative upward and backward flow phases that could induce flow coiling and vortex rings formations. To investigate these vortices, a steady flow experiment was conducted on AD2 phantom and AD1.ROI2 was imaged. The results showed the same vortex rings development on left and right sides of a central high velocity path (not shown here). The vorticity patterns similar to $k = 7$ case in figure 4.10 are observed. The experiment tends to show that the connector is responsible for the vorticity pattern. The connector's shape influences flow distribution. To compare *in vivo*/*in silico* and *in vitro* data, one may question the bias induced by the connector.

$$\vec{\omega} = \nabla \times \vec{u}, \quad \omega_z = \frac{\partial u_y}{\partial x} - \frac{\partial u_x}{\partial y} \quad (4.4.1)$$

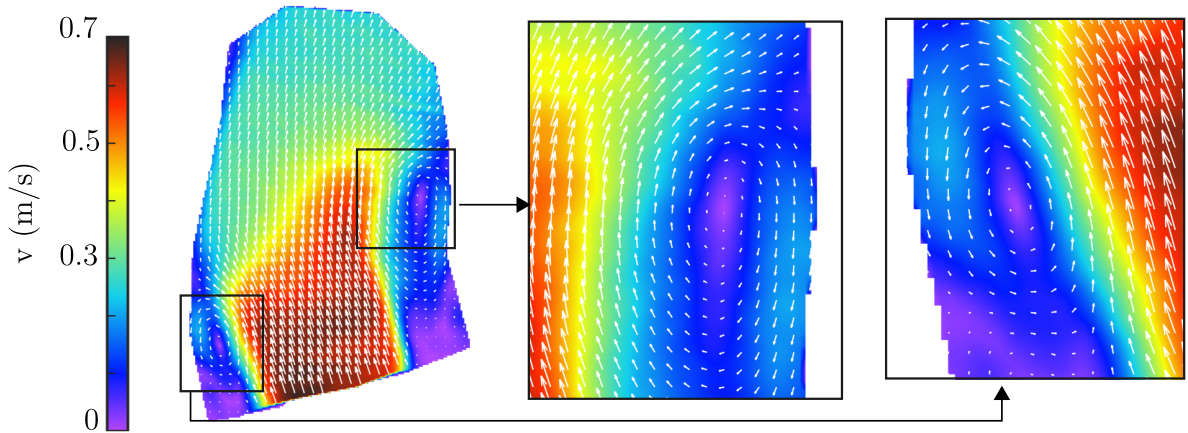


Figure 4.11: Maps zoom-in on vortex ring on AD1.ROI2 for $k = 6$. Two vortices are identified near the left and right walls.

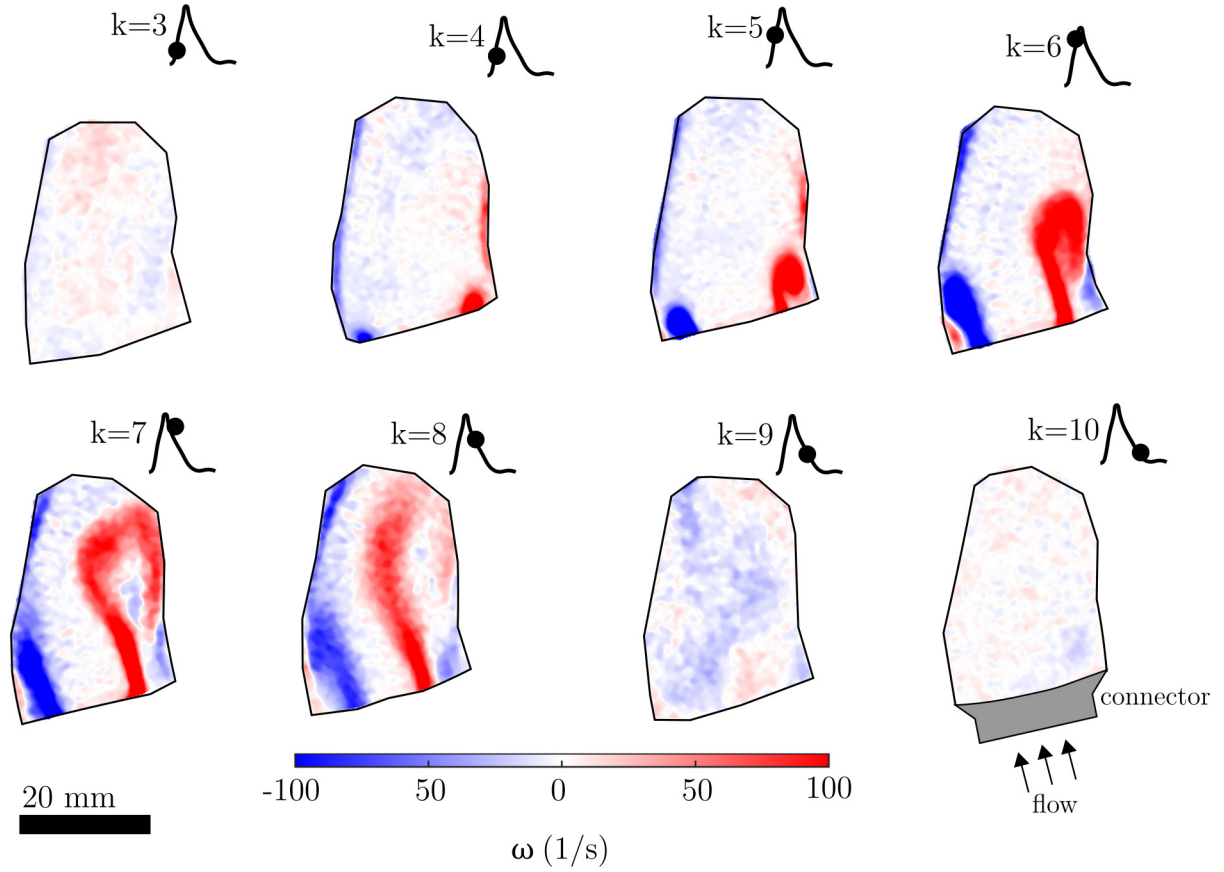


Figure 4.12: AD1_ROI2 vorticity maps. Each map is the mean velocity map computed for 200 images at each instant. The vorticity maps are calculated based the velocity maps in figure 4.10. The connector shape is illustrated on the $k = 10$ map.

Nevertheless, in human heart, a non-smooth connection between the heart and the aorta results from the valve transition. *In vivo*, similar vortex rings are observed in the ascending aorta at the sinus of vasalva region (outlet of the LV valve toward the ascending aorta). Vortices also emerge in the inner curvature of the arch (Natsume et al. (2017)) as observed on our phantom in $k = 8$ (figure 4.12). The current *in vitro* experimental observations are actually very similar to the flow distribution, vortex location and recirculation patterns observed in patients *in vivo*. The valve transition in human heart could be associated with our connector transition and completely smooth connector would not well represent the *in vivo* configuration.

4.4.3 Discussion and limitations

These two examples in AD1 highlight the difficulties in manufacturing a phantom compatible with PIV imaging requirements. Indeed, optical access to regions in the phantom were limited. In AD1_ROI1, PIV was focused on the entry tear region. The tricky shape and thickness of the intimal flap induced light distortions and reflections in the region generating blind areas for the camera. Results were provided with high uncertainties and blind areas did not allow to conduct a proper analysis on the tear region. Some optical

issues were expected as the printed phantom surface quality was less smooth in regions with non straight geometries such as the entry tear, the arch branches and the intimal flap. Moreover, conversely to AA silicone model experiments, the fact the phantom refractive index (about 1.50) and the BMF one (about 1.40) are different did not prevent light refraction and reflection problems. However, regarding the BMF composition, we did not find a way to maintain sufficient shear-thinning properties while matching the index of the 3D printed phantoms. These results are encouraging regarding the feasibility of PIV measurements in more complex phantom geometries. But the main limitation seems to be the phantom quality because of optical disturbances.

Moreover, regarding the PIV set up configuration, the same process as in chapter 2 section 2.3.2 was used. The tank was filled up with a fluid with the same RI than the BMF that loops in the circuit. Optical corrections were then applied with a calibration plate placed in the tank at the location of the laser sheet before inserting the phantom. These corrections were applied on all the experiments of this chapter. However, they do not take into account the phantom walls but only Plexiglas tank and fluids.²

In what follows, much higher quality results are obtained in AD2 because of better phantom surface quality and optical accessibility to regions of interest. The next section focuses on AD2 flows in the false channel.

4.5 Flow analysis: AD2 case

4.5.1 Flow distribution

AD2 case is a very interesting configuration with a strong narrowing (54% reduction) on the imaged false lumen. The shape and surface of this phantom's false lumen has a better quality than in AD1. Moreover, the incident angle of the laser sheet was less prone to reflections and refraction. Therefore, PIV images could be computed with interrogation windows down to 16 x 16 pixels resulting in higher resolution velocity fields. Moreover, computed velocity uncertainty was also better with a mean and maximum velocity uncertainties of 1.10^{-3} m/s and 3.10^{-3} m/s respectively. This high image quality and resolution allowed to visualize and compute more precise quantities of interest including velocity, shear stress, viscosity and streamline maps.

Velocity fields are presented in figures 4.13 and 4.14 for the 12 cycle instants. Corresponding position in the cycle curve is indicated for each field. Flows are described with strong differences between the upper (pre-narrowing area) and lower regions (post-narrowing area) where different patterns are observed depending on the cycle phase. During pre and early systolic phases ($k = 1, 2$, and 3), a large swirling structure is observed just before the narrowing region. Low velocity flows settle in the post narrowing region (almost stagnant) while a global backflow occurs upward from the diameter reduction. Around the systolic peak (from $k = 4$ to $k = 7$) a high velocity path develops in the narrowing and fuels the post-narrowing region. This particular channel geometry

²The ideal solution would be to insert a calibration plate in the phantom to computed optical corrections. In-house designed plates were manufactured for that purpose but were very difficult to insert in rigid tortuous AD model. This technique was not retained.

originates from the left wall curvature which deviates the flow and forces it in the reduced lumen. During systole, the accelerated velocity region moves from the inner curvature near the left wall to the right wall in the post-narrowing region. During late systole ($k = 8$ and $k = 9$), the flow coils just below the narrowing area as in typical divergent section pipe flows. Recirculation appears in this post-reduction region and a vortex is created. Finally, during diastole ($k = 10$ to $k = 12$), we observe the backflow phase starting from the lower part of the phantom where the flow goes up in the channel to fuel the upper region. During this flow rising phase, the upper region flow appears almost stagnant and all the swirling patterns disappear. In the lower region, the flow has very sharp, organized and parallel streamline structures as in a laminar flow.

4.5.2 Shear quantities and vortices

Shear rate and shear stress were computed with the same method described in chapter 3 section 3.3.5. The working fluid is the non-Newtonian BMF with the same shear thinning properties as in experiments from chapter 3. Figure 4.15 shows shear stress maps for the 12 cycle instants. Overall, higher intensity shear stress are observed in the region of the narrowing and in regions where vortices were observed on velocity fields (figure 4.13 and 4.14). These areas correspond to higher velocity flows, fluid accelerations, and recirculation zones with significant velocity gradients. During diastole ($k = 10$ to $k = 12$), shear stress is much lower in accordance with a less chaotic flow observed on velocity fields with stagnant regions and absence of vortex.

Note that, the fluid flow is shear-thinning which involves a non-linear relationship between viscosity and velocity gradients. In line with this non-Newtonian approach, viscosity maps were drawn thanks to the relationship between the shear rate ($\dot{\gamma}$) and the shear-dependent viscosity ($\mu(\dot{\gamma})$) given by the non-Newtonian BMF rheology study (refer to chapter 3 section 3.3.5). Figure 4.18 shows viscosity maps at four distinct instants over the cycle. These instants were chosen as representative of different cycle phases and velocity patterns (from early to late systole and diastole). Because of the shear thinning property of the BMF, lower viscosities are expected in high shear rate regions, therefore in vortex areas, near walls and in the narrowing region. The obtained viscosity pattern meets these expectations with accentuated near wall lower viscosities (high shear rate) in the narrowing region especially along the left wall where the diameter reduction occurs and the flow is deviated. Stagnation flow (low shear rate) is also identified by the high viscosity regions at $k = 1$ (lower part) and $k = 12$ (upper part).

Finally, vortex maps are presented in figure 4.16 for the same four instants as in viscosity maps in parallel with streamline maps in figure 4.17. The two main vortices are clearly identified upward ($k = 1$, blue rounded shape) and then backward ($k = 9$, red rounded shape) from the narrowing area with the transitional phase in $k = 4$. The vortices have opposite signs with flow opposite rotational directions. This orientation is dictated by the coiling of the high velocity path when passing the narrowing region in upward and then in backward direction. As expected, in $k = 12$, no major high vorticity region is observed as no swirl were observed in velocity fields with mainly stagnant and in-line flow.

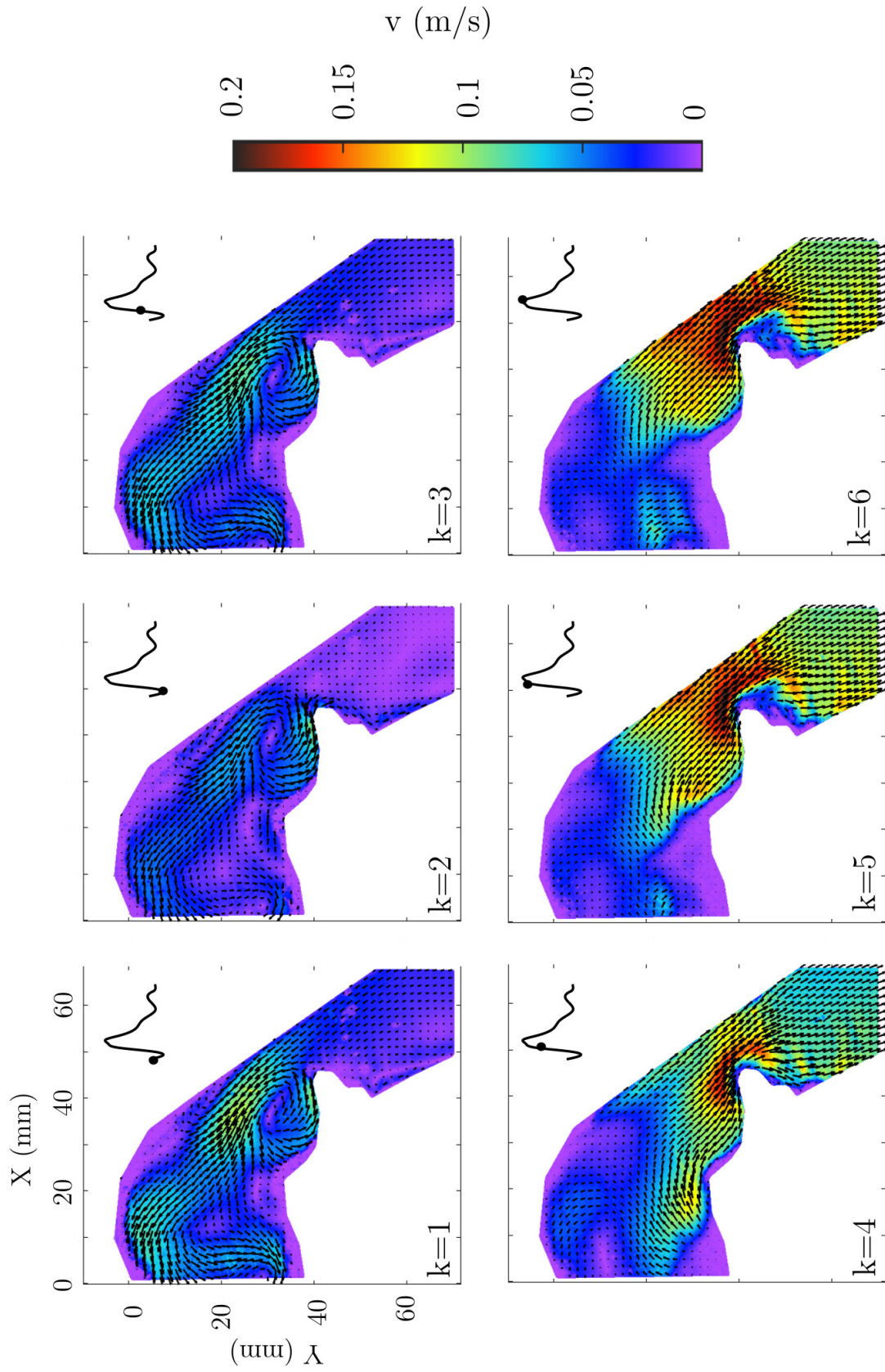


Figure 4.13: AD2 velocity fields. Each field is the mean velocity fields computed for 500 images at each instant.

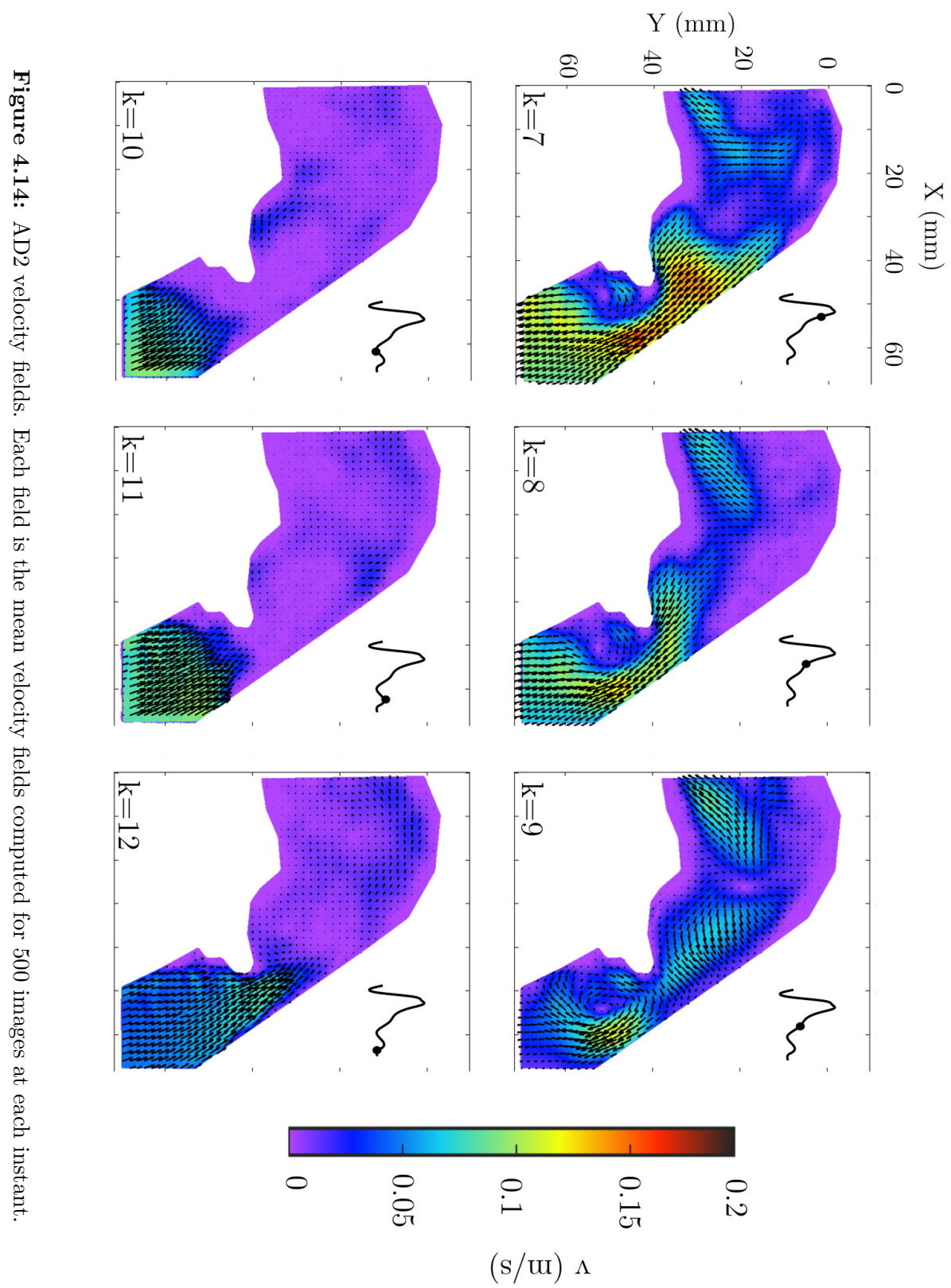


Figure 4.14: AD2 velocity fields. Each field is the mean velocity fields computed for 500 images at each instant.

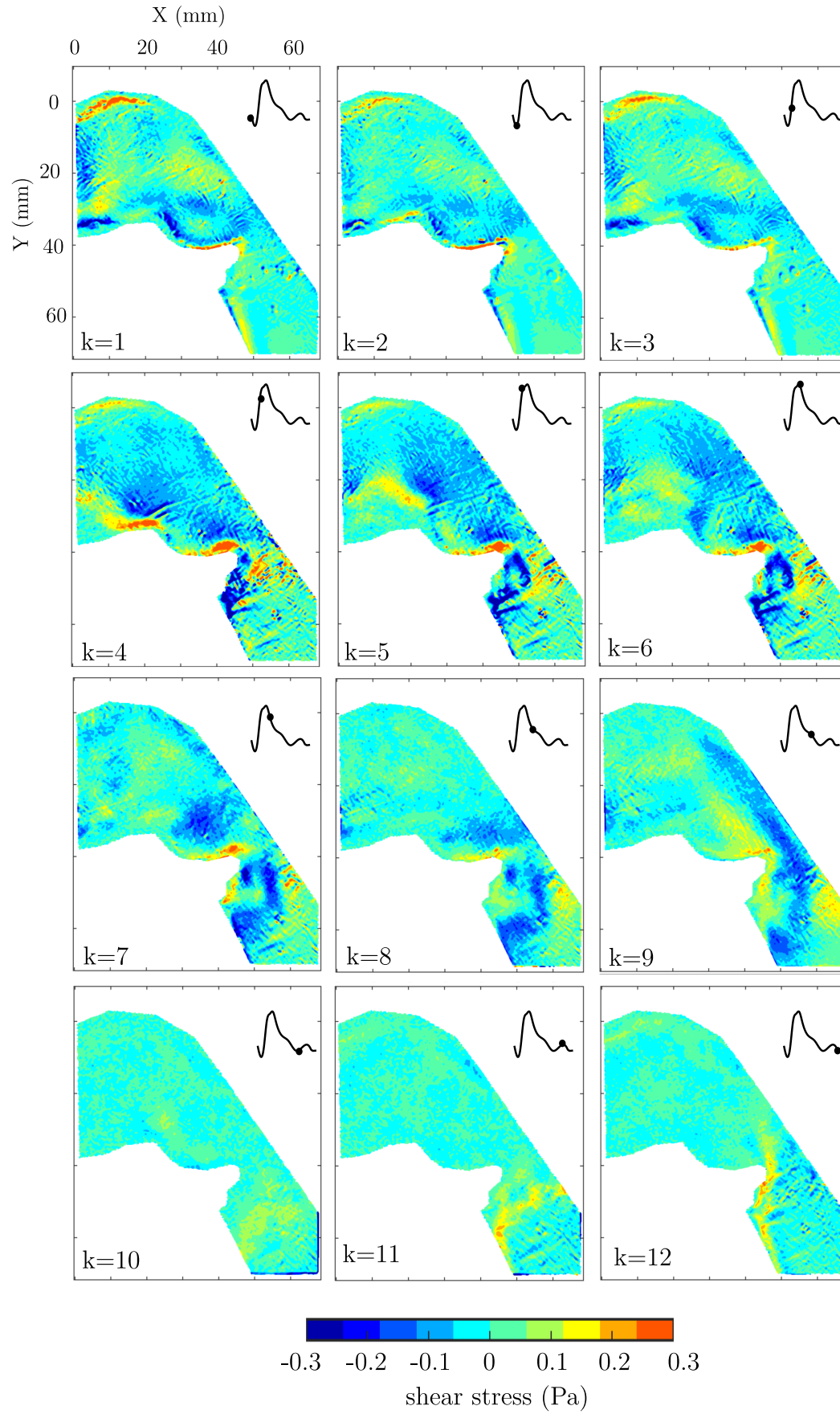


Figure 4.15: Shear stress maps for the 12 cycle instants on AD2_ROI2.

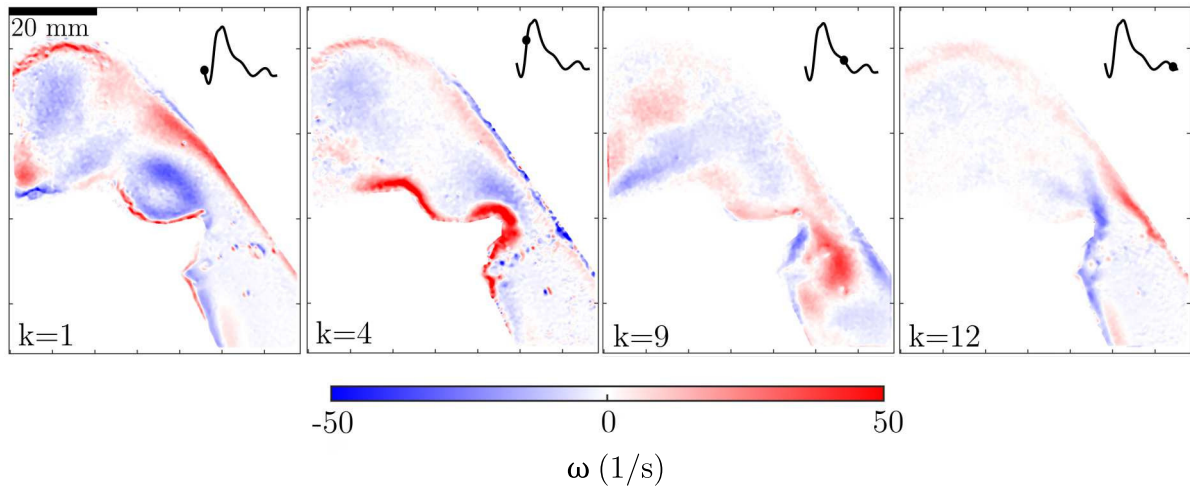


Figure 4.16: Vorticity maps for 4 cycle instants on AD2.ROI2.

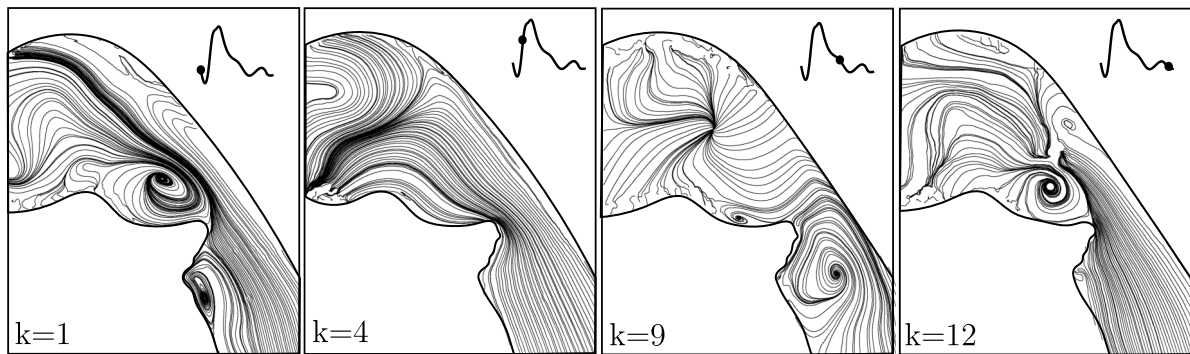


Figure 4.17: Streamlines maps for 4 cycle instants on AD2.ROI2.

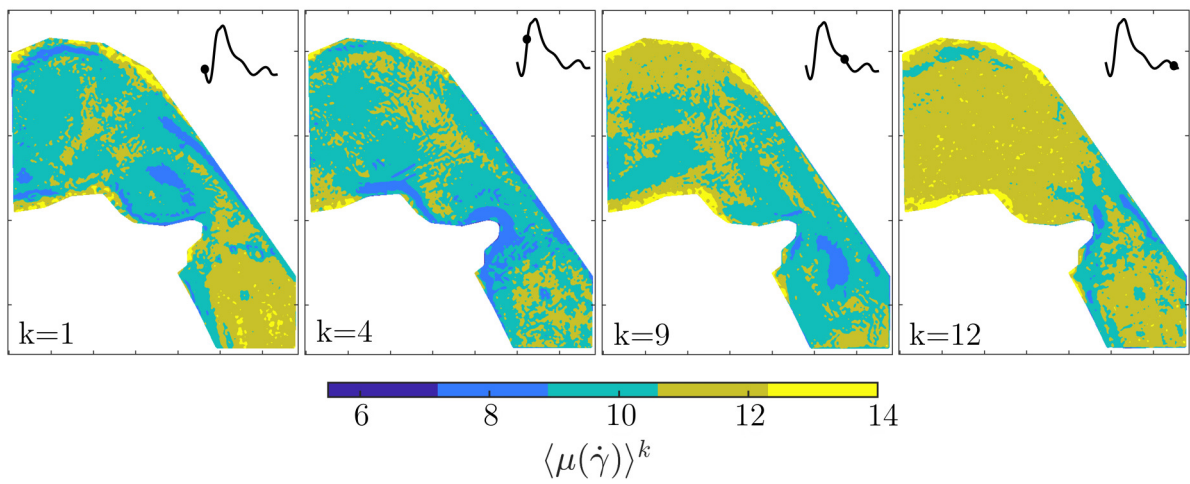


Figure 4.18: Viscosity maps for 4 cycle instants on AD2.ROI2.

4.5.3 Discussion

Flow, shear and vorticity

Extreme diameter constriction cases were studied in [Prahl Wittberg et al. \(2016\)](#) in a non-dissected thoracic aorta with numerical simulation. The flow distribution was not provided for the whole cycle but focused on late systole and backflow phases. In this article, the high velocity path with vortical structure just after the narrowing is very similar to the one observed in our experiments at $k = 7$ and $k = 8$ (figure 4.14). Current study data can also be compared to a study from [Hong et al. \(2017\)](#) who conducted PIV experiments on curved stenosed phantoms. Pulsatile flow was applied on the model with a Newtonian BMF. Similar high velocity path and recirculation region were observed in their stenosed channel. In [Hong et al. \(2017\)](#), additional comparisons with similar stenosed model but lower curvature are conducted. The curved model asymmetry, velocity and shear pattern is mainly associated with the centrifugal force induced by the model curvature. Higher WSS values were found in their most curved models showing that geometry factors are important in shear stress estimation. Increased flow asymmetry is also reported with increased asymmetry of the model. In our case, similar flow main direction change is generated by the channel shape. The fact that the dissection is partially located in the curved arch may induce higher shear stress than if it was in a straight region down in the descending aorta. Flow asymmetry and shear distribution asymmetry may also contribute to unbalanced endothelial cell stimulation and platelet deposit in the model.

In AD2 case, the curvature and narrowing are particularly pronounced. High and low wall shear stress regions play a major role in endothelial cells remodeling ([Pedersen et al. \(1999\)](#)). Indeed, high wall shear stress is associated with plaque rupture in atherosclerosis cases while low shear stress is associated with acceleration of plaque progression. The false lumen is subjected to the development of calcification plaque ([Jong et al. \(2014\)](#)), therefore shear stress distribution and fluctuation throughout the cardiac cycle is essential in the evaluation of risky areas.

Rotational and vortical flows are observed in healthy and pathological aorta but the development of a disease can alter these patterns. Indeed, vortices may play a role in maintaining shear stress, avoiding fluid stagnation, participating to platelet activation, deposit and aggregation ([Bluestein et al. \(1997\)](#); [Tippe et al. \(1992\)](#)). [Naim et al. \(2016\)](#), investigated the relation between vortical flows and WSS to predict thrombus formation and location in the false lumen. Vortical structures occupied the entire false lumen throughout the cardiac cycle. In this last article, high velocity, WSS and vortical structures grow around the entry tear and allowed to draw predictions on thrombus formation based on platelet activation and release locations. Their observed flow features near the entry tear are very similar to the current study flows in the narrowing region. In the case of [Naim et al. \(2016\)](#), the entry tear is the flow acceleration region while it is the diameter narrowing in our case.

With a similar analysis to [Naim et al. \(2016\)](#) some assumptions on flow patterns can be drawn. We observe a high shear stress pattern in the narrowing region which can favor platelet activation. Throughout the cycle, alternated vortical structures are observed over

and below the narrowing region which can cause repeated collision between platelets and result in aggregation. The breakdown of vortical structures occurs during the diastolic phase where low shear stress takes the lead in the ROI. Vortices break down can come with platelet release in low shear stress environment which could lead to the formation of thrombus because of plaque deposit on walls.

The current 2D view imposed by the PIV plane is too limited to conclude and validate such process but this type of observation and mechanism pattern could help locating risky areas. The confrontation of results with a 3D numerical simulation can provide more detailed view of shear, vorticity and pressure distributions. The third dimension and a focus on near wall flows allow to explore a wider panel of hemodynamics features that can reinforce current observations or open up new prospects. *In silico* results are presented in section 4.6.

Practical use of rigid phantom

To conclude on the *in vitro* part of AD studies, let us highlight an experimental limitation. Regarding practical use of those rigid phantoms a problem occurred in every experiment and led to the breaking of some phantoms. When turning on the pump to fuel the mock loop, air is always entrapped in the circuit when connecting the piping elements and the phantom. Bubbles often get stuck in bulged areas of the phantom. In the case of the compliant silicone phantom, bubbles could easily be evacuated by squeezing the phantom to carry them away with the flow. However, in the case of rigid models, the entrapped bubbles become highly problematic. This is worsened by the tortuous shape of AD phantoms with much more bulges where air can get stuck. The two consequences of the presence of air are flow disturbances and light reflections. Therefore, they need to be evacuated before running PIV imaging. Rigid phantom cannot be squeezed and only manipulation (rotation and reorientation) of the phantom when the flow is running with high velocity allows to evacuate air. These manipulations allow to guide bubbles to the outlet but tend to weaken the model when repeated many times on a large number of experiments. Indeed, they resulted in two phantoms breaking when preparing experiments. The breaking occurred either at the glued connection between phantom pieces (epoxy glue bounding) or in small artery branches transitions (region between the arch and emerging arteries). Even though the phantom material and bounding glue could endured the pulsatile flow pressure, it could not tolerate successive manipulations when installing the setup. These phantoms cannot be used on long term experiments with the current setup and design. They need to be manipulated carefully which is not compatible with successive handling to extract bubbles.

The *in vitro* mock loop was used to conduct experiments on rigid aortic dissection models. Depending on the phantom and the imaged area, PIV provided variable quality of velocity fields. The main limitation in those experiments is the phantom material, that is fragile, has non-homogeneous surface quality and limited optical access. The imaged areas that fulfilled PIV requirements gave access to specific flow patterns in tricky regions such as the dissection entry tear and a false lumen with an extreme local narrowing.

These results will be compared to numerical simulations of non-Newtonian flow in the same aorta models with rigid walls.

4.6 Comparison with numerical simulation: preliminary study

As mentioned in the first chapter, optimal hemodynamical studies combine different approaches including *in vivo*, *in vitro* and *in silico* investigations. Numerical simulations can provide multiphysic evaluations of aortic flows with a wider range of computed physical quantities simultaneously (velocity, flowrate, pressure, vorticity, wall shear-stress). This approach is less limited in space and time resolution and complete 3D visualizations of aorta models can be achieved. However, *in silico* studies are always confronted to the question: how close to reality is the numerical model ? To answer this tricky question, results have to be compared with a reliable reference. In addition to *in vivo* 4D flow MRI confrontation, comparing *in silico* model to a corresponding *in vitro* experiment is one of the solution for inter-validation of the two approaches. This section presents results as preliminary confrontations between the two models. Note that the *in vitro* and *in silico* set up were not optimized to perfectly match each other's outlet boundary conditions. It corresponds to the Windkessel models at each outlet. Properly setting those outlet boundary conditions would require additional *in vitro* tests with different Windkessel configurations and long simulation runs (almost a month for each configuration) that are out of the project scope. These preliminary results aim to provide an overview of potential future applications for the *in vitro* bench in combined numerico-experimental studies.

4.6.1 Simulation setup

The simulations were conducted by the numerical team of the @NEDA project thanks to Wenyang Pan and Pascale Kulisa (Pan (2021)). They have recreated aortic flows in different AD models (not described here) thanks to simulations with the ability to vary flow parameters such as inlet flowrate, outlet boundary conditions, fluid viscosity, rheology model etc. To make a comparison with the present *in vitro* experiments, the same aorta models were used and parameters were set to match the experiment ones (inflow conditions, blood model, etc). The following paragraph is a non-exhaustive description of the simulation building. For more details on the simulations refer the PhD thesis of Wenyang Pan (Pan (2021)).

Numerical model

In the present study, CFD model with rigid wall aortas are used since the physical 3D printed models are rigid. Figure 4.19 shows an overview of the translation from *in vitro* to *in silico* regarding outlet boundary conditions, blood rheological model and inflow conditions. The numerical simulations were conducted with foam-extend a fork of the CFD open-source software OpenFOAM (OpenFOAM (2021)). Finite volume elements with RANS (Reynolds-average Navier-Stokes) model are implemented on the software.

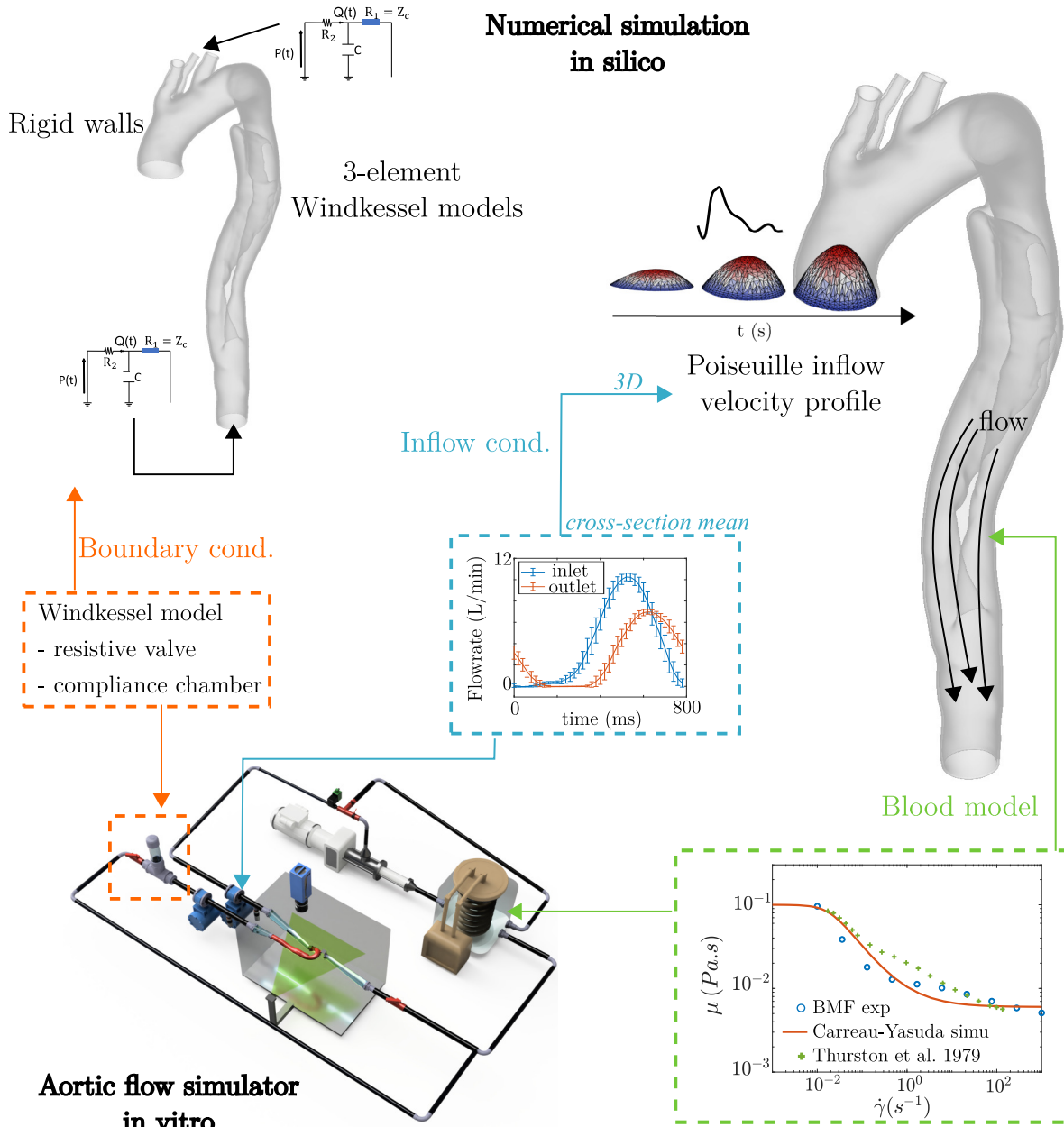


Figure 4.19: Overview of parameters and properties translation from the *in vitro* experiment to the numerical simulation.

Boundary conditions

At the entrance of the aorta, a pulsatile 3D-Poiseuille velocity profile is imposed to match the *in vitro* conditions. The simulation velocity magnitude is adapted to flowrate measurements from the inlet flowmeter (from previously described experiments in section 4.3.1). At each outlet (aortic arch branches and descending aorta), a 3-elements Windkessel model is implemented. On the circulatory mock loop, to deal with the rigid *in vitro* phantom, a Windkessel compliance chamber was implemented to dampen the flowrate and pressure signal. However, this 2-elements Windkessel model (resistive valve and compliance chamber) is less advanced than the numerical model one. Differences in boundary conditions are expected which can impact the amplitude of velocities throughout the cycle. In particular, backflow phases can be more or less intense depending on the energy

restored by the Windkessel capacity (in the simulation) and compliance chamber (in the experiment).

Blood model

A Carreau-Yasuda shear thinning model was applied to represent blood shear dependent viscosity. Parameters were set to fit the experimental designed BMF viscosity curve:

$$\mu = \mu_{\infty} + (\mu_0 - \mu_{\infty})(1 + (\lambda\dot{\gamma})^a)^{(n-1)/a}. \quad (4.6.1)$$

where $\mu_0 = 0.1$ Pa.s, $\mu_{\infty} = 0.006$ Pa.s, $n = 0.22$, $\lambda = 50$ s and $a = 2$.

4.6.2 Results and discussion

Comparison between the numerical simulations and the *in vitro* experiments are conducted with results from the the previously described PIV experiments on AD1_ROI1 and AD2_ROI1. Velocity fields are confronted on the same planes.

AD1

Figure 4.20 shows velocity in the 2D PIV plane for the *in vitro* and *in silico* cases at four cycle instants. Four regions 1, 2, 3 and 4 were highlighted as interesting regions to discuss similarities and differences. For $k = 1$ and 6, the PIV and simulation results appear very similar with a high velocity spot at upper corner of the FL/TL transition. At $k = 6$, the false lumen velocity are lower than in the TL. This tendency is observed in both approaches. At $k = 9$ and 10, regions 2, 3 and 4 are identified as high velocity locations while region 1 is associated to a stagnation area. At the same instants, the velocity in the false channel appeared lower in the *in vitro* experiment than in the numerical simulation. However, in both cases the near flap velocity is drastically lower in the false lumen. Regarding the true lumen, the same tendencies are observed in both approaches. Note that, the numerical simulation takes into account the out of plane component while PIV results only show in plane velocity components. Therefore, any location with a strong out-of-plane velocity component will be underestimated in the PIV measurements. This type of issue could explain the lower velocity observed in the FL at $k=9$ and $k=10$ in PIV compared to the simulation. This underestimation was also encountered in Bonfanti et al. (2020) where they compared PIV and numerical simulation results on a rigid AD model with a Newtonian BMF. A 3D view can help to determine if this out-of-plane flow can explain those differences in velocity fields.

A 3D velocity vector view is shown in figure 4.21 with the numerical simulation results. The entrance of the aorta and the entry tear regions are the highest velocity regions (without taking into account the aortic arch branches). Region 1 is again identified as a stagnation area with low velocity. Once the flow has crossed the entry tear toward the false channel, the preferred path is the way down. The tendencies of each region observed in the 2D view are confirmed with this 3D view.

However, in the post systolic peak instants the FL flow seems to rotate more toward the back (from the point-of-view of the reader) with a slight out of plane component. The

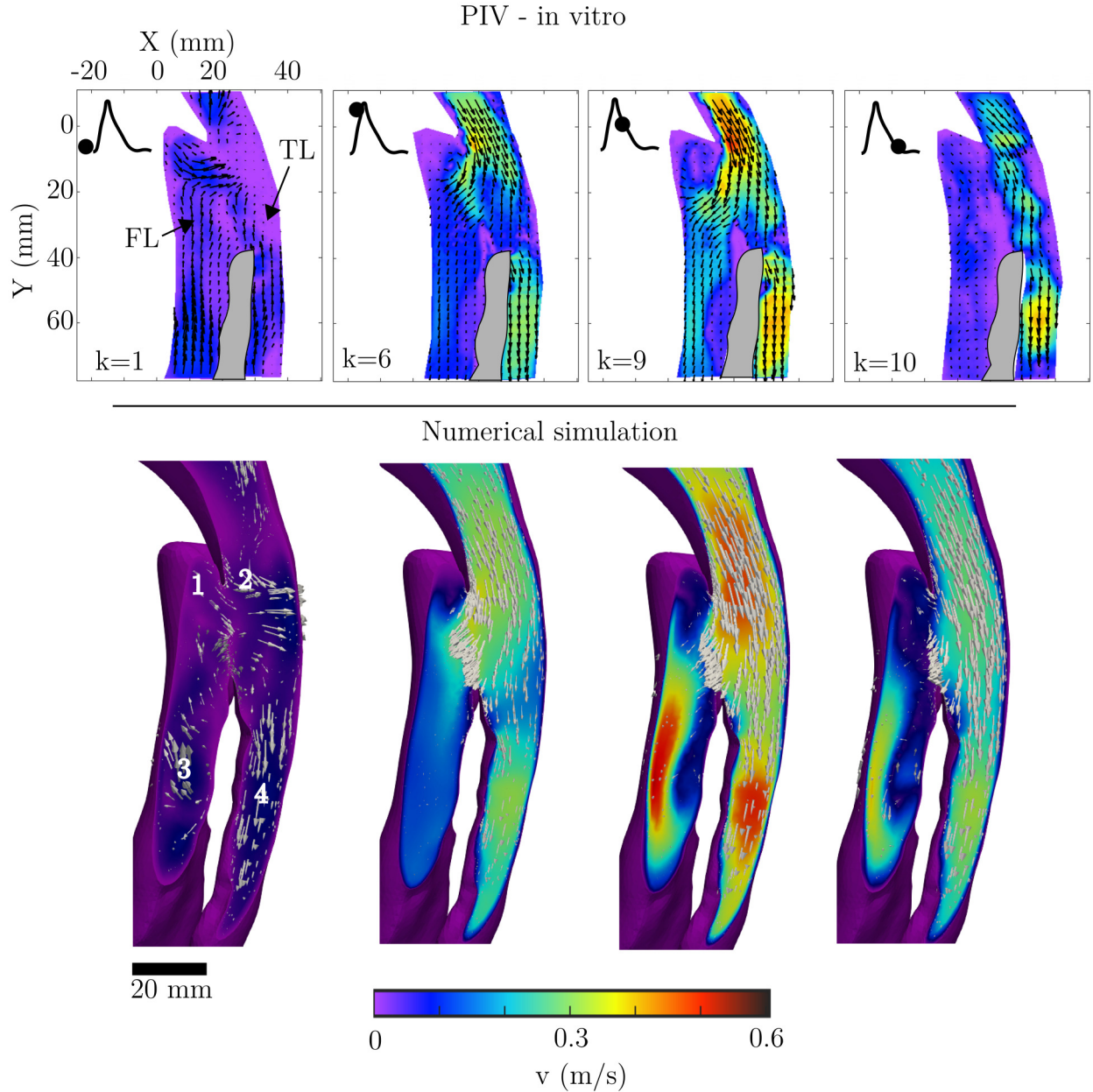


Figure 4.20: Comparison between PIV and numerical simulation velocity results for AD1_ROI1 at four cycle instants. Some regions are identified 1, 2, 3 and 4 as interesting locations to compare and discuss results.

orientation is slightly different that the systolic peak instant ($k = 6$) where more "in-line" flow was observed. This difference in orientation is not that significant and cannot fully explain the important differences observed in FL with the PIV results. According to these first observations, this aorta model is more simple than AD2 with an entry tear and a false channel in the continuity of the aortic arch. Thus, the flow is directed through a rather smooth path with no major direction disruption. The third dimension analysis does not bring a lot of noticeable information on the flow structure. AD2 case is a more interesting case to evaluate 3D view as stronger 3D disruptions are expected when considering the model shape and entry tear flow orientation. Indeed, in AD1 the entry tear is in-line with the flow orientation and in continuity with the arch curvature while in AD2, the entry

tear is strictly perpendicular to the flow natural path.

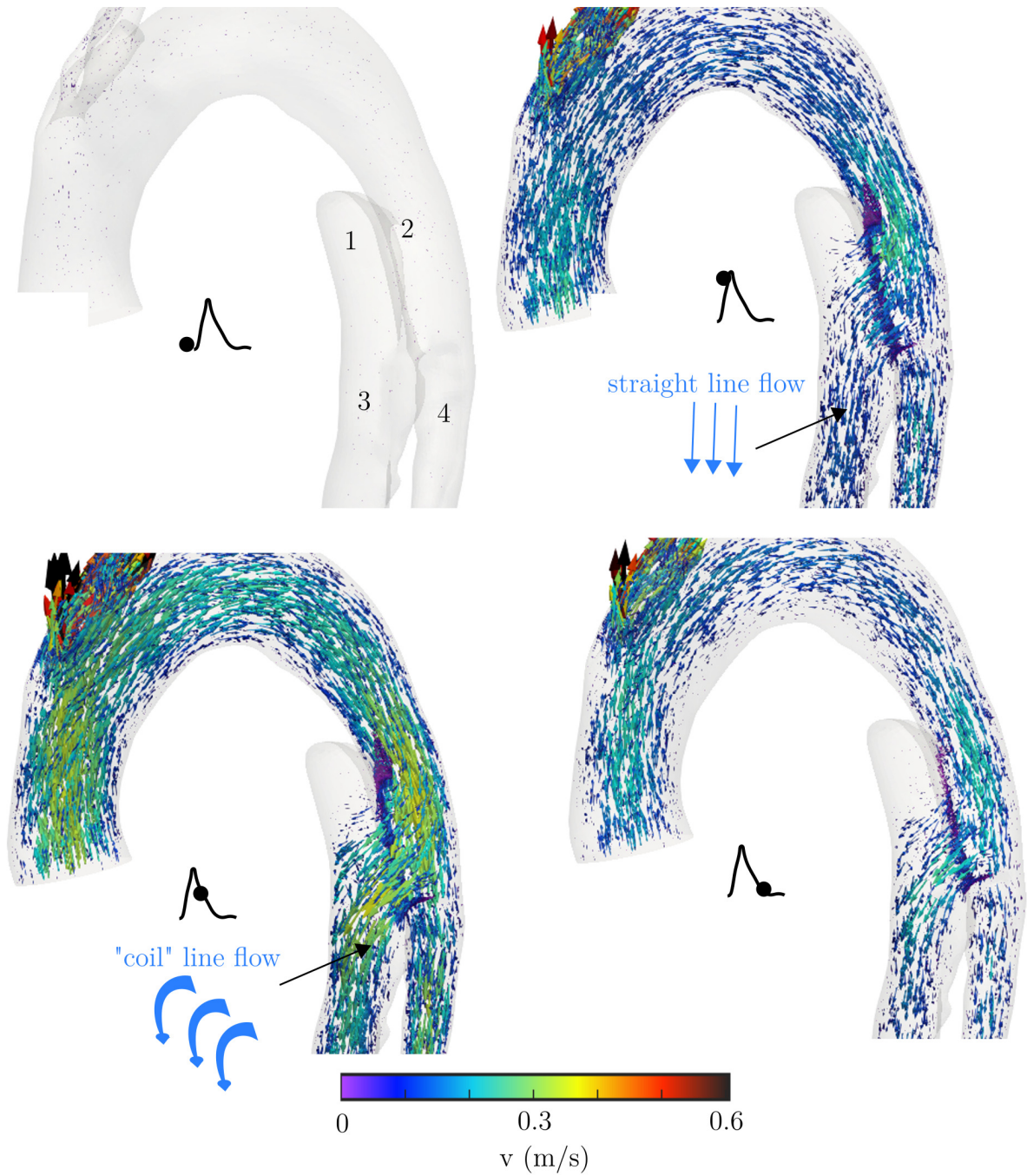


Figure 4.21: Numerical simulation velocity vector fields at four cycle instants. AD1-ROI1 and ROI2 are visible.

AD2

AD2 model has a more complex geometry with strong flow direction disruptions due to the location of the entry tear in the aortic arch and the diameter narrowing in the false channel. The 3D view offered by the numerical simulation is expected to bring more information than in AD1 case.

First, PIV and numerical simulations are compared in the same plane in figure 4.22. The three observed instants were chosen to show the two swirling structures labeled regions 2 and 4 (upward and backward from the diameter narrowing) and the high velocity path near the systolic peak in the narrowing (region 3). Region 1 is the entry tear which is located behind the PIV plane from the camera point of view. On the simulation results from figure 4.22, the dashed lines delimit the PIV ROI.

In $k = 6$ and $k = 9$, similar velocity results are observed in the PIV and numerical simulation in the narrowing region. At every instant, slightly higher velocities are observed near the entry tear (region 1). They are less pronounced in the PIV results. At the systolic peak ($k = 6$), region 1 is the highest velocity area in the simulation. By contrast, there is no major difference in velocity magnitude in PIV results for region 1 throughout the cycle. Note that because of the location of the entry tear, the emerging fluid mainly flows in an orthogonal direction to the imaged plane. This intense out-of-plane flow cannot properly be detected by our 2D-2C PIV system and can lead to underestimation of velocities. Our imaging technique and the chosen plane are not very appropriate to quantify velocities in this particular entry tear region.

Now let us focus on the narrowing regions where the flow mostly remains in the imaged plane. Region 3 is characterized by lower velocities and swirling structures. This rotational flow is observed in both *in vitro* and *in silico* results at $k = 9$. Additional similarities are observed at the systolic peak ($k = 6$), the higher velocity path appears in the narrowing for both approaches. In regions 2 and 4, the near wall velocity are also close to zero with stagnation areas in these two bulges.

However, differences are also observed in the PIV and numerical simulation results. The counterclockwise swirling structure upward from the narrowing is not observed at $k = 1$ in the numerical simulation. It actually never shows up throughout the cycle. The explanation probably comes from boundary condition differences. In the case of the numerical simulation, the backward phase is less intense and the upward velocity does not generate the swirling structure upward from the narrowing. Only the swirling structure downward to the narrowing is observed in both approaches. This last vortex persists longer throughout the cycle in the numerical simulation since the backward flow does not come to destroy it. This difference probably comes from the Windkessel compliance chamber design in the *in vitro* experiment. Indeed, too much compliance would generate higher energy restore in the system after systole and thus, stronger backward flow. The backward flow is over-represented in the *in vitro* experiment. The non-adaptability of the compliance system in the *in vitro* simulator is a weakness of the system which has to be further investigated to deal with those rigid walls models.

Finally, one of the most interesting observations from the numerical simulation is the entry tear flow. Because of the geometry of the model, the entry tear could not be correctly observed with the 2D plane of PIV. Indeed, figure 4.23 shows a 3D view of vectors in the false channel. The highest velocity region is the entry tear with vectors pointing in a direction out of the PIV 2D plane. Therefore, the entry tear velocities could not be assessed in the *in vitro* experiment with the chosen plane. It is interesting to note that the entry tear region may be a riskier region for the patient than the diameter narrowing region. Figure 4.23 (b) focuses on a precise instant at the end of the cycle deceleration

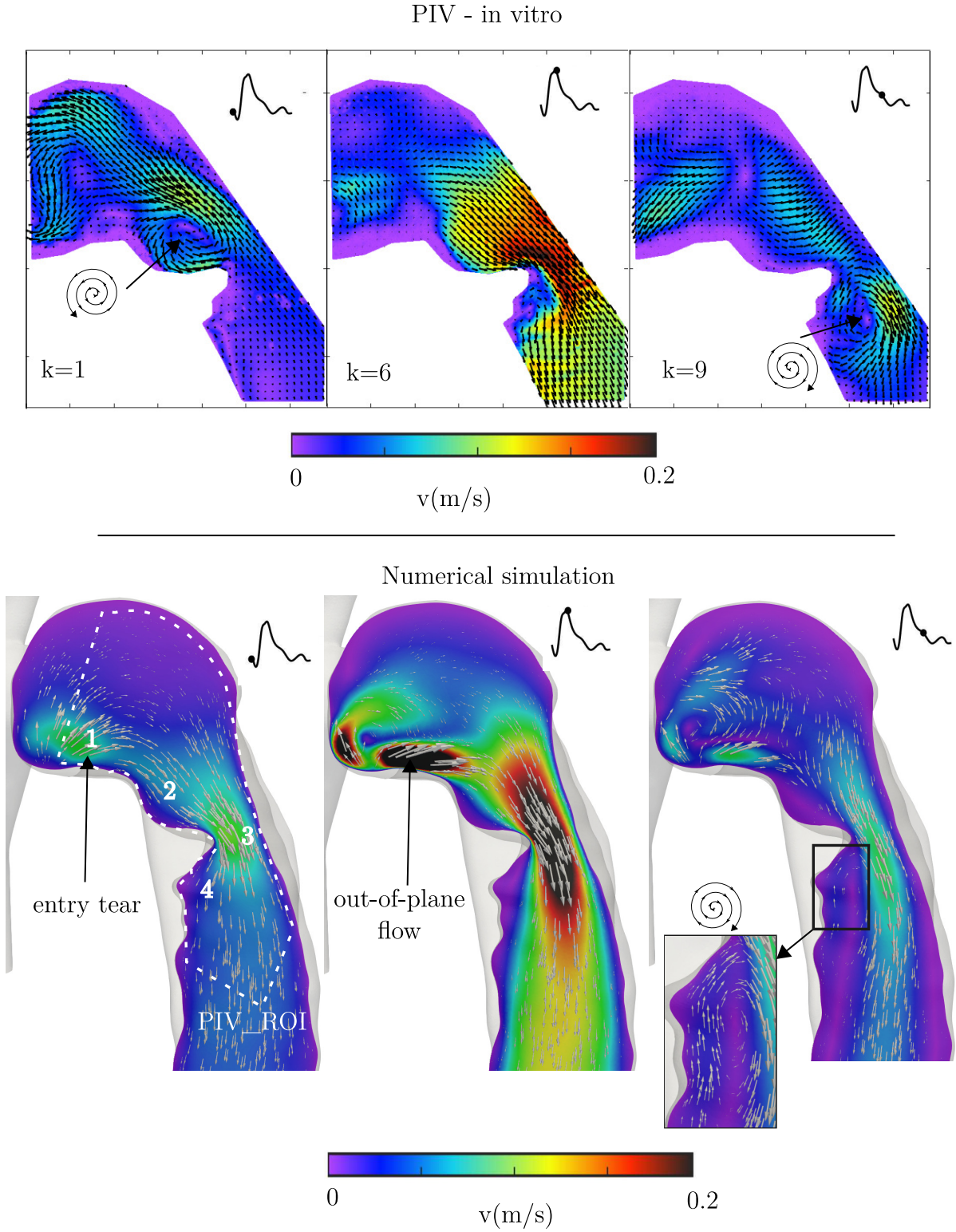


Figure 4.22: Comparison between PIV and numerical simulation velocity results for AD2_ROI1 at three cycle instants. Some regions are identified 1, 2, 3 and 4 as interesting locations to compare and discuss results. Region 1 corresponds to the entry tear. The dashed area on the first simulation plane delimits the PIV ROI.

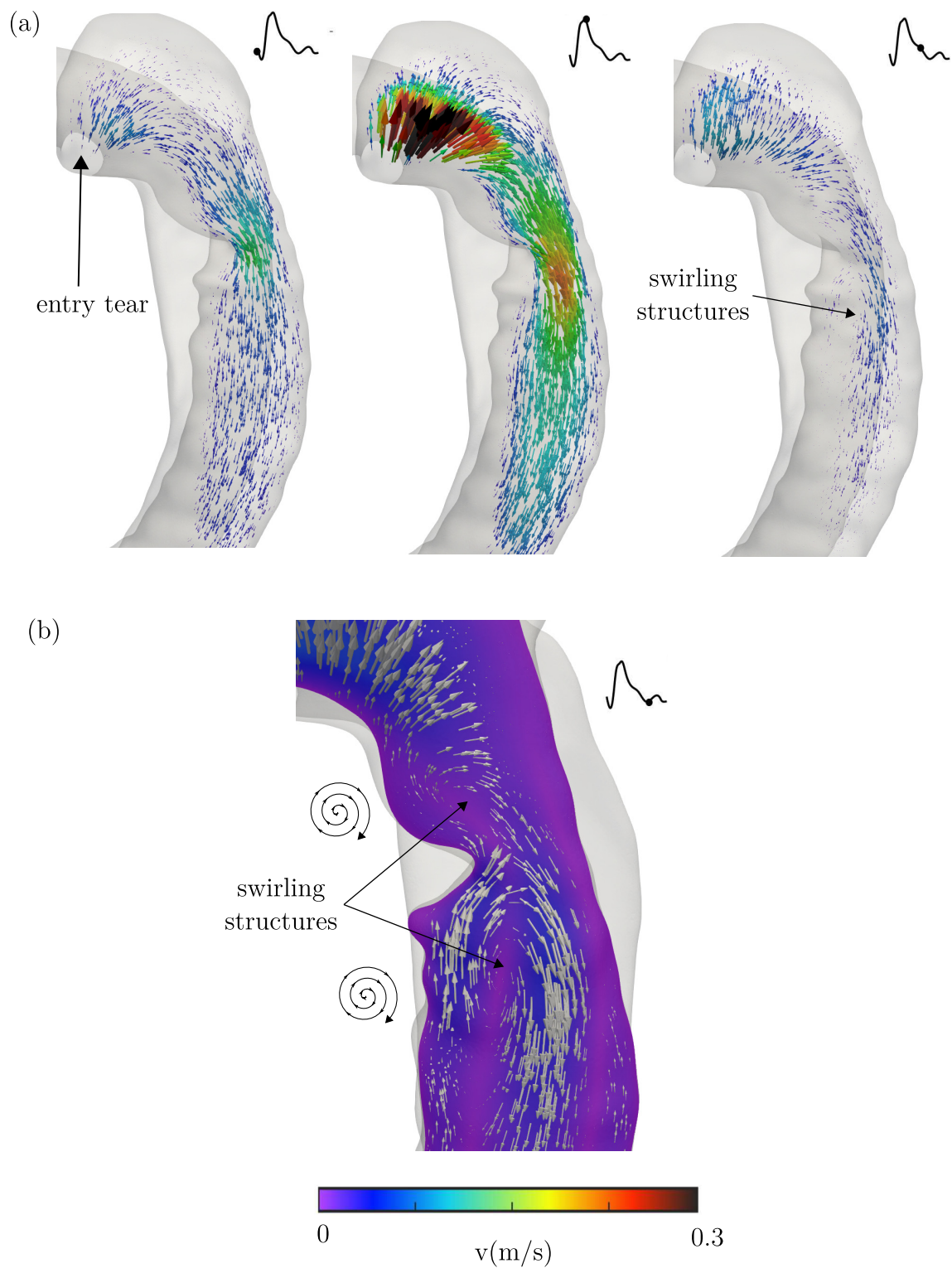


Figure 4.23: Numerical simulation velocity vector fields at three cycle instants in AD2_ROI1 are visible: (a) shows a 3D vector view of the false channel and (b) focuses on the narrowing region during diastole where two clockwise swirling structures are observed.

phase where the flow wraps to create two clockwise swirling structures. The vortex upward from the narrowing does not persist long (about 40 ms) and is quickly destroyed. This type of pattern was not observed on the PIV experiment where successive instants are separated by 50 to 100 ms. The numerical simulation successive cycle instants are separated by 10 ms and allow to observe faster phenomena. Obviously, this aorta model would require 3D observations to investigate flows. The 2D view is not sufficient to analyze flows and the 3D view with higher time resolution brings a lot of new information. The models would need to be optimized regarding inflow and boundary conditions for a proper analysis but this is a good example of where 2D experimental and 3D numerical simulation observations can complement.

4.6.3 Limitations and perspectives

The presented results are preliminary and were not conducted with setup optimization. The first results are very encouraging and flow tendency similarities are clearly identified. The differences seem to be mainly related to boundary condition mismatch. Indeed, the Windkessel compliance chamber which was implemented to deal with the phantom walls rigidity cannot be easily adapted on the *in vitro* simulator. The following paragraphs sums up these limitations and perspectives in optimizing the model for a more reliable confrontation.

Rigid walls

The CFD model and the *in vitro* AD experiment were conducted with rigid aorta models. Unfortunately, compliant aorta phantom could not be manufactured while fulfilling the material transparency requirement for PIV. The fluid-structure interaction model was implemented in the numerical study conducted for the PhD work of Wenyang Pan ([Pan \(2021\)](#)) by taking into account the wall mechanical response to the pulsatile flow. These results could not be compared with the *in vitro* model since aorta walls compliance could not be represented. For future applications, we believe that manufacturing compliant wall aorta models is the key to improve the blood flow simulator. It can already be implemented for more simple geometry such as the AA model presented in chapter 3 (with silicone injection). For more complex models such as AD, the 3D printing technology is constantly developing. New printing techniques, size and resins will probably meet these requirements in a few years. However, in the scope of a step-by-step validation, the rigid models are valuable for the CFD simulation (rigid walls) which is generally the first step of a fluid structure modeling.

Outlet boundary conditions

As mentioned earlier, to match the boundary conditions between the *in vitro* and the *in vivo* models, more complex Windkessel elements should be implemented on the physical aorta simulator. Such matching was achieved in [Bonfanti et al. \(2020\)](#) on an experiment involving an AD phantom with a Newtonian blood mimicking fluid. Their customizable Windkessel elements allow to match patient-specific conditions with a direct translation to the numerical model.

Toward a numerico-experimental study

The presented preliminary results show that the 3D view can bring new information on flow structure. The current *in vitro* experiment was mounted with a 2D-2C PIV system which only allows to image velocities in 2D planes. To reach the third component a stereo-PIV equipment could be implemented on the mock loop. In the case of AD1, this configuration would be sufficient as the third dimension contribution appeared negligible. Moreover, A 3D-PTV equipment could be implemented on models with strong 3D contribution such as AD2. This technique would allow to image 3D particles trajectories and to follow the path from the entry tear to the false channel. Such visualization technique would also provide information on the location of particles, their density, distribution and stagnation areas to identify platelet deposit risky areas.

Regarding the numerical confrontation, Windkessel elements could not be easily modified in the current *in vitro* setup to reach realistic conditions. Improving the Windkessel model could solve boundary condition differences. It would require an experimental campaign to optimize parameters until a good match between *in vitro* and *in silico* results is reached.

Why would the *in vitro* simulator still be required?

As the numerical simulation can provide much more information on the model than the *in vitro* one, the necessity of the *in vitro* setup is questioned. However, numerical simulations are fully built by the programmer who implements the model geometry, mesh, physical equations and boundary conditions up to a certain level of precision. All these features are representations of a physical reality but will never represent all the complexity of this reality. The goal is to reach a certain degree of biofidelity by representing the essential elements to virtually recreate aortic flows. To validate this implemented degree of biofidelity a confrontation has to be conducted with a real model which could be *in vivo* or *in vitro*. Obviously, the ideal solution is the *in vivo* one but can be limited by the flow visualization options. As an example, AD2 numerical case was confronted to the 4D-MRI of the patient (Pan (2021)). Good agreements were found in general velocities and true and false flow channel distribution but it was difficult to compare smaller and faster flow patterns such as vortices. An *in vitro* simulator provides more flexible flow visualization tools with higher resolutions. Moreover, inflow and boundary conditions can be adapted to test other situations and evaluate the robustness of a simulation. These tests are among the perspectives of this aortic flow simulation that can be implemented in a cross-study between numerical and experimental assessments for aortic flows but also for other types of physiological flows. In addition, this benchtop experiment can be used as a training simulator for surgeons to practice stent graft deployment. This future application has been thought since the beginning of the project which is one of the reason why the setup was designed in scale 1.

4.7 Conclusion

In this chapter, an aortic dissection case study was proposed on two patients cases. Two aorta models were 3D printed with a rigid and transparent resin and patient-specific

geometries. The models were tested on the simulator with the non-Newtonian BMF and under pulsatile inflow conditions. Three regions-of-interest (ROI) were imaged to visualize and analyze flows in tricky regions including the aorta entrance, dissection entry tear and false channel. The results were compared to numerical simulation as a preliminary study to observe flow tendencies with both approaches: *in vitro* and *in silico*. Results showed similar flow velocity trends in both models. In the case of AD1, the 3D visualization offered by the numerical simulation confirmed the tendencies observed in the 2D PIV plane. The third dimension did not bring a lot of noticeable information. On the contrary, the 3D view brought new features in the AD2 case which geometry had a 3D impact on the structure of flows. These comparisons encouraged the idea of having complementary flow visualization and analysis tools to better understand aortic flows. Differences were also observed, but as a preliminary comparison, the boundary conditions of each model were not optimized. More specifically, improving the Windkessel system on the experiment would provide more reliable results and better accordance between the *in vitro* and *in silico* conditions.

General conclusion and perspective

In vitro aortic flow simulators allow to study hemodynamics with a wider range of flow visualization techniques. This work aims to develop an experimental bench to emulate the pulsatile circulation in realistic aortic phantoms and flow conditions. A large majority of studies implemented either simplified tubes to represent the aorta or rigid models with compliant walls to mimic human aorta mechanical behavior. Moreover, blood mimicking fluids are often designed with the Newtonian hypothesis, thus neglecting the shear-thinning behavior of blood. The four main properties that define arterial circulation are pulsatile inflow conditions, the non-Newtonian behavior of blood, piping system with distinctive geometries, and compliant aortic walls response. In the literature, one or more of these features are neglected and the present thesis addressed these four properties on a single experimental bench.

Firstly, the blood flow simulator was designed to emulate aortic circulation with artificial elements. A circulatory mock loop was designed to recreate aortic pulsatile flows regarding flowrate and pressure. A compliant aorta phantom with a patient-specific geometry was manufactured thanks to a silicone injection technique. The aorta replica has compliant walls with a Young's modulus in the range of a human's one. To mimic blood shear thinning behavior, a non-Newtonian blood mimicking fluid was prepared with glycerin and xanthan gum polymer and was evaluated with a rheology study. Finally, Particle Image Velocimetry was implemented as a high-resolution flow visualization tool to draw 2D velocity fields. The phantom and the fluid were designed to be transparent with matched refractive indexes. It provided optical access to the flow inside the phantom and minimized optical distortions. The PIV setup was synchronized with the pulsatile flow control to target precise cycle instants for velocity fields computing. The simulator is a reliable tool in biofidelity and visualization accuracy thanks to the designed elements and PIV technique.

Secondly, the experimental bench was tested on the compliant aorta phantom to compare a Newtonian and a non-Newtonian BMF. Indeed, most studies claim that the Newtonian hypothesis is valid in large arteries such as the aorta but most of them were conducted on idealized models. Tortuous geometries can generate more chaotic flows and stronger shear which are related to the shear-thinning nature of blood. The present work highlighted some differences in flow distribution, shear patterns, and vortex structures which tend to invalidate that both fluids are equivalent in such geometries. The non-Newtonian BMF was thus adopted for the simulator. These experiments allowed evaluating the compliant phantom response to pulsatile flow. Wall displacements and diameter variations throughout the cardiac cycle were in accordance with *in vivo* aorta behavior. The simulator was thus validated regarding the choice of fluid and phantom material.

Finally, aortic dissection case studies were addressed in the last chapter. Two phantoms with patient-specific geometries, transparent and rigid walls were designed with 3D printing technique. Because of the tortuous geometry of AD models, the silicone injection technique could not be used to manufacture compliant phantoms. The two models were tested on the simulator with non-Newtonian BMF and pulsatile inflow conditions. Three critical zones were images with PIV: aorta entrance, true/false channel entry tear, and an abnormal reduction in the false channel. Flow distribution, shear stress, and vorticity were computed and compared to CFD numerical simulations. *In silico* and *in vitro* methods showed results with good agreements regarding flow patterns. Further investigation has to be conducted in optimizing the *in vitro* and *in silico* model regarding boundary conditions and more specifically Windkessel compliance models. As in [Franzetti et al. \(2019\)](#) more customization physical Windkessel elements could be designed to fit the numerical model and patient specific conditions. Unfortunately, only rigid models could be tested and the aortic wall mechanical response could not be represented. This compliance feature would also participate in optimizing boundary conditions and could simplify the Windkessel compliance problem.

The main limitation in the simulator is the aorta phantom. Indeed, the AA model with compliant walls fulfilled all the requirements regarding transparency, the possibility to match the index with the BMF, and mechanical properties. When it comes to more complex geometries such as AD with parallel channels the silicone injection technique could not be implemented because of molds removal difficulties. The 3D printing technique is very powerful to manufacture complex geometries. After a lot of testing on resins, a solution to make transparent models was found. However, the material refractive index was too high to suit the BMF. The resulting PIV visualization was less qualitative than with the AA model because of optical distortions and reflections. The design of AD models was a difficult task and the obtained phantoms were not fully satisfying. However thanks to the rapid progress of 3D printing technique, we believe that the phantom manufacturing problem will not be an issue in 2 to 3 years. The ideal solution would be to combine silicone injection and 3D printing. A first step would consist in printing a negative mold of the aorta with wax. The second step would consist in injecting the silicone into the mold to shape the phantom. Finally, the mold could be destroyed with heat or chemicals to isolate the silicone phantom. These techniques already exist but for now they are limited in surface state quality and size of models.

Finally, the experimental bench was designed at scale 1. A long-term project is to use the simulator as a surgery training bench. Rapidly designing a 3D phantom for a specific patient, testing it on the mock loop with patients custom inflow conditions, and perform surgery with stent-graft deployment can be implemented on the current setup. The PIV system can be used to capture flow pre and post-surgery to better predict the impact of the stent positioning. The numerical simulations were conducted with FSI modeling and with the catheter insertion process. Combining the scale 1 physical simulator and corresponding simulation would make a powerful tool in aided surgery for aortic dissection.

Bibliography

- Abdi, M., Karimi, A., Navidbakhsh, M., Pirzad Jahromi, G., and Hassani, K. (2015). A lumped parameter mathematical model to analyze the effects of tachycardia and bradycardia on the cardiovascular system. *International Journal of Numerical Modelling: Electronic Networks, Devices and Fields*, 28(3):346–357.
- Alimohammadi, M., Sherwood, J. M., Karimpour, M., Agu, O., Balabani, S., and Díaz-Zuccarini, V. (2015). Aortic dissection simulation models for clinical support: fluid-structure interaction vs. rigid wall models. *BioMedical Engineering OnLine*, 14(1):34.
- Altnji, H.-E., Bou-Said, B., and Berre, H. W.-L. (2013). Numerical simulation of the migration phenomena and type 1a endoleak of thoracic aneurysm endograft. *Computer Methods in Biomechanics and Biomedical Engineering*, 16(sup1):36–38.
- Amabili, M., Balasubramanian, P., Bozzo, I., Breslavsky, I. D., Ferrari, G., Franchini, G., Giovanniello, F., and Pogue, C. (2020). Nonlinear Dynamics of Human Aortas for Material Characterization. *Physical Review X*, 10(1):011015.
- Amornsamankul, S., Wiwatanapataphee, B., Wu, Y. H., and Lenbury, Y. (2007). Effect of Non-Newtonian Behaviour of Blood on Pulsatile Flows in Stenotic Arteries. *International Journal of Biological and Medical Sciences*, 1(1):42–46.
- Anastasiou, A. D., Spyrogianni, A. S., Koskinas, K. C., Giannoglou, G. D., and Paras, S. V. (2012). Experimental investigation of the flow of a blood analogue fluid in a replica of a bifurcated small artery. *Medical Engineering & Physics*, 34(2):211–218.
- Apostolidis, A. J., Moyer, A. P., and Beris, A. N. (2016). Non-Newtonian effects in simulations of coronary arterial blood flow. *Journal of Non-Newtonian Fluid Mechanics*, 233:155–165.
- Armour, C. H., Guo, B., Pirola, S., Saitta, S., Liu, Y., Dong, Z., and Xu, X. Y. (2021). The influence of inlet velocity profile on predicted flow in type B aortic dissection. *Biomechanics and Modeling in Mechanobiology*, 20(2):481–490.
- Arzani, A. and Shadden, S. C. (2015). Characterizations and Correlations of Wall Shear Stress in Aneurysmal Flow. *Journal of Biomechanical Engineering*, 138(014503).
- Bae, S., Kim, S. R., Kim, M.-N., Shim, W. J., and Park, S.-M. (2021). Impact of cardiovascular disease and risk factors on fatal outcomes in patients with COVID-19 according to age: a systematic review and meta-analysis. *Heart*, 107(5):373–380.

- Bardera, R., Barcala-Montejano, M., Rodríguez-Sevillano, A., and León-Calero, M. (2019). Wind flow investigation over an aircraft carrier deck by PIV. *Ocean Engineering*, 178:476–483.
- Barquera, S., Pedroza-Tobias, A., Medina, C., Bibbins-Domingo, K., Lozano, R., and Moran, A. (2015). Global Overview of the Epidemiology of Atherosclerotic Cardiovascular Disease. *Archives of Medical Research*, 46.
- Baskurt, O. K. (2003). Blood Rheology and Hemodynamics. *Seminars in Thrombosis and Hemostasis*, 29(5):16.
- Belmont, B. (2020). Biomedical engineering: the fluid, the flow : <https://barrybelmont.com/physiology/blood-flow/>.
- Ben Ahmed, S., Dillon-Murphy, D., and Figueroa, C. (2016). Computational Study of Anatomical Risk Factors in Idealized Models of Type B Aortic Dissection. *European Journal of Vascular and Endovascular Surgery*, 52(6):736–745.
- Birjiniuk, J., Ruddy, J. M., Iffrig, E., Henry, T. S., Leshnower, B. G., Oshinski, J. N., Ku, D. N., and Veeraswamy, R. K. (2015). Development and testing of a silicone in vitro model of descending aortic dissection. *Journal of Surgical Research*, 198(2):502–507.
- Bluestein, D., Niu, L., Schoepfoerster, R. T., and Dewanjee, M. K. (1997). Fluid mechanics of arterial stenosis: relationship to the development of mural thrombus. *Annals of Biomedical Engineering*, 25(2):344–356.
- Bonfanti, M., Balabani, S., Alimohammadi, M., Agu, O., Homer-Vanniasinkam, S., and Díaz-Zuccarini, V. (2018). A simplified method to account for wall motion in patient-specific blood flow simulations of aortic dissection: Comparison with fluid-structure interaction. *Medical Engineering & Physics*, 58:72–79.
- Bonfanti, M., Balabani, S., Greenwood, J. P., Puppala, S., Homer-Vanniasinkam, S., and Díaz-Zuccarini, V. (2017). Computational tools for clinical support: a multi-scale compliant model for haemodynamic simulations in an aortic dissection based on multi-modal imaging data. *Journal of The Royal Society Interface*, 14(136):20170632.
- Bonfanti, M., Franzetti, G., Homer-Vanniasinkam, S., Díaz-Zuccarini, V., and Balabani, S. (2020). A Combined In Vivo, In Vitro, In Silico Approach for Patient-Specific Haemodynamic Studies of Aortic Dissection. *Annals of Biomedical Engineering*, 48(12):2950–2964.
- Bonfanti, M., Franzetti, G., Maritati, G., Homer-Vanniasinkam, S., Balabani, S., and Díaz-Zuccarini, V. (2019). Patient-specific haemodynamic simulations of complex aortic dissections informed by commonly available clinical datasets. *Medical Engineering & Physics*, 71:45–55.
- Boutier, A. (2012). *Vélocimétrie laser pour la mécanique des fluides*. Lavoisier.

- Boyd, A. J., Kuhn, D. C. S., Lozowy, R. J., and Kulbisky, G. P. (2016). Low wall shear stress predominates at sites of abdominal aortic aneurysm rupture. *Journal of Vascular Surgery*, 63(6):1613–1619.
- Boyd, J., Buick, J. M., and Green, S. (2007). Analysis of the Casson and Carreau-Yasuda non-Newtonian blood models in steady and oscillatory flows using the lattice Boltzmann method. *Physics of Fluids*, 19(9):093103.
- Bramwell, J. C. and Hill, A. V. (1922). The velocity of pulse wave in man. *Proceedings of the Royal Society of London. Series B, Containing Papers of a Biological Character*, 93(652):298–306. Publisher: Royal Society.
- Bărdaș, A. and Bordei, P. (2018). The Morphologic Characteristics of the Ostium of the Collateral Branches of the Abdominal Aorta. *Romanian Journal of Functional & Clinical, Macro-& Microscopical Anatomy & of Anthropology/Revista Româna de Anatomie Functionala si Clinica, Macro si Microscopica si de Antropologie*, 17(2):6.
- Bürk, J., Blanke, P., Stankovic, Z., Barker, A., Russe, M., Geiger, J., Frydrychowicz, A., Langer, M., and Markl, M. (2012). Evaluation of 3D blood flow patterns and wall shear stress in the normal and dilated thoracic aorta using flow-sensitive 4D CMR. *Journal of Cardiovascular Magnetic Resonance*, 14(1):84.
- Brookshier, K. and Tarbell, J. (1993). Evaluation of a transparent blood analog fluid: Aqueous Xanthan gum/glycerin. *Biorheology*, 30(2):107–116.
- Brunette, J., Mongrain, R., and Tardif, J. C. (2004). A realistic coronary artery phantom for particle image velocimetry: Featuring injection-molded inclusions and multiple layers. *Journal of Visualization*, 7(3):241–248.
- Büsen, M., Arenz, C., Neidlin, M., Liao, S., Schmitz-Rode, T., Steinseifer, U., and Sonntag, S. J. (2017). Development of an In Vitro PIV Setup for Preliminary Investigation of the Effects of Aortic Compliance on Flow Patterns and Hemodynamics. *Cardiovascular Engineering and Technology*, 8(3):368–377.
- Büsen, M., Kaufmann, T. A., Neidlin, M., Steinseifer, U., and Sonntag, S. J. (2015). In vitro flow investigations in the aortic arch during cardiopulmonary bypass with stereo-PIV. *Journal of biomechanics*, 48(10):2005–2011.
- Bäumler, K., Vedula, V., Sailer, A. M., Seo, J., Chiu, P., Mistelbauer, G., Chan, F. P., Fischbein, M. P., Marsden, A. L., and Fleischmann, D. (2020). Fluid–structure interaction simulations of patient-specific aortic dissection. *Biomechanics and Modeling in Mechanobiology*, 19:1607–1628.
- Caballero, A. and Laín, S. (2015). Numerical simulation of non-Newtonian blood flow dynamics in human thoracic aorta. *Computer Methods in Biomechanics and Biomedical Engineering*, 18(11):1200–1216.

- Campo-Deaño, L., Dullens, R. P. A., Aarts, D. G. A. L., Pinho, F. T., and Oliveira, M. S. N. (2013). Viscoelasticity of blood and viscoelastic blood analogues for use in polydimethylsiloxane in vitromodels of the circulatory system. *Biomicrofluidics*, 7(3):034102.
- Canaud, L., Alric, P., Laurent, M., Baum, T.-P., Branchereau, P., Marty-Ané, C. H., and Berthet, J.-P. (2008). Proximal Fixation of Thoracic Stent-Grafts as a Function of Oversizing and Increasing Aortic Arch Angulation in Human Cadaveric Aortas. *Journal of Endovascular Therapy*, 15(3):326–334.
- Carew, T. E., Vaishnav, R. N., and Patel, D. J. (1968). Compressibility of the Arterial Wall. *Circulation Research*, 23(1):61–68.
- Chen, C.-W., Tseng, Y.-H., Lin, C.-C., Kao, C.-C., Wong, M. Y., Ting, H., and Huang, Y.-K. (2021). Aortic dissection assessment by 4D phase-contrast MRI with hemodynamic parameters: the impact of stent type. *Quantitative Imaging in Medicine and Surgery*, 11(2):490–501.
- Chen, H., Li, D., Bai, R., and Wang, X. (2018). Comparison of swirling strengths derived from two- and three-dimensional velocity fields in channel flow. *AIP Advances*, 8(5):055302.
- Cheng, C. P., Herfkens, R. J., and Taylor, C. A. (2003). Comparison of abdominal aortic hemodynamics between men and women at rest and during lower limb exercise. *Journal of Vascular Surgery*, 37(1):118–123.
- Cheng, Z., Juli, C., Wood, N., Gibbs, R., and Xu, X. (2014). Predicting flow in aortic dissection: Comparison of computational model with PC-MRI velocity measurements. *Medical Engineering & Physics*, 36(9):1176–1184.
- Cheng, Z., Tan, F. P. P., Riga, C. V., Bicknell, C. D., Hamady, M. S., Gibbs, R. G. J., Wood, N. B., and Xu, X. Y. (2010). Analysis of Flow Patterns in a Patient-Specific Aortic Dissection Model. *Journal of Biomechanical Engineering*, 132(5).
- Chien, S. (1970). Shear Dependence of Effective Cell Volume as a Determinant of Blood Viscosity. *Science*, 168(3934):977–979.
- Chien, S., Usami, S., Taylor, H. M., Lundberg, J. L., and Gregersen, M. I. (1966). Effects of hematocrit and plasma proteins on human blood rheology at low shear rates. *Journal of Applied Physiology*, 21(1):81–87.
- Chiu, J.-J. and Chien, S. (2011). Effects of Disturbed Flow on Vascular Endothelium: Pathophysiological Basis and Clinical Perspectives. *Physiological Reviews*, 91(1):327–387.
- Clough, R. E., Waltham, M., Giese, D., Taylor, P. R., and Schaeffter, T. (2012). A new imaging method for assessment of aortic dissection using four-dimensional phase contrast magnetic resonance imaging. *Journal of Vascular Surgery*, 55(4):914–923.

- Cocconi, G., De Angelis, E., Frohnäpfel, B., Baevsky, M., and Liberzon, A. (2017). Small scale dynamics of a shearless turbulent/non-turbulent interface in dilute polymer solutions. *Physics of Fluids*, 29(7):075102. arXiv: 1612.05979.
- Comolet, R. (1984). *Biomécanique Circulatoire*. Elsevier Masson, masson edition.
- Craiem, D., Alsac, J.-M., Casciaro, M. E., El Batti, S., Mousseaux, E., Sirieix, M.-E., and Simon, A. (2016). Association Between Thoracic Aorta Calcium and Thoracic Aorta Geometry in a Cohort of Asymptomatic Participants at Increased Cardiovascular Risk. *Revista Española de Cardiología (English Edition)*, 69(9):827–835.
- Criado, F. J. (2011). Aortic Dissection. *Texas Heart Institute Journal*, 38(6):694–700.
- Cuissa, J. R. C. and Steiner, O. (2020). Vortices evolution in the solar atmosphere - A dynamical equation for the swirling strength. *Astronomy & Astrophysics*, 639:A118.
- Dahl, K. N., Kalinowski, A., and Pekkan, K. (2010). Mechanobiology and the microcirculation: cellular, nuclear and fluid mechanics. *Microcirculation*, 17(3):179–191.
- Davies, P. F. (2009). Hemodynamic shear stress and the endothelium in cardiovascular pathophysiology. *Nature clinical practice. Cardiovascular medicine*, 6(1):16–26.
- Davis10 (2017). DaVIs 10 Manual.
- de Winter, D. A. M., Weishaupt, K., Scheller, S., Frey, S., Raoof, A., Hassanizadeh, S. M., and Helmig, R. (2021). The Complexity of Porous Media Flow Characterized in a Microfluidic Model Based on Confocal Laser Scanning Microscopy and Micro-PIV. *Transport in Porous Media*, 136(1):343–367.
- Deplano, V., Guivier-Curien, C., and Bertrand, E. (2016). 3D analysis of vortical structures in an abdominal aortic aneurysm by stereoscopic PIV. *Experiments in Fluids*, 57(11):167.
- Deplano, V., Knapp, Y., Bailly, L., and Bertrand, E. (2014). Flow of a blood analogue fluid in a compliant abdominal aortic aneurysm model: Experimental modelling. *Journal of Biomechanics*, 47(6):1262–1269.
- Deplano, V., Knapp, Y., Bertrand, E., and Gaillard, E. (2007). Flow behaviour in an asymmetric compliant experimental model for abdominal aortic aneurysm. *Journal of Biomechanics*, 40(11):2406–2413.
- Devos, D. G. H., De Groote, K., Babin, D., Demulier, L., Taeymans, Y., Westenberg, J. J., Van Bortel, L., Segers, P., Achten, E., De Schepper, J., and Rietzschel, E. (2017). Proximal aortic stiffening in Turner patients may be present before dilation can be detected: a segmental functional MRI study. *Journal of Cardiovascular Magnetic Resonance*, 19(1):27.
- Devos, D. G. H., Rietzschel, E., Heyse, C., Vandemaele, P., Bortel, L. V., Babin, D., Segers, P., Westenberg, J. M., and Achten, R. (2015). MR pulse wave velocity increases

- with age faster in the thoracic aorta than in the abdominal aorta. *Journal of Magnetic Resonance Imaging*, 41(3):765–772.
- Di Lascio, N., Stea, F., Kusmic, C., Sicari, R., and Faita, F. (2014). Non-invasive assessment of pulse wave velocity in mice by means of ultrasound images. *Atherosclerosis*, 237(1):31–37.
- Dotter, C. T., Roberts, D. J., and Steinberg, I. (1950). Aortic Length: Angiocardiographic Measurements. *Circulation*, 2(6):915–920.
- Eurostat (2021). Population projections at regional level.
- Faure, E. M., Canaud, L., Cathala, P., Serres, I., Marty-Ané, C., and Alric, P. (2014). Human ex-vivo model of Stanford type B aortic dissection. *Journal of Vascular Surgery*, 60(3):767–775.
- Fernandes, L., Bessa, G., Gomes, B., and Azevedo, L. (2019). Stereoscopic PIV study of the influence of aortic valve tilt angle on the flow pattern in the ascending aorta region. page 11, Munich, Germany.
- Franzetti, G., Díaz-Zuccarini, V., and Balabani, S. (2019). Design of an In Vitro Mock Circulatory Loop to Reproduce Patient-Specific Vascular Conditions: Toward Precision Medicine. *Journal of Engineering and Science in Medical Diagnostics and Therapy*, 2(4):041004.
- Fung, Y.-C. (1993). *Biomechanics*. Springer New York, New York, NY.
- Fung, Y. C. (2013). *Biomechanics: Circulation*. Springer Science & Business Media.
- Galdi, G. P., Rannacher, R., Robertson, A. M., and Turek, S. (2008). *Hemodynamical flows: modeling, analysis and simulation*. Number v. 37 in Oberwolfach seminars. Birkhäuser ; Springer, distributor], Basel : [London.
- Galvin, S. D., Perera, N. K., and Matalanis, G. (2016). Surgical management of acute type A aortic dissection: branch-first arch replacement with total aortic repair. *Annals of Cardiothoracic Surgery*, 5(3):236–244.
- Garcia-Ochoa, F., Santos, V., Casas, J., and Gomez, E. (2000). Xanthan gum: production, recovery, and properties. *Biotechnology Advances*, 18(7):549–579.
- Geoghegan, P. H., Buchmann, N. A., Jermy, M. C., Nobes, D., Spence, C. J., and Docherty, P. D. (2010). SPIV and image correlation measurements of surface displacement during pulsatile flow in models of compliant, healthy and stenosed arteries. *15th Int Symp on Applications of Laser Techniques to Fluid Mechanics*, page 1595.
- Gijssen, F. J. H. (1999). The influence of the non-Newtonian properties of blood on the flow in large arteries: steady flow in a carotid bifurcation model. *Journal of Biomechanics*, 32:601–608.

- Gülan, U., Lüthi, B., Holzner, M., Liberzon, A., Tsinober, A., and Kinzelbach, W. (2012). Experimental study of aortic flow in the ascending aorta via Particle Tracking Velocimetry. *Experiments in Fluids*, 53(5):1469–1485.
- Grotenhuis, H. B., Westenberg, J. J. M., Steendijk, P., Geest, R. J. v. d., Ottenkamp, J., Bax, J. J., Jukema, J. W., and Roos, A. d. (2009). Validation and reproducibility of aortic pulse wave velocity as assessed with velocity-encoded MRI. *Journal of Magnetic Resonance Imaging*, 30(3):521–526.
- Harada, A., Okada, T., Niki, K., Chang, D., and Sugawara, M. (2002). On-line noninvasive one-point measurements of pulse wave velocity. *Heart and Vessels*, 17(2):61–68.
- Herrington William, Lacey Ben, Sherliker Paul, Armitage Jane, and Lewington Sarah (2016). Epidemiology of Atherosclerosis and the Potential to Reduce the Global Burden of Atherothrombotic Disease. *Circulation Research*, 118(4):535–546.
- Holzapfel, G. A. (2006). Determination of material models for arterial walls from uniaxial extension tests and histological structure. *Journal of Theoretical Biology*, 238(2):290–302.
- Hong, H., Yeom, E., Ji, H. S., Kim, H. D., and Kim, K. C. (2017). Characteristics of pulsatile flows in curved stenosed channels. *PLOS ONE*, 12(10):e0186300.
- Houriez-Gombaudo-Saintonge, S., Mousseaux, E., Bargiotas, I., De Cesare, A., Dietenbeck, T., Bouaou, K., Redheuil, A., Soulat, G., Giron, A., Gencer, U., Craiem, D., Messas, E., Bollache, E., Chenoune, Y., and Kachenoura, N. (2019). Comparison of different methods for the estimation of aortic pulse wave velocity from 4D flow cardiovascular magnetic resonance. *Journal of Cardiovascular Magnetic Resonance*, 21(1):75.
- Howard, D. P. J., Sideso, E., Handa, A., and Rothwell, P. M. (2014). Incidence, risk factors, outcome and projected future burden of acute aortic dissection. *Annals of Cardiothoracic Surgery*, 3(3):278–284.
- Hütter, L., Geoghegan, P. H., Docherty, P. D., Lazarjan, M. S., Clucas, D., and Jermy, M. (2016). Fabrication of a compliant phantom of the human aortic arch for use in Particle Image Velocimetry (PIV) experimentation. *Current Directions in Biomedical Engineering*, 2(1):493–497.
- Humphrey, J. D. (1995). Mechanics of the Arterial Wall: Review and Directions. *Critical Reviews & Trade; in Biomedical Engineering*, 23(1-2).
- Humphrey, J. D. (2002). *Cardiovascular Solid Mechanics*. Springer New York, New York, NY.
- Iasiello, M., Vafai, K., Andreozzi, A., and Bianco, N. (2017). Analysis of non-Newtonian effects within an aorta-iliac bifurcation region. *Journal of Biomechanics*, 64:153–163.
- Imura, T., Yamamoto, K., Satoh, T., Kanamori, K., Mikami, T., and Yasuda, H. (1990). In vivo viscoelastic behavior in the human aorta. *Circulation Research*, 66(5):1413–1419.

- Jesty, J., Yin, W., Perrotta, P., and Bluestein, D. (2003). Platelet activation in a circulating flow loop: combined effects of shear stress and exposure time. *Platelets*, 14(3):143–149.
- Joh, J. H., Ahn, H.-J., and Park, H.-C. (2013). Reference Diameters of the Abdominal Aorta and Iliac Arteries in the Korean Population. *Yonsei Medical Journal*, 54(1):48–54.
- Jones, C. J. H., Sugawara, M., Kondoh, Y., Uchida, K., and Parker, K. H. (2002). Compression and expansion wavefront travel in canine ascending aortic flow: wave intensity analysis. *Heart and Vessels*, 16(3):91–98.
- Jong, P. A. d., Hellings, W. E., Takx, R. A. P., Išgum, I., Herwaarden, J. A. v., and Mali, W. P. T. M. (2014). Computed Tomography of Aortic Wall Calcifications in Aortic Dissection Patients. *PLOS ONE*, 9(7):e102036.
- Jung, H., Choi, J. W., and Park, C. G. (2004). Asymmetric flows of non-Newtonian fluids in symmetric stenosed artery. *Korea-Australia Rheology Journal*, 16(2):101–108.
- Kahraman, H., Ozaydin, M., Varol, E., Aslan, S. M., Dogan, A., Altinbas, A., Demir, M., Gedikli, O., Acar, G., and Ergene, O. (2006). The Diameters of the Aorta and Its Major Branches in Patients with Isolated Coronary Artery Ectasia. *Texas Heart Institute Journal*, 33(4):463–468.
- Karmonik, C., Bismuth, J., Davies, M. G., Shah, D. J., Younes, H. K., and Lumsden, A. B. (2011). A Computational Fluid Dynamics Study Pre- and Post-Stent Graft Placement in an Acute Type B Aortic Dissection. *Vascular and Endovascular Surgery*, 45(2):157–164.
- Khanafer, K. M., Gadhoke, P., Berguer, R., and Bull, J. L. (2006). Modeling pulsatile flow in aortic aneurysms: Effect of non-Newtonian properties of blood. *Biorheology*, 43:19.
- Kim, O. V., Litvinov, R. I., Alber, M. S., and Weisel, J. W. (2017). Quantitative structural mechanobiology of platelet-driven blood clot contraction. *Nature Communications*, 8(1):1274.
- Kolipaka, A., Illapani, V. S. P., Kalra, P., Garcia, J., Mo, X., Markl, M., and White, R. D. (2017). Quantification and comparison of 4D-Flow MRI-derived wall shear stress and MRE-derived wall stiffness of the abdominal aorta. *Journal of magnetic resonance imaging : JMRI*, 45(3):771–778.
- Kung, E. O., Les, A. S., Medina, F., Wicker, R. B., McConnell, M. V., and Taylor, C. A. (2011). In Vitro Validation of Finite Element Analysis of Blood Flow in Deformable Models. *Journal of biomechanical engineering*, 133(4):041003.
- Lima, R., Wada, S., Tsubota, K.-i., and Yamaguchi, T. (2006). Confocal micro-PIV measurements of three-dimensional profiles of cell suspension flow in a square microchannel. *Measurement Science and Technology*, 17(4):797–808.

- Liu, D., Fan, Z., Li, Y., Zhang, N., Sun, Z., An, J., Stalder, A. F., Greiser, A., and Liu, J. (2018). Quantitative Study of Abdominal Blood Flow Patterns in Patients with Aortic Dissection by 4-Dimensional Flow MRI. *Scientific Reports*, 8(1):9111.
- Long, J. A., Undar, A., Manning, K. B., and Deutsch, S. (2005). Viscoelasticity of Pediatric Blood and its Implications for the Testing of a Pulsatile Pediatric Blood Pump. *ASAIO Journal*, 51(5):563–566.
- Lotz, J., Meier, C., Leppert, A., and Galanski, M. (2002). Cardiovascular Flow Measurement with Phase-Contrast MR Imaging: Basic Facts and Implementation. *RadioGraphics*, 22(3):651–671. Publisher: Radiological Society of North America.
- Lu, Q., Hofferbert, B. V., Koo, G., and Malinauskas, R. A. (2013). In Vitro Shear Stress Induced Platelet Activation: Sensitivity of Human and Bovine Blood. *Artif Organs*, 37(10):11.
- Mann, D. E. and Tarbell, J. M. (1990). Flow of non-Newtonian blood analog fluids in rigid curved and straight artery models. *Biorheology*, 27(5):711–733.
- Marieb, E. and Hoehn, K. (2014). *Anatomie et physiologie humaines*. Pearson Education France.
- Medero, R., Hoffman, C., and Roldán-Alzate, A. (2018). Comparison of 4D Flow MRI and Particle Image Velocimetry Using an In Vitro Carotid Bifurcation Model. *Annals of biomedical engineering*, 46(12):2112–2122.
- Melvinsdottir, I. H., Lund, S. H., Agnarsson, B. A., Sigvaldason, K., Gudbjartsson, T., and Geirsson, A. (2016). The incidence and mortality of acute thoracic aortic dissection: results from a whole nation study. *European Journal of Cardio-Thoracic Surgery: Official Journal of the European Association for Cardio-Thoracic Surgery*, 50(6):1111–1117.
- Menut, M. (2017). *Chirurgie endovasculaire virtuelle pour patient-spécifique: Application au traitement de l'anévrisme de l'aorte thoracique (Doctoral dissertation)*. PhD thesis, INSA de Lyon.
- Merrill, E. W. and Pelletier, G. A. (1967). Viscosity of human blood: transition from Newtonian to non-Newtonian. *Journal of Applied Physiology*, 23(2):178–182.
- Moore, J. E., Blirki, E., and Brunner, H. R. (1994). A device for subjecting vascular endothelial cells to both fluid shear stress and circumferential cyclic stretch. *Annals of Biomedical Engineering*, 22:416–422.
- Mouktadiri, G. (2013). *Angiovision - Pose d'endoprothèse aortique par angionavigation augmentée (Doctoral dissertation)*. PhD thesis, INSA de Lyon.
- Naeini, M. B., Sahebi, M., Nikbakht, F., Jamshidi, Z., Ahmadimanesh, M., Hashemi, M., Ramezani, J., Miri, H. H., and Yazdian-Robati, R. (2021). A meta-meta-analysis: Evaluation of meta-analyses published in the effectiveness of cardiovascular comorbidities on the severity of COVID-19. *Obesity Medicine*, 22:100323.

- Naidu, O., Srinivas, R., Nagula, P., and Parvathareddy, K. (2020). Significance of Aortic Propagation Velocity in Patients with Coronary Artery Disease – A Novel Echocardiographic Parameter of Atherosclerosis. *Journal of the Practice of Cardiovascular Sciences*.
- Naim, W. N. W. A., Ganesan, P. B., Sun, Z., Liew, Y. M., Qian, Y., Lee, C.-J., Jansen, S., Hashim, S. A., and Lim, E. (2016). Prediction of thrombus formation using vortical structures presentation in Stanford type B aortic dissection: A preliminary study using CFD approach. *Applied Mathematical Modelling*, 40(4):3115–3127.
- Najjari, M. R., Hinke, J. A., Bulusu, K. V., and Plesniak, M. W. (2016). On the rheology of refractive-index-matched, non-Newtonian blood-analog fluids for PIV experiments. *Experiments in Fluids*, 57(6):96.
- Najjari, M. R. and Plesniak, M. W. (2016). Evolution of vortical structures in a curved artery model with non-Newtonian blood-analog fluid under pulsatile inflow conditions. *Experiments in Fluids*, 57(6):100.
- Najjari, M. R. and Plesniak, M. W. (2018). Secondary flow vortical structures in a 180 $^{\circ}$ elastic curved vessel with torsion under steady and pulsatile inflow conditions. *Physical Review Fluids*, 3(1):013101.
- Natsume, K., Shiiya, N., Takehara, Y., Sugiyama, M., Satoh, H., Yamashita, K., and Washiyama, N. (2017). Characterizing saccular aortic arch aneurysms from the geometry-flow dynamics relationship. *The Journal of Thoracic and Cardiovascular Surgery*, 153(6):1413–1420.e1.
- Negoita, M., Hughes, A. D., Parker, K. H., and Khir, A. W. (2018). A method for determining local pulse wave velocity in human ascending aorta from sequential ultrasound measurements of diameter and velocity. *Physiological Measurement*, 39(11):114009.
- Neofytou, P. (2006). Transition to asymmetry of generalised Newtonian fluid flows through a symmetric sudden expansion. *Journal of Non-Newtonian Fluid Mechanics*, 133(2):132–140.
- Nienaber, C. A., Clough, R. E., Sakalihasan, N., Suzuki, T., Gibbs, R., Mussa, F., Jenkins, M. P., Thompson, M. M., Evangelista, A., Yeh, J. S. M., Cheshire, N., Rosendahl, U., and Pepper, J. (2016). Aortic dissection. *Nature Reviews Disease Primers*, 2(1):16053.
- OECD (2020). Mortality from circulatory diseases | Health at a Glance: Europe 2020 : State of Health in the EU Cycle | OECD iLibrary.
- Ogden, R. W. and Hill, R. (1972). Large deformation isotropic elasticity – on the correlation of theory and experiment for incompressible rubberlike solids. *Proceedings of the Royal Society of London. A. Mathematical and Physical Sciences*, 326(1567):565–584.
- Olson, R. M. (1968). Aortic blood pressure and velocity as a function of time and position. *Journal of Applied Physiology*, 24(4):563–569.

- OpenFOAM (2021). www.openfoam.org.
- Pacini, D., Di Marco, L., Fortuna, D., Belotti, L. M. B., Gabbieri, D., Zussa, C., Pignini, F., Contini, A., Barattoni, M. C., De Palma, R., and Di Bartolomeo, R. (2013). Acute aortic dissection: Epidemiology and outcomes. *International Journal of Cardiology*, 167(6):2806–2812.
- Pagoulatou, S. and Stergiopoulos, N. (2017). Evolution of aortic pressure during normal ageing: A model-based study. *PLOS ONE*, 12(7):e0182173.
- Pahwa, R. and Jialal, I. (2020). Atherosclerosis. In *StatPearls*. StatPearls Publishing, Treasure Island (FL).
- Palanca, M., Tozzi, G., and Cristofolini, L. (2016). The use of digital image correlation in the biomechanical area: a review. *International Biomechanics*, 3(1):1–21.
- Pan, W. (2021). *Computer aided surgery : application to aortic dissection*. PhD thesis, INSA Lyon.
- Pan, W., Kulisa, P., Escriva, X., Bou, B., Menut, M., Lermusiaux, P., and Millon, A. (2020). Computer Aided Surgery: Application to Aortic Dissection. *Annals of Vascular Medicine & Research Cite*, 7(5):1120.
- Payan, Y. and Ohayon, J., editors (2017). *Biomechanics of living organs: hyperelastic constitutive laws for finite element modeling*. Academic Press series in biomedical engineering. Academic Press, an imprint of Elsevier, London ; San Diego, CA, world bank publications. edition.
- Pazos, V., Mongrain, R., and Tardif, J. C. (2010). Deformable Mock Stenotic Artery With a Lipid Pool. *Journal of Biomechanical Engineering*, 132(3):034501.
- Pedersen, E., Oyre, S., Agerbæk, M., Kristensen, I., Ringgaard, S., Boesiger, P., and Paaske, W. (1999). Distribution of Early Atherosclerotic Lesions in the Human Abdominal Aorta Correlates with Wall Shear Stresses Measured In Vivo. *European Journal of Vascular and Endovascular Surgery*, 18(4):328–333.
- Perktold, K., Thurner, E., and Kenner, T. (1994). Flow and stress characteristics in rigid walled and compliant carotid artery bifurcation models. *Medical & Biological Engineering & Computing*, 32(1):19–26.
- Perrin, D., Badel, P., Orgeas, L., Geindreau, C., du Roscoat, S. r., Albertini, J.-N., and Avril, S. (2016). Patient-specific simulation of endovascular repair surgery with tortuous aneurysms requiring flexible stent-grafts. *Journal of the Mechanical Behavior of Biomedical Materials*, 63:86–99.
- Petersson, S., Dyverfeldt, P., and Ebbers, T. (2012). Assessment of the accuracy of MRI wall shear stress estimation using numerical simulations. *Journal of Magnetic Resonance Imaging*, 36(1):128–138.

- Poiseuille, J. L. (1840). Recherches experimentale sur les mouvement des liquides dans les tubes de très petits diamètres. I, II, III. *C. R. Acad. Sci.*
- Prahl Wittberg, L., van Wyk, S., Fuchs, L., Gutmark, E., Backeljauw, P., and Gutmark-Little, I. (2016). Effects of aortic irregularities on blood flow. *Biomechanics and Modeling in Mechanobiology*, 15(2):345–360.
- Rachid, K. (2018). *Estimation de la pression aortique à l’aide de l’imagerie par résonance magnétique : développement d’un modèle biomécanique d’écoulement*. Thèse, Université Paris-Saclay.
- Rodríguez, J. F., Ruiz, C., Doblaré, M., and Holzapfel, G. A. (2008). Mechanical Stresses in Abdominal Aortic Aneurysms: Influence of Diameter, Asymmetry, and Material Anisotropy. *Journal of Biomechanical Engineering*, 130(2):021023.
- Rognoni, A., Cavallino, C., Veia, A., Bacchini, S., Rosso, R., Facchini, M., G. Secco, G., Lupi, A., Nardi, F., Rametta, F., and S. Bongo, A. (2015). Pathophysiology of Atherosclerotic Plaque Development. *Cardiovascular & Hematological Agents in Medicinal Chemistry (Formerly)*, 13(1):10–13.
- Rudenick, P. A., Bijmens, B. H., García-Dorado, D., and Evangelista, A. (2013). An in vitro phantom study on the influence of tear size and configuration on the hemodynamics of the lumina in chronic type B aortic dissections. *Journal of Vascular Surgery*, 57(2):464–474.e5.
- Sakariassen, K. S., Orning, L., and Turitto, V. T. (2015). The impact of blood shear rate on arterial thrombus formation. *Future Science OA*, 1(4).
- Scarano, F., Ghaemi, S., Caridi, G. C. A., Bosbach, J., Dierksheide, U., and Sciacchitano, A. (2015). On the use of helium-filled soap bubbles for large-scale tomographic PIV in wind tunnel experiments. *Experiments in Fluids*, 56(2):42.
- Schirmer, C. M. and Malek, A. M. (2007). Wall shear stress gradient analysis within an idealized stenosis using non-Newtonian flow. *Neurosurgery*, 61(4):853–864.
- Schoephoerster, R. T., Oynes, F., Nunez, G., Kapadvanjwala, M., and Dewanjee, M. K. (1993). Effects of local geometry and fluid dynamics on regional platelet deposition on artificial surfaces. *Arteriosclerosis and Thrombosis: A Journal of Vascular Biology*, 13(12):1806–1813.
- Secomb, T. W. (2016). Hemodynamics. *Comprehensive Physiology*, 6(2):975–1003.
- Shampine, L. F. and Reichelt, M. W. (1997). The MATLAB ODE Suite. *SIAM Journal on Scientific Computing*, 18(1):1–22.
- Shi, Y., Zhu, M., Chang, Y., Qiao, H., and Liu, Y. (2016). The risk of stanford type-A aortic dissection with different tear size and location: a numerical study. *BioMedical Engineering OnLine*, 15(Suppl 2):128.

- Singh, A. and Mehta, Y. (2015). Intraoperative aortic dissection. *Annals of Cardiac Anaesthesia*, 18(4):537–542.
- Sonesson, B., Länne, T., Vernerström, E., and Hansen, F. (1994). Sex difference in the mechanical properties of the abdominal aorta in human beings. *Journal of Vascular Surgery*, 20(6):959–969.
- Soudah, E., Rudenick, P., Bordone, M., Bijmens, B., García-Dorado, D., Evangelista, A., and Oñate, E. (2015). Validation of numerical flow simulations against *in vitro* phantom measurements in different type B aortic dissection scenarios. *Computer Methods in Biomechanics and Biomedical Engineering*, 18(8):805–815.
- Stalder, A. F., Russe, M. F., Frydrychowicz, A., Bock, J., Hennig, J., and Markl, M. (2008). Quantitative 2D and 3D phase contrast MRI: Optimized analysis of blood flow and vessel wall parameters. *Magnetic Resonance in Medicine*, 60(5):1218–1231.
- Stamatopoulos, C., Mathioulakis, D. S., Papaharilaou, Y., and Katsamouris, A. (2011). Experimental unsteady flow study in a patient-specific abdominal aortic aneurysm model. *Experiments in Fluids*, 50(6):1695–1709.
- Stankovic, Z., Allen, B. D., Garcia, J., Jarvis, K. B., and Markl, M. (2014). 4D flow imaging with MRI. *Cardiovascular Diagnosis and Therapy*, 4(2):173–192.
- Sugimoto, K. (2015). Effects of arterial blood flow on walls of the abdominal aorta: distributions of wall shear stress and oscillatory shear index determined by phase-contrast magnetic resonance imaging. *Heart Vessels*, 31:1168–1175.
- Tabakova, S., Nikolova, E., and Radev, S. (2014). Carreau model for oscillatory blood flow in a tube. pages 336–343, Albena, Bulgaria.
- Thirugnanasambandam, M., Canchi, T., Piskin, S., Karmonik, C., Kung, E., Menon, P., Avril, S., and Finol, E. A. (2021). Design, Development and Temporal Evaluation of an MRI-Compatible In-Vitro Circulation Model Using a Compliant AAA Phantom. *Journal of Biomechanical Engineering*, 5:143.
- Thomas, D. M., Hultén, E. A., Ellis, S. T., Anderson, D. M. F., Anderson, N., McRae, F., Malik, J. A., Villines, T. C., and Slim, A. M. (2014). Open versus Endovascular Repair of Abdominal Aortic Aneurysm in the Elective and Emergent Setting in a Pooled Population of 37,781 Patients: A Systematic Review and Meta-Analysis. *ISRN Cardiology*, 2014:1–9.
- Thompson, S. G., Ashton, H. A., Gao, L., Buxton, M. J., and Scott, R. A. P. (2012). Final follow-up of the Multicentre Aneurysm Screening Study (MASS) randomized trial of abdominal aortic aneurysm screening. *The British Journal of Surgery*, 99(12):1649–1656.
- Thurston, G. B. (1979). Rheological parameters for the viscosity viscoelasticity and thixotropy of blood. *Biorheology*, 16(3):149–162.

- Thurston, G. B. and Henderson, N. M. (2006). Effects of flow geometry on blood viscoelasticity. *Biorheology*, 43(6):729–746.
- Tippe, A., Reimnger, A., Reininger, C., and Rieß, R. (1992). A method for quantitative determination of flow induced human platelet adhesion and aggregation. *Thrombosis Research*, 67(4):407–418.
- Tokgoz, S., Elsinga, G. E., Delfos, R., and Westerweel, J. (2012). Spatial resolution and dissipation rate estimation in Taylor–Couette flow for tomographic PIV. *Experiments in Fluids*, 53(3):561–583.
- Tomkins, C. D. and Adrian, R. J. (2003). Spanwise structure and scale growth in turbulent boundary layers. *Journal of Fluid Mechanics*, 490:37–74.
- Tsai Thomas T., Evangelista Arturo, Nienaber Christoph A., Trimarchi Santi, Sechtem Udo, Fattori Rossella, Myrmel Truls, Pape Linda, Cooper Jeanna V., Smith Dean E., Fang Jianming, Isselbacher Eric, and Eagle Kim A. (2006). Long-Term Survival in Patients Presenting With Type A Acute Aortic Dissection. *Circulation*, 114(1.supplement):I–350.
- Ulug, P., Powell, J. T., Sweeting, M. J., Bown, M. J., and Thompson, S. G. (2016). Meta-analysis of the current prevalence of screen-detected abdominal aortic aneurysm in women. *The British Journal of Surgery*, 103(9):1097–1104.
- Valdez-Jasso, D., Bia, D., Zócalo, Y., Armentano, R. L., Haider, M. A., and Olufsen, M. S. (2011). Linear and Nonlinear Viscoelastic Modeling of Aorta and Carotid Pressure-Area Dynamics under in vivo and ex vivo Conditions. *Annals of biomedical engineering*, 39(5):1438–1456.
- van Elderen, S. G. C., Westenberg, J. J. M., Brandts, A., van der Meer, R. W., Romijn, J. A., Smit, J. W. A., and de Roos, A. (2011). Increased Aortic Stiffness Measured by MRI in Patients With Type 1 Diabetes Mellitus and Relationship to Renal Function. *American Journal of Roentgenology*, 196(3):697–701.
- Vande Geest, J. P., Sacks, M. S., and Vorp, D. A. (2006). The effects of aneurysm on the biaxial mechanical behavior of human abdominal aorta. *Journal of Biomechanics*, 39(7):1324–1334.
- VanderLaan Paul A., Reardon Catherine A., and Getz Godfrey S. (2004). Site Specificity of Atherosclerosis. *Arteriosclerosis, Thrombosis, and Vascular Biology*, 24(1):12–22.
- Vito, R. P. and Hickey, J. (1980). The mechanical properties of soft tissues—II: The elastic response of arterial segments. *Journal of Biomechanics*, 13(11):951–957.
- Vlachopoulos, C., O’Rourke, M., and Nichols, W. W. (2011). *McDonald’s Blood Flow in Arteries: Theoretical, Experimental and Clinical Principles*. CRC Press.
- Walker, A. M., Johnston, C. R., and Rival, D. E. (2014). On the Characterization of a Non-Newtonian Blood Analog and Its Response to Pulsatile Flow Downstream of a Simplified Stenosis. *Annals of Biomedical Engineering*, 42(1):97–109.

- Weber, T., Ammer, M., Rammer, M., Adj, A., O'Rourke, M. F., Wassertheurer, S., Rosenkranz, S., and Eber, B. (2009). Noninvasive determination of carotid–femoral pulse wave velocity depends critically on assessment of travel distance: a comparison with invasive measurement. *Journal of hypertension*, 27(8):1624–1630.
- Weddell, J. C., Kwack, J., Imoukhuede, P. I., and Masud, A. (2015). Hemodynamic Analysis in an Idealized Artery Tree: Differences in Wall Shear Stress between Newtonian and Non-Newtonian Blood Models. *PLOS ONE*, 10(4):e0124575.
- Whitcomb, P. J. and Macosko, C. W. (1978). Rheology of Xanthan Gum. *Journal of Rheology*, 22(5):493–505.
- Wilson, J. S., Baek, S., and Humphrey, J. D. (2012). Importance of initial aortic properties on the evolving regional anisotropy, stiffness and wall thickness of human abdominal aortic aneurysms. *Journal of The Royal Society Interface*, 9(74):2047–2058.
- Womersley, J. R. (1955). Method for the calculation of velocity, rate of flow and viscous drag in arteries when the pressure gradient is known. *The Journal of Physiology*, 127(3):553–563.
- Yang, Y., Van Reeth, E., and Poh, C. L. (2013). Adapting registration-based-segmentation for efficient segmentation of thoracic 4D MRI. In *2013 IEEE Symposium on Computational Intelligence in Healthcare and e-health (CICARE)*, pages 42–45.
- Yazdi, S. G., Geoghegan, P. H., Docherty, P. D., Jermy, M., and Khanafer, A. (2018). A Review of Arterial Phantom Fabrication Methods for Flow Measurement Using PIV Techniques. *Annals of Biomedical Engineering*, 46(11):1697–1721.
- Yoneyama, S. (2016). Basic principle of digital image correlation for in-plane displacement and strain measurement. *Advanced Composite Materials*, 25(2):105–123.
- Yousif, M. Y., Holdsworth, D. W., and Poepping, T. L. (2011). A blood-mimicking fluid for particle image velocimetry with silicone vascular models. *Experiments in Fluids*, 50(3):769–774.
- Zhong, L., Oostrom, M., Truex, M., Vermeul, V., and Szecsody, J. (2013). Rheological behavior of xanthan gum solution related to shear thinning fluid delivery for subsurface remediation. *Journal of Hazardous Materials*, 244-245:160–170.
- Zhou, J., Adrian, R. J., Balachandar, S., and Kendall, T. M. (1999). Mechanisms for generating coherent packets of hairpin vortices in channel flow. *Journal of Fluid Mechanics*, 387:353–396.
- Zimmermann, J., Loecher, M., Kolawole, F. O., Bäuml, K., Gifford, K., Dual, S. A., Levenston, M., Marsden, A. L., and Ennis, D. B. (2021). On the impact of vessel wall stiffness on quantitative flow dynamics in a synthetic model of the thoracic aorta. *Scientific Reports*, 11(1):6703.

- Zimpfer, D., Schima, H., Czerny, M., Kasimir, M.-T., Sandner, S., Seebacher, G., Losert, U., Simon, P., Grimm, M., Wolner, E., and Ehrlich, M. (2008). Experimental Stent-Graft Treatment of Ascending Aortic Dissection. *The Annals of Thoracic Surgery*, 85(2):470–473.
- Zupančič Valant, A., Žiberna, L., Papaharilaou, Y., Anayiotos, A., and Georgiou, G. C. (2011). The influence of temperature on rheological properties of blood mixtures with different volume expanders—implications in numerical arterial hemodynamics simulations. *Rheologica Acta*, 50(4):389–402.

APPENDIX A

Experimental setup

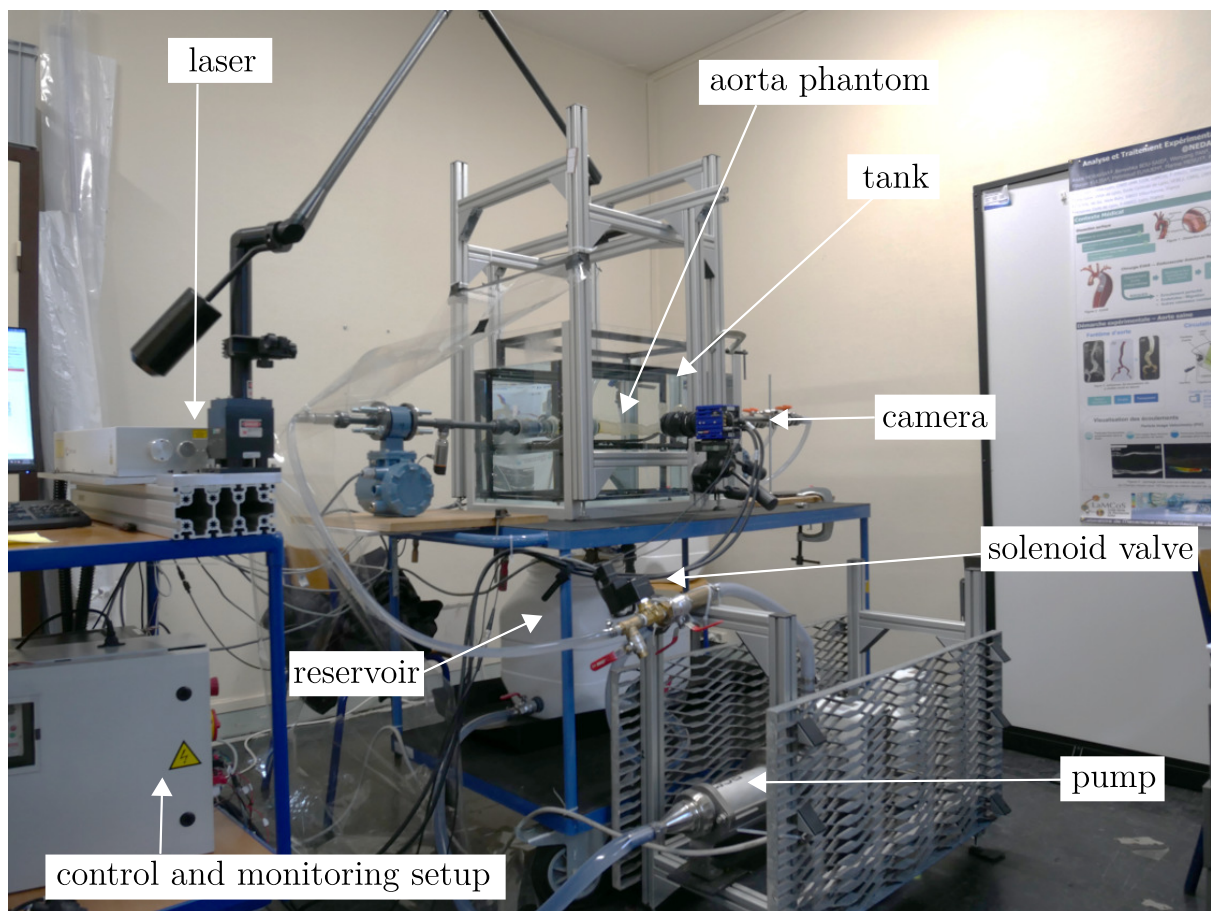


Figure A.1: Photo of the experimental setup.

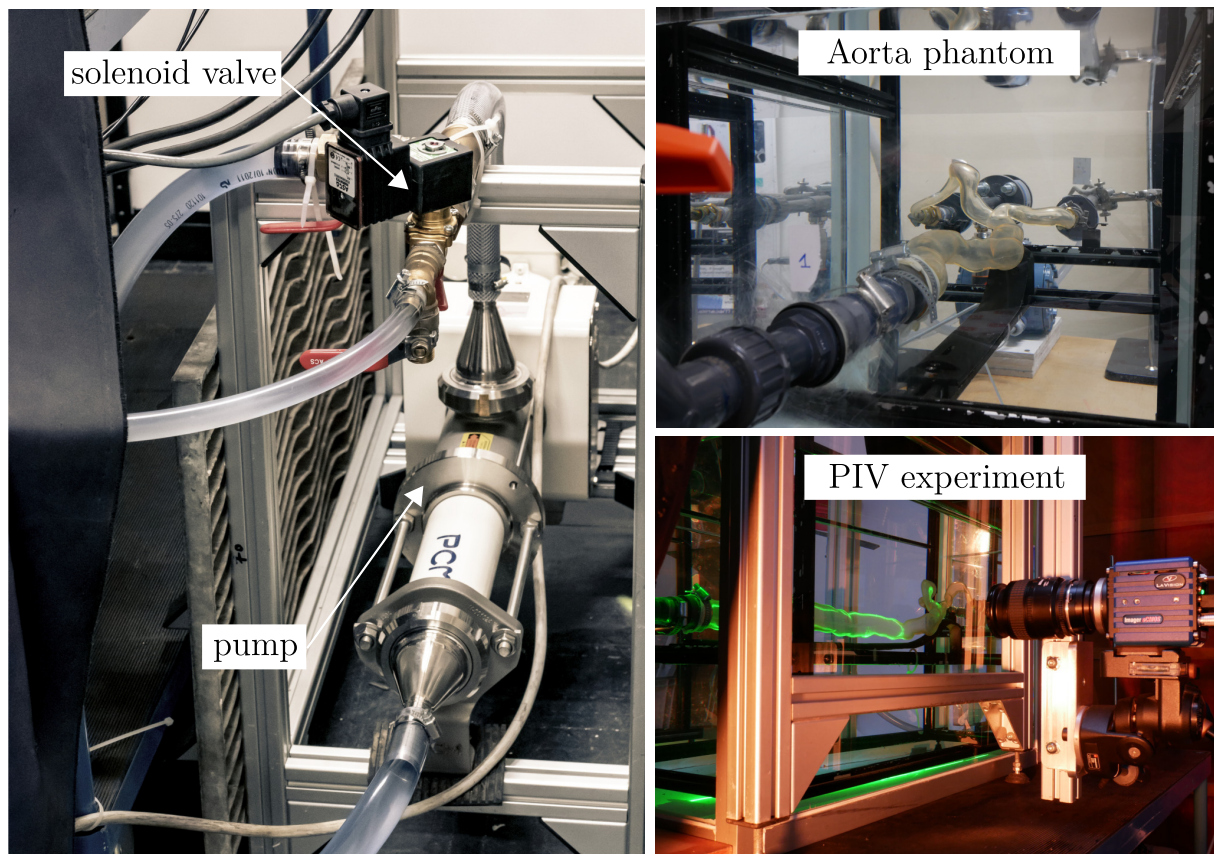


Figure A.2: Photo of the experimental setup with the AA phantom immersed in water.

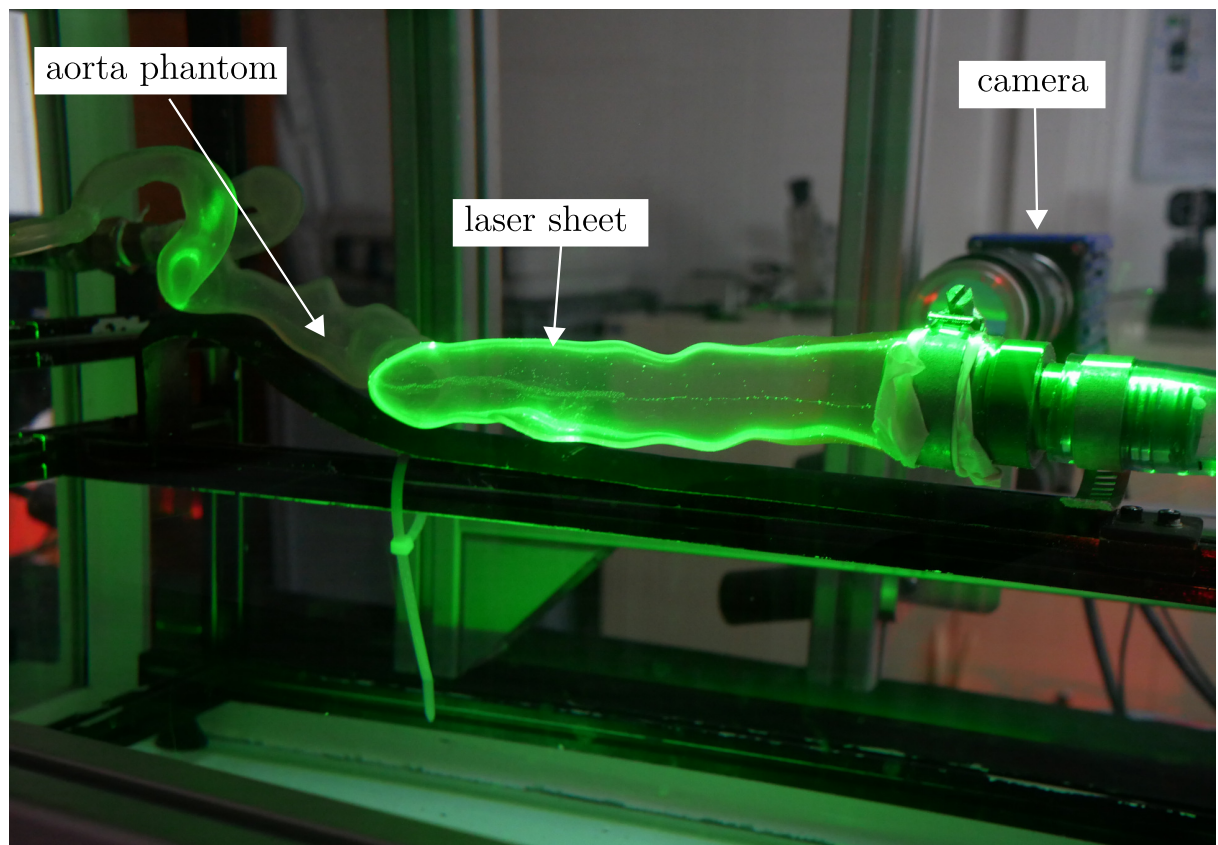
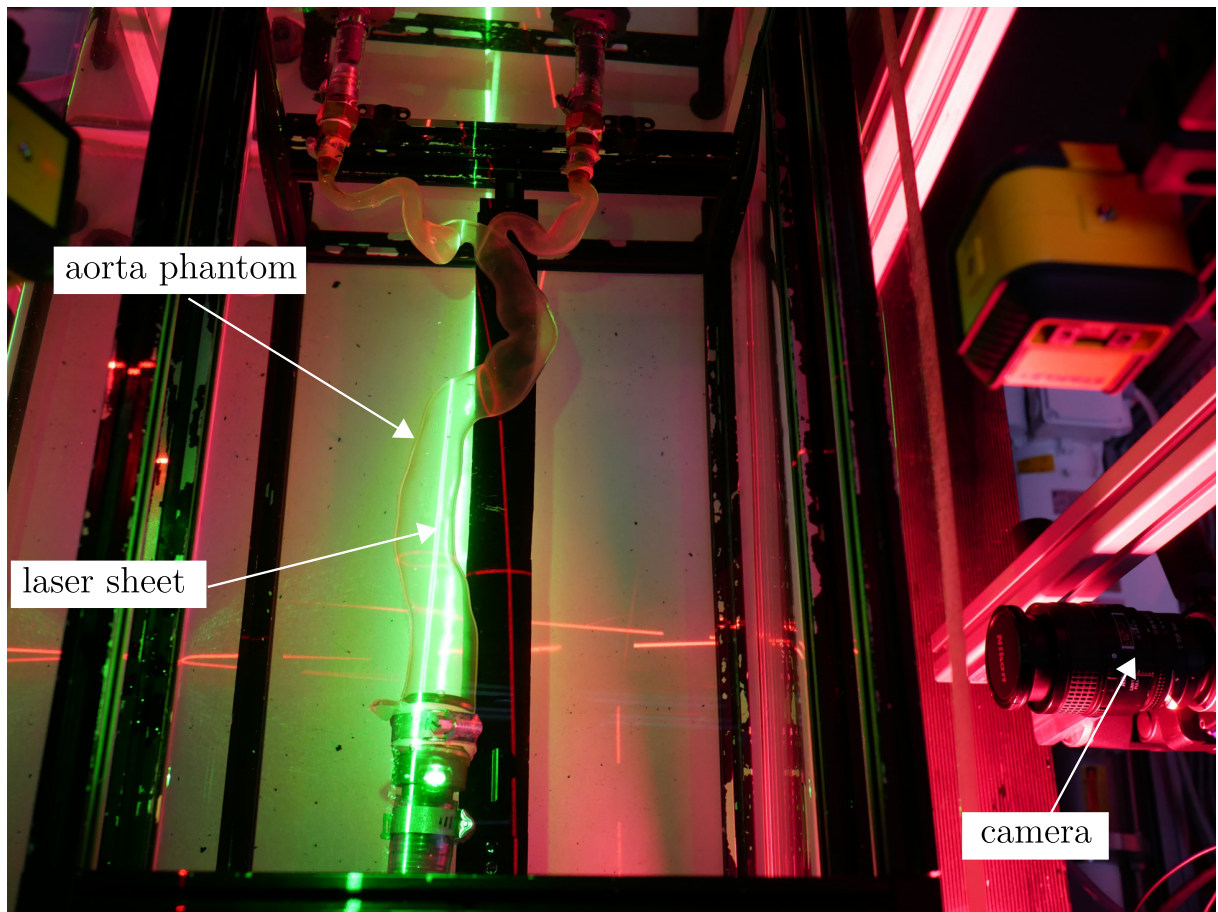


Figure A.3: Photo of the experimental setup with the AA phantom immersed in water during laser sheet thickness and parallelism setting.

Sensors installation and characteristics

On the experimental setup, a pair of pressure sensors and a pair of flowmeters are installed. It is essential to check if each pair is calibrated on the same base and shows same response times to identical signals. The measurements conducted with the mock loop are evaluated with comparison between inlet and outlet values, time delay with cycle flow conditions and synchronization with the PIV system. Checking sensors measured values matching in magnitude and time is thus crucial.

Sensors installation

The circulatory mock loop was equipped with two magnetic flowmeters and two pressure sensors to monitor flowrate and pressure upstream and downstream in the aorta phantom. Sensors were located on rigid PVC tube sections with sufficient length of straight-run to guarantee fluid flow full development and reliable measurements. Straight PVC sections were 15 mm diameter tubes and each sensors had an upstream 150 mm (10 diameters) and downstream 75 mm (5 diameters) straight-run.

Static pressure test

Static pressure steps were imposed to the system to check if inlet and outlet pressures sensors measured the same value (figure B.1). These experiments were conducted with tap water. After sensors calibration with atmospheric pressure, it appeared that the outlet pressure sensor was always 2.93 mbar lower than the inlet one. On the mock loop, the outlet pressure sensor was 30 mm higher than the inlet one which corresponded to a 2.94 mbar static pressure difference. Typical measured pressure for cardiac cycle were in the range of 80-120 mmHg (approximately 107-160 mbar). Each of the static pressure test was conducted on 100 measurements. For a specific pressure, measured values varied in a range of ± 1 mbar (0.75 mmHg) which was equivalent to an error of 0.83 - 1.25% of pressure value in the typical cardiac cycle pressure range. Calibration of sensors was validated with these experiments.

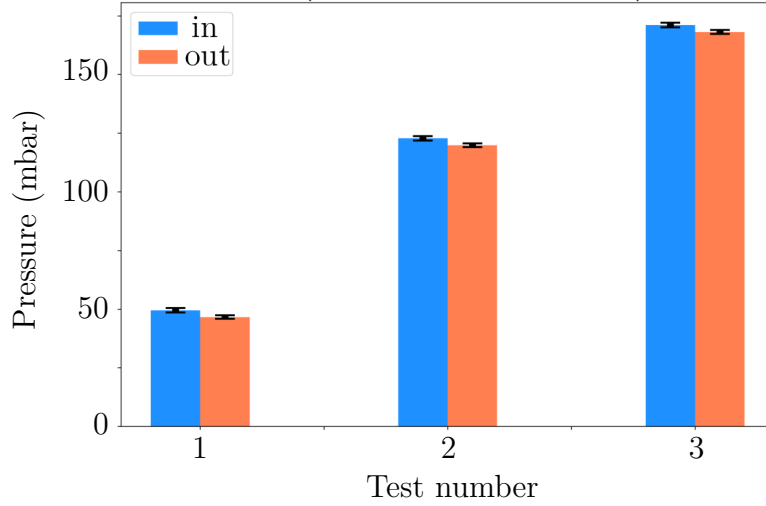


Figure B.1: Static pressure measured with inlet and outlet pressure sensors at 3 different levels.

Continuous flowrate tests

The same kind of experiments were conducted to check if flowmeters were identically calibrated. Flowmeters were placed in series on a straight rigid tube section in the mock loop. Continuous flowrate steps were applied so the two flowmeters should measure the same values if well calibrated. Results are presented in figure B.2 for 6 experiments. Considering mean flowrate and standard deviation, we admitted that the two flowrates are adjusted on the same calibration base.

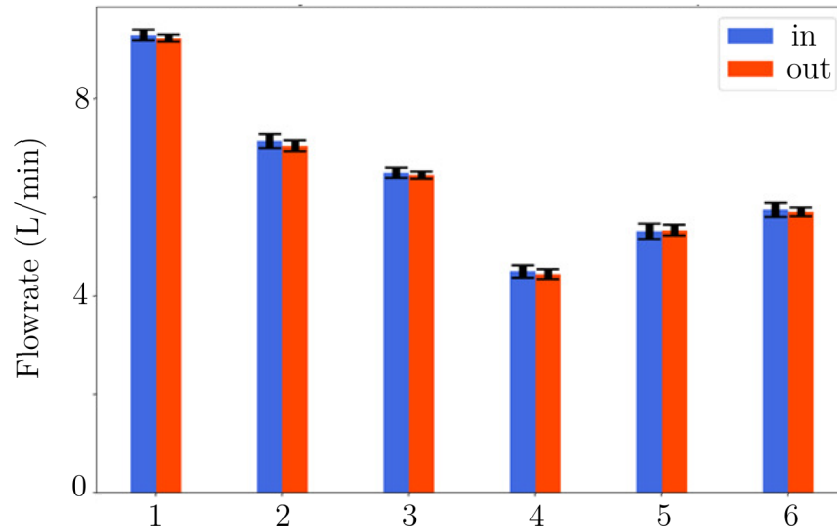


Figure B.2: Continuous flowrates measured with inlet and outlet flowmeters at 6 different levels. Bar chart represent mean values and error bars (standard deviation) bases on 100 measurements.

Recording rate

The NI-LabVIEW system was set to emit and save signals every 20 ms. Regarding the number of saved and emitted signals with real-time visualization, a higher rate resulted in data overload, time lags and missing data in recordings. If needed, FPGA (Field Programmable Gate Arrays) programming enables to reach higher recording rates and could be implemented on the setup with no additional devices. However, it was not needed for the present study experiments and for convenience purpose and real-time programming possibilities, FPGA was not developed.

Sampling

In the present work, sampling is achieved with a frequency $f_s = 50$ Hz (signal emitting and acquisition every 20 ms). Shannon sampling theorem affirms that an analog signal can be recovered as long as the sampling rate is at least twice higher than the highest frequency component of the analog signal (equation [B.0.1](#)).

$$f_s > 2f_{max} \quad (\text{B.0.1})$$

The standard recorded signals were pressure and flowrate signals close to human aortic flow conditions. Considering the reference abdominal aorta flowrate signal from [Cheng et al. \(2003\)](#), maximum detected frequency from Fast Fourier Transform was $f_{max} = 12.69$ Hz. Shannon sampling theorem is thus validated for this configuration.

BMF fabrication and rheometry

C.1 Fabrication

The BMF is a mixture of water, glycerin, xanthan gum and NaCl. To obtain a homogeneous solution, components need to be added and mixed in the right order in proper ratio. The main difficulty is the mixing of xanthan gum in an aqueous solution as it tends to agglomerate and form lumps. This section provides a technique to avoid lump formations and quickly obtain an homogeneous solution. Proportions are provided for 32 kg of our optimized BMF (table C.1). This quantity is adapted for a experimental trial on the mock loop with extra in case of leak.

Table C.1: BMF components proportions.

Component	Proportion (%wt)	Weigth (kg)	Volume (L)
Water	55.6%	20.0	20.0
Glycerin	37%	13.3	10.6
Xanthan gum	0.02%	0.0027	x
NaCl	7.40%	7.2	x
Total	100 %	36	30.6

- **Step 1:** First mix water in glycerin in the right proportion to obtain the final BMF. Reserve some glycerin (about 10% of its total quantity) for mixing apart with xanthan gum (step 2). The water-glycerin is homogenized with strong agitation thanks to a power drill with a paint mixer. Heating at 30 °C is applied in the solution when mixing.
- **Step 2:** In a separate container, add the reserved glycerin, put it under mixing with strong agitation with a magnetic stir bar. With a spatula, progressively add the xanthan gum power to the glycerin. If the quantity of xanthan gum is added to fast, the risk is to obtain xanthan lumps at the surface of the mixture. Once formed, those lumps are almost impossible to mix. However, this risk is highly minimized

by mixing xanthan in glycerin and not in water or water-glycerin mixture. Let the solution under mixing during an hour after adding all the xanthan gum.

- **Step 3:** Add the glycerin-xanthan solution to the water-glycerin one and mix during an hour with strong agitation (drill and paint mixer).
- **Step 4:** Finally, add the salt NaCl to the solution and mix it during 2 to 3 hours. Heating at 30 °C helps to dissolve the salt in the solution.

C.2 Rheometry

The rheometry setup are described in table C.2.

Table C.2: Rheometer parameters

Parameter	Value
Rheometer	MCR302
Measuring tool	CP50-1
Temperature	25°C
Moving profile	Low viscosity
Gap	0.103 mm
Variable	shear-rate
Initial	10 s
Final	200 s
Profile	Logarithmic ramp
Number of points	10
Duration per points	Logarithmic ramp
Initial	1000 s ⁻¹
Final	0.01 s ⁻¹
Temperature	25°C
Moving profile	Low viscosity
Gap	0.103 mm

Newtonien vs non-Newtonian velocity fields

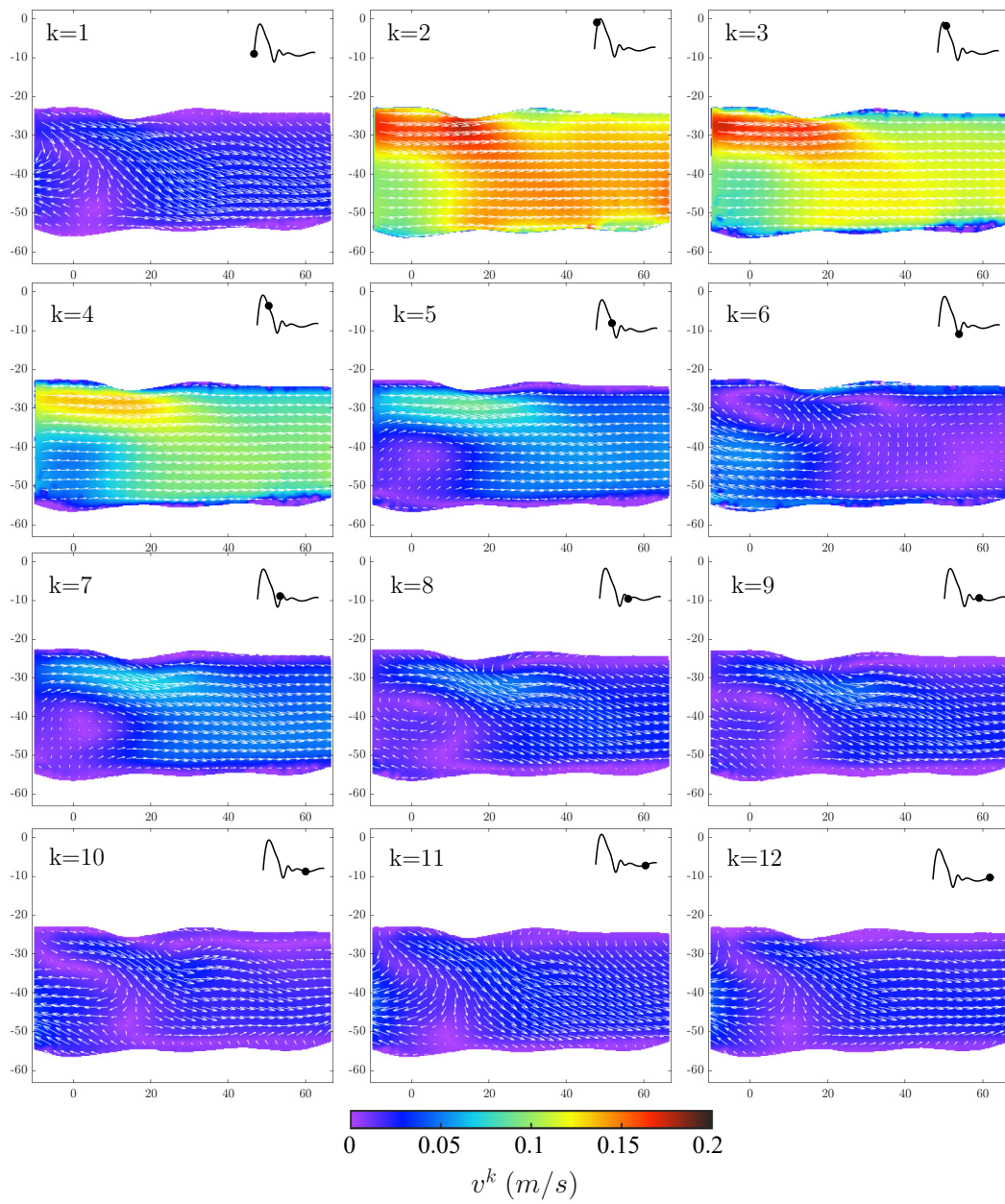


Figure D.1: Newtonian fluid flow experiment fields.

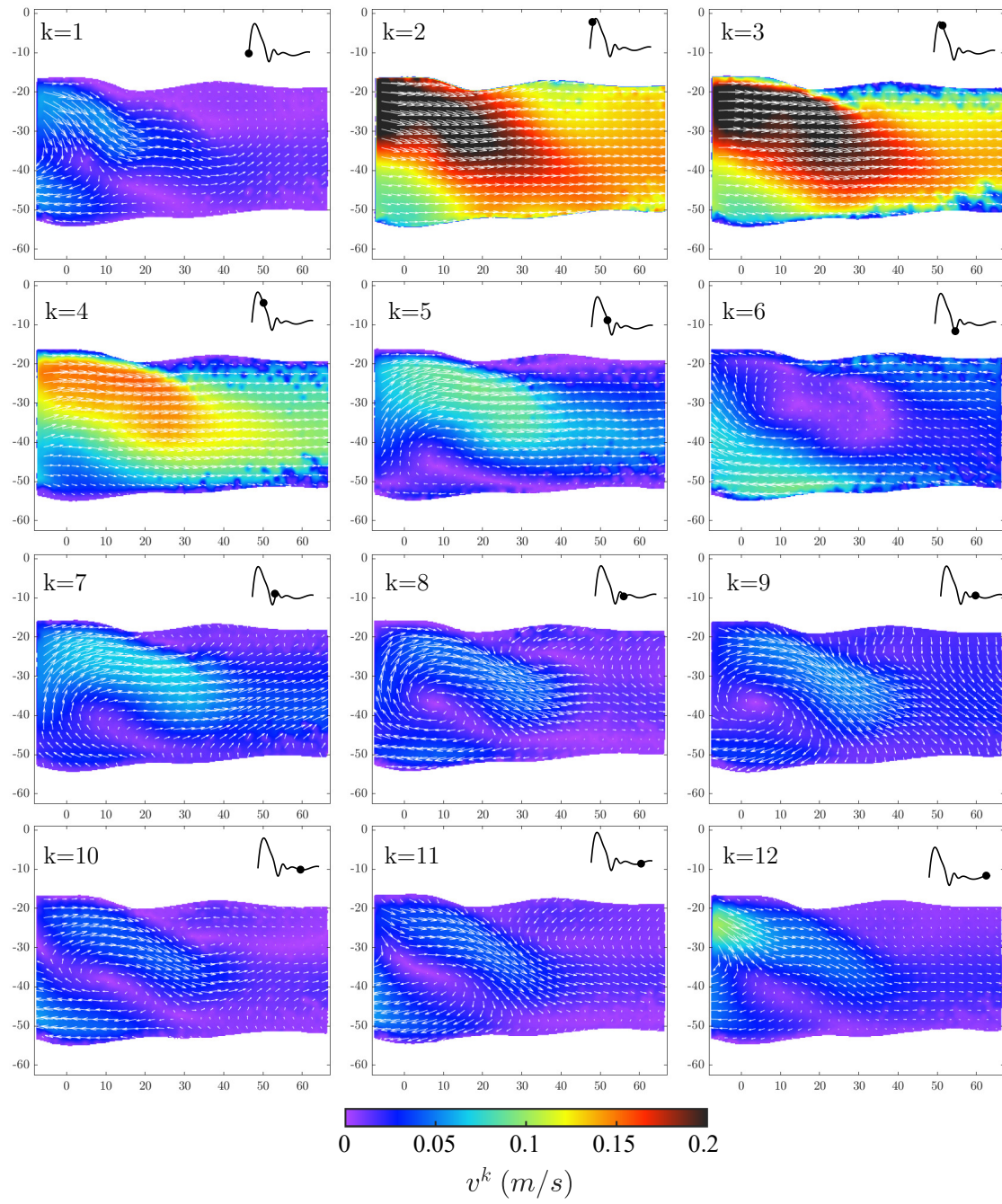


Figure D.2: Non-Newtonian fluid flow experiment fields.

Vortex identification

Identifying swirling motions can be executed with different methods. The most common criteria is the use of vorticity to localize and quantify rotational structures in a flow. However, vorticity is not the optimal parameter when studying shear flows. Indeed, the vorticity equation does not make the difference between actual vortices and shear. To avoid misinterpretation, other criteria were developed to better identify vortex motions. A good candidate is the use of swirling strength that only detects vortices and does not detect shear flow (Zhou et al. (1999)). This method is based on the analysis of the velocity gradient tensor and its eigenvalues. However, conversely with vorticity, the definition and time evolution equation of the swirling strength are not well defined (Cuissa and Steiner (2020)). Therefore, this criterion is not adapted in certain context of rapid evolution in flows or in quantifying and comparing vortex motions with other experiments, flow conditions, or types of fluid. The swirling strength criterion is often adapted to a specific fluid flow study and is not universal. The following sections provide short definitions of each criterion, advantages and drawbacks of each method, and applications to our aorta phantom cases.

E.0.1 Vorticity

Vorticity is a good indicator of rotational flow and can be used to understand the formation of vortex rings. The two previously cited criteria are based on the velocity gradient tensor \overline{D} which can be written as:

$$D_{ij} = \frac{\partial u_i}{\partial x_j} \quad (\text{E.0.1})$$

This second order tensor can be decomposed as a symmetric and an asymmetric tensors,

$$D_{ij} = S_{ij} + \Omega_{ij} \quad (\text{E.0.2})$$

where

$$S_{ij} = \frac{1}{2} \left(\frac{\partial u_i}{\partial x_j} + \frac{\partial u_j}{\partial x_i} \right) \quad (\text{E.0.3})$$

$$\Omega_{ij} = \frac{1}{2} \left(\frac{\partial u_i}{\partial x_j} - \frac{\partial u_j}{\partial x_i} \right) \quad (\text{E.0.4})$$

S_{ij} and Ω_{ij} are the rate-of-strain and vorticity tensors respectively.

It is generally accepted to mathematically define vorticity as the rotational of the velocity vector in a 2D plane xy thus omitting the factor $1/2$ from previous equation ¹:

$$\vec{\omega} = \nabla \wedge \vec{v} = \left(\frac{\partial u_y}{\partial x} - \frac{\partial u_x}{\partial y} \right) \vec{e}_z \quad (\text{E.0.5})$$

where \vec{e}_z is the unit vector in the z -axis perpendicular to xy plane. In this case, the rotation is supposed to occur in the xy plane and to remain in this plane from time to time.

Vorticity is not always related to an observable rotation of flow. It is more related to a local spin of a fluid particle and not necessarily to a body rotation of the fluid mass. If particles are flowing along straight lines in parallel but line speeds are different, shear exists in the flow. The partial derivatives in the vorticity equation can be non null. As a consequence this quantity is not always adapted to detect vortex rings, especially in the context of shear flows.

However, vorticity is a well defined quantity with an equation related to partial derivatives of velocity vectors. Therefore, this quantity and its magnitude can be compared directly between experiments, cycle instants, aorta models, inflow conditions etc. It makes the criterion and its definition are universal.

E.0.2 Swirling strength

The swirling strength criterion was first introduced by [Zhou et al. \(1999\)](#). Vortices are associated with regions where the velocity gradient tensor \overline{D} has complex eigenvalues. \overline{D} can be decomposed as :

$$\overline{D} = [v_r v_{cr} v_{ci}]^T \begin{bmatrix} \lambda_r & 0 & 0 \\ 0 & \lambda_{cr} & \lambda_{ci} \\ 0 & -\lambda_{ci} & \lambda_{cr} \end{bmatrix} [v_r v_{cr} v_{ci}]^T \quad (\text{E.0.6})$$

There are two scenarios for the properties of eigenvalues. Either the three eigenvalues are real or one is real λ_r and two are complex conjugates λ_+ , and λ_- such that $\lambda_{\pm} = \lambda_{cr} \pm \lambda_{ci}$ ². v_r , v_+ , and v_- are \overline{D} eigenvectors such that $v_{\pm} = v_{cr} \pm v_{ci}$. The complex part λ_{ci} provides information about curve motion of the flow and can be used to identify rotation.

Thus, the intensity of the swirling motion is given by the λ_{ci} which is called the swirling strength. To localize vortices, a threshold ϵ can be applied on λ_{ci} . Regions where $\lambda_{ci} > \epsilon$ indicate the presence of a vortex but do not provide information about the rotational direction. In theory, any value over zero should correspond to a vortex. Experimentally,

¹the factor $1/2$ is interesting to simplify calculus when focusing on the rotational period $T = 2\pi/|\Omega|$ but simply using the rotational is more convenient as a well defined mathematical tool.

²This property is imposed by the 3rd degree characteristic polynomial of the velocity gradient tensor and the fact that \overline{D} is a real matrix.

a threshold is often apply to manage velocity measurement errors and noise. However, this threshold is not well defined, lacks from a universal value, and is often adapted to the flow context.

To obtain more precise results, vorticity can be used to find the rotational direction of identified swirling structure with λ_{ci} (Tomkins and Adrian (2003)) thanks to a new quantity:

$$\Lambda_{ciXY} = \lambda_{ciXY} \frac{\omega_z}{|\omega_z|} \quad (\text{E.0.7})$$

Finally, as the λ_{ci} magnitude strongly depends on the studies system. Chen et al. (2018) recommend to normalize the swirling strength by the root mean square to ensure uniformity:

$$\Lambda_{ciXY}^{norm} = \frac{\Lambda_{ciXY}}{\Lambda_{ciXY}^{rms}} \quad (\text{E.0.8})$$

where Λ_{ciXY}^{rms} is the root mean square of Λ_{ciXY} . This technique allows to normalize the swirling strength with a property of the studies flow system. The goal is to propose a universal threshold value ϵ that could be applied to any vortex identification study. As an example, Chen et al. (2018) proposed two thresholds: 0.8 for 3D flow investigation and 1.5 for 2D flows. These threshold are applied to the quantity in equation E.0.8.

In the current study, vortices are tracked throughout time in a pulsatile flow. The flow structure strongly varies from one cycle instant to the other and so does the root mean square. As an example, during systole the flow is very organized in straight lines but becomes more chaotic in the diastolic phase. All along the cycle the two large vortices that are tracked maintain a coherent structure. In this context, the Λ_{ciXY} dividing tends to bias swirling strength analysis due to strong flow variations. As a consequence, only the Λ_{ciXY} criterion is computed to identify vortex locations. In our case, a threshold of $\epsilon = 10^{-3}$ is applied. This value was empirically determined .

In the present study, we mainly focus on vortex identification, localization and displacement but not on vortex rotational intensity quantification. The swirling strength quantity Λ_{ciXY}^{rms} is therefore perfectly adapted in our shear flow context. However, vorticity would be useful in the AD cases comparison as parallel data are available with numerical simulations and 4D-MRI. A more universal quantity would be more adapted for methods confrontation. The following sections show examples of the two criterion applications on our aorta phantom experiments.

E.0.3 Practical case on AA phantom

In the case of AA, figure E.1 shows the result of velocity fields, swirling strength and vorticity at a specific instant $k = 10$ where two swirling structures are visible. The swirling stress criterion allows to locate the two rotational structures that are visible on the velocity field. On the vorticity map, those swirling elements are surrounded by high vorticity regions (all in all, actual vortex and shear flow) and cannot be clearly identified for an observer or with a computer program. Even if focusing on a certain level of vorticity, the program would detect the near wall region upward from the narrowing that appear in

red on figure E.1 (c) which was associated to high shear rate in chapter 3, section 3.3.5. This is a typical example of the impossibility to use vorticity as a rotational flow detection tool. Indeed, the shear flow is too strong and is also detected by the vorticity criterion which does not make the difference between rotation and shear. On the contrary, the swirling strength criterion that was used in chapter 3 was very efficient. The drawback is that the quantity Λ_{ciXY}^{rms} cannot be directly compared to other fluid flows. The detection criteria was set to suit this specific experiment.

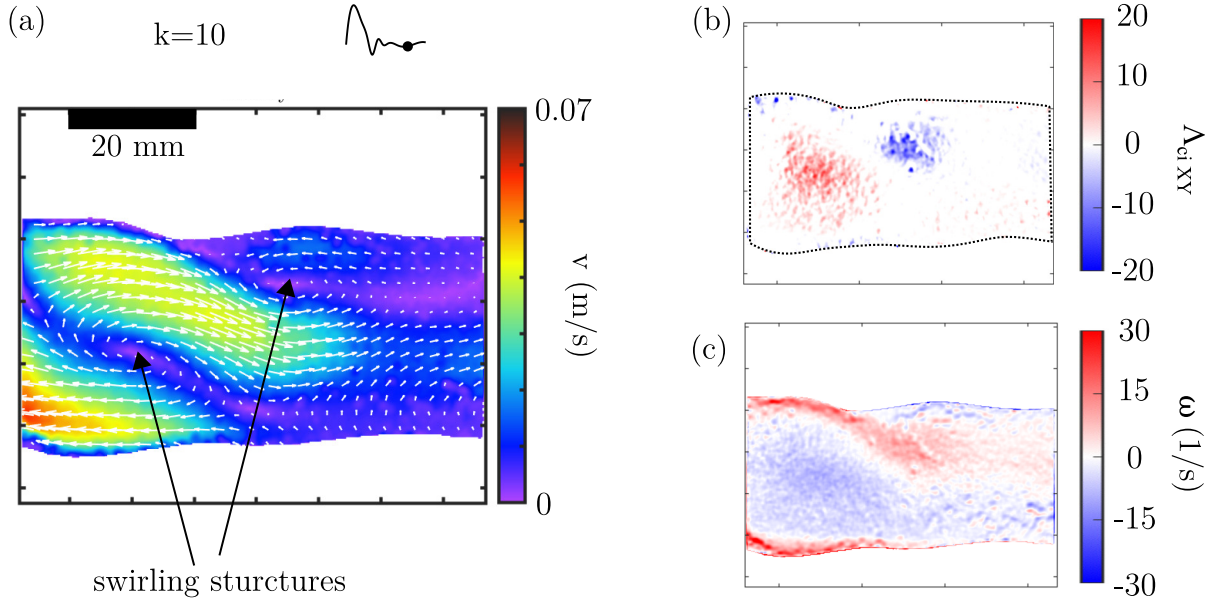


Figure E.1: Swirling structure identification at instant $k = 10$, (a) velocity fields with visible rotational flow regions, (b) swirling strength with vorticity sign criteria, and (c) vorticity.

E.0.4 Practical case on AD phantoms

In the case of AD1, figure E.1 shows the result of velocity field, swirling strength and vorticity at a specific instant $k = 5$ where two swirling structures are visible. Conversely with the AA case, both swirling strength and vorticity allows to locate the two visible rotational structures. Indeed, in all the rigid AD phantom, vorticity could be used as high intensity ω indicated the location of vortices. Shear flow is also detected — mostly near walls — but with much lower intensity than observable swirling structures. In this case, a threshold on ω allows to isolate rotational from shear flow. The difference with the previous AA study, is the phantom wall rigidity. Indeed, rigid walls tend to under-represent shear flows. Of course these observations are conducted with only one compliant and two rigid models that have different geometries. More experiments should be conducted to determine on which criteria is more adapted to which system. But it is interesting to note that swirling strength and vorticity are strongly dependent on the flow system with this concrete example.

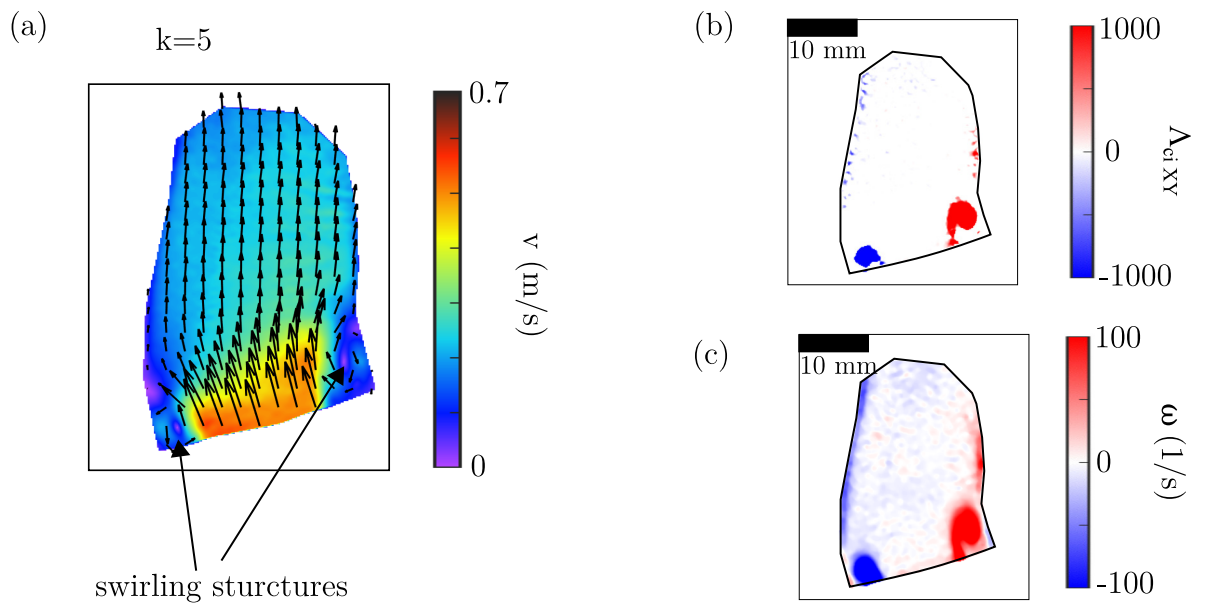


Figure E.2: Swirling structure identification at instant $k = 5$, (a) velocity fields with visible rotational flow regions, (b) swirling strength with vorticity sign criteria, and (c) vorticity.

Gradient underestimation

Computing velocity gradients with PIV imaging strongly depends on post treatment procedure. The fact that velocity fields are calculated with a certain "resolution" involves smoothing of vector fields depending on the how fine the resolution is. In PIV image post-processing, cross-correlation is achieved with a specified interrogation window size (pixel x pixel) and overlap (%). Tokgoz et al. (2012) showed that increasing the overlap and/or decreasing the interrogation window size increases the computed dissipation energy which derives from velocity gradients.

To illustrate this resolution dependency, velocity gradients $\left| \frac{du}{dy} \right|$ and $\left| \frac{dv}{dx} \right|$ were computed on a PIV image from the Newtonian experiment (chapter 3). First, the interrogation window were kept the same (1st pass 64x64, second and third pass 32x32 (pixel x pixel)) and the overlap varied from 0% to 87.5% (figure F.1, (left)). Second, the overlap was maintained constant (1st pass at 0%, second and third pass at 75%) but the interrogation windows size varied from 96x96 to 24x24 (figure F.1, (right)). Presented data correspond to mean absolute gradient averaged on the whole imaged ROI. Note that the results do not show an asymptotically limit for gradients. We may not identify the optimal cross-correlation settings by we may highlight the impact of those settings on computed velocity gradients.

To minimize underestimation, one may choose to decrease window size and increase overlap at their maximum. However, reliable cross-correlation requires a good match between window size, particles size and displacement and number of particles in an interrogation window. A number of 10 particles per window and displacement of 1/3 of the window size is often recommended as priority criteria when choosing cross-correlation parameters. Extremely decreasing the windows size may result in obtaining particle free areas, particles loss from one image to the other etc.

Therefore, one should bear in mind that computed velocity gradient cannot be directly compared to absolute values extracted from 4D flow-MRI. Indeed they are also concerned by velocity gradients smoothing because of MRI voxel resolution. However, concerning PIV experiments, they still allow to draw distributions and tendencies in the aorta phantom with quantities that derive from velocity gradients such as shear rates and shear stress.

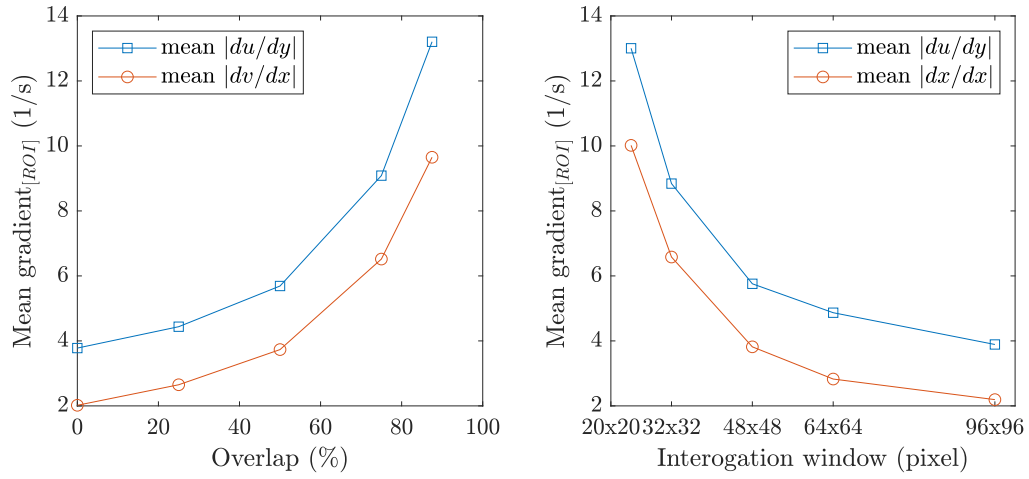


Figure F.1: Computed velocity gradient evolution when varying PIV cross-correlation parameters: interrogation windows overlap variations (left) and window size (right).

3D printing techniques : resins and material jetting

3D resin printing is based on polymerizing a resin to transform it in solid plastic by selective application of light. They are made up of a resin tank, a light source to solidify the resin, a platform that supports the 3D printed object and an elevator to rise up the platform. The principle is to solidify a 3D object layers by layers in the resin tank. In most cases, the light source always lights the same layer, thus traveling from one layer to the next one is ensured by the elevation of the platform that supports the object. Figure G.1 illustrates the principle of printing layers by layers.

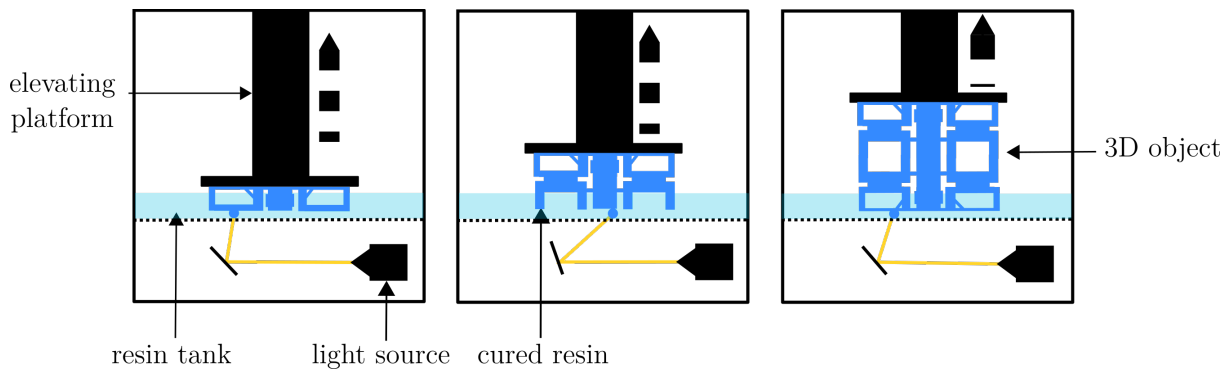


Figure G.1: 3d resin printing principle.

Most common 3D resin printing technologies are Stereolithography (SLA), Dark Light Projection (DLP), and Liquid Crystal Display(LCD). Those techniques are described and compared in the following paragraphs where the fundamental difference is the light source they use to cure the resin (figure G.2).

Stereolithography (SLA)

SLA uses a laser beam to selectively solidify parts of the resin which is stored in a resin tank. The laser beam is emitted at the bottom tank and is directed by mirrors to light a specific area in the resin to be cured. Thus, the laser beam cures the liquid spot by spot for each layer. When a layer is cured, the platform that supports to model rises up the height of a single layer. The process is repeated until the 3D model is completely

cured. The great advantage of this technique is the precision and the smooth surface finish (figure G.3).. The drawback of this technique is longer time to cure each layer as the laser beam has to trace the whole cross-section spot by spot.

Dark light projection (DLP)

DLP is similar to the SLA technique but it uses a digital projection surface instead of a laser beam as a light source. Therefore, instead of curing the resins spot by spot, it lights up the image of a complete layer at once thanks to the DLP screen. The light is projected on the resin thanks to LED screens or UV screen combined with a Digital Micro-mirror device (DMD). The last one is a array of moving micro-mirrors that direct the light projection to create a light pattern on the surface.

The disadvantage is the printing resolution, as it depends on the DMS mirrors density. These can be compared to square pixels that light up the resin. Expressed as a volume with the resin layer thickness, the final object is composed of voxels that depend on the DMD "resolution" and platform elevator steps. For complex and curved surfaces, it results in a staircase effect on the object as shown in figure G.3..

Liquid Crystal Display (LCD) / masked Stereolithography (mSLA)

LCD printing is a cost effective manufacturing technique compared to the previous one. It uses a LED light source that shines light through a LCD panel. The LCD panel blocks off this light on the areas that are not to be cured (hence the other name 'masked' Stereolithography). Like the DLP, the LCD photomask is composed of square pixels. Therefore the resolution of the LCD defines the resolution of the 3D printed object. Furthermore, the same issue with staircase effect can appear on the object surface (figure G.3).. The great advantage is the price thanks to the LCD screen that avoids using complex projection systems with lenses and mirrors.

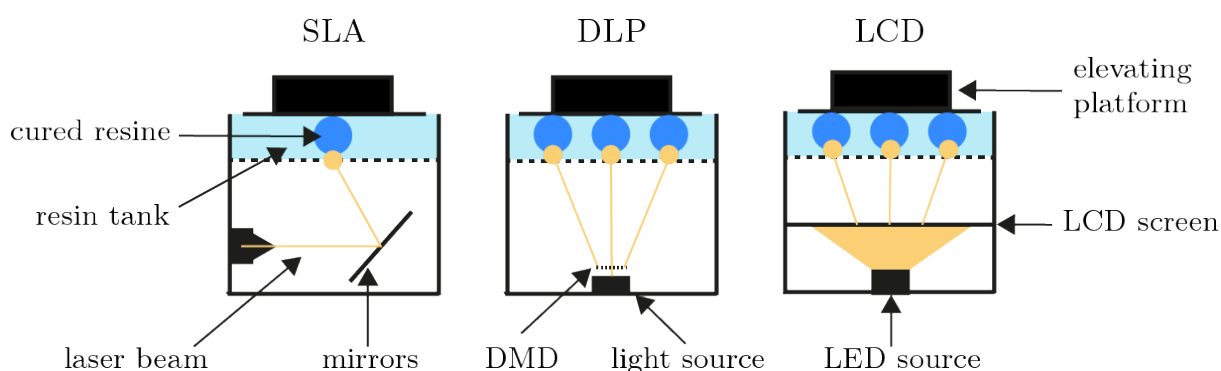


Figure G.2: 3d printing techniques SLA, DLP and LCD.

Material Jetting

This technique involves projecting droplets of resin or wax that are selectively deposited

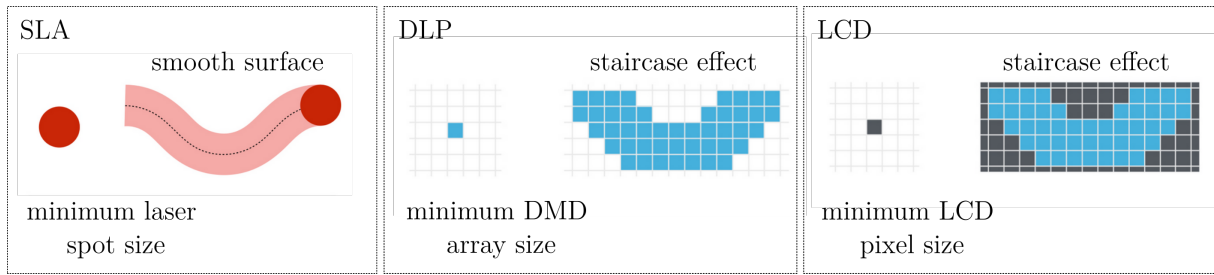


Figure G.3: 3d printing techniques and resolution specificities for SLA, DLP and LCD adapted from <https://theorthocosmos.com/wp-content/uploads/2017/03/MSLA.001.jpeg>

and cured on a platform. When using a photopolymer resin, droplets are cured with exposure to specific light source. The process is also executed layers by layers (figure G.4). This technique allows to mix different materials on a same 3D printed object with the use of multiple resin tanks. The weakness of the material jetting technique is the production of brittle 3D objects that are not always suitable for mechanical parts.

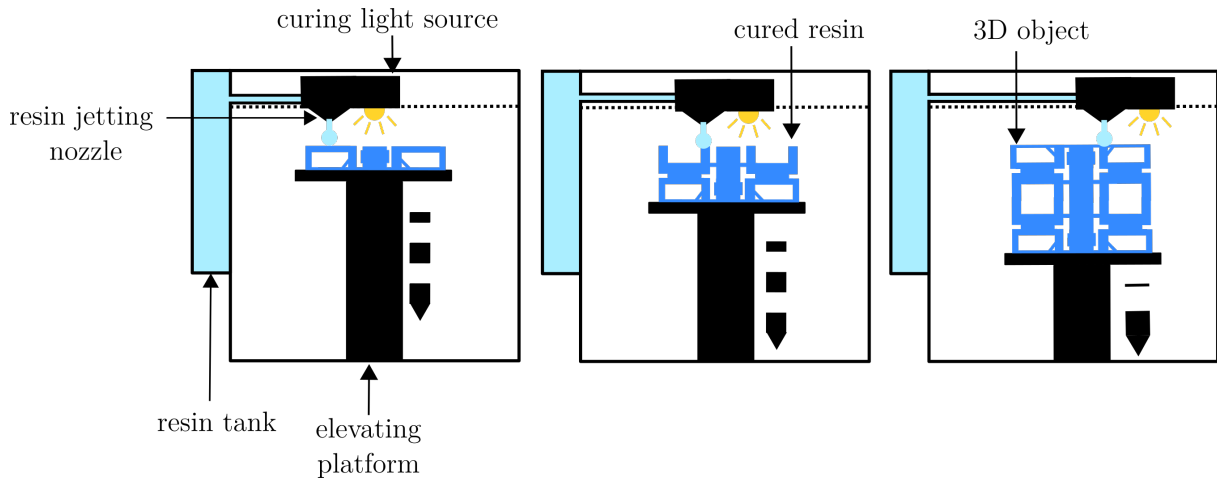


Figure G.4: Material jetting technique

Aortic dissection phantoms

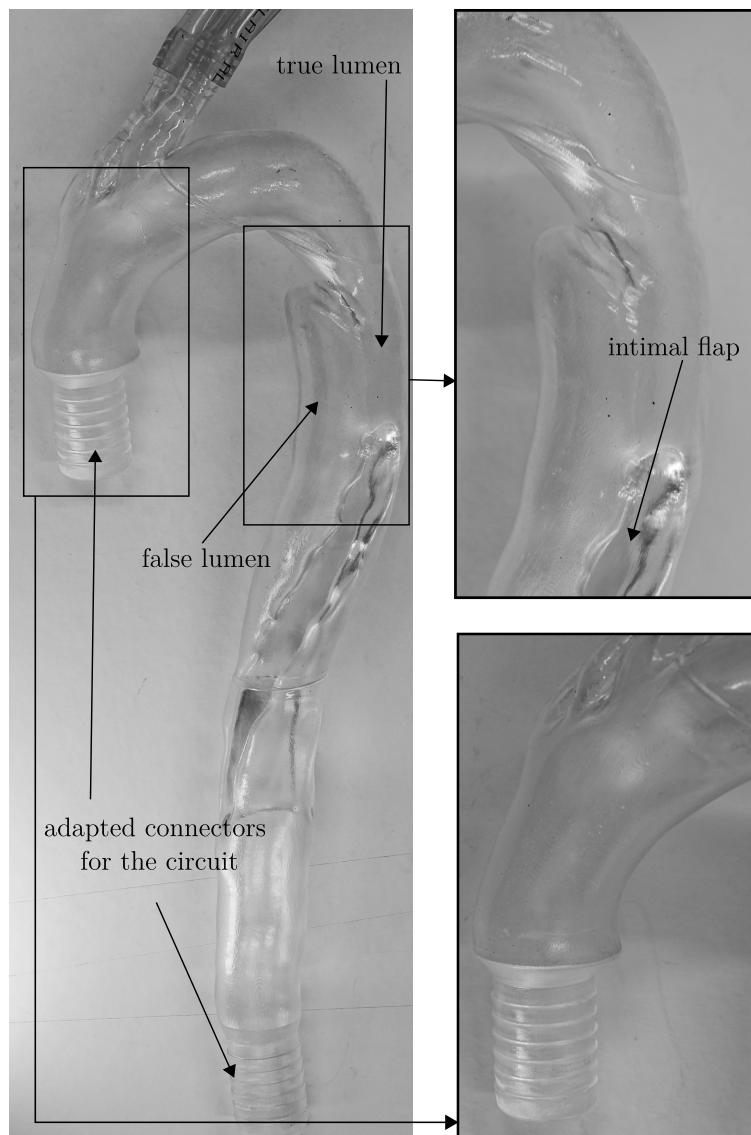


Figure H.1: AD1 phantom with focus on the intimal flap region with abnormal thinness. This region generates light distortions and reflections. Models inlet and outlet were reshaped to enable connection with mock loop.

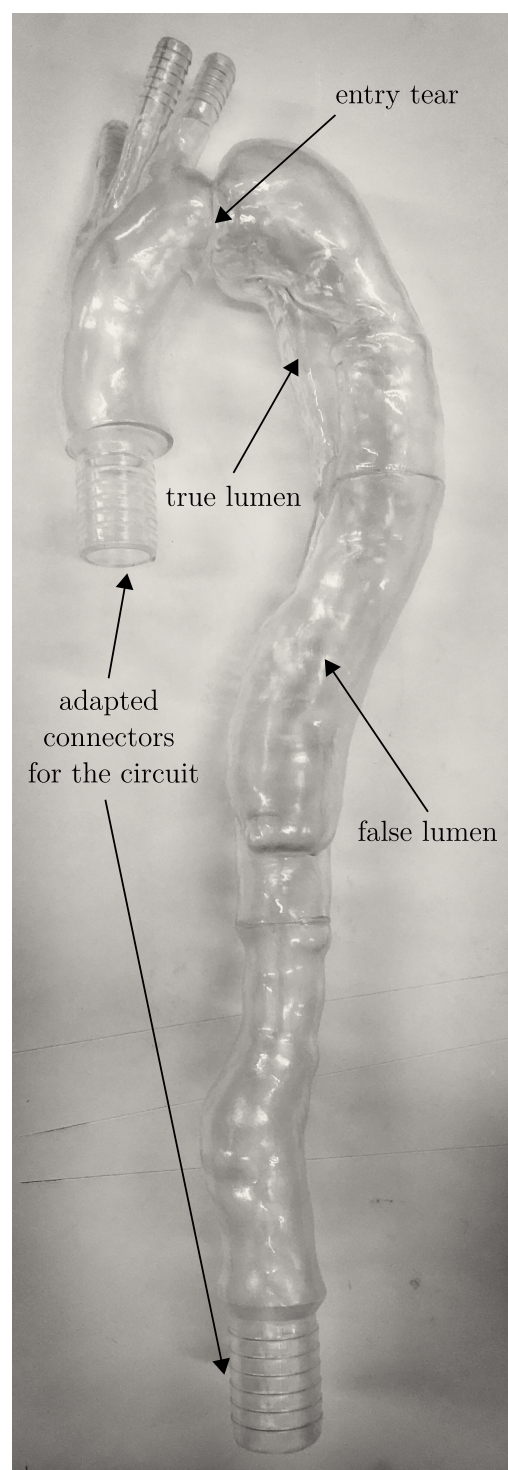
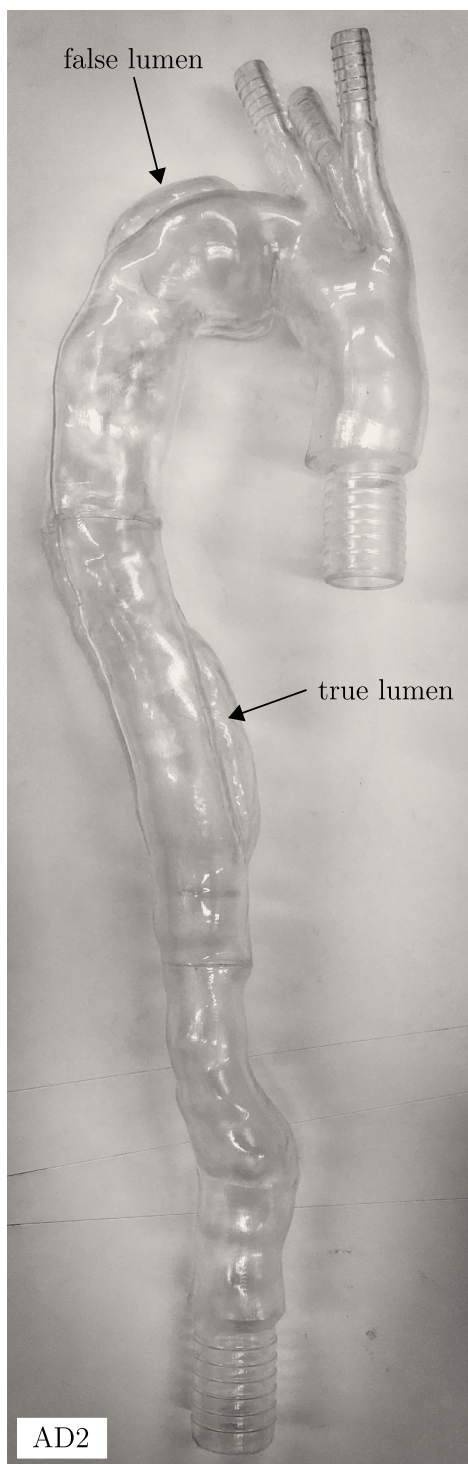


Figure H.2: AD2 phantom.

Publications and Conferences

Moravia, A., Simoëns, S., El Hajem, M., Bou-Saïd, B., Kulisa, P., Della-Schiava, N., & Lermusiaux, P. (2021). In vitro flow study in a compliant abdominal aorta phantom with a non-Newtonian blood-mimicking fluid. *Journal of Biomechanics*, 110899.

Moravia, A., Simoëns, S., Bou-Saïd, B., El Hajem, M., Pan, W., Kulisa, P., & Lermusiaux, P. (2021, June). In Vitro Assessment of Non-Newtonian Hemodynamics in Aorta Phantom with Particle Image Velocimetry. In *The 19th International Symposium on Flow Visualization (ISFV-19)* Shanghai Jiao Tong University, Shanghai, China, June 28-30, 2021.

Moravia, A., Pan, W., Walter-Le Berre, H., Menut, M., Bou-Saïd, B., El Hajem, M., ... & Naudin, I. (2019, August). In vitro assessment of abdominal aortic dissection hemodynamics based on particle image velocimetry. In *24ème Congrès Français de Mécanique CFM 2019*.

Moravia, A., Pan, W., Walter-Le Berre, H., Menut, M., Bou-Saïd, B., El Hajem, M., ... & Naudin, I. (2019, July). In vitro assessment of abdominal aorta non-newtonian hemodynamics based on particle image velocimetry. In *European Symposium of Biomechanics*.

AUTORISATION DE SOUTENANCE

Vu les dispositions de l'arrêté du 25 mai 2016,

Vu la demande du directeur de thèse

Monsieur S. SIMOENS

et les rapports de

Mme B. FROHNAPFEL

Professeure - Karlsruher Institut für Technologie (KIT) - ISTM - Kaiserstrasse 10
76131 Karlsruhe - Allemagne

et de

Mme N. KACHENOURA

Directrice de Recherche INSERM - Laboratoire d'Imagerie Biomédicale - Sorbonne Université
Campus des Cordeliers - 15 rue de l'Ecole de Médecine - 75006 Paris

Madame MORAVIA Anaïs

est autorisée à soutenir une thèse pour l'obtention du grade de **DOCTEUR**

Ecole doctorale Mécanique, Energétique, Génie Civil et Acoustique

Fait à Ecully, le 7 décembre 2021

Pour le directeur de l'Ecole centrale de Lyon
Le directeur des Formations



Grégory VIAL
